Properties of Ellerman Bombs and Implications about Formation Mechanisms

Christopher James Nelson

Submitted for the degree of
Doctor of Philosophy

School of Mathematics and Statistics

June 2015

Supervisors: Professor Robertus Erdélyi University of Sheffield

& Professor John Gerard Doyle Armagh Observatory

The University of Sheffield

Acknowledgements

Firstly, deserved official acknowledgments for the instrument teams who made this research possible. SDO/AIA and SDO/HMI data are used courtesy of NASA/SDO and the AIA and HMI science teams. Hinode is a Japanese mission developed and launched by ISAS/JAXA, collaborating with NAOJ as a domestic partner, NASA and STFC (U.K.) as international partners. Scientific operation of the Hinode mission is conducted by the Hinode science team organized at ISAS/JAXA. This team mainly consists of scientists from institutes in the partner countries. Support for the post-launch operation is provided by JAXA and NAOJ (Japan), STFC (U.K.), NASA, ESA, and NSC (Norway). DST/ROSA and DST/IBIS data used in this thesis were obtained with the facilities of the National Solar Observatory, which is operated by the Association of Universities for Research in Astronomy, Inc. (AURA), under cooperative agreement with the National Science Foundation. The Swedish 1-m Solar Telescope is operated on the island of La Palma by the Institute for Solar Physics of Stockholm University in the Spanish Observatorio del Roque de los Muchachos of the Instituto de Astrofsica de Canarias.

Secondly, I would like to express my gratitude to all of the funding bodies and institutions who have contributed financially to my studies, including my stipend and travel budget which came from STFC (U.K.) and was administered by Armagh Observatory. A big thank you must also go to the University of Sheffield and Armagh Observatory (and everyone involved) who have both found extra funds for me to go on research and observing visits (and probably many other things which I'm not aware of!) which have proved invaluable to my development as a researcher. I would also like to acknowledge the funding offered to me by the Solarnet Consortium through the Mobility of Young Researchers scheme for a research trip to the National Solar Observatory at Sunspot, New Mexico. Finally, I would like to thank Northumbria University, the University of Oslo, and the INAM 2014 organisers for their help with funding seminar and conference talks.

However, this funding would have been wasted if it wasn't for the people who were at the other end. Zhenghua, Kamalam, and Maria from Armagh showed incredible patience in getting me started in

the first few months. Mihalis Mathioudakis, Sergiy Shelyag, Rick Morton, Kevin Reardon, Han Uitenbroek, the staff at Debrecen Observatory, and the support staff at the DST (Doug, Mike, Joe, and Crystal) have all proved wonderful hosts to me as well. Your welcoming natures have made me feel at home wherever I have been. It really did help to make each trip something I look back on with fondness! I would also like to thank Martin Murphy in Armagh and Dave Robson in Sheffield for their technical support. A special thank you must go to Eamon Scullion who has always been keen to help, either with science or by inviting me for talks. Also, the table tennis in La Palma was just about the only thing that kept me sane!

To all of the people I've met in both Armagh and Sheffield over the course of this PhD, you have helped make the good bits of this PhD enjoyable and the difficult bits bearable. Aswin: Thank you for your hospitality on many occasions, hopefully we'll be able to head out for a curry and a couple of Cobras again soon. Adam: Thanks for letting me trade your petrol for Guinness and all of your help settling in in first year. All of my office mates in Sheffield: What can I say? It's been loud, often ridiculous, and definitely coffee-fueled over the last three-and-a-half years but the company in the office and the occasional beer over a game of snooker has been incredible. You have made coming to work (even during the write-up) a joy. Tom: Apart from one incident around Christmas where we lost a perfectly good deck chair, the random nights out and golf sessions have been great.

My sincerest thanks must go out to my supervisors Robertus and Gerry. I can't quite believe I have been so lucky as to have two such excellent mentors. You have both been so generous with your time and efforts over the past three-and-a-half years and have given me something to really aspire to. I would not be in the position I am today if it hadn't been for your support and belief.

I am also so grateful to my extended family, particularly Caroline and Richard. You have always been so kind letting me stay when we've been looking for a house after I've been away for a while. Trips to CentreParcs, random places in Europe, and the more-than occasional healthy meal were also very much enjoyed!

To my parents, thank you for everything. I'm sure you'll have a look through for any wrong 'k's! All of your care and love throughout my life is the reason I am where I am today.

Finally, thank you so much to Helen (soon to be Dr. Helen!). You have put up with me being away so much over the last few years (especially birthdays...), being 'mardy', and my inability to squeeze toothpaste tubes. I hope I can be as supportive to you when you're writing up as you have been to me. You have been wonderful.

Refereed Publications

Nelson, C. J., Doyle, J. G., Erdélyi, R.: (submitted), *On the Role of Flux Cancellation in Ellerman Bomb Formation*, *Mon. Not. Roy. Astron. Soc.*

Nelson, C. J., Scullion, E. M., Doyle, J. G., Freij, N., Erdélyi, R.: (2015), *Small-scale Structuring of Ellerman Bombs at the Solar Limb*, *Astrophys. J.*, **798**, 19.

Freij, N., Scullion, E. M., **Nelson, C. J.**, Mumford, S. J., Wedemeyer, S., Erdélyi, R.: (2014), *The Detection of Upwardly Propagating Waves Channeling Energy from the Chromosphere to the Low Corona*, *Astrophys. J.*, **791**, 61.

Erdélyi, R., Hague, A., **Nelson, C. J.**: (2014), *Effects of Stratification and Flows on P_1/P_2 Ratios and Anti-Node Shifts within Closed Loop Structures*, *Solar Phys.*, **289**, 167.

Nelson, C. J., Doyle, J. G.: (2013), *Excitation of an outflow from the lower solar atmosphere and a co-temporal EUV transient brightening*, *Astron. Astrophys.*, **560**, 31.

Nelson, C. J., Shelyag, S., Mathioudakis, M., Doyle, J. G., Madjarska, M. S., Uitenbroek, H., Erdélyi, R.: (2013), *Ellerman Bombs – Evidence for Magnetic Reconnection in the Lower Solar Atmosphere*, *Astrophys. J.*, **779**, 125.

Nelson, C. J., Doyle, J. G., Erdélyi, R., Huang, Z., Madjarska, M. S., Mathioudakis, M., Mumford, S. J., Reardon, K.: (2013), *Statistical Analysis of Small Ellerman Bomb Events*, *Solar Phys.*, **283**, 307.

Abstract

Ellerman bombs and surges are studied in this thesis in order that inferences about the formation mechanism of these features can be made. General introductions to the solar atmosphere and relevant observational techniques will be presented in Chapters 1 and 2, respectively.

Chapter 3 discusses the properties of small-scale brightenings in the Hα line wings. An automated detection algorithm identifies and tracks bright regions, before a null set of confidently identified Ellerman bombs is isolated and compared to the results of previous researches and the smaller features identified by the algorithm. Chapter 4 then compares numerical simulations of magnetic reconnection to the signatures of 7 Ellerman bombs. Each Ellerman bomb occurs co-spatial to a magnetic bi-pole, six of which exhibit flux cancellation or emergence offering potential evidence that magnetic reconnection is the driver of these features.

The properties of 22 Ellerman bombs at the solar limb are inferred in Chapter 5. Two in-depth case studies are presented which highlight the dynamical nature of individual features, including their morphological properties and potential links to the magnetic field. Chapter 6 discusses the physical properties of Moving Magnetic Features, the cancellation rates of which are measured, and how such properties fit into the hypothesised theory of magnetic reconnection as the driver of Ellerman bombs. An algebraic model of magnetic reconnection is employed such that upflow velocities, extension lengths, and local number densities can be derived. The outputs from this model agree well with measurements of Ellerman bombs returned in previous Chapters.

Finally, an isolated surge is studied in Chapter 7. The temporal evolution of the line-of-sight magnetic field shows no evidence of magnetic reconnection co-spatial to this surge; however, a blinker forms co-spatially with this feature. This offers compelling evidence that blinkers may be linked to photospheric mass supply.

Contents

Chapter 1

Introduction

1.1 Introduction

The Sun is the main source of light and energy to the Earth. Situated at a distance of 1.5×10^8 km (or 1 Astronomical Unit) from the Earth, the Sun has an approximate radius of 696 Mm which is around 109 times larger than the radius of the Earth. Overall, it is estimated that the Sun has a composition of around 90 per cent hydrogen and 10 per cent helium (with other elements occurring in small quantities). The 1.5×10^7 K temperature in the core of the Sun facilitates fusion, which supplies energy, through a series of steps, into the surrounding inter-planetary medium and eventually to the Earth. Without the Sun, specifically without the exact positioning of the Earth to the Sun, uninhabitable conditions would have inhibited the development of life on this planet, life which could easily be extinguished any second by a devastatingly large eruption of super-heated plasma from the Sun. It is not only the terrestrial significance of the Sun which interests scientists. The wider ranging processes which occur throughout its structure on both large and small-scales can shed light on the overall make-up of the Sun and a plethora of other stars. Understanding such processes can lead to a more comprehensive knowledge of the local surroundings in the solar system and the Universe.

1.2 The Solar Interior

1.2.1 The Core

The inner-most part of the Sun is the core, where temperatures of 15 MK facilitate thermonuclear fusion. With a radius of around 150 Mm (corresponding to one-fiftieth of the total volume of the Sun) and a density of 1.6×10^5 kg m^{-3} (see Fig. 1.1 which is made using values from Christensen-Dalsgaard et al. 1996), the core of the Sun fuses hydrogen to form helium and energy. The dominant mechanism by which helium is formed is known as the proton-proton cycle. A brief overview of this process will be presented here, however, the reader can see BOREXINO Collaboration (2014) (and references within) for a more in-depth discussion of these processes. The first step of the proton-proton cycle can be written as:

$$\mathrm{H}^1 + \mathrm{H}^1 \rightarrow {}_2\mathrm{D}^3 + \nu + e^+ + 1.44\ \mathrm{M}eV, \tag{1.1}$$

where 1 eV/k_B=11604 K. In this reaction, inverse-β decay leads to the formation of a positron and a neutron from the nucleus of one of the approaching H atoms. The unchanged H^1 atom then interacts with the neutron to form a deutron and a neutrino, releasing energy. The second step in the chain sees the newly formed deutron interact with another H^1 atom to form a helium isotope (missing one of the neutrons required to form a normal nucleus) and to release a high energy gamma ray. This step can be written as:

$${}_2\mathrm{D}^3 + \mathrm{H}^1 \rightarrow {}_2\mathrm{H}e^3 + \gamma + 5.49\ \mathrm{M}eV. \tag{1.2}$$

Finally, two helium isotypes interact, forming a stable helium atom, as well as two hydrogen atoms in the following reaction:

$${}_2\mathrm{H}e^3 + {}_2\mathrm{H}e^3 \rightarrow {}_2\mathrm{H}e^4 + \mathrm{H}^1 + \mathrm{H}^1 + 12.85\ \mathrm{M}eV. \tag{1.3}$$

The overall energy release from the process totals approximately 26.73 MeV (BOREXINO Collaboration 2014). Although photons would escape the Sun within seconds at the speed of light, the short mean free path (the average distance a photon travels unimpeded) slows, and increases the wavelength of, photons such that visible light emission at the solar surface occurs hundreds of thousands of years after the initial fusion (see, for example, Mitalas and Sills 1992).

As tiny particles which do not interact easily with matter, neutrinos escape through the Sun at almost the speed of light, out into the solar system (BOREXINO Collaboration 2014). Due to the temperature dependence of photon-photon neutrino production, the development of equipment which could measure the density of solar neutrino emission in the 1960s was hailed as a major step in confirming the correctness of solar models. Unfortunately, such corroboration did not occur. Multiple experiments recorded short-falls in the number of neutrino detections to those expected for a solar core of 15 MK and the 'solar neutrino problem' was formed. One popular solution to this problem which has gained weight in recent years is the Mikheyev-Smirnov-Wolfenstein (MSW; see Wolfenstein 1978, Mikheyev and Smirnov 1985 for more information) theory, whereby neutrinos are able to change type from the initial electron neutrinos to muon or tau neutrinos. The short-fall in electron neutrino measurements could, therefore, be explained by the conversion of many of these particles into different types. Modern experiments have begun to measure multiple types of neutrinos, adding weight to the theory.

1.2.2 The Radiative Zone

The radiative zone is found outside the core of the Sun at around 0.25 $R_{\odot}$ and reaches out to approximately 0.713 $R_{\odot}$. Solar models suggest that this region of the Sun rotates as a solid-body (as discussed by Thompson et al. 1996, Charbonneau 2010). Within this region, as the name suggests, radiative equilibrium is conserved and energy is transported by photons through absorption and re-

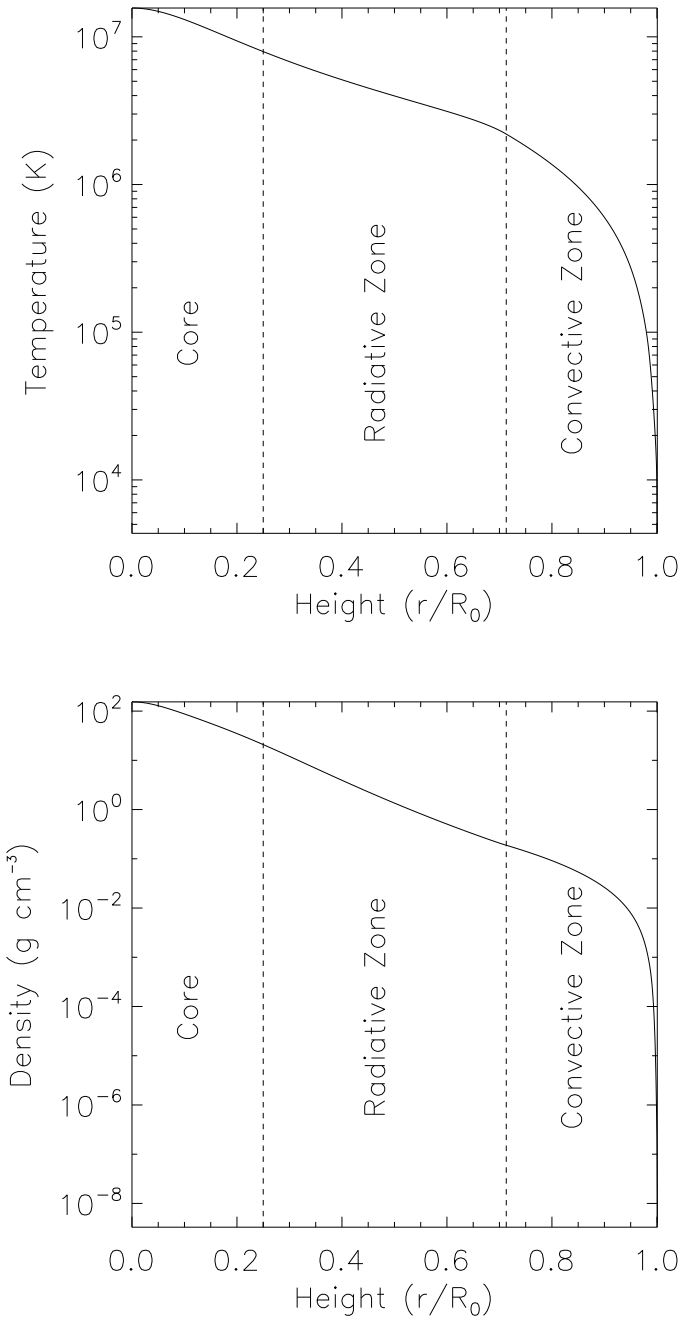

Figure 1.1: The temperature (top) and density (bottom) profiles of the interior of the Sun (where height is give as a function of solar radius, $R_\odot$). Each profile comes from the Dalsgaard Model S for the solar interior (see Christensen-Dalsgaard et al. (1996) for more details). Vertical lines indicate the suggested heights of each region of the solar interior.

emission. Such interactions occur at a high frequency and scatter the photons, at a higher wavelength, along an arbitrary path. If one were to plot a map which detailed the chain of absorptions and subsequent emissions occurring through time, one would observe a traditional random walk (as was discussed by Mitalas and Sills 1992). According to the Dalsgaard Model S (Christensen-Dalsgaard et al. 1996), both the temperature and density decrease exponentially with radius in the radiative zone (as can be seen in Fig. 1.1). The density falls around two orders of magitude from approximate values of 20 g cm^{-3} to 0.2 g cm^{-3} or, in a more accessible form, from the density of gold to cork; the temperature drops from 10 MK to around 2 MK. Mathematically, the radial temperature gradient in the radiative zone can be written as:

$$\frac{dT}{dr} = -\frac{3\kappa(r)\rho(r)L}{64\sigma_{\rm SB}T(r)^3\pi r^2}, \tag{1.4}$$

where T, κ, ρ, L, and $\sigma_{\rm SB}$ are the temperature, Rosseland mean opacity, density, luminosity, and Stefan-Boltzmann constant, respectively.

1.2.3 The Convective Zone

In the convective zone, the solid-body rotation exhibited within the radiative zone is replaced by differential rotation (where angular velocity can be written as a function of latitude). At the equator, the rotational period is around 25 days, however, this increases to approximately 35 days at the poles (see Thompson et al. 1996 for more information). On top of this, the lower temperatures in the convective zone facilitate the reduction in the percentage of fully-ionised elements. Heavier elements are able to retain their inner electrons, thereby, increasing the opacity of the plasma such that convective heating replaces radiative transfer as the dominant energy supply method to outer regions of the Sun. The on-set of convective motions are governed by the Schwarzschild

criteria (see Schwarzschild 1906) which can be written as:

$$\left|\frac{dT}{dr}\right| > \frac{\gamma - 1}{\gamma}\frac{gm}{k_{\mathrm{B}}}, \tag{1.5}$$

where g, m, and k_{B} are the gravitational acceleration, mean particle mass, and Boltzmann constant, respectively. In a fully ionised monatomic gas, $\gamma = 5/3$.

Should a plasma region satisfy the required conditions, the Schwartzschild criterion leads to vertical motions which supplement the differential flows. If the temperature gradient is sufficient, a 'blob' of plasma which is displaced vertically can expand sufficiently to reduce the density and induce bouyancy. Once the plasma reaches the surface of the Sun, radiation is able to escape into the solar system, hence reducing the opacity and returning the plasma to convective stability. The plasma then cools and falls, being replaced by hotter convectively unstable plasma from below. Essentially, this mechanism is comparable to the process of boiling water, where the bottom of a pan heats the liquid until it rises and loses energy at the surface before falling. The physical parameters in the convective zone (plotted in Fig. 1.1 from Christensen-Dalsgaard et al. 1996) change rapidly with height. The temperature falls two orders of magnitude to around 6000 K and the density drops to approximately 10^{-7} g cm^{-3} (which is an order of magnitude lower than the air density at sea level).

Solar dynamo models (reviewed in Charbonneau 2010) often cite a fourth interior region between the radiative zone and the convective zone called the *tachocline*. Believed to be almost negligible in width, the tachocline is a region of high shear induced by the interaction of the solid-body radiative zone rotation and the differential rotation of the convective zone. Despite the relative narrowness of the tachocline, it is thought to play a vital role in the generation of strong magnetic fields which emerge as active regions (ARs) in the photosphere (for more information, see Charbonneau 2010).

1.3 The Solar Atmosphere

1.3.1 The Photosphere

The photosphere is the lowest of the four regions which are commonly cited to comprise the solar atmosphere (along with the chromosphere, the transition region, and the corona). A plot similar to Fig. 1.1 is included for reference for the solar atmosphere (outlining the standard temperature and density profiles) in Fig. 1.2. With a name derived from the Greek word for light, the photosphere emits the dominant visible light from the Sun and, hence, forms the solar disk as observed from the Earth. In the photosphere, small-scale convective motions, generated in the solar interior, can be easily observed in high-resolution data as granules within, for example, the G-band continuum (as plotted in Fig. 1.3). Each individual granular cell has a diametre on the order of 1-2 Mm and a typical characteristic lifetime of 10 minutes. These cells are formed by hot, rising plasma which reaches the top of the convective 'bubble', before cooling and concurrently getting pushed aside by the continued rise of warmer plasma and then sinking down at the edge of the granule in the inter-granular lanes (similar to the process of boiling water).

In Fig. 1.3, a $30'' \times 30''$ field-of-view (FOV) sampled by the Rapid Oscillations of the Solar Atmosphere (ROSA) instrument at the Dunn Solar Telescope (DST) in Sunspot, New Mexico is plotted to depict such granulation. The top right portion of the image depicts a sunspot umbra and penumbra to compare to the small-scale structuring in the remainder of the image. A white box outlines the FOV considered in Fig. 1.4 where a co-spatial FOV, temporally separated by 10 minutes is portrayed. The white contours overlaid on both frames outline the dark inter-granular lanes from the initial (left hand) frame which, it is easy to see, do not correspond to the frame 10 minutes later (right frame). Such dynamics are typical of the evolution of the lower regions of the photosphere.

The high plasma-β (the ratio of magnetic pressure to gas pressure) in the photosphere indicates the dominance of convective forces over magnetic forces.

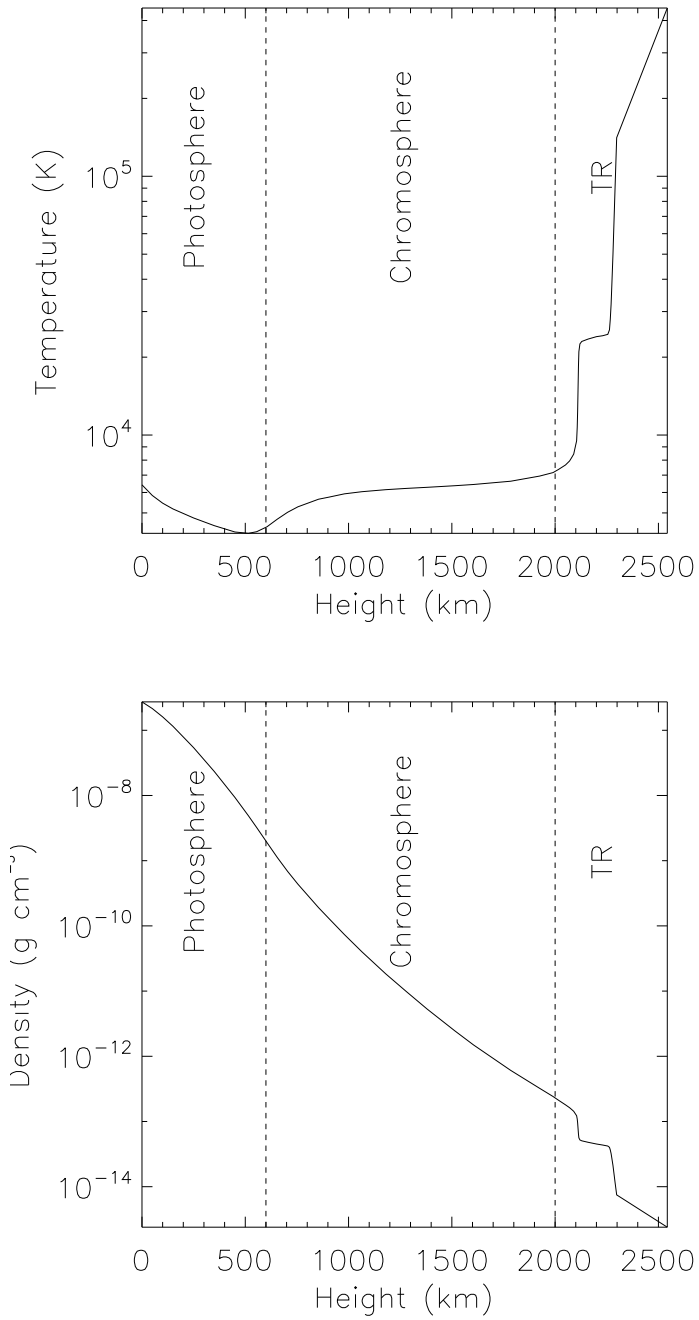

Figure 1.2: Temperature (top) and density (bottom) values for heights in the solar atmosphere according to the VAL-C quiet Sun solar model. The approximate boundaries between each region of the solar atmosphere are indicated by vertical lines on both plots (the reader should note the use of the word 'approximate').

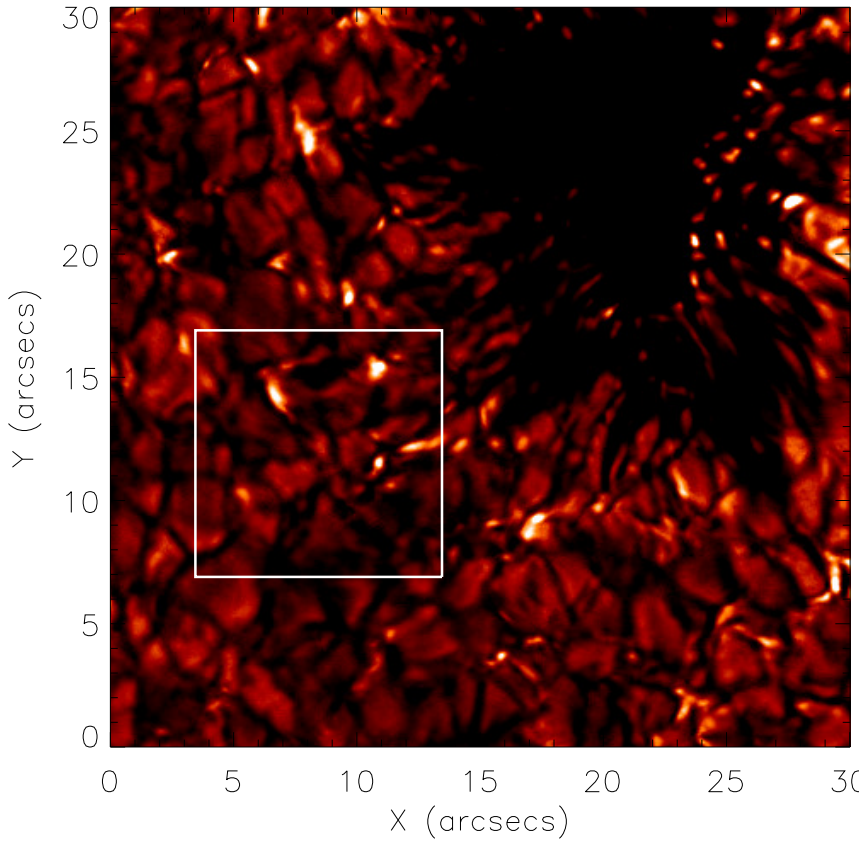

Figure 1.3: A $30'' \times 30''$ FOV close to a sunspot (the large, dark fragmented patch evident at $x_c = 20''$, $y_c = 25''$) in AR 11126 sampled in the G-band continuum by the DST/ROSA instrument. These data were observed by Professor J. G. Doyle and collaborators on 18th November 2010. The white box outlines the region plotted in Fig. 1.4.

As such, small-scale magnetic fields, which emerge into the photosphere with granular up-flows, are swept into the inter-granular lanes, allowing the build-up of flux densities of 10^3 Mx cm^{-2} (as simulated by, for example, Shelyag et al. 2007). Evidence of this flux build-up is observed within the inter-granular lanes as phenomena known as magnetic bright points (or MBPs). These events are believed to form as a result of the reduced pressure and increased temperature in the plasma occupied by the magnetic field, hence reducing the opacity and allowing the observer to sample deeper into the Sun (recent analysis of these features can be found in, *e.g.*, Utz et al. 2010, Keys et al. 2011). Observations of the G-band continuum (presented in Fig. 1.3) are excellent for observing MBPs. The lifetimes and spatial scales of these events are both close to the limits of current observational instrumentation (with lifetimes on the order of minutes and diametres of around 400 km estimated by Crockett et al. 2010); however, their links to the small-scale magnetic fields present in the photosphere provide an excellent diagnostic tool for solar observers (Shelyag et al. 2007).

Not all phenomena observed within the photosphere evolve on such short timescales. ARs, where strong magnetic fields penetrate through the solar surface to extend away into the outer atmosphere and inter-planetary medium, often contain sunspots and pores which can remain for days or even weeks. These events, which are characterised by dark 'blobs' on the solar surface in white-light or continuum images, have radii ranging between 2 Mm and 200 Mm and magnetic field strengths of thousands of Gauss. The lower intensity and size of sunspots has allowed them to be observed from the Earth for centuries (famously, for example, Galileo traced the outlines of sunspots as they crossed the solar disk) and, as such, they make up one of the oldest topics of study in solar physics. The strong magnetic fields which exist within the sunspot are believed to act as a waveguide from the lower solar atmosphere, into the outer layers, potentially allowing the upward propagation of waves (see, for example, Freij et al. 2014).

The physical properties of the photosphere are summarised within the 'Pho-

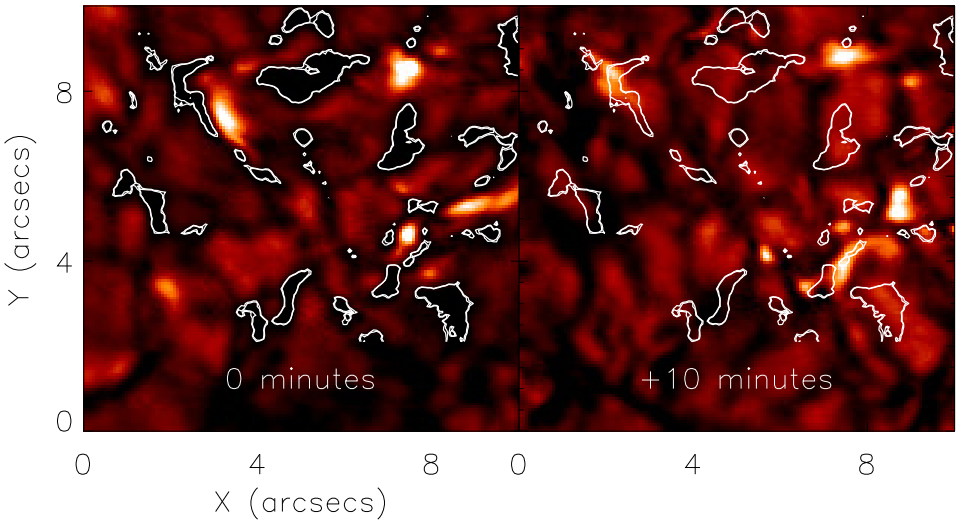

Figure 1.4: Two $10'' \times 10''$ FOV highlighting the dynamic evolution of the *G*-band continuum on temporal scales of around 10 minutes. These data were observed by the Professor J. G. Doyle and collaborators on 18th November 2010.

tosphere' segments of Fig. 1.2 (which is plotted given values from the VAL-C model suggested by Vernazza et al. 1981). It can be inferred that the temperature decreases with height from around 6000 K at the $\tau_{5000} = 1$ continuum to 4500 K at the temperature minimum region (which is situated around 500 km in height) before slowly increasing up to approximately 7000 K at the base of the chromosphere. A sharp, exponential drop-off in density is also observed, falling two orders of magnitude in only 600 km to approximately 10^{-9} g cm^{-3}.

1.3.2 The Chromosphere

The chromosphere is the layer which forms above the photosphere. This region of the solar atmosphere is traditionally classified as forming between 800 km and 2000 km in height. More modern researches, however, have begun questioning this traditional view (see, for example, Rutten 2012), inspired by the continuing complexities which have been observed as better observational equipment

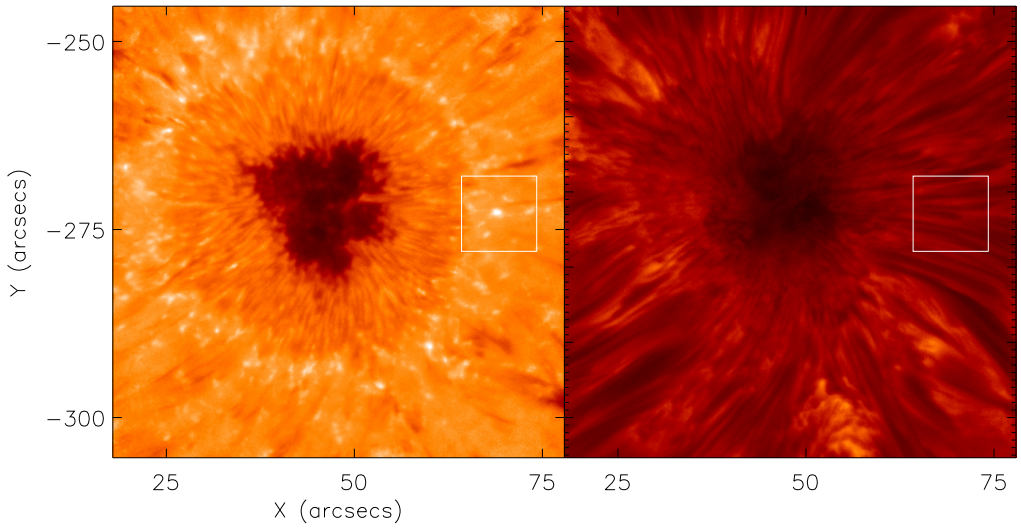

Figure 1.5: A 60″ by 60″ field-of-view (FOV) sampled in the Hα line wing (left frame) and the Hα line core (right frame) portraying the upper photosphere and chromosphere around a sunspot in AR 11579, respectively. These data were collected by the author and collaborators on 30th September 2012 using the DST/IBIS instrument. The white box outlines the FOV analysed in Fig. 1.6.

has been developed. It is now generally accepted that the chromosphere is not a fixed layer around the Sun. Instead, it is thought to be compressed or expanded in specific regions, or to form higher or lower due to the relationships of the chromosphere with the under-lying photosphere or the over-lying transition region. In Fig. 1.5, a FOV containing a large sunspot is plotted for the blue wing (left frame) and line core (right frame) of the Hα line profile. The overlying chromosphere (line core) is easily observed to obscure the photosphere (line wings). The white box outlines the FOV analysed in Fig. 1.6. A general overview of the current understanding of the Hα line profile will be presented in Chapter 2.

Recent high-resolution observations have highlighted the ubiquitous nature of waves within the chromosphere. Here, a brief excerpt of research is introduced to give the reader a sense of the magnitude of analyses into chromospheric os-

cillations. Spicules, for example, are commonly observed as vertical extensions away from the disk at solar limb (which can be considered as being similar to blades of grass) and have been put forward as an excellent candidate for guiding waves into the outer solar atmosphere (see, for example, De Pontieu et al. 2007); however, their abilities to heat the outer layers of the Sun, such as the corona, are still debated (*e.g.*, Vanninathan et al. 2012). More horizontal structures, such as mottles, have also been analysed using chromospheric time-lapses, with evidence of energetic, standing sausage waves being found (see Morton et al. 2012). On a larger scale, upwardly propagating waves (UPWs) around sunspots and pores have been shown to propagate into the lower transition region, potentially depositing significant amounts of energy (as discussed by Freij et al. 2014). Overall, it can be summarised that the chromosphere is an incredibly dynamic layer of the solar atmosphere which somehow couples with the photosphere to provide energy into the outer layers of the solar atmosphere. Energy estimates for waves which have been observed to date over-subscribe the amount of energy required to heat the corona (by several orders of magnitude), suggesting that the question to answer is no longer about whether the required energy exists, but more about how such energy is transported to, and dissipated in, the corona.

Once again, this subsection ends with a short discussion of the physical properties of this region for the quiet Sun as shown in Fig. 1.2 (suggested by Vernazza et al. 1981). The section of interest here is within the portion of the plots labelled 'Chromosphere'. The temperature within this region of the solar atmosphere is relatively constant for much of its height (with temperatures around 8000 K), however, towards the top of the chromosphere, sharp increases in temperature are found up to around 20000 K. The density continues to drop off exponentially to values close to 10^{-12} g cm^{-3}.

1.3.3 The Transition Region

The transition region is the thin layer in the solar atmosphere between the chromosphere and corona where temperature and density gradients are large. Numerous instruments have been launched on space-borne satellites with the specific aim of furthering understanding of this complex region. Indeed, the Transition Region And Coronal Explorer (TRACE; Handy et al. 1999), the SOlar and Heliospheric Observatory (SOHO; Domingo et al. 1995), and the Solar Dynamics Observatory (SDO; Pesnell et al. 2012) all carry instruments specifically designed to probe the physics of this system. Two main theories have been presented to account for the rapid temperature increases which occur within this layer of the Sun (see, for example, Zirker 1993). These are magneto-hydrodynamic (MHD) waves which transfer energy from other regions of the Sun and magnetic reconnection occurring within the transition region itself (see Anderson-Huang 1998). To date, no consensus exists from the community as to which of these processes is the most likely candidate for supplying the required energy.

The recent Hi-C sounding-rocket mission (Kobayashi et al. 2014), which was launched from White Sands missile base, New Mexico, did observe small-scale 'sparkles' (see Régnier et al. 2014) in the transition region. The sparkles were hypothesised to be the observational signature of small-scale reconnection events, known as nano-flares, occurring in the transition region which could be supplying the required energy to heat the local plasma to temperatures of millions of degrees Kelvin. Another larger-scale event observed around the transition region are blinkers (first presented by Harrison 1997 and recently by Roussev et al. 2001, Marik and Erdélyi 2002, Madjarska et al. 2006, Subramanian et al. 2012), which form with diametres of the order of several Mm. These events have also been hypothesised to be caused by reconnection within the upper atmosphere. Data collected by the Interface Region Imaging Spectrograph (IRIS; De Pontieu et al. 2014) has recently begun to shed light on this complex region of the solar atmosphere (see, for example, Testa et al. 2014, Hansteen et al.

2014, Huang et al. 2014) and should offer further clues about the make-up of this layer in the future.

The physical properties of the quiet Sun transition region are plotted in the section of Fig. 1.2 (again, taken from the model presented by Vernazza et al. 1981) labelled 'TR'. As with the upper section of the chromosphere, sharp increases in temperature occur in the transition region according to this model with temperatures reaching up to hundreds of thousands of Kelvin. The density continues to drop a further two orders of magnitude. It is interesting to note how the temperature and density profiles are no longer smooth curves as in the photosphere and chromosphere, with plateaus in both profiles indicative of the complex physics which undermines the huge temperature increases.

1.3.4 The Corona

After our long journey from the core of the Sun, this Section finally discusses the solar corona. This region of the solar atmosphere is widely identified as the faint halo which visually surrounds the Moon during a total solar eclipse. Despite being almost unobservable from the Earth ($\sim 10^6$ times fainter than the photosphere), the corona is an extremely interesting region of the solar atmosphere. By using a variety of space-borne satellites, the temperature of the corona has been estimated to reach over 1 MK (well over the 4500 K temperature of the photosphere). Energy supply into the corona is one of the main questions which requires answering in modern solar physics. As any budding physicist will tell you, as you move away from a heat source (in this case, the core of the Sun), you expect the temperature to drop, yet this does not occur for the corona.

Many theories have been put forward to explain the extreme temperatures of the corona. Each of these theories falls into one of two categories which can be concisely listed as magnetic reconnection and MHD waves. Magnetic reconnection, the mechanism by which complex magnetic fields are relaxed and energy released into the solar atmosphere, is the driver of large scale solar flares and coronal mass ejections (CMEs) which launch plasma into the inter-planetary

medium at speeds of up to 3000 km s^{-1}. Such plasma ejections can interact with both satellites around the Earth and the magnetic field on the Earth, leading to electrical black-outs as well as spectacular aurora, known as the Northern and Southern lights in the Arctic and Antarctic, respectively. During the periods of solar minimum, large X-Class flares (the most energetic known flares) can be absent from the solar atmosphere for periods of months to years, however, the temperature of the quiet Sun corona does not drop below the average of ~ 1.5 MK. This means that the ability of the magnetic reconnection hypothesis to heat the corona relies more on ubiquitous small-scale reconnection events known as nano-flares which occur below the spatial-resolution of current instrumentation (suggested by, for example, Doyle and Butler 1985, Parker 1988). To complicate this issue further, there is a lack of coronal magnetogram data (quantitative measurements of the coronal magnetic field components) meaning any small-scale events observed in the corona can not be tied conclusively to the magnetic field.

MHD wave-based heating theories are focused around the concept that energy in the photosphere and chromosphere propagates along magnetic waveguides in the form of oscillations which dump this energy in the upper atmosphere. The existence of magnetic field in the solar atmosphere modifies hydrodynamical wave theory from simple acoustic waves, to both magneto-acoustic waves and purely magnetic waves (a good introduction to such waves can be found in Roberts 1981a, Roberts 1981b, Edwin and Roberts 1983; Goedbloed and Poedts 2004 presented an excellent overview). These waves can take many forms (meaning it would be futile to attempt to fully describe them in this brief introduction) and have been observed both locally, guided by structures such as coronal loops and filaments, and globally, as Moreton waves (large-scale solar tsunamis which sweep across the surface of the Sun). Although energy estimates for wave energy transport into the corona have over-subscribed the 200-400 W m^{-2} required to heat the quiet Sun corona, no universal wave heating theory has been accepted by the solar physics community.

As in previous subsections, this brief introduction is concluded by outlining the physical properties of the corona. The temperatures in the corona are of the order of 10^6 K. The high temperatures in the corona were inferred thanks to the discovery of highly ionised heavy elements, such as iron, strongly emitted in the coronal EUV spectrum. Due to the protective nature of the terrestrial atmosphere which blocks coronal EUV light, most observations of the corona are taken by space-borne instruments. The density in the corona is lower than any vacuum which can currently be created on Earth, and continues to drop as the corona stretches out, past the Earth and into the far reaches of the solar system.

1.4 Analysed Features

1.4.1 Ellerman Bombs

Basic Information

On the 21st September 1915, a curious phenomenon was recorded to occur in a sunspot group by Ferdinand Ellerman. Observing the Hα line (6562.8 Å) at the Mount Wilson Solar Observatory, Ellerman (1917) noted a "very brilliant and very narrow band extending four or five angstroms on either side of the line, but not crossing it" which lasted a couple of minutes and then "faded away and was not seen again". This was the first recorded observation of an Ellerman bomb (although the event was originally called a 'hydrogen bomb'). Over the following years, further observations were completed and spectrograms recorded of these features to estimate initial measurements of their statistical properties. With lifetimes of between 3-10 minutes, Ellerman concluded that these events occurred exclusively in ARs, "especially groups which are developing and composed of many members". It should be noted that Ellerman suggested that such phenomena could be similar to an event reported by Mitchell (1909) using the Haverford College Observatory. It was

concluded that this Ellerman bomb "must have been an unusually large one to have been seen by the instrument used by Dr Mitchell".

Following on from their discovery, these 'hydrogen bombs' have been extensively researched by the community. These events were reported under a variety of names, such as 'petit points' (Lyot 1944) and 'moustaches' (Severny 1956), before they were linked together under the umbrella term of 'Ellerman bombs' by McMath et al. (1960). Due to the occurrence of Ellerman bombs in emerging ARs, McMath et al. analysed the statistical correlation between the formation of these events and the release of solar flares, large-scale explosive phenomena which were easily observable using the available instrumentation. It was found that Ellerman bombs were not pre-cursors for flares, either in temporal or spatial terms. In a further review, Severny (1964) discussed the similarity of Ellerman bomb spectra with larger-scale flares. It was also suggested that Ellerman bombs formed in the photosphere and could, occasionally, be linked to "the appearance of dark material or filaments emerging from the point-like region that generates moustaches".

The potential link between Ellerman bombs and the ejection of filamentary material suggested by Severny (1964) formed the basis of the following decades research. Rust (1968, 1972) noted the co-spatial occurrence of surges (discussed in the following Section) and Ellerman bombs around satellite sunspots which were undergoing drastic evolution, however, no large-scale study was attempted. It was not until Roy (1973) that a number of surges (30 in total) were analysed, finding each formed co-spatial to an Ellerman bomb structure. Indeed, it was observed that "the surge follows the bomb evolution in a way suggesting that its material is squeezed out from the bomb". The results of Bruzek (1972), however, disagreed and implied that neither event was necessary for the other to form. Despite more recent analysis (for example, Madjarska et al. 2009), the relationship between surges and Ellerman bombs is still unclear.

As magnetogram measurements became more common, researchers began focusing on the relationship between Ellerman bombs and regions of vertical

magnetic field. Indeed, Howard and Harvey (1964) concluded their study by suggesting that "the magnetic field plays an important role in the occurrence of Ellerman bombs". It would not be until the work of Georgoulis et al. (2002), however, that adequate magnetic field measurements would be collected such that a statistical study of Ellerman bomb formation could be attempted. It was found that Ellerman bombs often formed over regions of strong magnetic field, mainly over bi-polar regions. Therefore, the hypothesis that Ellerman bombs formed at sites of magnetic reconnection (a hypothesis which had initially been proposed by Pikel'Ner 1974) began to become more plausible.

Ever since their discovery, Ellerman bombs have been estimated to have lifetimes on the order minutes. Through a detailed analysis of one hundred and seventy eight Ellerman bombs, Roy and Leparskas (1973) found an average lifetime of between 10-20 minutes for these phenomena depending upon where in the Hα line profile the event was observed. Lifetimes of these orders have also been returned by more recent studies (for example: Zachariadis et al. 1987; Georgoulis et al. 2002; Watanabe et al. 2011). Shorter "bursts" of higher-intensity within the Ellerman bomb structure were also observed by Roy and Leparskas (1973) to occur on scales as low as tens of seconds. These changes in brightness have also been attributed to Ellerman bombs by, for example, Kurokawa et al. (1982), Zachariadis et al. (1987), Qiu et al. (2000), indicating potentially interesting physics. It is, however, difficult to assign a cause to these pulsations due to observational limitations. For example, as Ellerman bombs are small-scale events, often defined by intensity thresholding, both physical traits (such as oscillations or repetitive drivers) and changes in "seeing" (the refraction introduced by the Earth's atmosphere) could induce rapid changes in intensity.

The area of Ellerman bombs has been widely cited to be around $1''$ in diameter (which is around the size of Great Britain). These measurements have been almost constant since the original photographic observations and can be found in articles such as Vorpahl and Pope (1972) Zachariadis et al. (1987), Georgoulis

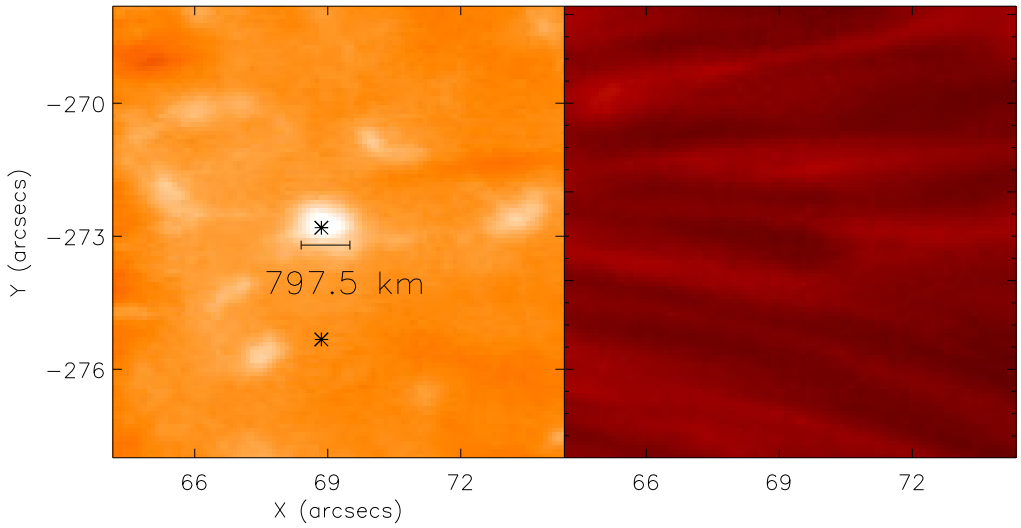

Figure 1.6: A zoomed FOV indicated by the white box in Fig. 1.5 (observed by the author and collaborators) with an Ellerman bomb highlighted. The approximate width of the Ellerman bomb is indicated by the black line. The two black stars indicate the pixels plotted in Fig. 1.7.

et al. (2002). However, recent work by both Matsumoto et al. (2008b) and Hashimoto et al. (2010) suggested that Ellerman bombs are, in fact, composed of a number of smaller sub-structures (which are indicative of a repetitive driver and could explain the fluctuations in intensity observed by Qiu et al. 2000) as well as a less intense 'halo'. In Fig. 1.6, the zoomed FOV indicated by the white box in Fig. 1.5 is plotted to depict a typical Ellerman bomb observed in the wings of the Hα line profile (left frame). The Hα line core (right frame) appears to be unaffected by the presence of this feature. The heights of Ellerman bombs were estimated by analysing data collected at the solar limb. Studies such as those of Bruzek (1972), Roy and Leparskas (1973), and Kurokawa et al. (1982) presented such observations concluding that Ellerman bombs had lengths, on average, of around 1.1″. Further work with more modern observations is required to fully understand the vertical evolution of Ellerman bombs at the solar limb.

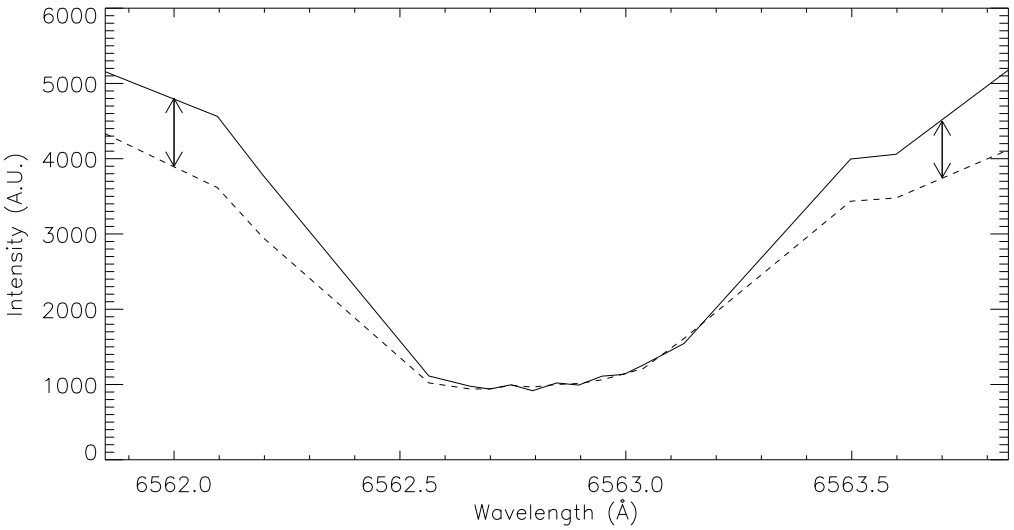

Figure 1.7: The intensity profile of the Hα line scan plotted for the two black crosses indicated in Fig. 1.6. The solid line corresponds to the Ellerman bomb region and the dashed line corresponds to the background profile. The arrows highlight the changes in intensity between the two regions in the line wings.

As modern spectrometers are able to quickly scan through a number of wavelengths with high spectral accuracy, it is also possible to analyse the spectral properties of each individual pixel in an image. In Fig. 1.7, the Hα line profile for the cross situated on the Ellerman bomb depicted in Fig. 1.6 is plotted and compared to a quiet Sun profile. It is immediately apparent that the Ellerman bomb has a higher intensity in the line wings, but there is no change in intensity between the event and the Hα background in the line core. This is indicative of the observational traits described by Ellerman (1917). This high wing intensity has lead to the popular use of thresholding in identifying Ellerman bombs in imaging data. Due to large disparities in the sensitivity of different instrumentation, the conditions of seeing from one observation to the next, and image restoration techniques, it is not a trivial task to assign the correct threshold to a set of observations. This can be summarised by the varying thresholds suggested by Georgoulis et al. (2002) (105-130% of the background intensity)

and Rutten et al. (2013) (150% of the background intensity). It is important, therefore, to assess each dataset individually.

The analysis of scans through the Hα line can also give information about line-of-sight velocity profiles. By completing studies of both photospheric and chromospheric dopplergrams, a number of authors (for example: Kitai 1983; Georgoulis et al. 2002; Matsumoto et al. 2008a) have discovered bi-directional flows within Ellerman bomb structures. The upflow velocities have been reported to be around 4-8 km s^{-1}, similar to vertical velocities measured in Ellerman bombs at the limb by Kurokawa et al. (1982), whereas the down-flow velocities are much smaller, often below 1 km s^{-1}. These flows were attributed to the evacuation of plasma from a reconnection site in the upper-photosphere. However, Watanabe et al. (2008) observed Ellerman bombs occurring over the inversion lines between larger-scale up- and down-flows in the lower atmosphere, and suggested that such flows were caused by emerging flux tubes which facilitated the formation of magnetic reconnection.

To further supplement the vertical flows, strong horizontal motions in ARs lead to drifts in the spatial positioning of Ellerman bombs. Measurements of speeds for these proper motions have lead to values of between 0.6 km s^{-1} and 2 km s^{-1} (see, for example: Zachariadis et al. 1987; Denker et al. 1995; Nindos and Zirin 1998), which is close to the flow speed in the photosphere. Indeed, Denker et al. noted that the paths of these motions followed the inter-granular lanes and are buffeted by evolving granules. In an effort to explain Ellerman bomb formation, Diver et al. (1996) suggested that these horizontal flows could lead to the formation of a Kelvin-Helmholtz instability which could be compressed until the tearing mode instability facilitated magnetic reconnection. Both the spatial positioning within inter-granular lanes and the horizontal velocities are similar to those reported within G-band MBPs by both Utz et al. (2010) and Keys et al. (2011). Further to this, Jess et al. (2010a) observed merging MBPs which appeared to drive micro-flare activity within the Hα line profile (which was interpreted as an Ellerman bomb).

It is widely known that the Hα line profile can be used to identify Ellerman bombs, however, it has been replaced or supplemented by other lines in specific studies. For example, Severny (1956) stated that Ellerman bombs were observed "at the sides of undisturbed Fraunhofer lines". As well as this, Qiu et al. (2000) found that approximately 50% of Ellerman bombs occurred co-spatially with UV bright points observed in the 1600 Å continuum. This correlation was also observed by Georgoulis et al. (2002). Studies of Ellerman bombs have also been carried out using the Ca II line (see, for example: Socas-Navarro et al. 2006; Pariat et al. 2007; Matsumoto et al. 2008b). The line wings of the Ca II line profile also indicated the on-set of an Ellerman bomb through increases in intensity. By semi-empirically computing atmospheric models which agreed with observed Hα and Ca II profiles, both Kitai (1983) and Fang et al. (2006) were able to suggest that the excess emission in the line wings was caused by localised temperature and density increases in the photosphere co-spatial to an Ellerman bomb event (these results have been recently corroborated by Berlicki and Heinzel 2014, Hong et al. 2014).

Numerical Modelling

Although the majority of Ellerman bomb studies have been carried out using observational data, numerical modelling has been attempted by a number of authors. Stellmacher and Wiehr (1991), for example, compared observations of Ellerman bombs in the Mg B1 5183 Å, Fe I 5434.5 Å, and Fe I 6302.5 Å lines with an empirically calculated model atmosphere. Although the numerical model did not match observations well when a background magnetic field was assumed, these authors were able to accurately reproduce the observational profiles (including the 'gap' in the Fe I 6302.5 Å line core) of Ellerman bombs based on temperature enhancements in the lower solar atmosphere. Further to this, both Hu et al. (1995) and Chen et al. (2001) conducted numerical simulations, finding that magnetic reconnection, potentially driven by emerging flux from the solar interior, could occur in the photosphere. The simulations

presented by Chen et al. also accounted for a number of the observational traits of Ellerman bombs (such as lifetime and up-flow velocity). It was suggested that strong increases in temperature in the chromosphere would be caused by such reconnection.

More recently, using the Coordinate Astronomical Numerical Softwares (CANS) code, Isobe et al. (2007) studied a two-dimensional model (where one co-ordinate was height) stretching from the upper convection layer into the corona. A current sheet was observed to develop at the inversion line between two opposite polarity fields which began to reconnect. Through the reconnection phase, up-flows of plasma were observed to occur, as well as temperature enhancements in the photosphere. It was theorised that these increases in density and temperature would lead to the observational signatures associated with Ellerman bombs although, unfortunately, no line synthesis was completed. These results were further supported by those of Archontis and Hood (2009), who modelled flux emergence into the solar atmosphere in three-dimensions using the CANS code. The formation of temperature and density increases, as well as up-flows, were driven by magnetic reconnection in the lower solar atmosphere. Comparisons between the physical properties of observed Ellerman bombs and the reconnection sites gave a good comparison (including lifetime and up-flow velocity).

Analytical Modelling

A number of studies have attempted to analytically represent the Ellerman bomb phenomena. A two-fluid approach, modified by a ponderomotive force, was applied by Hu et al. (1995) for an incompressible plasma in order to model observed parameters of Ellerman bombs. It was found that, given standard observational estimates of length and magnetic field strength, the lifetime of Ellerman bombs was accurately returned. As these results were supported by numerical simulations, it was speculated that this flux emergence model could explain Ellerman bomb formation. Diver et al. (1996), on the other hand, modelled Ellerman bombs as a Kelvin-Helmholtz instability where, once again, given

standard values, the lifetime of Ellerman bombs was well-captured. A similar model was depicted in a cartoon in Georgoulis et al. (2002) showing potential magnetic field topologies which could lead to Ellerman bomb formation.

Although it has not yet been applied to Ellerman bombs, one interesting analytical model of photospheric magnetic was proposed by Litvinenko (1999). In this order-of-magnitude model, two opposite polarity magnetic field regions are allowed to approach one another before a Sweet-Parker current sheet is formed with width proportional to the density scale height. The input required for the model consists of observational properties (such as in-flow speeds and the flux-cancellation rate). This model was deemed accurate for low magnetic field strengths ($|B| < 100$ G) similar to those observed in cancelling features in the quiet Sun. This research was quickly followed up by Litvinenko and Martin (1999), who tested the model against observations of a large cancelling region in the photosphere. Again, the model appeared to accurately predict the flux-cancellation rate as well as predicting the up-flow speed of a jet which was observed at the site. Interestingly (given the potential relationship between Ellerman bombs and surges), the model allowed estimates of the out-flow mass to be calculated. This mass was sufficient for the filling of a Hα filament.

Despite the initial success of the model, several down-falls of this method were presented by Chae et al. (2002) and Chae et al. (2003). In their observations, it was apparent that the flux in-flow speed was insufficient to faciliate fast enough reconnection in the photosphere. In order to rectify this issue, both articles stated that higher magnetic diffusivity would increase the in-flow speeds adequately, however, measurement of this quantity in the solar atmosphere is currently not feasible. More recently, Litvinenko et al. (2007) have suggested that the addition of magnetic flux pile-up to the model could speed up the reconnection process to observed values. As Ellerman bombs are believed to be magnetic reconnection events that are linked to small-scale bi-polar (and often cancelling) regions, it would be of specific interest to test whether this model describes the properties of these events accurately.

Alternatives to Reconnection

It should certainly be noted, however, that magnetic reconnection in the lower solar atmosphere is not the only hypothesis which has been suggested to explain the formation of Ellerman bombs. Indeed, Dara et al. (1997) analysed co-spatial Hα data and magnetograms finding no co-spatial relationship between Ellerman bomb formation and small-scale magnetic features. One competing theory which has received significant interest is the modification of the Hα line profile due to the injection of a high-energy proton beam into the photosphere from the corona. By analysing the linear polarisation of the Hα and Hβ spectral lines, Firstova (1986) was able to suggest that a flux of energetic particles exciting the local hydrogen population could cause the polarisation of Ellerman bomb signatures in the Hα line profile.

This work was continued by Ding et al. (1998), who conducted non-LTE calculations of particle injection into the lower atmosphere. It was found that two seperate cases could occur which were consistent with the Hα observational properties of Ellerman bombs, namely, the injection of high-energy (60 KeV) particles from the corona or lower-energy particles from the chromosphere. The Hα profiles modelled by this study did not, however, capture the level of intensity increases in the line wings (except near the solar limb). Henoux et al. (1998) followed up on this article, finding that the heightened line wing intensities of the Hα line profile could be explained by proton-hydrogen charge exchange. This would involve an energetic interaction between the background atmosphere and a proton beam excited in the chromosphere travelling horizontally along a magnetic field (perpendicular to the line of sight).

1.4.2 Moving Magnetic Features

Basic Information

Moving Magnetic Features (MMFs) were originally observed by Sheeley (1969) during an analysis of a time-series sampling the photospheric network. An

apparent horizontal out-flow of small bright features from a sunspot in spectroscopic data was identified (with speeds of approximately 1 km s^{-1}) and attributed to flows in the photosphere. Although magnetograms with sufficient resolution were unavailable for analysis in the study, Sheeley (1969) did infer the magnetic nature of the observed bright points, stating '...several closely-spaced bright features may come into contact and disappear together as if a 'cancelling' of opposite magnetic polarity were taking place.' In subsequent years, further observations of these events were presented as minor points during research of other phenomena (by authors including Vrabec 1971), before a concerted effort to understand these moving features was undertaken by Harvey and Harvey (1973), using co-temporal spectral and magnetic data. These authors found a strong link between the horizontally propagating phenomena observed by Sheeley (1969) and regions of high vertical flux, therefore, naming these events MMFs. In recent years, the correlations between these events and vertical magnetic fields has been confirmed (see Li and Zhang 2013 for a comprehensive review of the literature).

The movement of MMFs through the region surrounding sunspots is intriguing. Vrabec (1974) noted the existence of two different traits exhibited by MMFs, namely that they either flowed outwards from the sunspot before merging with a region of stable, existing flux or that they displayed significant cancellation and became unobservable (also see, *e.g.*, Harvey and Harvey 1973, Brooks et al. 2007). These separate traits have lead to the definition of three individual types of MMF within the literature (as discussed by Zuccarello et al. 2009). However, how these sub-sets (consisting of bi-poles, uni-polar fields with the same polarity field as the local sunspot, and uni-polar fields with opposite polarity flux to the sunspot) differ is still unknown. The research of Lin et al. (2006), though, suggested one possible avenue for future study, finding that several uni-polar MMFs with opposite polarity flux to the local sunspot resulted in transition region counterparts.

The majority of MMFs appear to have lifetimes of around one hour and

magnetic fluxes around 10^{18} Mx (as was shown convincingly by Li and Zhang 2013). It is interesting that magnetic fluxes of one order of magnitude higher have been hypothesised as drivers of filament formation (by, for example, Litvinenko and Martin 1999, Litvinenko et al. 2007). The research of Brooks et al. (2007), who suggested that the cancellation of MMFs with standing flux could lead to the formation of surges, could imply that these features are important with respect to the driving of jets from the photosphere into the outer layers of the solar atmosphere. However, other supporting evidence of co-spatial MMF-surge formation is conspicuous by its absence, perhaps indicating that specific, rare conditions are required for ejections of mass to occur.

In a detailed analysis of these features, Vrabec (1974) inferred that most MMFs appeared to form on spatial scales smaller than $2''$, well below the spatial resolution of the data analysed in that study. It was noted that only through time-series analysis could these features confidently be extracted from noise due to their 'persistence'. Indeed, recent work using higher resolution data (see, for example, Lim et al. 2012, Criscuoli et al. 2012, Li and Zhang 2013) confirmed this area estimate. It is possible, however, that significantly larger MMFs can occur, having been observed by a number of authors (including Criscuoli et al. 2012). A recent statistical analysis, conducted by Li and Zhang (2013), inferred that the average diameter of these features was around $1.5''$.

Finally, numerous explosive events observed within the solar atmosphere have been observed to form co-spatially with MMFs. Ellerman bombs, for example, were analysed with respect to MMFs by authors such as Nindos and Zirin (1998) and Socas-Navarro et al. (2006), who both found spatial correlations between these two phenomena. Interestingly, both Ellerman bombs and MMFs have been linked to 'sea-serpent' like magnetic field structures (by Pariat et al. 2004 and Harvey and Harvey 1973, respectively) indicating that further research, using modern instrumentation, into the link between these features should be undertaken. Such research shall be conducted in Chapter 6 of this thesis.

1.4.3 Surges

Basic Information

The surge phenomena have been observed within the solar atmosphere for decades (see, for example, Newton 1942, Ellison 1949). These features form as long, dark, sometimes curved ejections away from the solar disc often observed in the Hα line core. Even early researches (with limited magnetic field measurement capabilities) hypothesised that surges were intrinsically linked to strong magnetic fields in the solar photosphere. To further test this assertion, Rust (1968) considered a statistical sample of surges situated in a FOV containing a large sunspot and a trailing satellite spot of opposite polarity. This analysis suggested that every observed surge formed close to magnetic neutral lines where, it was considered, a process such as magnetic reconnection could occur. As has previously been mentioned, a number of authors (including Rust 1968, Rust 1972, Roy 1973) presented some evidence of a link between these phenomena and Ellerman bombs, however, this shall not be further discussed in this Section to avoid repetition.

In general, surges have lengths of approximately 10-100 Mm and widths around 1-10 Mm (see, *e.g.*, Roy 1973, Kurokawa and Kawai 1993, Guglielmino et al. 2010). Lifetimes of these features are widely reported as being between 10-40 minutes (as was discussed by, for example, Roy 1973, Kayshap et al. 2013, Bong et al. 2014). This lifetime is comparable to longer-lived Ellerman bombs as well as Explosive Events (EEs; which were suggested to be the coronal response to surges by authors such as Madjarska et al. 2009). Surges are observed to form co-spatial to bi-polar regions within ARs. It is possible that MMFs (as discussed in the previous Section) could play a role in surge formation (suggested by Brooks et al. 2007). It is, therefore, also plausible that MMFs in the solar atmosphere could drive both Ellerman bombs and surges if the cancellation rate is sufficient.

In order to calculate the cancellation rate, both Rust (1968) and Roy (1973)

estimated the magnetic energy within bi-poles co-spatial to surges to be around 10^{18}-10^{19} Mx (similar to those measured for MMFs). Indeed, for one region in their study, Roy (1973) derived a cancellation rate of 3×10^{15} Mx s^{-1} co-spatial to surge formation; however, such flux reduction was not deemed necessary as several events were observed in flux emergence regions. As well as this, Guglielmino et al. (2010) discussed the formation of surges co-spatial to flux emergence, further implying that rapid dynamics in the photospheric magnetic field could drive mass into the upper layers of the solar atmosphere. In Chapter 6, a study of co-spatial MMFs and Ellerman bomb will be undertaken in order to quantify any cancellation, which can then be compared to the values of Roy (1973).

1.4.4 Blinkers

Basic Information

Blinkers are small-scale bright features with diameters between around 3-10 Mm and lifetimes of the order of 20 minutes. Extensive research has been conducted on these phenomena which were initially observed by Harrison (1997) using the Coronal Diagnostic Spectrometer (CDS; Harrison et al. 1995) onboard SOHO. These transient events, often observed within EUV filters were also discussed by Harrison et al. (1999), who suggested that the observed increase in emission could be a signature of increases in density or filling factor caused by the injection of plasma from the photosphere (also see, *e.g.*, Teriaca et al. 2001, Marik and Erdélyi 2002, Bewsher et al. 2003, Madjarska and Doyle 2003).

A number of authors have researched the spatial positioning of blinkers compared to the magnetic field (discussed by Bewsher et al. 2002, Parnell et al. 2002) within both the quiet Sun and ARs. The majority (up to around 75 %) of blinkers appeared to occur co-spatially with regions of strong uni-polar field, for example plage regions. It was, therefore, inferred that magnetic reconnection within the upper atmosphere was unlikely to be the driver of these events. To

account for this, Priest et al. (2002) suggested mass supply from the lower solar atmosphere into the transition region and corona could produce the observational signatures of blinkers. In the quiet Sun, blinkers are often absent from coronal filters (see, *e.g.*, Harrison 1997, Bewsher et al. 2002, Madjarska and Doyle 2003). Within ARs, however, blinkers are observed in coronal lines (see Parnell et al. 2002). Links between blinkers and Explosive Events (EEs) have also been presented in the literature (for example, Marik and Erdélyi 2002).

1.5 Overview of this Thesis

The general aim of this thesis is to analyse the lower solar atmosphere using a variety of techniques in order to infer further details about the physical processes occurring in this complicated system. Specifically, the research discussed here shall focus on the Ellerman bomb phenomena and solar surges. This work shall be formatted as follows: In Chapter 2, the observational techniques and equipment exploited to collect the data analysed in this thesis are presented. Chapter 3 comprises a statistical study of a large number of potential Ellerman bomb events in the wings of the Hα line profile with specific interest paid to their statistical properties. A comparison of numerical simulations of Ellerman bomb events to their observational signatures in the Hα and Fe I line profiles is conducted in Chapter 4. The properties of Ellerman bombs at the solar limb are analysed in Chapter 5 before the potential ability of MMFs to drive these features is discussed in Chapter 6 by testing a basic analytical model of photospheric magnetic reconnection (initially suggested by Litvinenko 1999) with the aim of validating outputs with observations. An isolated surge event is analysed in Chapter 7 in order to assess the relationship of this event with a blinker which is observable in EUV wavelengths. Finally, conclusions are presented in Chapter 8.

Chapter 2

Observing the Sun

2.1 Introduction to Solar Observations

2.1.1 General Overview

Observations of the Sun produce a wonderful array of data, from which analysis into a plethora of solar processes and features (such as those discussed in the previous Chapter) can be conducted. The development of telescopes and instruments which are capable of collecting high-resolution, high-cadence data, however, is an artform and requires complex and novel engineering. The time and resources invested in developing such tools has so far proved worthwhile with a variety of specialised instruments and individual set-ups being available. For example, high-cadence time sequences sampled at an individual wavelength can showcase area oscillations of waveguides or bulk motions of mass in an isolated region of the solar atmosphere; whereas, the co-temporal collection of data at multiple positions within a line scan or at a number of wavelengths can depict line-of-sight motions and coupling between events at different heights in the solar atmosphere.

There are, in essence, two types of solar telescopes: ground-based and space-borne. Both have strengths and weaknesses. By way of illustration, ground-

based telescopes and instruments are relatively cheap to upgrade and are not limited by weight or size (within reason) meaning optimally engineered conditions for high-resolution, high-cadence data can be achieved; however, data collected by these instruments are limited by, *e.g.*, 'seeing' and wavelength filtering introduced in the Earth's atmosphere. On the other hand, space-borne instruments must fit within the spatial confines of the spacecraft, cannot be easily upgraded, and are limited in the amount of data they can transmit by the download speed available. These data can, though, provide near constant seeing-free observations of the Sun and are capable of observing coronal wavelengths which do not pass through the Earth's atmosphere. Therefore, it is desirable that a wide range of instruments be analysed by an observer in order to build up a complete and accurate picture of the solar atmosphere. In this Chapter, descriptions of the four telescopes which provided data for analysis in this thesis are presented.

2.1.2 Observational Wavelengths

The collection of solar data by modern telescopes can be conducted using a variety of methods. In this Chapter, we only discuss a limited number of these techniques including high-resolution narrow-band spectroscopic imaging, wide-band spectroscopic imaging, and spectropolarimetry. Each of these methods relies on the formation of spectral lines, which are unique finger prints of specific ions or molecules that exist in a target object and detail the interactions between the material and photons. This useful property of spectral lines allows them to act as a diagnostic tool to measure physical properties, such as the chemical composition of extra-terrestrial objects or the structuring of any existent magnetic fields. The development of the field of spectroscopy has allowed researchers to further understand the solar atmosphere, as well as improving our knowledge of the Universe in general. Indeed, it is through analysis of the solar spectra that some basic elements, such as helium, have been discovered.

Spectral lines can manifest as both absorption and emission from a back-

ground profile, dependent on the physical properties of the observed target. Absorption occurs when light is passed through a cooler plasma source. Photons at specific wavelengths are absorbed by atoms, exciting the transition of electrons from one state to a higher-energy state. As the electrons transition back to their relaxed states, a new photon is released; however, this photon can propagate in any direction, scattering the original beam of light and causing a reduction in the measurement of photons reaching the observer. Emission profiles, on the other hand, occur from a hot source, where thermal energy leads to increased transitions of electrons between states, increasing the total number of photons directed towards the observer.

Each element and molecule can be identified by its individual fingerprint (or set of wavelengths). One can then target observations such that particular transitions in the solar atmosphere are measured. This allows for inferences about the energy levels of the sampled plasma to be made. Therefore, a number of stand-alone filters and prisms can be employed by an observer to isolate specific wavelengths before this light is passed into cameras to be read out. Dependent on the size of the filter, or 'bandpass', the recorded observations can be classed as either narrow-band or wide-band. In addition to this, traits of the observed light (such as Zeeman splitting, where the spectral line separates into two individual lines) and additional tools in the path of the incident light (such as a Wollaston prism) allow for inferences about the target objects magnetic field to be made.

Hα

The main observational wavelength analysed in this thesis is Hα, which has been considered an excellent tool for chromospheric research for nearly 150 years (see, for example, Lockyer 1868). Indeed, Rutten (2008) stated that 'Hα remains the principle diagnostic of this regime'. Forming with a central wavelength of 6562.8 Å, the Hα profile manifests as an absorption line with wings sampling the photosphere and a core observing the chromosphere (see,

for example, Leenaarts et al. 2007, Rutten 2010, Rutten 2012). This line exists due to the transition of electrons between the second and third rings of Hydrogen atoms (as discussed by, *e.g.*, Rutten 2008). In Fig. 2.1, a FOV at the solar limb is plotted for both the far blue wing (left panel) and the core (right panel) of the Hα line profile to highlight the apparent build-up of material evident in the line core. These 'fibrils' (see, *e.g.*, Rutten 2012 for a discussion of these features) comprise the chromospheric canopy which appears to obscure the photosphere at this wavelength.

Despite the plethora of researches which have analysed this wavelength, understanding of the physical mechanisms which sustain the absorption in the Hα line core ubiquitously around the Sun is still lacking. Therefore, a brief overview of the extensive literature dedicated to the formation of the Hα line core will be presented in this Section. Because Ellerman bombs form in the wings of the line profile and not in the line core this brevity can be justified in this thesis; however, readers should be directed to Rutten (2012) and Leenaarts et al. (2012) (and references within both articles) for detailed descriptions of Hα. Overall, the Hα line core forms in the chromosphere, the layer of the solar atmosphere at which the strong kiloGauss magnetic fields previously confined to photospheric intergranular lanes (see Stenflo 1973) expand to cover the whole solar surface (due to a reduction in the gas pressure with respect to the magnetic pressure as was discussed by, for example, Gabriel 1976, Solanki and Steiner 1990, Judge and Peter 1998).

A recent review by Rutten (2008) detailed the problems posed by analysing purely imaging observations of the Hα line core. Changes in a number of properties within the local plasma (including opacity, Doppler shifts, Doppler broadening) can modify the observed intensity within a pixel meaning finely sampled line profiles must be collected to attempt to understand the physical processes manifesting in collected data. As well as this, due to the small-scale nature of fibrilar structures in the Hα line core, high-resolution observations are required (such as those analysed by Morton et al. 2012). It is, therefore, possible that

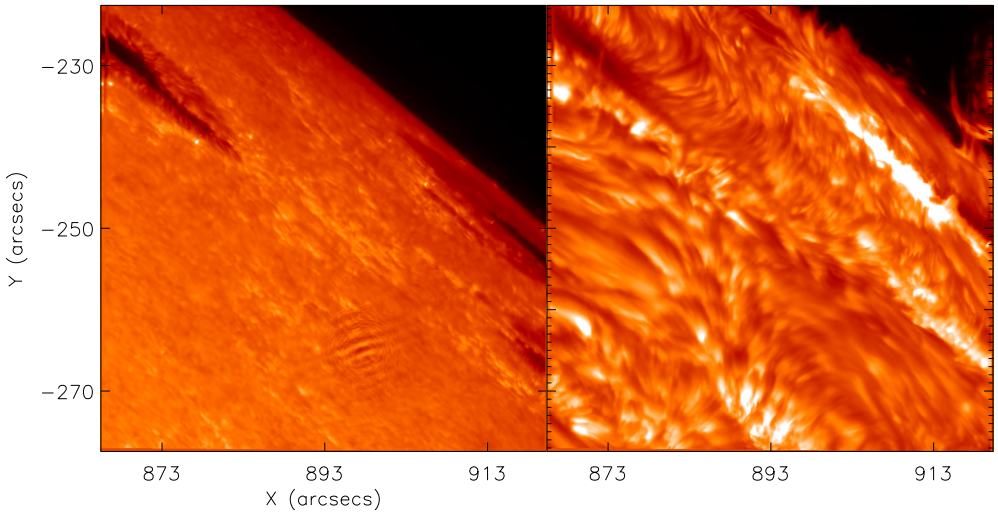

Figure 2.1: The far blue wing (left frame) and core (right frame) of the Hα line profile at the solar limb. These data were collected by R. Erdélyi and collaborators on the 21st June 2012. The apparent build-up of material over the photospheric line wing is immediately evident in the line core.

future developments in observational capabilities (either ground-based or space-borne) could dramatically improve the knowledge of the community about the Hα line profile.

In order to further understand this line profile, efforts have also been directed to developing realistic numerical simulations which return the properties of Hα; however, due to the complexity of the physics in the chromosphere and the limitations in computing power, advances with this aim have been slow. A series of articles (namely, Carlsson and Stein 1992, 1995, 2002) discussed the influence of non-equibrium ionisation on one-dimensional simulations. It was found that the ionisation rate of Hydrogen in the solar atmosphere remained fairly constant due to ionisation by shocks from the photosphere occurring on similar timescales to the relaxation of electrons from the third to the second ring of Hydrogen atoms. More recently, Leenaarts et al. (2007) and Leenaarts et al. (2012) have implemented non-equilibrium ionisation in two-dimensional and three-dimensional simulations, respectively. These studies suggest that the

non-equilibrium ionisation of Hydrogen in the solar atmosphere is the reason why the Hα line profile is so ubiquitous.

2.2 Observing Tools

2.2.1 Adaptive Optics

Most modern ground-based observatories operate with the help of Adaptive Optics (A.O.) systems, which attempt to measure the influence of atmospheric perturbations on the incoming wavefront. Such perturbations are introduced by the inhomogeneity of the air between the telescope and the Sun and can lead to significant 'stretching' of features within an image. Many systems employ a loop where an image is read by a wavefront sensor, which then calculates the distortion from a reference image before passing this information as an array to a deformable mirror which is manipulated to invert the atmospheric perturbations. This process can occur hundreds of times each second and has the potential to stabilise the 'seeing' conditions and create smooth datasets. Unfortunately, these A.O. systems are by no means perfect, meaning post-collection data processing techniques must be applied to make science-ready data. These techniques will be further discussed later in this Chapter.

Given ideal conditions, a telescope with circular aperture could achieve diffraction-limited observations, governed by the following relationship:

$$\alpha = 1.22\frac{\lambda}{D} \tag{2.1}$$

where α is the limiting diffraction angle (radians), λ is the wavelength of the observed light (cm), and D is the diameter of the aperture (cm). As the diameter of the telescope is unchanging, the only variable in Equation 2.1 is the wavelength of the observed light meaning shorter wavelengths are capable of achieving higher-resolution observations. For example, if the wavelength of the incoming light is 4000 Å (4×10^{-5} cm), the diffraction limits of observations

from a 76 cm aperture telescope and a 98 cm aperture telescope would be 96 km and 74 km, respectively.

2.2.2 Fabry-Pérot Interferometers

One widely used piece of equipment to collect solar data are Fabry-Pérot interferometers. Fabry-Pérot interferometers are often exploited by observers as they allow accurate and rapid scanning of specific spectral lines. Filtering is accurately induced within a Fabry-Pérot interferometer by two parallel, narrowly separated, highly reflective 'etalons' (perpendicular to the optical path) which, through the process of interference, produce a family of reflected and transmitted beams of light. The quality of the recorded image depends largely on the phase difference between the transmitted beams of light. If the beams are in phase, then constructive interference will lead to a large transmission peak meaning high-quality images can be obtained. Out of phase beams of light will, however, cause destructive interference, lowering the transmission peak and blurring the image. The use of multiple interferometers in sequence allows for the reduction of unwanted modes in a system and has been well known for nearly a century (see, for example, Houston 1927).

It is important, therefore, to understand the relationship between the phase difference of transmitted light and the physical set-up of an instrument (*i.e.*, with respect to the refractive index of the etalons, the separation of the etalons, and the angle between the incident light and the etalons). Mathematically, one can write the phase difference of a system of transmitted beams as:

$$\delta = \left(\frac{2\pi}{\lambda}\right) 2nl\cos\theta \tag{2.2}$$

where δ is the phase difference, λ is the wavelength of the incident light, n is the refractive index, l is the etalon separation, and θ is the incident angle between the beam and the etalon. It is simple to see from Equation 2.2, that constructive interference occurs when $2nl\cos\theta$ is equal to an integer. If incidental light is

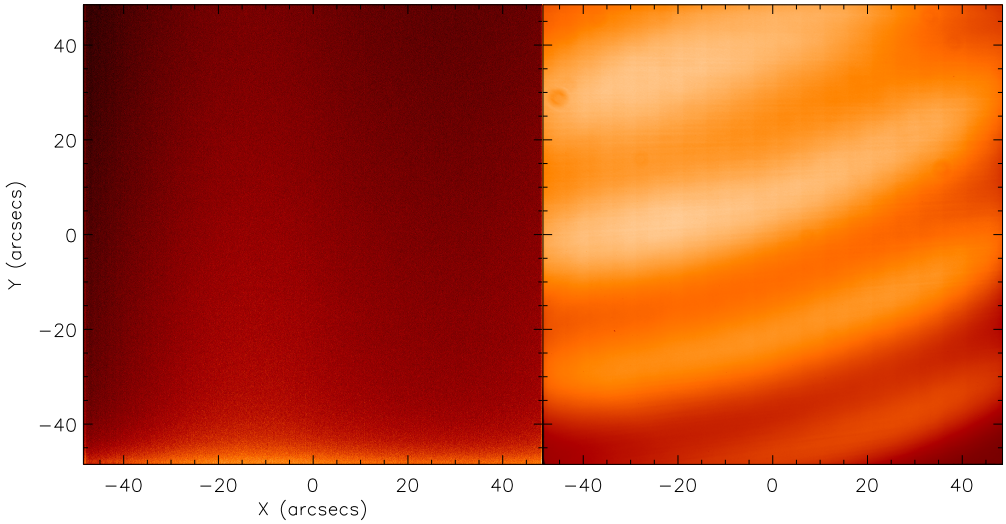

Figure 2.2: An example of dark (left frame) and flat-fielding (right frame) images collected for Hα observations collected by the author and collaborators on the 30th September 2012. Note the increased noise generated at the lower edge of the dark image and the sweeping patterns evident on the flat-fielded image.

limited to propagation perpendicular to the etalons, Equation 2.2 simplifies to:

$$\delta = \left(\frac{2\pi}{\lambda}\right) 2nl. \tag{2.3}$$

With a fixed refractive index, this means that the intereference phase difference is only dependent on the width of etalon separation.

2.2.3 Dark and Flat-Fields

Charge Coupled Devices (CCDs) are widely used in solar physics. Originally discussed by Boyle and Smith (1970), these revolutionary pieces of equipment earned their inventors a Nobel prize in Physics in 2009 and have proved essential in the development of astronomical instrumentation. In essence, CCD cameras measure the intensity of an incident light beam by expoiting the photoelectric effect, whereby photons cause electrons to be released by a semiconducting sur-

face (usually silicon based in astronomical CCDs) with the number of released electrons proportional to the intensity of the light. Electrons are then stored in wells within each pixel before migrating in sequence to a port to be read-out and saved digitally. By incorporating millions of pixels in a two-dimensional array and using a number of read out ports, it is possible to generate a two-dimensional image of a target with high-spatial accuracy and a high-cadence.

As the accurate collection data for scientific analysis is reliant upon the number of electrons generated within each pixel of a camera, it is important to understand the quantity of electrons which should be classified as noise. In CCDs, a small electric current is present even when no photons are entering the equipment leading to counts being measured by the CCD. This process is known as the 'dark current'. As solar observations benefit from high photon counts in general, the impact of this dark current on observations is usually minimal (*i.e.*, there is a high signal-to-noise ratio), however, it is possible to measure any systematic errors generated this way by collecting dark-field data (*i.e.*, blocking light from entering the CCD and measuring the output) before removing this from raw images. A single dark frame is plotted in the left frame of Fig. 2.2.

As well as dark-fields, flat-field corrections are also required to produce science-ready data from raw images. Flat-fielding involves collecting multiple images of the Sun with the specific scientific set-up used to collect the raw science data whilst the FOV of the telescope moves rapidly across the quiet-Sun. This blurs any small-scale structuring in the recorded images and allows, hypothetically, for the measurement of a perfectly even image when multiple frames are averaged. In practice, however, pixel-to-pixel sensitivity changes and two-dimensional patterns introduced by non-homogeneities on the observing table form structuring which must be removed from the science data. In the right frame of Fig. 2.2, an example of a flat-field image collected in the blue wing of the Hα line is plotted, highlighting several sweeping structures.

2.3 Solar Observatories

2.3.1 Richard B. Dunn Solar Telescope

General Overview

The Richard B. Dunn Solar Telescope (DST) is a large ground-based facility at the National Solar Observatory (NSO) site in Sunspot, New Mexico. Situated in the Lincoln National Forest at an altitude of 2800 m in the Sacramento Peak mountains, the DST is one of the predominant solar telescopes in the world. As a ground-based site, the DST has managed to stay at the fore-front of high-resolution solar observations (despite first-light being achieved in 1969) through the incorporatation of new and improved instrumentation, such as an A.O. system. In this Section, the physical properties of the DST will be discussed, as well as the properties of the two instruments from this telescope which have provided data for analysis in this thesis, namely the *Interferometric BIdimensional Spectrometer* (IBIS; Cavallini and IBIS Team 2004) and the *Rapid Oscillations of the Solar Atmosphere* (ROSA; Jess et al. 2010b) apparatus.

In order to minimalise the influence of the local environment on observations collected by the incorporated instruments, several novel engineering techniques have been employed at the DST. For example, light enters the telescope through a 0.76 m aperture window at the top of a 41.5 m tall tower, which is coated in a white titanium dioxide solution to reduce localised turbulence. An image of this tower is shown in Fig. 2.3. Once the sunlight enters the building, two 1.1 m diameter mirrors (which accurately track the elevation and azimuthal components of the Sun throughout the day) direct the light along a 1.2 m diameter vacuum tube which runs down the telescope to a depth of 67 m below ground level. After travelling along the length of the tube, the light is reflected off a 1.6 m diameter spherical main mirror before being extracted onto a rotating observing table (where the instruments are positioned) at ground-level through a 0.6 m aperture window. Interestingly, facilitating the rotation of the entire structure (including the observation table) requires that the whole system (which weighs

Figure 2.3: The tower section of the DST. The telescope also consists of an underground section, which goes deeper than the height of the tower.

approximately 226796 kg) is hung from a mercury float bearing, held in place by three 7.6 cm diameter steel pins at the top of the tower. This allows the DST to provide data over long time periods with a constant FOV and stable observing orientation which is extremely useful when observing the temporal evolution of small-scale events.

Interferometric BIdimensional Spectrometer

The DST/IBIS instrument was developed by the Italian National Institute for Astrophysics (INAF) and has been in operational at the DST facility since 2003. Light is directed into the DST/IBIS instrument on the observing table before two tunable Fabry-Pérot interferometers with independent etalon separations, placed perpendicular to the optical path, allow quick scans of a number of user defined wavelengths between the range of 5400 Å to 8600 Å (listed in Table 2.1). The use of two Fabry-Pérot inteferometers with different etalon separations increases the spectral resolution of the instrument by removing unwanted modes of the transmitted light, as was discussed by Houston (1927).

The DST/IBIS instrument is highly flexible, allowing a plethora of individual set-ups to be selected by the user. Observing sequences (and the subsequent read out sequence) of the DST/IBIS instrument must be chosen by the user and programmed into the control computer before data are collected. Once this is completed, the incident light beam is split early on in the DST/IBIS setup, with one beam entering a CCD camera collecting wide-band observations ideal for data post-processing, and one beam entering the dual Fabry-Pérot system and the into a second CCD camera. Both cameras collect a 1000×1000 pixel image, which samples an $80''$ diameter FOV with pixel sizes of around $0.097''$, and are controlled by the same electronic shutter allowing for the simultaneous capture of images. Data are read-out into flexible image transport system (FITS) format from both cameras, with each repetition of the user-defined sequence getting its own file. These data can then be read into a variety of computational languages, such as Python and IDL, with ease for reduction and scientific analysis.

Pre-filter	Wavelength (Å)	FWHM (Å)
Fe I	5434	3
He I D3	5876	3
Na I D2	5890	3
Na I D1	5896	3
Fe I	6173	3
Fe I	6301/6302	3
H I	6563	3
Ni I	6768	3
Fe II	7090	3
Fe II	7224	3
K I	7699	3
Ca II	8542	5

Table 2.1: Summary of the wavelength filters available for selection on the DST/IBIS instrument.

With respect to the observing sequence, a number of the wavelengths listed in Table 2.1 can be selected by the observer for data collection. Narrow-band images collected using these filters can have high-spectral resolutions between 20-40 mÅ (see, Asensio Ramos et al. 2006). In order to increase the cadence of the sequence such that small-scale analysis as presented in this thesis can be conducted, it is prudent to limit the number of wavelengths selected to two or three. Each wavelength can then be sampled at a number of positions, from the far wings to the line core, returning a line profile such as the example plotted in Fig. 2.4. Depending on the goal of the sequence, a number of images can be rapidly collected at each line position in order that post-processing techniques can be applied (which shall be discussed further later in this Chapter). By finely sampling a specific wavelength, the DST/IBIS instrument allows the user to make line profiles with high spectral accuracy and, therefore, collect important information such as line-of-sight velocities. Due to the plethora of potential sequences which are available with the DST/IBIS instrument, each individual observation analysed within this thesis will be described in more detail within

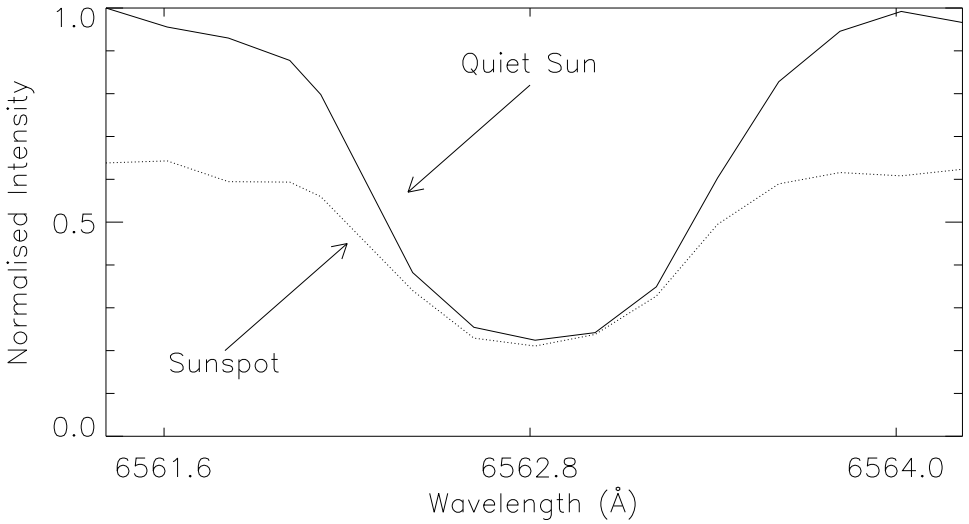

Figure 2.4: Two example Hα line profiles collected using the DST/IBIS instrument. The solid line plots a normalised average profile for a quiet Sun region. The dotted line is similar except for being centred on a sunspot.

each of the relevant Chapters.

Rapid Oscillations of the Solar Atmosphere

The DST/ROSA system is the second instrument at the DST which provided data for analysis in this thesis. DST/ROSA was originally commissioned in 2008 and is a common-user instrument consisting of six CCD cameras, each comprising 1004×1002 pixels. Every pixel samples with a pixel scale of $0.069''$ giving an overall FOV of approximately $69'' \times 69''$, that is positioned entirely within the DST/IBIS FOV. The CCDs are capable of capturing 30 frames per second, with a precision control unit (or "sync" box) providing a trigger to each camera such that co-temporal image acquisition can be achieved. However, as the photon counts at different wavelengths are not homogeneous, a variety of exposure times are required in practice in order to avoid any saturation of the CCDs. It is also, therefore, possible for the sync box to control each of the cameras individually.

With a frame rate of 30 frames s^{-1}, the DST/ROSA instrument can collect around 1.3 TB of data every hour. It is, therefore, required that each camera is connected to an individual server to avoid data saturation. Data is then written onto these servers in FITS format, with each file containing 256 images, collected at a single wavelength, which can then be combined in any ratio of input-to-output images using post-processing techniques. As users must physically transfer data from the DST to their host institution using portable hard-drives (which are large and heavy), it is often desirable that data is only collected using the DST/ROSA instrument during periods of excellent seeing or that only a selection of the CCD cameras are employed for data collection. In this thesis, the DST/ROSA instrument only contributes data sampled with the *G*-band continuum filter. These data are perfect for observing photospheric granulation structures.

The DST/ROSA instrument is set-up as follows. The incident beam of light which exits the vacuum tower onto the observing table is split and focused such that each camera can observe an individual wavelength. Typically, the DST/ROSA instrument is used to produce several high-cadence time-series of the lower solar atmosphere, using filters sampling, for example, the *G*-band continuum or the Hα line core. However, using the Universal Birefringent Filter (UBF) and a Wollaston prism in sequence, it is possible to split an incident beam with a relevant pre-filter (such as the Fe I 6302.5 Å line) into its left and right circularly polarised states. These data can be combined to estimate the line-of-sight magnetic field configuration of the photosphere with high-spatial and temporal resolutions.

2.3.2 Swedish 1-m Solar Telescope

General Overview

The Swedish 1-m Solar Telescope (SST; Scharmer et al. 2003) is situated at the Roque de los Muchachos site on the Spanish island of La Palma, at an

Figure 2.5: The tower section of the SST.

altitude of approximately 2360 m. The telescope is the successor to the Swedish Vacuum Solar Telescope (SVST; which was removed from the Roque de los Muchachos site on the 28th August 2000). The telescope is much newer than the DST, being built in 2001 and achieving first light with a limited set-up on 2nd March 2002. Having been constructed in the 21st Century, the SST benefits from being designed with A.O. systems in mind. The telescope has an aperture of 98 cm and a wealth of modern equipment which facilitate the collection of theoretically improved observations, in comparison to the DST. This system often produces diffraction limited datasets. In this thesis, only one instrument from the SST provides data for analysis, namely the *CRisp Imaging SpectroPolarimeter* (CRISP; see Scharmer 2006, Scharmer et al. 2008).

The SST is a refractor telescope, employing a vacuum tower design. Light enters the structure at the top of a white tower (shown in Fig. 2.5), before being

directed down into the heart of the building by two 1.4 m mirrors which track the Sun through the day. Incoming light is passed through a Schupmann corrector, which focuses all observable wavelengths onto a single focus such that a variety of solar observations can be collected, and then onto an observing table. Once on the table, the light is passed through beam splitters and pre-filters to isolate the required wavelengths. A portion of this light is then passed into the A.O. system to correct for variable seeing throughout the period of data collection. The rest of the light is passed into instruments. In contrast to the DST, the observing table at the SST does not rotate through the day meaning that the orientation of collected images changes through time.

CRisp Imaging SpectroPolarimeter

The SST/CRISP instrument was installed at the SST in March 2008. In many ways, the SST/CRISP is similar to the DST/IBIS instrument, in that it employs a dual Fabry-Pérot interferometer system in order that high-spatial and spectral resolution images can be obtained. The SST/CRISP was designed to operate between 5100-8600 Å (see Table 2.2), with spectral resolutions of around 60 mÅ (as discussed by Scharmer and Henriques 2012), which is perfect for analysis of the lower solar atmosphere (including the Fe I 6302.5 Å magnetically sensitive line and the Hα line core). Three 1024×1024 pixel CCD cameras are employed by the SST/CRISP instrument for data collection, consisting of one wide-band camera before the Fabry-Pérot system and two cameras after. The wide-band image recorded by the first CCD camera can be used for image reconstruction following the collection of data by the other cameras. Each of these cameras has a pixel scale of around $0.07''$ which is comparable to both the DST/ROSA and DST/IBIS instruments.

When light enters the observing table at the SST, a beam splitter directs the red portion of the visible light towards the SST/CRISP instrument. A synchronisation unit, known as the 'chopper', external to all of the cameras then ensures accurate co-temporal collection of images. The transmitted light then

Pre-filter	Wavelength (Å)	FWHM (Å)
Mg b	5173.3	3
Fe I	5250.5	3.3
C I	5382.7	3.3
Fe I	5578	3
Na D	5897	3.8
Fe I	6174.4	4.3
Fe I	6302.6	4.4
H I	6563.8	4.9
O I	7772.8	6.6
Ca II	8541.6	9.3

Table 2.2: Summary of the wavelengths observable with SST/CRISP.

passes through a filterwheel, that permits a small-section of the incident beam to continue through to a beam-splitter, where some of the light is directed to a wide-band camera for immediate collection. The other portion of the light is passed into the parallel dual Fabry-Pérot system, where rapid line scanning can be achieved by the horizontal movement of etalons. Finally, the light passes through a polarisation beam splitter and into the two final SST/CRISP cameras, allowing the co-temporal collection of left and right circularly polarisation light. Therefore, an approximate maps of the photospheric and chromospheric magnetic field topologies can be obtained.

2.3.3 Hinode

Overview

The Hinode (Kosugi et al. 2007) satellite, which was known as Solar-B before launch, is a Japan Aerospace Exploration Agency (JAXA) mission, developed in collaboration with the USA and the UK's Science and Technology Facilities Council (STFC). Lauched on the 22 September 2006, Hinode was the successor of the highly successful Yohkoh (or Solar-A) satellite and had the aim of inves-

tigating the role of magnetic fields in solar processes. Situated in a 98 minute Sun-synchronous orbit, data from Hinode are downloaded to the Svalsat station on Svalbard, Norway before being transferred along fibre-optic cables to the European mainland. The satellite was originally designed to operate for three years but has, to date, been operational for over eight years, providing a wealth of data that have given insights into a plethora of solar processes, from the granulated photosphere to the multi-million degree flaring corona (see, for example, Katsukawa et al. 2007, De Pontieu et al. 2011, Berger et al. 2011).

The 900 kg Hinode satellite hosts three scientific instruments: the *Solar Optical Telescope* (SOT; Tsuneta et al. 2008); the *X-ray Telescope* (XRT; Golub et al. 2007); and the *Extreme-Ultraviolet Imaging Spectrometer* (EIS; Culhane et al. 2007). Around 20 GB of data are collected by the satellite every day, stored at a ratio of 70:15:15 between the instruments in the order listed above. Each of these instruments is supplemented by a library of computer routines that facilitate the reduction and analysis of these data. These routines can easily be downloaded with the open-source *SolarSoft* IDL library. In this thesis, only data collected by the Hinode/SOT are researched and, as such, only this instrument is discussed below.

Solar Optical Telescope

The Hinode/SOT consists of two separate components, namely the *Optical Telescope Assembly* (OTA; Suematsu et al. 2008) and the *Focal Plane Package* (FPP; Tarbell et al. 2007), and is one of the largest and most complex space-borne instruments currently available (see Tsuneta et al. 2008 for details). The OTA acts as the initial point of contact for light entering the telescope and consists of a 50 cm aperture Gregorian reflecting telescope, diffraction limited within the range of 3880-6700 Å giving spatial resolutions of around $0.2''$-$0.3''$. Two field-stops situated at the primary and Gregorian focus' restrict the maximum observable FOV of the Hinode/SOT instrument to $361'' \times 197''$, before the incident light is passed through a collimating lens unit, a polarisation modulator,

Filter (Å)	Observable	Filter width (Å)	Purpose
3883.5	CN I	7	Magnetic network
3968.5	Ca II H	3	Chromosphere
4305.0	CH I	8	MBPs
4504.5	Blue Continuum	4	Temperature
5550.5	Green Continuum	4	Temperature
6684.0	Red Continuum	4	Temperature

Table 2.3: A general overview of the Hinode/SOT/BFI.

and on to a tip-tilt mirror. Using these tools, the OTA then passes a parallel beam of pointing-stabilised light to the FPP for read-out.

Upon initial contact with the FPP, the light is passed through a beam-splitter which segments the beam into four optical paths. Each beam is passed into one of four sub-instruments: the narrow-band filter instrument (NFI); the broad-band filter instrument (BFI); the spectro-polarimeter (SP); and the correlation tracker (CT). The CT is an important piece of equipment, observing granulation patterns in the solar photosphere using a 50×50 pixel CCD. Real-time comparisons between a live feed (passed through the OTA) to a systematically updated (approximately every 40 seconds) reference frame are made, before corrections for jitter and group motions are sent to the tip-tilt mirror in the OTA. This system acts as the A.O. for the Hinode/SOT and facilitates the high levels of spatial stability required for polarimetric observations to be achieved continuously. The SP exploits this spectral accuracy to scan a given FOV using a $0.16''$ wide slit to yield Stokes I, Q, U, and V profiles from the magnetically sensitive Fe I 6301.5 Å and 6302.5 Å profiles, which can be used to infer the photospheric vector magnetic field structure.

These corrections are also made to benefit the collection of imaging data from the further two Hinode/SOT instruments. Two-dimensional images of the lower solar atmosphere are obtained by both the BFI and NFI in a variety of user-defined wavelengths. Light is split into both of these instruments at the

Spectral line (Å)	Purpose
Mg I b 5172.7	Chromospheric Doppler and magnetograms
Fe 5247.1	Photospheric magnetograms
Fe I 5250.2	Photospheric magnetograms
Fe I 5250.6	Photospheric magnetograms
Fe I 5576.1	Photospheric dopplergrams
Na I D 5896.0	Chromospheric magnetograms
Fe I 6301.5	Photospheric magnetograms
Fe I 6302.5	Photospheric magnetograms
Ti I 6303.8	Umbral magnetograms
H I 6562.8	Chromospheric structuring

Table 2.4: A general overview of the Hinode/SOT/NFI.

beam-splitter situated at the entrance to the FPP. These beams pass through separate filters before both beams are directed to a shared 4K×2K CCD camera for data collection. As the name suggests, the BFI samples the solar plasma over a wide spectral range with short exposure times (typically less than one second) and a high spatial sampling (around $0.054''$ pixel^{-1}). The six available wavelengths which can be observed by the BFI instrument, and their properties, are included in Table 2.3. Overall, the BFI samples a maximum FOV of $218''\times109''$ and can achieve a cadence of under 10 s. The NFI, on the other hand, samples with narrow spectral resolutions of around 0.09 Å, returning two-dimensional imaging, Doppler, and magnetic field maps of the photosphere and chromosphere. These data have pixel scales of approximately $0.08''$ giving an overall unvignetted FOV of approximately $264''\times164''$. Due to the quantity of data collected using this instrument, the summing of pixels can be conducted to lower the required storage space. The ten available NFI spectral lines are summarised in Table 2.4.

2.3.4 Solar Dynamics Observatory

Overview

The Solar Dynamics Observatory (SDO; Pesnell et al. 2012) is a NASA '*Living with a Star*' satellite mission that was originally launched in 2010 and exists in a geosynchronous orbit, with a period of 1436 minutes. The scientific goal of this satellite is to understand the generation of 'space weather' (the out-flow of material from the Sun which interacts with the Earth's atmosphere) through the analysis of ubiquitous small-scale dynamics as well as the photospheric line-of-sight components of the Sun's magnetic field vector. The high-resolution, high-cadence data collected by the instruments on this satellite allow unprecedented inferences of the full-Sun evolution at scales relevant to flare formation. To attain this detail, ~ 1.5 TB of data are collected by the satellite every day and are constantly transmitted to a dedicated ground-station in White Sands (New Mexico, USA) at a transfer rate of around 150 MB s^{-1}. Following this, data are made publicly available for download and reduction, using specific SDO routines included in the *SolarSoft* IDL library.

The SDO satellite hosts three instrument suites, namely, the *Atmospheric Imaging Assembly* (AIA; Lemen et al. 2012), the *Extreme Ultraviolet Variability Experiment* (EVE; Woods et al. 2012), and the *Helioseismic Magnetic Imager* (HMI; Scherrer et al. 2012). Each instrument was designed in order to fulfil the specific scientific goals outlined for the mission. Combined, these instruments weigh around 300 kg and were scheduled for five years of initial service, with the potential for five more years if sufficient fuel is available for continued operations. In this thesis, data from both the SDO/AIA and the SDO/HMI are used to supplement data collected by ground-based instruments. These instruments shall, therefore, be discussed in detail here.

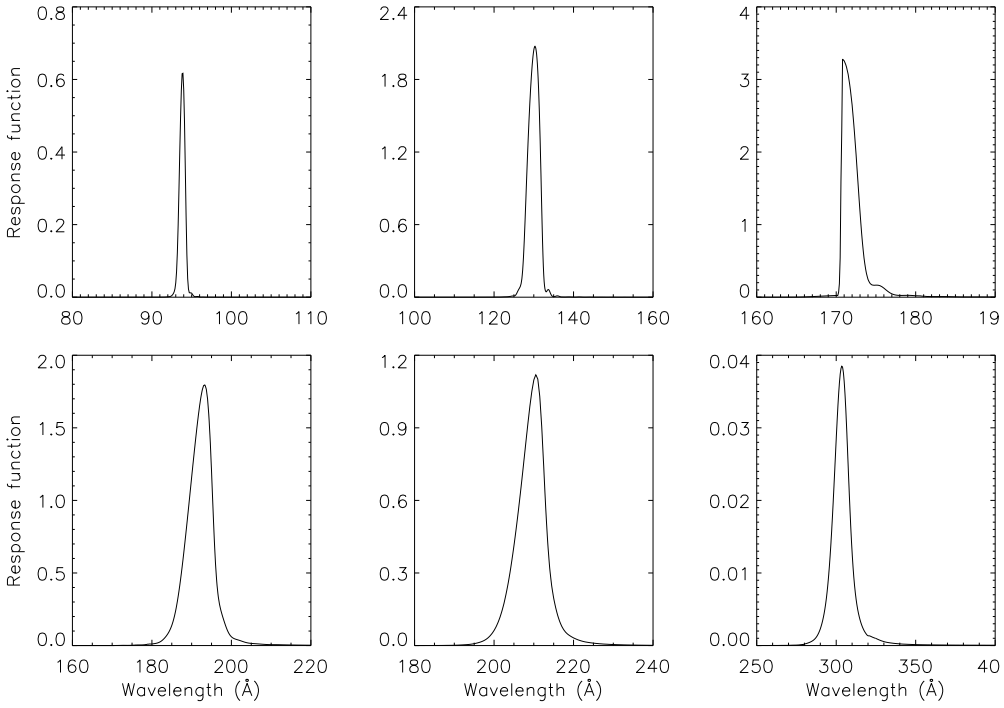

Figure 2.6: The response functions of six of the SDO/AIA EUV filters computed using the *SolarSoft aia_get_response.pro* function. Clockwise from top left, the 94 Å, 131 Å, 171 Å, 193 Å, 211 Å, and 304 Å filters are plotted.

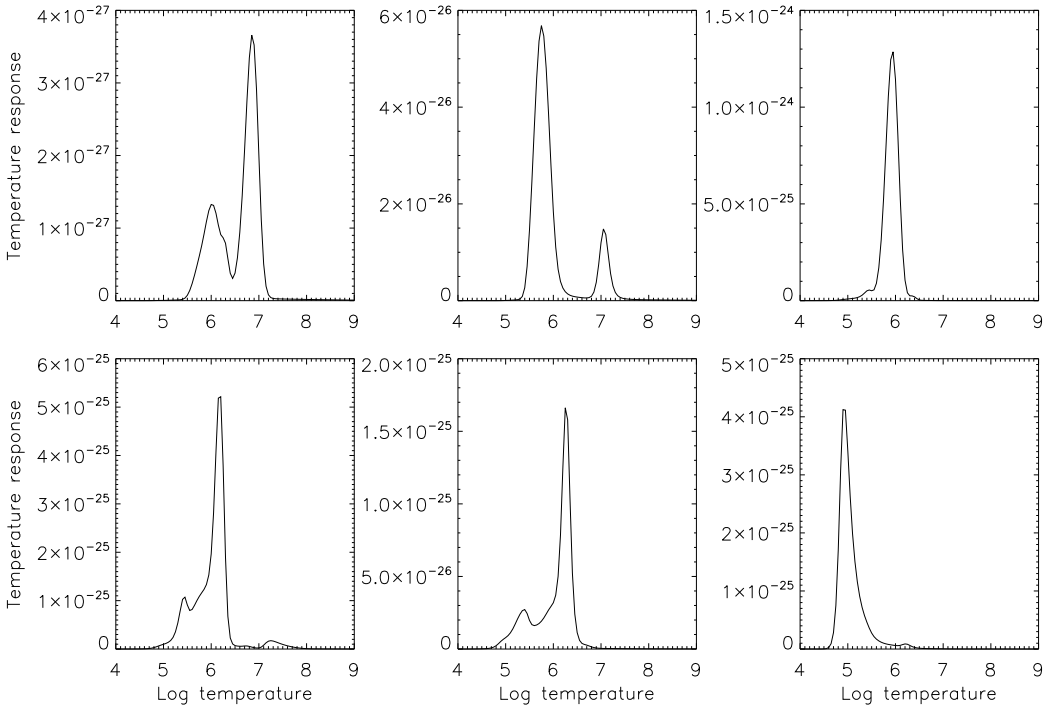

Figure 2.7: Same as for Fig. 2.6 but for the estimated temperature responses of each filter. The multiple peaks in several of these plots indicates that no one-to-one relationship between emission and temperature of the sampled plasma exists. However, see O'Dwyer et al. (2010) for a discussion on which spectral lines may dominate at particular temperatures.

Filter (Å)	Primary Ions	Cadence (s)	Layers	Log. Temp. (K)
4500	Cont.	3600	PH	3.7
1700	Cont.	24	PH	3.7
304	He II	12	CH + TR	4.7
1600	Cont. + C IV	24	PH + TR	5.0
171	Fe IX	12	TR + C	5.8
211	Fe XIV	12	C	6.3
335	Fe XVI	12	C	6.4
94	Fe XVIII	12	C	6.8
131	Fe VIII, Fe XXI	12	TR + C	5.6, 7.0
193	Fe XII, Fe XXIV	12	C	6.2, 7.3

Table 2.5: A general overview of the SDO/AIA instrument. Estimated heights (PH = photosphere, CH = chromosphere, TR = transition region, and C = corona) of the plasma sampled by each filter and their approximate temperature logarithms are included as a guide. All filters (except for the 4500 Å and 1600 Å filters) are plotted in Fig. 2.8.

Atmospheric Imaging Assembly

The SDO/AIA instrument images the entire solar disk in order that global dynamical processes on the Sun can be analysed. Four 4096×4096 cameras are employed, which sample a total of 10 filters with an approximate pixel size of $0.6''$, observing from the photospheric continuum to the super-heated active region (AR) corona. This instrument collects eight high-resolution images every 12 seconds, including seven EUV images and one continuum image. Overall, SDO/AIA is capable of transferring an impressive 2 TB of data every day in FITs format to the ground at a rate of 67 MB s^{-1}. In Table 2.5, information about the set-up of this instrument is included, highlighting the wavelengths, primary ions, cadences, approximate layer of the atmosphere observed, as well as the estimated temperatures of each filter.

By combining data from multiple SDO/AIA filters, it is possible to gather information about the temperature evolution of events in the solar atmosphere, specifically with regards to coronal heating. It should be noted that the loga-

rithmic temperatures included within Table 2.5 are estimates of the temperatures expected when the primary ions are the dominant emission within a filter. Unfortunately, but necessarily, these data are collected using filters which encompass a number of spectral lines, each of which can significantly increase localised emission but form at different temperatures (as is plotted in Fig. 2.6 and Fig. 2.7). Therefore, care must be taken with interpretation of these data (see O'Dwyer et al. 2010). A number of techniques have been developed over the past decades including Differential Emission Measures (DEMs) and the CHIANTI (Dere et al. 1997, Landi et al. 2013) tool in order to estimate coronal properties; however, the correctness of these methods is currently unknown.

As the pointing of each of the CCDs incorporated into the SDO/AIA instrument are consistent, co-alignment between different filters is not a required step in the data preparation. Continuum images collected by the SDO/AIA instrument can, therefore, be aligned to ground-based photospheric data easily allowing for research into the response of coronal filters to features observed in the lower solar atmosphere. A dedicated software library exists for analysis of data collected by the SDO/AIA instrument within the open-source *SolarSoft* IDL library. These codes can be used to return science ready images from downloaded data, as well as facilitating further reduction (such as region tracking through time). A sample FOV of these data is plotted in Fig. 2.8 including a whole disk image sampled with the 1700 Å filter and smaller regions outlined by the white box for seven EUV filters and the SDO/HMI line-of-sight magnetic field.

Helioseismic and Magnetic Imager

The SDO/HMI instrument was specifically designed to infer the line-of-sight magnetic and Doppler components of the solar photosphere. This instrument is the successor of the Solar and Heliospheric Observatory's *Michelson Doppler Imager* (SOHO/MDI; Scherrer et al. 1995), however, it does mark a significant improvement in the available diagnostic capabilities. Light enters the SDO/HMI

Property	Value
Spectral Line	Fe I 6173 Å
FWHM	±0.1 Å
Pixel Size	0.505″
CCD Size	4096 × 4096
FOV	> 2000″
Cadence	45 seconds
Aperture	14 cm
Data Transfer Rate	55 MB s^{-1}

Table 2.6: A general overview of the SDO/HMI instrument.

through a 14 cm aperture window before passing through a 50 Å bandpass filter which rejects 99 % of the heat from the Sun. The focused incident light then passes through the optics system, including a Lyot filter and two Michelson interferometers, and is read in to two 4096 × 4096 pixel CCD cameras. One camera is dedicated to the collection of photospheric Doppler and line-of-sight magnetic field data, both of which are calculated on the ground with a total of 12 images of the Sun. These 12 images are collected at different wavelength tunings or polarisation states with a total cadence of 45 s and pixel size of 0.5″. The second camera computes photospheric vector magnetic fields with a cadence of 90 s. The basic physical properties of the SDO/HMI instrument, as well as the line-of-sight magnetic field data used in this thesis, are outlined in Table 2.6.

The spatial resolution of data collected by the SDO/HMI instrument is ideal for analysing small-scale changes in the magnetic field in the solar photosphere and can be used to highlight the dynamics of flaring regions. Full-disk images of the Sun collected by the SDO/HMI instrument have delivered a plethora of data which have been used to study AR formation, the magnetic evolution of flaring regions, and the dynamics of MMFs amongst many other interesting topics. Numerous techniques have been developed in recent decades with the aim of conducting extrapolations of magnetic field lines into the upper layers

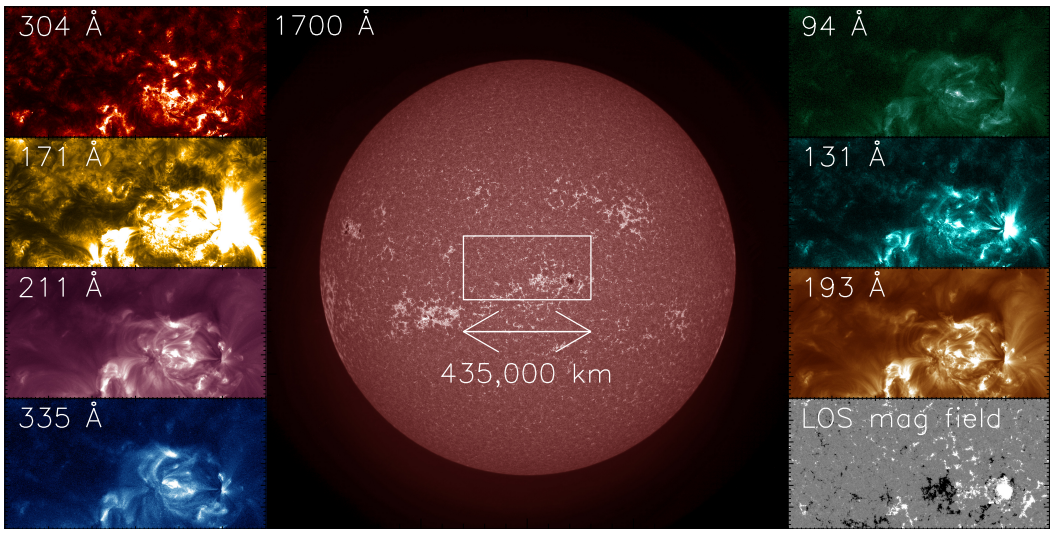

Figure 2.8: The Sun observed by the SDO satellite on the 9th December 2014. The central subplot depicts plasma sampled by the 1700 Å SDO/AIA filter. The surrounding subplots show a zoomed in FOV (co-spatial to the white box) collected by a range of SDO/AIA and SDO/HMI filters. The respective SDO/AIA wavelengths or SDO/HMI observable are included in each individual subplot.

of the solar atmosphere from these photospheric magnetograms (such as the MPOLE package; see, for example, Longcope and Magara 2004). These techniques allow for insights to be gathered about the three-dimensional topology of the solar magnetic field and possible linkages between photospheric magnetic field configurations and coronal responses inferred by the SDO/AIA instrument.

2.4 Data Reduction Techniques

Although the A.O. systems at modern ground-based telescopes are specifically designed to account for the effects of atmospheric seeing, they are rarely 100% effective. Small density and temperature perturbations in the Earth's atmosphere cause the incident wavefront to become non-homogeneous on scales which cannot be corrected, reducing the quality of the collected data. These perturbations cause 'blurring' to occur in images, significantly lowering the observed spatial resolution and limiting the usefulness of data for scientific analysis. It is, therefore, required that further processing of the data is conducted by the observer prior to any research. In general, data reduction techniques exploit short-exposure images and assume that the influence of the atmosphere is 'frozen' during the sampling. Then, multiple images (collected over a time-scale which is almost negligible on the Sun) can be combined to return a single higher resolution image. Two such techniques have been applied to data analysed in this thesis, namely the speckle code (see von der Luehe 1993) and multi-frame blind deconvolution (MFBD; described by Schulz 1993).

The speckle code used in this thesis is the Kiepenheuer-Institute Speckle Interferometry Package (KISIP) translated into the *C* language by Wöger et al. (2008). This technique has been widely tested and used in solar physics in recent years (see, for example, Wöger et al. 2009, Morton et al. 2012, Jess et al. 2014). Speckle interferometry requires a large number (usually 30 or more) of individual frames to be acquired quickly (in order that the seeing conditions and the solar atmosphere do not evolve markedly) such that a 'real'

image can be returned. As well as this, high signal-to-noise ratios are required, making this technique ideal for solar observations. To construct a single high-resolution image, the Fourier transform of each frame is calculated and the Speckle Transfer Function (STF) is estimated from given models (depending of Freid's parameter, r_0). By averaging these quantities through time, it is possible to obtain a more accurate representation of the sampled FOV. In Fig. 2.9, the left-hand side of the image plots half of the unreduced data whereas the right-hand side plots speckle processed data depicting the change in quality after the implementation of this technique.

In this thesis, the multi-object multi-frame blind deconvolution (MOMFBD; developed by van Noort et al. 2005) variety of MFBD is also used. As with the speckle procedure, the MOMFBD process requires the collection of a number of images within a short time frame (such that the target object does not evolve significantly during observations) as was discussed by, for example, van Noort et al. 2005. The benefit of the MOMFBD process over speckle interferometry is the reduced number of images required for an accurate calculation of the atmospheric turbulence which, in turn, improving the required cadence of an observational sequence. Indeed, van Noort et al. (2006) suggest that less than 10 frames would be required.

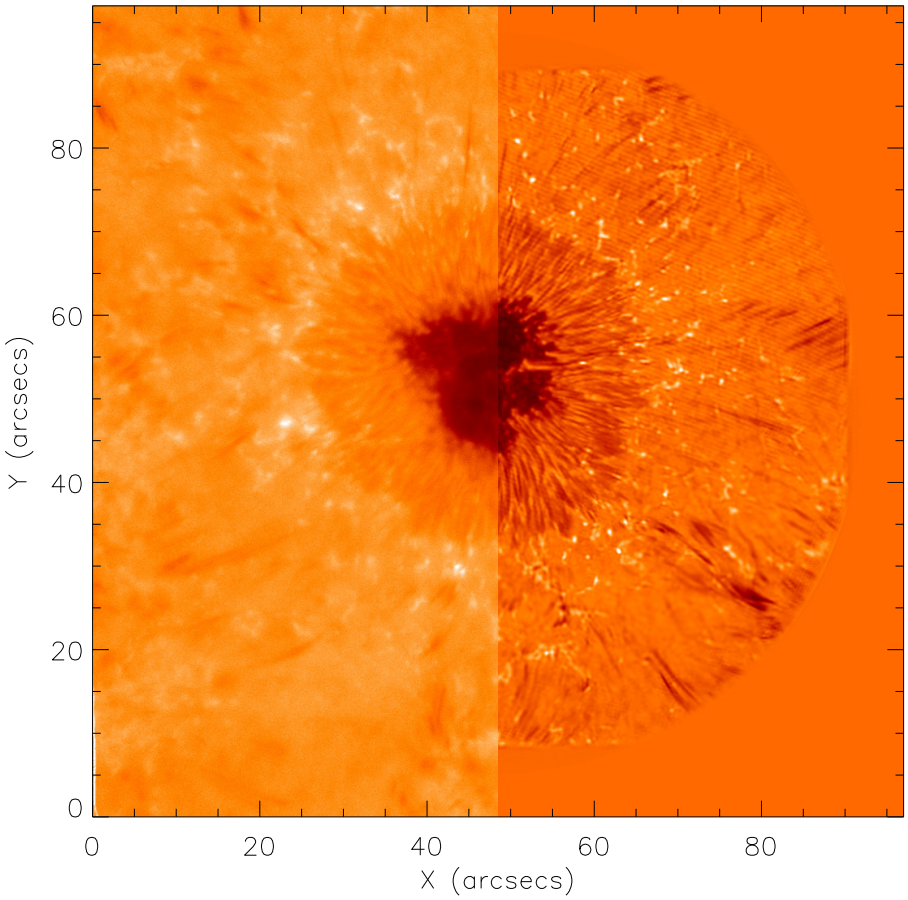

Figure 2.9: A single image plotting half of one input frame (left) and half of the corresponding speckle output frame (right). Dark and flat fields corrections have been applied to the input image.

Chapter 3

Statistical Properties of Ellerman Bombs

3.1 Overview

Ellerman bombs have been of interest to the solar physics community ever since their discovery by Ellerman (1917). However, a clear understanding of these events has not been achieved to date, largely due to the sizes (around 1″; see, for example Zachariadis et al. 1987; Georgoulis et al. 2002) and lifetimes (approximately 10 minutes as found by, *e.g.*, Watanabe et al. 2011) of these features. These are close to the spatial and temporal resolutions of even the best modern ground-based telescopes. Small-scale Ellerman bombs are intriguing, though, manifesting as brightenings in the wings of the Hα line profile, which exhibit apparently energetic 'flaring' (rapid increases in intensity and area discussed by, for example, Watanabe et al. 2011) characteristics. These dynamical flaring signatures have been widely hypothesised to be a result of an energetic driver in the photosphere, such as magnetic reconnection (see, *e.g.*, Georgoulis et al. 2002). Unfortunately, analysis of these features is somewhat complicated as not all brightenings in the wings of the Hα line profile are Ellerman bombs (discussed by Rutten et al. 2013).

In this Chapter, an automated detection algorithm will be applied to identify bright features in the wings of Hα line profiles. Automated detection algorithms have been used by a variety of authors for a number of studies including those of MBPs (see, for example, Utz et al. 2010, Keys et al. 2011, Bodnárová et al. 2014) and Ellerman bombs (*e.g.*, Watanabe et al. 2011). Therefore, such codes provide a viable route for analysis. High-resolution, high-cadence data collected by the DST/IBIS instrument will be used as an input to the algorithm before a range of properties from the output are returned, including lifetimes, areas, and energies (using the method employed by Georgoulis et al. 2002). Finally, co-spatial SDO/HMI magnetograms and DST/ROSA *G*-band images are then considered, providing information about the photospheric line-of-sight magnetic field and the granulated photosphere, respectively, co-spatial to the DST/IBIS FOV.

The research conducted in this Chapter is set out as follows. In Section 2, the observational data are discussed. Section 3 details the data analysis, while Section 4 discusses the relevance of the obtained results. This Chapter consists of results published in: **C. J. Nelson**, J. G. Doyle, R. Erdélyi, Z. Huang, M. S. Madjarska, M. Mathioudakis, S. J. Mumford, K. Reardon, 'Statistical Analysis of Small Ellerman Bomb Events', *Solar Phyics, Volume 283 (2013), Page 307.*

3.2 Observations

In this Chapter, ground-based data from the DST/IBIS and DST/ROSA instruments and space-borne data sampled by the SDO/HMI instrument are analysed. These data were centred on a sunspot in NOAA AR 11126 (situated at approximately x_c=60″, y_c=−540″ from the centre of the disc), which was selected for observation between 15:02 UT and 17:04 UT on the 18th November 2010. The observing sequence conducted by the DST/IBIS instrument to collect these data consisted of a 15-point Hα line scan which sampled unevenly between −1.4 Å to +1.4 Å (with respect to the line core at 6562.8 Å). For reference, all further

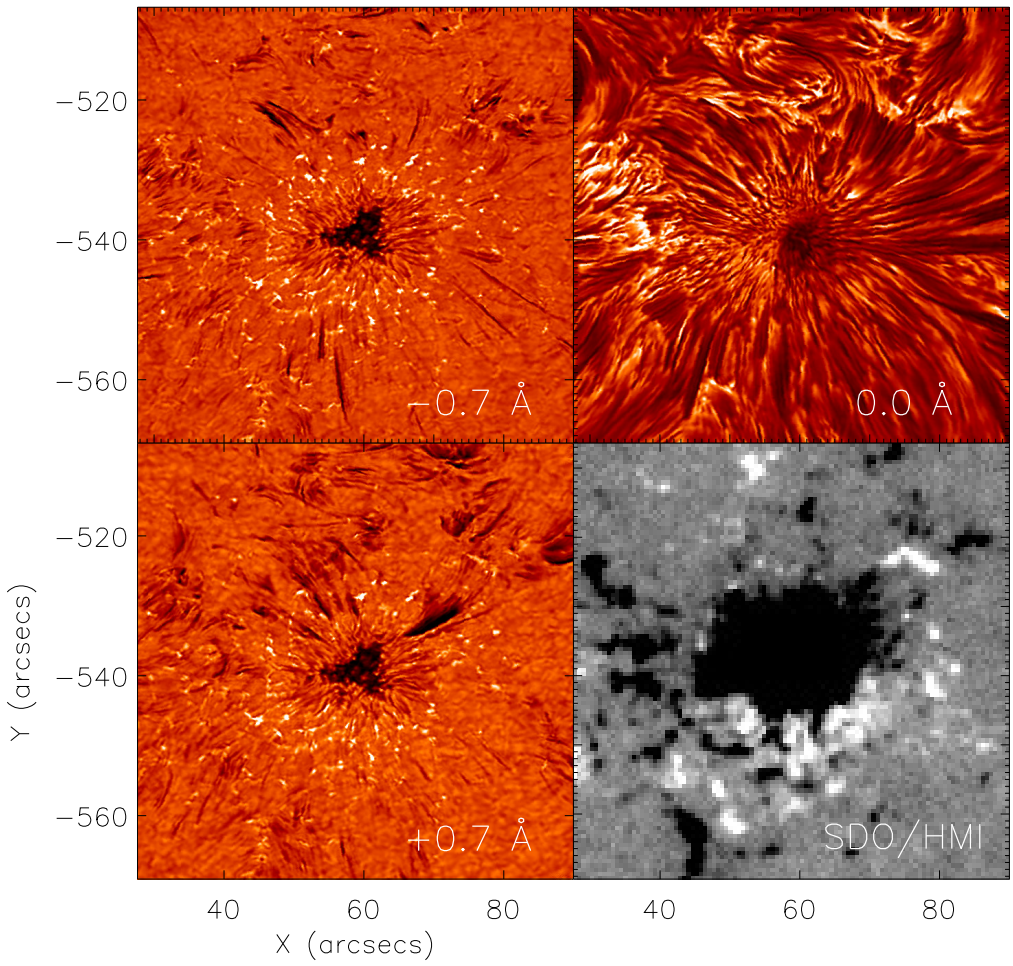

Figure 3.1: The FOV within NOAA AR 11126 analysed in this Chapter sampled at approximately 15:03 UT on the 18th November 2010. The three Hα images (with wavelengths of -0.7 Å, 0.0 Å, and 0.7 Å from the line core clockwise from the top left, respectively) in the blue wing (top left), line core (top right), and red wing (bottom left) are speckle processed. The SDO/HMI image (bottom right) was cropped and aligned to the DST/IBIS FOV before being plotted with minima and maxima of ± 100 G.

measurements of wavelength in this Chapter will be given with respect to the Hα line core. Each line scan was followed by 50 repetitions at three wavelengths within the Hα line profile (situated at approximately -0.7 Å, 0 Å, and $+0.7$ Å). Each of the sets of 50 images was then reduced using the speckle method (see Wöger et al. 2008 for more information). Overall, 275 iterations of this sequence were collected with a cadence of 26.9 seconds and a pixel size of around $0.097''$. It should be noted that due to deteriorations in the seeing quality after 16:30 UT, only the first 90 minutes of observations are considered in this research (leaving around 200 frames). Finally, a destretching algorithm was applied to consecutive frames of the speckled images to reduce jitter.

To supplement the spectroscopic measurements obtained by DST/IBIS, the DST/ROSA instrument was also used to collect observations of the lower solar atmosphere. Four of the available CCD cameras collected data using a variety of filters, however, only G-band images are analysed in this Chapter due to the nature of this work. As with DST/IBIS data, each science-ready G-band image was reconstructed using the speckle process, with 32 short exposure images being combined. These data had a cadence of 0.64 seconds and a pixel size of approximately $0.069''$ (equivalent to approximately 50 km on a transverse scale). Finally, photospheric line-of-sight magnetograms were inferred by the SDO/HMI instrument (with a spatial resolution of $1''$ and a cadence of 45 seconds). These data were reduced using standard *SolarSoft* routines before being cropped, aligned, and de-rotated to follow the FOV of these ground-based data.

In Fig. 3.1, the FOV of these data is plotted, with images from each of the speckled Hα wavelength positions and a SDO/HMI magnetogram being included. Within the Hα line wing images (top and bottom left), the sunspot umbra and penumbra are immediately conspicuous, as well as a plethora of small-scale structures in the surrounding plasma. Over the course of these observations, the large-scale structuring of the FOV remains relatively constant with no major morphological changes to the sunspot and no large-scale flares

occuring. On small spatial scales, however, the surrounding plasma changes on the time-scale of minutes with bright network bright points (NBPs) and Ellerman bombs, as well as the dark dynamic fibrils, rapidly appearing, disappearing, and evolving in the time-series. Overall, this FOV offers an interesting test-bed for the implementation of an automated tracking algorithm to track bright features within the Hα line wings.

3.3 Data Analysis

3.3.1 Feature Identification

In this Chapter, an automated tracking algorithm is exploited in order to define regions of increased intensity in the line wings of the Hα line profile. This research aims to address whether Ellerman bombs have a lower limit of size and area which are measureable with available data. In essence, both NBPs and Ellerman bombs are brightenings in the wings of the Hα line profile, that are often also visible in the wings of other chromospheric lines (for example, Ca II) and photospheric continua (*e.g.*, *G*-band, 1600 Å). The majority of researches focusing on these features have found no evidence of a response from either phenomena in the upper layers of the solar atmosphere, including the Hα line core and SDO/AIA EUV filters (a recent exception to this is the work by Bello González et al. 2013, who discussed one Ellerman bomb with a signal in the Hα line core), agreeing with the original work on the topic, where Ellerman (1917) identified these solar Hydrogen bombs as "a very brilliant and very narrow band extending four or five Å either side of the line, but not crossing it". Example line profiles for phenomena visible in this FOV can be found in Fig. 3.2.

As can be seen in Fig. 3.2, both NBPs and Ellerman bombs are visible as increases in intensity in the wings of the Hα line profile. Large Ellerman bombs also have a tendency to 'flare' (as discussed by, for example, Watanabe et al. 2011), rapidly increasing in intensity and area such that these events are conspicuous in imaging data. The initial aim of this Chapter is to discuss whether

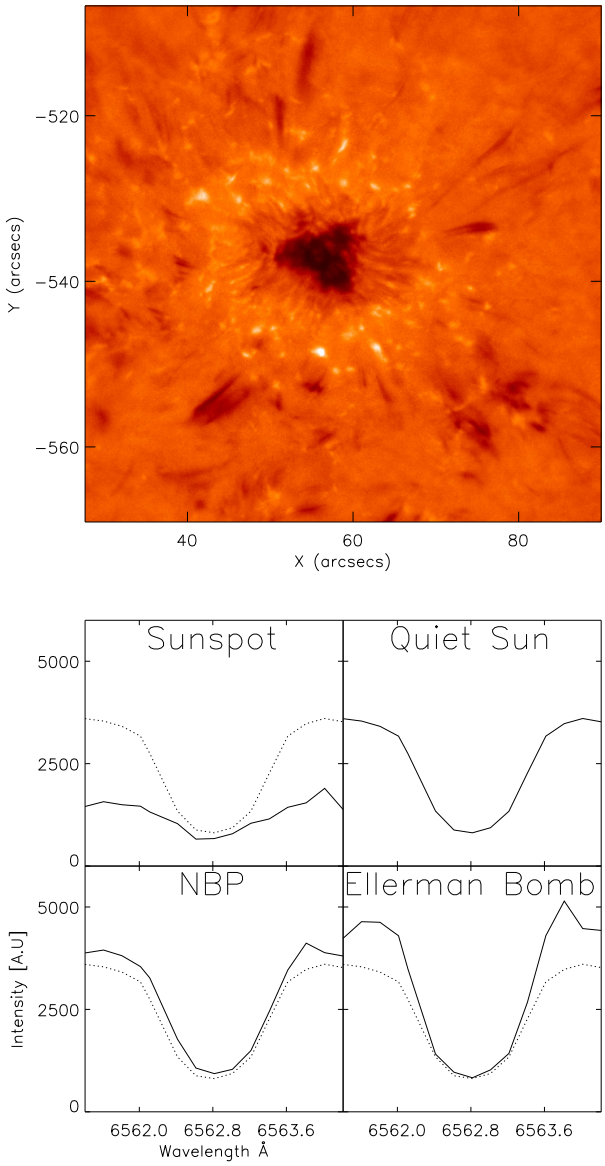

Figure 3.2: Blue wing image (−0.7 Å) from a Hα line scan collected at approximately 15:03:15 UT (top) and four representative line profiles of identifiable features. Clockwise from the top left, these features are: the sunspot; a pixel in the quiet Sun; a NBP; and an Ellerman bomb. The overlaid dotted lines plot the quiet Sun profile for easy comparison.

a coherent relationship can be found between small-scale brightenings (where flaring could occur below the spatial resolution of these data) and the larger-scale obvious Ellerman bomb events. To research small-scale brightenings, the following properties are incorporated into the automated detection algorithm for the selection of events:

- A region has an intensity higher than a user-defined level in both of the Hα line wings.
- A bright feature has an initial spatial overlap in the line wings and an area of greater than two pixels.
- Features 'continue' between frames if a sufficient intensity increase exists in consecutive frames with a spatial overlap (for both wings).
- If multiple events with spatial overlaps exist between frames, the one with the largest spatial correlation is assumed as the continuation of the feature; the others are neglected.
- Any features that occur in the first or last frame are removed from the sample so that only events with a complete lifetime are returned.

Although numerous limitations are immediately evident with respect to this algorithm (for example, changes in seeing could artifically alter the output), the aims of this study can still be fulfilled to a self-consistent level for further analysis. In Fig. 3.3, the output from the automated detection algorithm is plotted for three different threshold levels. Initially, a threshold value of 120 % of the average intensity is considered in the top left panel, where the black contours outline the detected features. It is immediately obvious that significant noise exists within this output, specifically relating to extremely small-scale events at the periphery of the FOV, potentially diluting further analysis. A threshold value selecting features with intensities in excess of 130 % of the average FOV intensity identifies fewer events (contoured in blue in the top right panel of Fig. 3.3), including all obvious Ellerman bombs evident through a visual inspection of time-lapse movies of the Hα line wings. Most features appear to occur

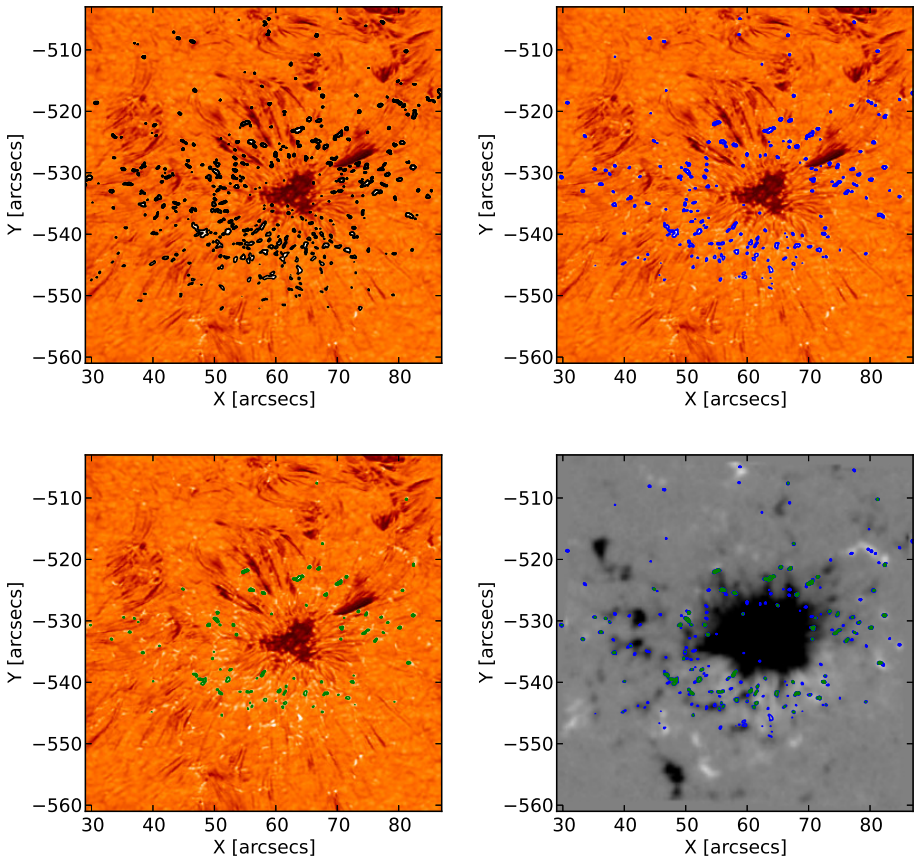

Figure 3.3: DST/IBIS red wing images with contours of several brightness threshold values overplotted with: 120 % (top left), 130 % (top right), and 140 % (bottom left), respectively. A temporally aligned HMI image (±400 G) is also plotted (bottom right) with 130 % and 140 % contours overlaid.

in a ring around the sunspot, often co-spatially with regions of strong, vertical magnetic flux. Increasing the threshold value to 140 %, focuses the returned events to a smaller ring around the sunspot (features are highlighted with the green contours), however, several events which can potentially be classed as Ellerman bombs (through a visual inspection) are not selected by the algorithm. Most likely, changes in seeing and the requirement that brightenings over this threshold must be achieved in both wings for an event to be registered will cause the algorithm to drop relevant features from frame-to-frame with a threshold this high. Therefore, an intensity threshold value of 130 % of the background intensity (as chosen by Georgoulis et al. 2002) is deemed suitable to research the aims of this Chapter using these data.

Fig. 3.3(d) plots the vertical magnetic field within this FOV sampled by the SDO/HMI instrument and overlays the spatial positioning of features detected with a threshold of 130 % with blue contours. Assuming the co-spatial relationship between brightenings in the Hα line wings and strong vertical magnetic fields, it is obvious that a good co-alignment is achieved. For example, at approximately $x_c = 55''$, $y_c = -543''$ a short line of negative polarity magnetic flux that is mirrored exactly by detected features. Another example (corresponding to a region of positive polarity flux) can be observed at $x_c = 80''$, $y_c = -519''$. As both NBPs (Berger and Title 2001, Rutten et al. 2013) and Ellerman bombs (Georgoulis et al. 2002, Pariat et al. 2004, Pariat et al. 2007) are highly cited as forming co-spatially with strong vertical magnetic fields, this algorithm is, therefore, assumed to return features relevant to the research aims of this Chapter.

After deciding on an intensity threshold value, one final condition must be considered to create two individual sub-sets from the returned data. Specifically, an area threshold must be selected such that events which fit both the intensity and area estimates of Ellerman bombs found in previous researches can be isolated as a subset and compared to the overall output from the algorithm. In this Chapter, the approximate spatial resolution of the Flare Genesis

Experiment is used as this area threshold as this provides a method to contrast results with the literature. Therefore, a subset of 42 events with peak areas over $0.64''^2$ are considered to be the null data set of features against which the output from the algorithm can be tested. In the following sections, these events shall be called Ellerman bombs. As well as this, 3528 further features are registered over the course of the 90 minute duration of these data.

3.3.2 Lifetime of Detected Features

Fig. 3.4 plots the lifetimes of Ellerman bombs and other features analysed in this Chapter. Ellerman bombs are included in blue and have an approximate lifetime average of 7.2 minutes (with a relatively large standard deviation of 6 minutes), comparable to previous researches (such as Zachariadis et al. 1987, Georgoulis et al. 2002, Watanabe et al. 2011). The similarity between the areas, intensity increases, and lifetimes of these Ellerman bombs and respective properties in previous articles is taken as a confirmation that the selection criteria included in this Chapter are sufficient. Considering the remainder of features (plotted in red of Fig. 3.4), the function $y \propto \exp(-x/C)$ (where y and x are the total number and lifetime of Ellerman bombs respectively and C is a constant) accurately fits the trend plotted in the histogram for lifetimes less than 20 minutes. Interestingly, this function was also found to fit the distribution of bright points in the research presented in Watanabe et al. 2011.

The short-lived nature (less than 5 minutes) of some Ellerman bombs is intriguing and agrees with the recent suggestion by De Wijn et al. (2009) that magnetic restructuring can occur on scales below the current spatial and temporal resolutions of modern ground-based instruments. As the thresholding technique applied to discern these events from other brightenings in the wings of the Hα line profile is taken as the significantly worse spatial resolution of the Flare Genesis Experiment, it is possible that smaller Ellerman bombs existing within these data are not included in the sample plotted in blue in Fig. 3.4. Therefore, the average lifetime of all features identified by the algorithm was

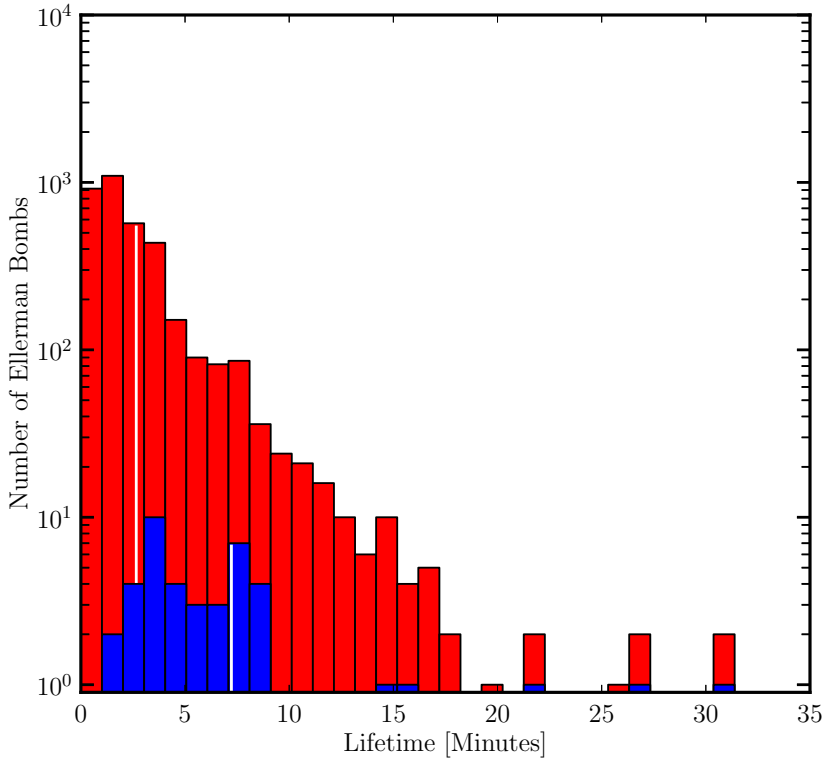

Figure 3.4: An Ellerman bomb-lifetime frequency plot. Ellerman bombs with a maximum area larger than $0.64''^2$ (circular diameter of approximately $0.45''$) are included with blue bars such that a comparison to estimates made in previous researches can be completed. All other features are plotted in red. The vertical white lines depict the average lifetimes of the two samples.

calculated and found to be around 2.6 minutes (with a large standard deviation of 2.6 minutes). Unfortunately, as the cadence of these data is 26.9 seconds, and a large number of features occur with lifetimes below one minute, it is difficult to assert with any confidence that a lower limit on lifetimes has been found. In future Chapters, research will be conducted to further understand whether short-lived events (such as those returned by this algorithm) could potentially be Ellerman bombs or whether a lower limit on their lifetime is evident.

3.3.3 Area of Detected Features

In the literature, Ellerman bombs have often been described as elliptical brightenings with lengths on the order of $1''$ (as was discussed by, for example, Zachariadis et al. 1987, Georgoulis et al. 2002, Pariat et al. 2004). Obviously, the parameters used for feature identification in this Chapter return a large number of extremely small, less bright phenomena (which can be easily observed in Fig. 3.3) which are of interest in this Section. If one considers that the spatial and temporal resolutions of the data analysed in this Chapter are one-fifth and one-seventh of the Flare Genesis Experiment resolutions, respectively, the identification of more small-scale events with the same intensity threshold (as used by Georgoulis et al. 2002) is unsurprising. Overall, the majority of features identified in this Chapter have diameters much smaller than the estimates of Ellerman bomb lengths in previous researches. Indeed, only 42 events have maximum areas through their lifetime of over $0.64''^2$. The average area properties of all features are plotted in Fig. 3.5.

During their evolution, Ellerman bombs often exhibit rapid changes in area and intensity over the course of seconds to minutes (see, for example, Qiu et al. 2000, Watanabe et al. 2011). These dynamical processes are often referred to as 'flaring'. This flaring can consist of the rapid extension of thin 'arms' away from the main structure or of a more general area expansion and shall be discussed in more detail in the following Chapters of this thesis during detailed analyis of confidently analysed Ellerman bomb events. Through a visual inspection

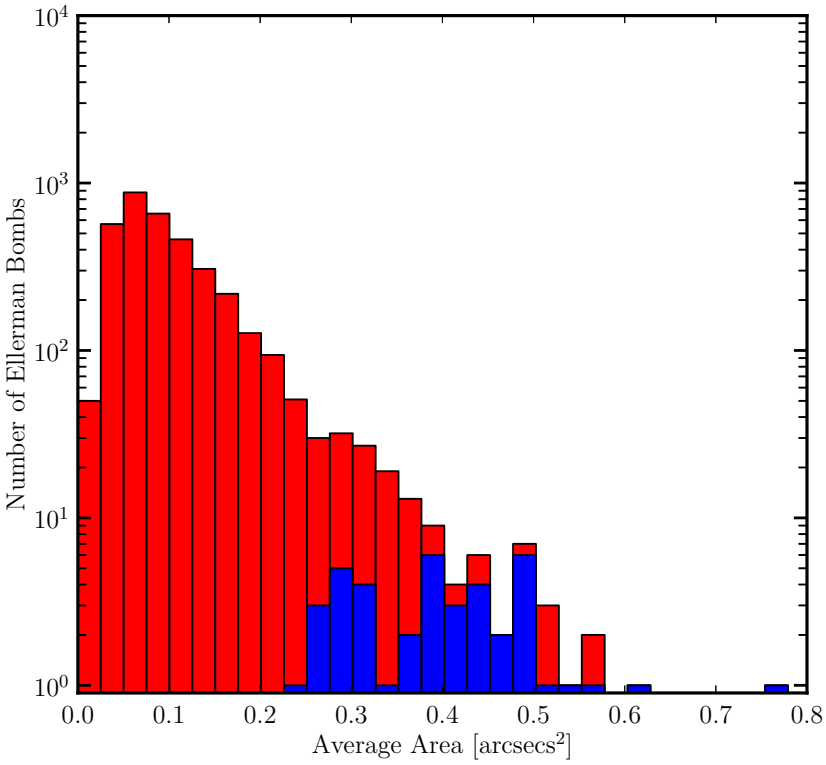

Figure 3.5: The average area of each feature analysed in this Chapter through time. Again, the blue features reach an area over $0.64''^2$ during the course of their lifetime and the red columns indicate all other events.

of large-scale features, such dynamical evolution was evident, giving further confirmation at the accuracy of this algorithm. The sub-structuring (such as the extension of the narrow arms) found within Ellerman bombs in these data occurs on scales well below the size of the overall structure. Therefore, small-scale features with average areas close to the spatial resolutions of these data could flare but on scales smaller than currently observable. As the average area of all smaller features returned by this algorithm is $0.11''^2$, much higher resolution observations that those analysed here would be required to decipher such flaring.

3.3.4 Energetics of Detected Features

In the previous sections of this Chapter, numerous Ellerman bombs and other bright features in the wings of the Hα line profile have been identified around a sunspot in NOAA AR 11126. Analysing data from the Flare Genesis Experiment, Georgoulis et al. (2002) estimated the energies of each Ellerman bomb in each individual frame ($P_{\rm rad}$) and over the course of their entire lifetime ($E_{\rm rad}$). In this Section, the model used in that article is applied to all of the events identified in these data regardless of size. In Georgoulis et al. (2002), the maximum and total energy release for Ellerman bombs was calculated as follows:

$$P_{\rm rad} \approx \epsilon_{\rm rad} f V_{\rm EB;max} \quad \text{and} \quad E_{\rm rad} \approx \frac{P_{\rm rad} D}{2} \tag{3.1}$$

where $\epsilon_{\rm rad}$ is the net radiative loss rate initially discussed by Nagai (1980) and estimated as:

$$\epsilon_{\rm rad} \approx a(T) n^2 \chi g(T), \tag{3.2}$$

f is the radiative filling factor (assumed as being unity), $V_{\rm EB;max}$ is the maximum volume of the Ellerman bomb and D is the lifetime of each feature. Defining $a(T)$ as the radiative reduction coefficient, n as the total numerical density of electrons and neutral hydrogen, χ as the ionization degree and $g(T)$ as a semi-empirical function of the temperature from Nagai (1980). Assuming $T \approx 10^4$

K and $n \approx 10^{12}$ cm^{-3}, Georgoulis et al. (2002) found $\epsilon_{\rm rad} \approx 0.89$ erg cm^{-3} s^{-1}. Letting the height of an average Ellerman bomb be 100 kilometres, it is possible to produce estimates for the maximum and total energies of each of our Ellerman bombs (as plotted in Fig. 3.6). Fitting power laws to these data at different spacings gives indexes of between -0.18 and -2.09, the latter of which is the same as the index found by Georgoulis et al. (2002).

It is found that the energetics of the features studied in this Chapter are around three to four orders of magnitude smaller than those stated in Georgoulis et al. (2002). Simply, this discrepancy can be explained by the short lifetimes (often a factor of six less than those discussed by Georgoulis et al. 2002) and small areas (around 2-3 orders of magnitude smaller) of many of the events analysed in this Chapter. The difference is unsurprising as many of these events may not fit into the category of Ellerman bombs. A log-log plot of the number of features with respect to energy is plotted in Fig. 3.6 and appears to show a power-law function, $\mathrm{d}N(x)/\mathrm{d}x \propto x^{-\alpha}$. Interestingly, this total energy release histogram shows energies in the region 2×10^{22}- 4×10^{25} ergs. The energies returned in this study have been suggested as the possible energies of 'nano-flares' by, for example, Parnell and Jupp (2000). However, as Ellerman bombs occur in the photosphere, and only in certain conditions, and do not routinely have a coronal component (see, for example, Schmieder et al. 2004), the role of these events in heating the corona is likely minimal.

It should be firmly noted that these values are based on a large number of, possibly erroneous, assumptions such as the height over which Ellerman bombs form, the temperature and total numerical densities assumed here. For example, the temperature of $T \approx 10^4$ K assumed in this Section is, perhaps, a factor of two larger than average photospheric temperatures (as discussed by Vernazza et al. 1981) and the modelled temperature of Ellerman bombs (see, for example, Fang et al. 2006). The individual brightness of each event is also not included in this method, therefore not differentiating between extremely bright (potentially high-energy) events and less bright (potentially low-energy) features. Overall,

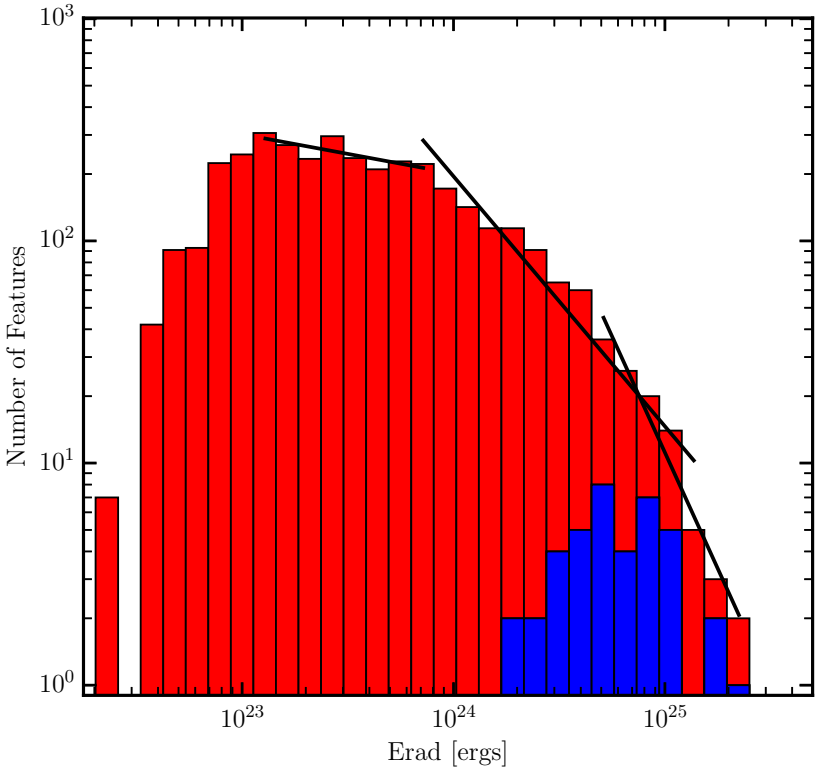

Figure 3.6: The total energy release for each feature, taking into account the measured lifetime of each event returned from the algorithm. Once again, large features are plotted in blue. The black lines overlaid on the plot indicate three power laws calculated for the data with indexes of (from left to right) -0.18, -1.13, -2.09.

it is suggested that the estimates of Ellerman bomb energies presented in this Chapter should be further considered and either corroborated or dismissed by future studies.

3.3.5 Evolution and Motion of Features

Recent analyses of Ellerman bombs have detected horizontal motions exhibited by these features (see, for example, Georgoulis et al. 2002, Watanabe et al. 2011). Specifically, these motions are of interest due to the assertions of previous researches (see , for example, Denker et al. (1995), Nindos and Zirin (1998), Watanabe et al. 2011) who suggested that Ellerman bombs could migrate with moat flows around sunspots. As well as this, numerous authors have discussed the recurrence of Ellerman bombs (see, *e.g*, Dara et al. 1997, Qiu et al. 2000, Georgoulis et al. 2002) from specific spatial positions. It is, therefore, meaningful to analyse the motions of the features selected by the algorithm used in this Chapter. The top frame of Fig. 3.7 plots the whole FOV of these data sampled in the Hα red wing. Numerous bright features are immediately evident, many of which appear to move along flows in a similar manner to discussions in previous researches. With respect to recurrence, all recurring bright features (potentially Ellerman bombs) within these data displayed one of two distinct traits. The black lines overlaid on the top frame of Fig. 3.7 outline the slits used to calculate time-distance diagrams to display each type of recurrence in the two distance-time plots.

The middle panel of Fig. 3.7 plots a time-distance diagram averaged across the width of slit '(b)' overlaid on the top frame. This averaged slit technique was exploited due to the motions of these features, and their small-scale nature, meaning it proved difficult to isolate a single line of pixels which accurately portrayed the observed motions through time. In this frame, two temporally separated bright features (labelled with arrows numbered '1' and '2', respectively) are observed to form at the same spatial position. Both of these brightenings flow away from the sunspot at speeds comparable to moat flows (such as the

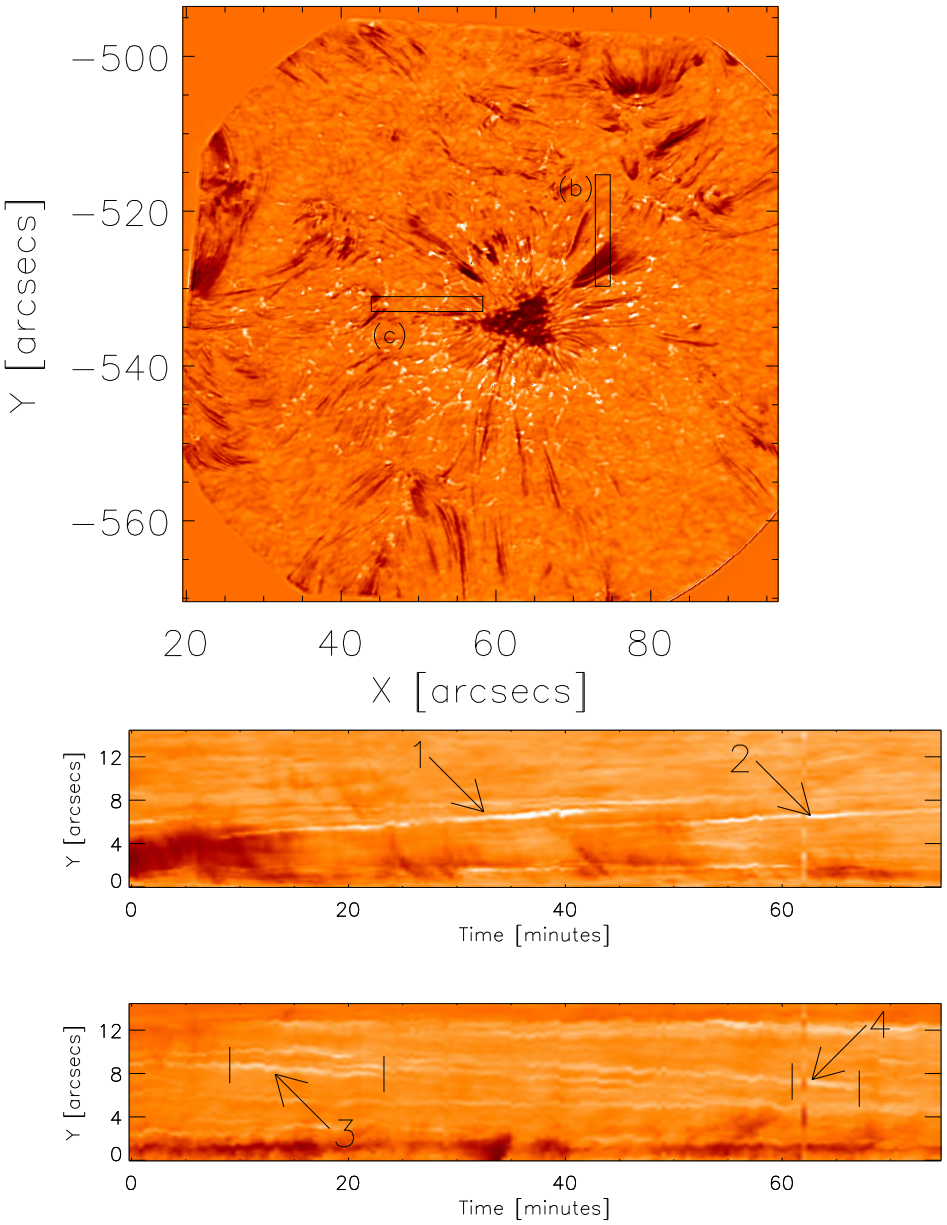

Figure 3.7: The initial frame of these DST/IBIS red wing data (top frame). Two distance-time diagrams plotting regions (b) and (c), respectively. Arrows 1 and 2 (middle frame) highlight the recurring bright features formed at the same spatial position. Arrows 3 and 4 indicate the recurrence of an apparently linked event.

values of 1 km s^{-1} found by Sheeley 1969) before fading from view. These properties are comparable to the traits attributed to Ellerman bombs by Nindos and Zirin (1998). It is easily inferred that the temporal separation of the formation of these events is around 40 minutes, however, much shorter separations were also observed within these data.

The lower panel of Fig. 3.7 depicts the second definition of recurrence that is prevalent in these observations. Many examples of extreme brightenings in the wings are observed which then fade before becoming brighter again, often after migrating away from the sunspot. Bars are situated around the bright features (indicated by arrows '3' and '4') to show the extent of the lifetime of each event. One should note, however, that this is an averaged distance-time plot and, therefore, does not accurately convey relative brightness (*e.g.* if 20 pixels are around 110 % of the background brightness, this may appear similar to a ten pixel 130 % brightness). A visual inspection of the feature plotted in the lower panel in imaging data indicated that the two bright features (highlighted by the vertical bars) had the following morphological properties: 1) A bright feature appeared in the Hα line wings; 2) This feature then reduced in intensity before propagating with the moat flow away from the sunspot; 3) The intensity of this event increased again in a different spatial position. Many Ellerman bombs tend to follow such a pattern of fading before regaining brightness at a later time, perhaps due to a recurrence of a triggering event such as magnetic reconnection. In the following Chapters, such apparent motions shall be analysed in further detail in order to understand the occuring processes more clearly.

3.3.6 Correlation Between *G*-band MBPs and Detected Features

After coalignment of the Hα line-wing and *G*-band datasets, a thorough visual inspection indicated that a co-spatial relationship between many of the features studied in this Chapter and MBPs situated within inter-granular lanes was common. However, other features, including larger events appeared to have no

links to MBPs. A representative zoomed FOV from a representative frame is plotted in Fig. 3.8 in order to display this relationship. Feature A in Fig. 3.8, for example, is a relatively large event situated over an intergranular lane, co-spatial to a group of MBPs in the G-band image. As has been shown by *e.g.* Jess et al. (2010a), it is possible that explosive phenomena similar to Ellerman bombs can be driven by interactions between two photospheric MBPs within inter-granular lanes.

As well as relatively large brightenings, smaller events (such as those indicated by arrows B and C in Fig. 3.8) can also occur co-spatial to MBPs. Indeed, feature C does not increase in size compared to its form in this image throughout its short lifetime. These two typical examples show a similar spatial relationship between MBPs within intergranular lanes and the small features selected by this algorithm as that possessed by larger Ellerman bomb events. It has been reported that two MBPs interacting can create Ellerman bomb brightenings in the Hα line wings (Jess et al. 2010a); however, for events B and C, no evidence of fragmented MBPs is evident (*i.e.* only a single MBP is observable). Whether fragmenting occurs on scales smaller than the spatial-resolution presented here must be answered using higher-resolution data.

It is possible that the potential link between small bright regions in the wings of the Hα line profile and MBPs supports the assertion that a sub-set of the smaller events, which have been neglected in other studies, could perhaps be Ellerman bombs. De Wijn et al. (2009) proposed that magnetic structuring within the photosphere should happen on a spatial scale well below the diffraction limit of current telescopes; this has been supported by numerical simulations run by Crockett et al. (2010) who found the mode MBP size to be around 45000 km^2 (or a circular diameter of approximately $0.32''$) and an equal number of events with sizes 10000 km^2 and 100000 km^2 (circular diameters of $0.16''$ and $0.49''$, respectively). Therefore, if there is a connection between magnetic structuring and Ellerman bombs as widely anticipated (Georgoulis et al. 2002; Pariat et al. 2004; Jess et al. 2010a; Watanabe et al. 2011), then

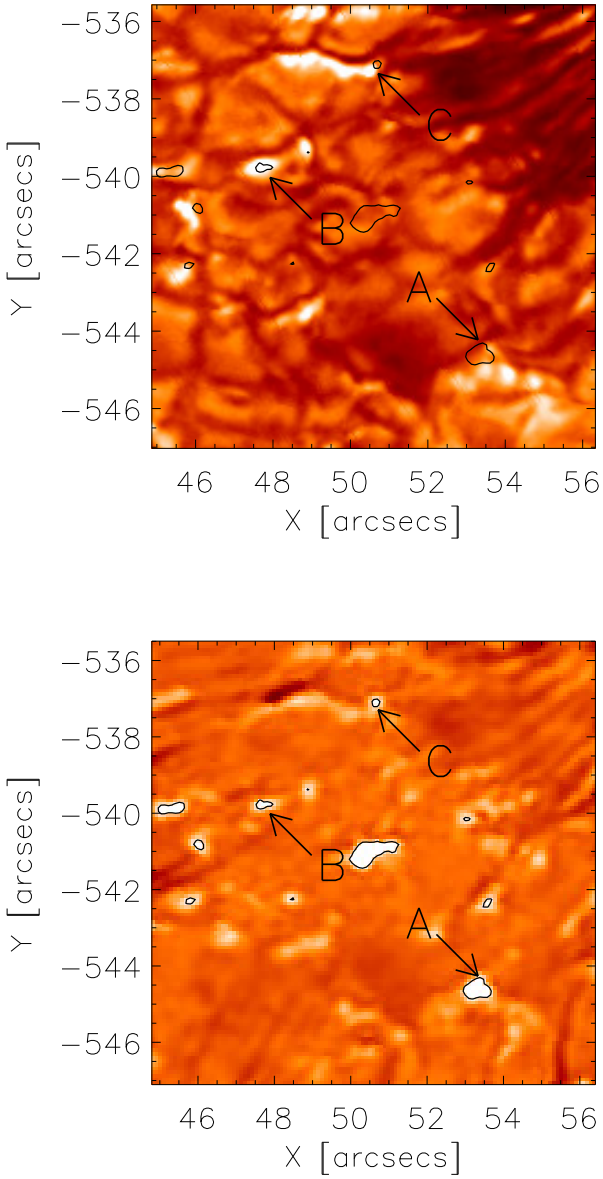

Figure 3.8: A *G*-band image with basic intensity contours from a single Hα line wing image overlaid in black (left frame). Three characteristic examples of brightenings co-spatial with MBPs are shown with arrows. A temporally aligned Hα blue wing image with the arrows pointing to the characteristic features is also plotted (right frame).

high-resolution data, collected during periods of excellent atmospheric seeing, as presented here, could find Ellerman bombs to be, on average, extremely small. It is then possible that many of the small-scale features plotted in Fig. 3.4 could be Ellerman bombs.

3.4 Discussions

In this Chapter, a statistical analysis has been undertaken which has focused on small-scale brightening events in the wings of the Hα line profile, specifically with respect to potential lower limits of the properties of Ellerman bombs. These events have been widely linked to the photospheric line-of-sight magnetic field, as well as to magnetic reconnection (see, for example, Zachariadis et al. 1987, Georgoulis et al. 2002, Watanabe et al. 2011). The initial statistical results presented in this Chapter were derived from the use of an automated detection algorithm which selected brightenings in speckled images sampled within the Hα line wings (at approximately ± 0.7 Å) by the DST/IBIS instrument. Each detected brightening was tracked through time before being read-out such that its properties (for example, lifetime, area, and energy) could be analysed during this research.

Overall, the automated detection algorithm identified 3570 potential Ellerman bomb events for analysis within 90 minutes of data. To test the algorithm, events over the spatial resolution of previous researches were included as a null dataset. These features (which had maximum areas over $0.64''^2$) had a lifetime of approximately 7.2 minutes (with a standard deviation of 6 minutes) which is comparable to previous researches, hinting that these features form a sub-set of traditional examples of Ellerman bombs. The average lifetime of all other detected features was 2.6 minutes (with a standard deviation of 2.6 minutes), which is less than previous estimates of Ellerman bomb lifetimes (which range between $5 - 15$ minutes as presented by Georgoulis et al. 2002; Pariat et al. 2004; Watanabe et al. 2011). The average area of the smaller features found in

this research was 0.41 $''^2$ which, again, is much smaller than previous estimates of Ellerman bombs.

Using the method suggested by Georgoulis et al. (2002), the energy of each of the small-scale events was estimated. These features had diminished values from previous studies with these data yielding estimated energies for the features returned by the algorithm of between 2×10^{22} and 4×10^{25} ergs. Fitting a number of power laws to the small-scale events analysed in this Chapter returned indexes between -0.18 and -2.09. However, due to the occurrence of many of the identified features with resolutions close to the limitations of the instruments used to collect these data, it is possible that these power laws do not accurately capture the background physics and, therefore, should be studied further in future research. These energy estimates (combined with the decreased lifetimes and areas of many of the smaller scale features) imply that Ellerman bombs, if they make up a subsection of the events plotted in red in Figs. (3.4)-(3.6), may form on smaller-scales than has previously been observed. This possibility agrees well with the arguments of De Wijn et al. (2009), who suggested that magnetic reconnection and structuring could occur on spatial scales well below current observational resolutions. The continued advancement of observational instruments should lead to more detailed studies of small-scale events as analysed here to discuss their morphology in comparison to larger events.

The motions of the selected features were also analysed through time. Of specific interest was the concept of recurrence which has been discussed by a number of authors including Dara et al. (1997), Qiu et al. (2000), Georgoulis et al. (2002). A thorough visual inspection of these data indicated that two distinct recurrence types for identified features occurred. The first involved multiple features forming in the same spatial position at different times, before exhibiting horizontal motions consistent with flows around a sunspot (see, for example, Sheeley 1969). The second mechanism involved a bright region, again displaying horizontal motions, which diminished in intensity and area before appearing to flare again in a different spatial location later. In the later Chapters

of this thesis, these recurrence methods shall be discussed in further detail.

Finally, links to the photospheric magnetic field were inferred through SDO/HMI magnetograms and DST/ROSA *G*-band images. These instruments showed a strong correlation between detected features and line-of-sight magnetic field measurements and MBPs, respectively. However, this correlation was not one-to-one and a number of detected bright features did not display any co-spatial relationship with inferred magnetic fields. It is possible that such features belong to the sub-set of emission events in the wings of the Hα line wings, described as pseudo-Ellerman bombs by Rutten et al. (2013). In the coming Chapters of this thesis, the small-scale dynamics exhibited by Ellerman bombs and their links to the photospheric magnetic field will be examined in more detail.

Chapter 4

Comparison of Numerical Magnetic Reconnection to Observational Signatures of Ellerman Bombs

4.1 Overview

In order to advance the research presented in the previous Chapter, it is important to understand the feasibility of photospheric magnetic reconnection as a potential driver of the Ellerman bomb phenomena. Within ARs, examples of cancellation can often be observed through a visual inspection of magnetogram data (such as MMFs as discussed by: Sheeley 1969; Harvey and Harvey 1973). This observed cancellation is an indication of the rapid evolution of the magnetic configuration within the photosphere, and could be a signature of a number of processes including magnetic reconnection or the submergence of magnetic fields. With respect to Ellerman bombs, however, these observed cancellation features are interesting due to their compatibility with the cartoon reconnection models suggested by Georgoulis et al. (2002). In this Chap-

ter, therefore, high-resolution, high-cadence observations from the DST/IBIS and DST/ROSA instruments are considered in order that small-scale Ellerman bomb events situated within NOAA AR 11579 can be studied. These data are combined with SDO/AIA and Hinode/SOT images which provide information about the co-aligned upper solar atmosphere and the photospheric line-of-sight magnetic field, respectively. To progress this work on from a mere co-spatial relationship between Ellerman bombs and magnetic features, magnetic reconnection events within state-of-the-art numerical simulations made using the MPS/University of Chicago Radiative MHD (MURaM) code by Dr. Sergiy Shelyag are compared to these observations.

Modern magnetic field data collected by instruments (including SDO/HMI) are a wonderful tool for analysing large-scale structures in the solar atmosphere. At the spatial and temporal scales of photospheric features such as Ellerman bombs, however, these data are, unfortunately, less useful. For example, the pixel sizes of data collected by the SDO/HMI instrument are larger than the average size of the features detected by the algorithm in the previous Chapter, meaning subtle reconfiguration of the magnetic field on scales of hundreds of kilometers could go unnoticed. Due to this, it has proved difficult to identify whether certain topologies are required for the formation of Ellerman bombs (*e.g.*, whether bi-poles are required or if uni-polar fields can also drive these features). Strong observational evidence supporting photospheric magnetic reconnection as the driver for Ellerman bombs hypotheses has, therefore, been difficult to establish.

In response to this, several authors have conducted numerical simulations of the lower solar atmosphere to investigate the link between magnetic fields and brightening events in the photosphere. Using a two-dimensional implementation of the Coordinate Astronomical Numerical Softwares (CANS) code, Isobe et al. (2007) suggested that an emerging flux loop could incite reconnection events throughout the solar atmosphere by propagating upwards from the photosphere. It was suggested that Ellerman bombs could be formed in the photosphere before

the flux loop rose further, into the corona, to form features such as X-ray jets. Following on from this, simulations using the three-dimensional CANs code were conducted by Archontis and Hood (2009). These authors found U- and V-shaped magnetic topologies (similar to those suggested as topologies likely to be conducive to magnetic reconnection by, *e.g.*, Georgoulis et al. 2002, Pariat et al. 2004, Pariat et al. 2007) co-spatial with increases in temperature in the lower solar atmosphere which were hypothesised to be comparable to Ellerman bomb events in the Hα line wings. These researches, however, did not attempt any reconstruction of line profiles which could be directly compared to observations.

The lack of simulated line profiles for Ellerman bombs can be attributed to the difficulty of simulating the Hα line profile (see, for example, Leenaarts et al. 2012, Rutten 2012) as has been previously discussed. In this Chapter, therefore, Ellerman bombs are identified in the Hα line wings before the response of the Fe I 6302.5 Å profile to the driving mechanism is recorded. The Fe I 6302.5 Å wavelength has been extensively studied using the MURaM code, specifically with respect to magnetic cancellation. Indeed, Danilovic̀ (2009) presented an extensive study of simulated magnetic flux cancellation in the solar photosphere using the low-photospheric absorption lines: Fe I 6302.5 Å, Fe II 5197.58 Å, and Fe II 4923.92 Å. One magnetic reconnection event within MURaM simulations was studied, showing increases in temperature at the inversion line between two opposite polarity regions. In addition to this, Shelyag et al. (2007) found intensity enhancements and splitting of the Fe I line core co-spatial with bi-polar magnetic field concentrations in the photosphere, suggesting that signatures of reconnection could be observed in the 6302.5 Å line profile.

In this Chapter, observations and simulations are combined to investigate the Ellerman bomb phenomena with specific respect paid to the signatures of these events in Fe I 6302.5 Å line profiles and the relationship between these events and the line-of-sight photospheric magnetic field. The output from the MURaM code simulations are then compared with observational signatures. This Chapter is structured as follows: In Section 2, a brief overview of the

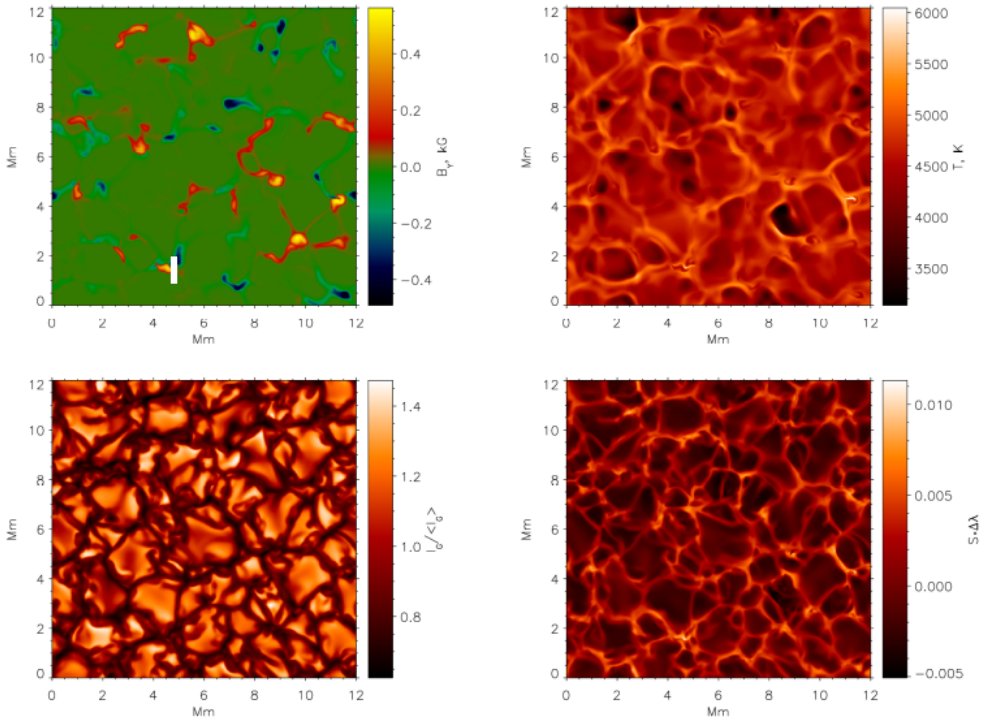

Figure 4.1: A snapshot of the simulations analysed in this Chapter. The top row depicts the vertical component of the magnetic field (left) and temperature (right) both measured at 500 km height above the continuum formation level. The bottom row plots the normalized G-band intensity (left) and Fe I 6302.5 Å line strength, S, multiplied by the line Doppler-shift, $\Delta\lambda$ (right). The cancellation feature discussed in this Chapter is marked by a short, white vertical line in the top left panel (x_c=4.5 Mm, y_c=1.5 Mm).

simulations conducted by Dr. Sergiy Shelyag is given. Section 3 then introduces the observations analysed in this Chapter, while Section 4 contains the data analysis. Finally, a discussion of the relevance of these results is made in Section 5. The research presented in this Chapter is published in: **C. J. Nelson**, S. Shelyag, M. Mathioudakis, J. G. Doyle, M. S. Madjarska, H. Uitenbroek, R. Erdélyi, 'Ellerman Bombs - Evidence for Magnetic Reconnection in the Lower Solar Atmosphere', *The Astrophysical Journal, Volume 779 (2013), Page 125*,

4.2 Simulated Domain and Analysis

The MURaM radiative MHD code (Vögler et al. 2005) was used to construct the simulated data analysed in this Chapter. A numerical box was formed with a horizontal extent of $12\times12\times1.4$ Mm^3, which was sampled by $480\times480\times100$ grid cells returning pixel sizes of 25 km and 14 km, respectively. These simulations began from a well-developed snapshot of non-magnetic photospheric convection before a bi-polar, checkerboard magnetic field structure with unsigned magnetic field strength of 200 G was introduced into the domain. The length of the individual squares of constant magnetic field was chosen to be 2 Mm. After the magnetic field was introduced, the simulated photosphere was allowed to evolve for approximately 1.5 solar hours. During the first few minutes of the simulation, large parts of the magnetic field were advected into the intergranular lanes and some magnetic flux was cancelled due to the opposite-polarity initial configuration (as was discussed by, *e.g.*, Cameron et al. 2011). Magnetic field concentrations of opposite polarity with unsigned strength of up to 1.6 kG at the continuum formation level were subsequently formed, which often moved due to the turbulent nature of the convection, came closer together, reconnected and cancelled out. In order to further understand these data, a radiative diagnostics code RH (see Uitenbroek 2001) was then used to calculate the Fe I 6302.5 Å and Hα line profiles.

In Fig. 4.1, a snapshot of these simulations is plotted approximately 1.5 hours after the beginning of these simulations. This allowed convection to become established and the magnetic field to be advected into intergranular lanes. The cancellation region selected for analysis in this Chapter is marked by a short vertical, white line in the top left panel at approximately x_c=4.5 Mm, y_c=1.5 Mm. The vertical component of magnetic field (top left panel) and temperature (top right panel) measured in the photosphere 500 km above the 5000 Å continuum formation level are plotted. Structures reminiscent of inter-granular lanes are immediately evident as well as localised temperature increases co-spatial to small, magnetic bi-poles. The *G*-band image (lower left

frame) depicts optimally these inter-granular lane structures and is comparable to actual observations at this wavelength. Finally, the Fe I 6302.5 Å intensity is plotted (bottom right panel). Data similar to these have been extensively tested and implemented in researches such as Shelyag et al. (2007), Shelyag et al. (2011), Cegla et al. (2013).

In Fig. 4.2, the slice of the simulated domain indicated by the slit overlaid on Fig. 4.1 is plotted for a number of parameters. The top two rows depict the magnetic field strength and the temperature of the slit with height. It is immediately obvious that a temperature enhancement exists at a spatial position of around x=0.6 Mm. This corresponds to the region of U-shaped magnetic fields (highlighted by the black and white lines which indicate negative and positive polarity fields, respectively). This opposite polarity flux region is observed to come together through time within these data before it restructures, or reconnects, as can be seen in this frame. This temperature enhancement corresponds well with the research of Fang et al. (2006) who attributed the increased in intensity in the Hα line wings within Ellerman bombs to localised density and temperature enhancements in the photosphere.

The bottom two frames of Fig. 4.2 plot profiles for the synthesised Fe I 6302.5 Å and Hα absorption lines for each column in the above slits. At the reconnection site, it is possible to identify the heightened line wing intensity within the Hα line profile similar to those observed for Ellerman bombs (at approximately x=0.6 Mm). The Fe I 6302.5 Å line profile, however, displays an increase in intensity in the line core, visible co-spatial to the temperature increase and cancellation. In Fig. 4.3, line profiles calculated from a single column within the reconnection site are plotted through time. Once again the increased emission in the Fe I 6302.5 Å line core and the Hα wings are visible. Finally, the physical properties of these brightenings can be crudely estimated from these plots. Overall, the length of the brightening in the Hα line wings and its lifetime can be estimated at approximately 100 km and 1 minute. These properties are smaller than for an average Ellerman bomb yet

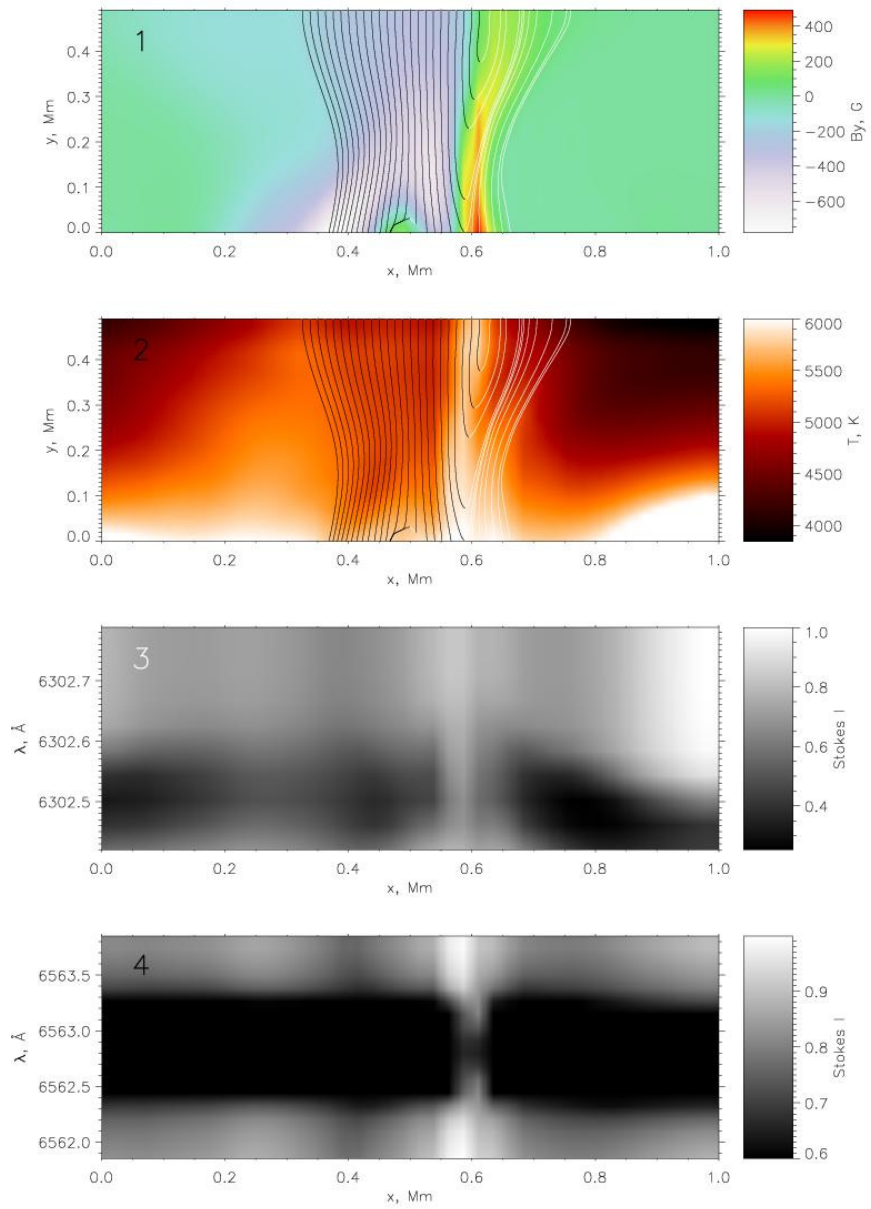

Figure 4.2: A reconnection event in the simulated photosphere. The frames correspond to the vertical magnetic field with white and black lines overlaid for positive and negative polarity (top row), the simulated temperature with the field lines overplotted (second row), the Fe I 6302.5 Å line profile for each pixel in the x-direction (third row) with a 'gap' in the reconnection region ($x \sim 0.6$ Mm), and the Hα line profile. Note the brightenings in the wings of the Hα line profile comparable to an Ellerman bomb (bottom row).

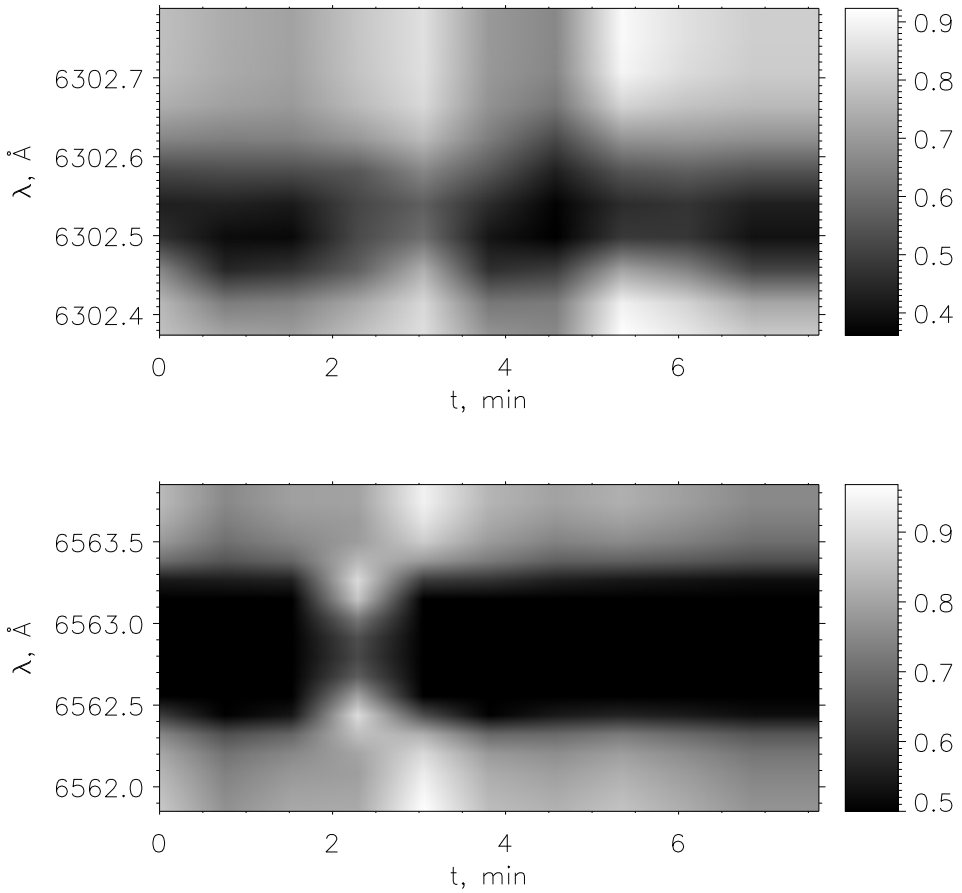

Figure 4.3: Line profile-time plots from a slit at approximately x=0.6 Mm in Fig. 4.2 including the Fe I 6302.5 Å (top row) and Hα line profiles (bottom row). Between 2.5 and 4.5 minutes, the Fe I 6302.5 Å profile includes a 'gap' corresponding to the reconnection event and Hα shows line wing increases.

they are not unreasonably different. In the following sections, observational signatures of Ellerman bombs will be presented such that these simulated data can be tested.

4.3 Observations

The ground-based data analysed in this Chapter were obtained with the DST/IBIS and the DST/ROSA instruments during a period of good seeing. The DST/IBIS instrument conducted a 26 frame sequence, repeated at a cadence of 5.5 seconds during the time series, sampling a sunspot within AR 11579. These data were collected between 14:50:59 UT and 15:05:34 UT on the 30th September 2012. The observational sequence included 17 Hα wavelength points, taken with unequal step sizes ranging between $\pm$ 1.0 Å from the line core, and 9 Fe I 6302.5 Å positions finely sampled between 6302.4 Å and 6302.75 Å. The pixel size of these data was approximately 0.097″. Two DST/ROSA CCDs were also employed during this time frame, sampling the granulated photosphere with the *G*-band filter and the chromosphere using the Ca II K 3933.7 Å wavelength. The reconstructed, science-ready cadence of data from these wavelengths was 2.112 seconds and 8.448 seconds, respectively. Both wavelengths were observed with approximate pixel sizes of 0.069″.

Space-borne SDO/AIA and Hinode/SOT data were used to supplement the ground-based data analysed in this Chapter. Data from the SDO/AIA instrument have pixel sizes of 0.6″ and a cadence of either 24 seconds (for the 1600 Å and 1700 Å filters) or 12 seconds (for all other filters used in this Chapter). Further to this, photospheric line-of-sight magnetic fields were inferred using Stokes V/I data collected by the Hinode/SOT instrument. These data have a pixel size of 0.155″ and a cadence of around one minute. Although the cadence of these data is slightly longer than SDO/HMI data, the increase in spatial resolution (by a factor of three) is essential when analysing small-scale events such as Ellerman bombs. Conversions between the Stokes V/I parameter and

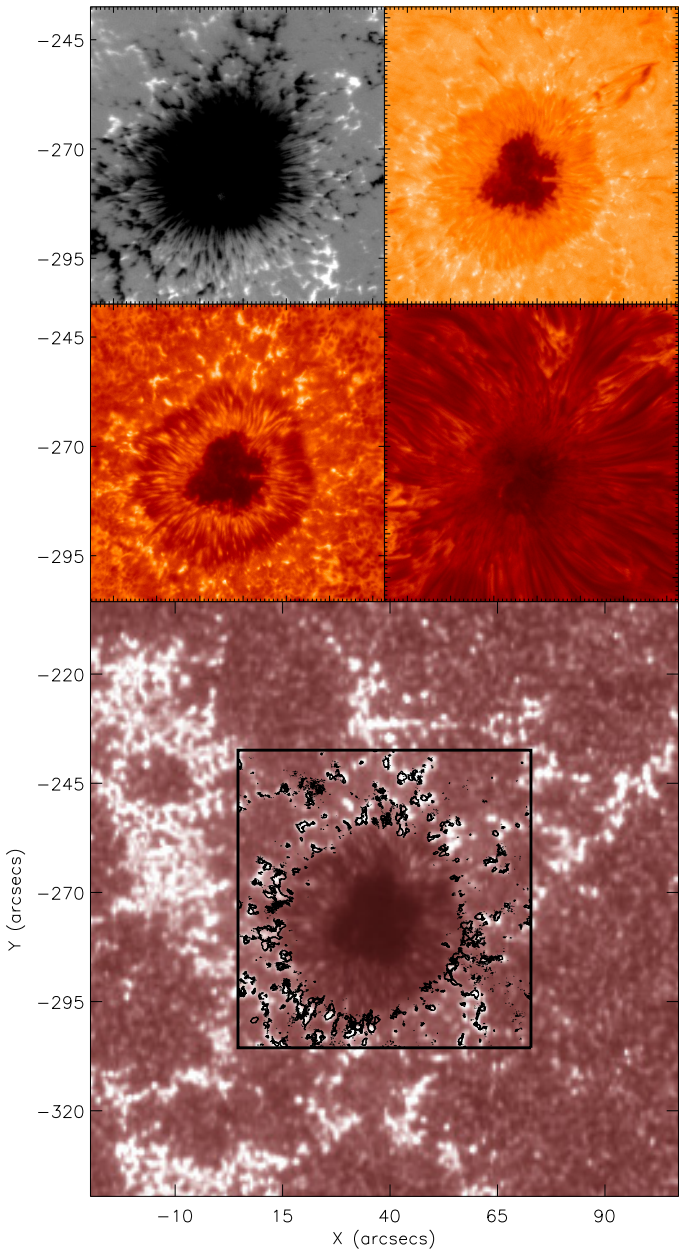

Figure 4.4: The FOV from the Hinode/SOT Stokes V/I (top left), DST/IBIS Hα blue wing (top right), Fe I 6302.5 Å line core (middle left), and Hα line core (middle right). An extended FOV from the SDO/AIA 1700 Å filter is plotted in the bottom frame. The black box indicates the FOV plotted in the above frames and the contours depict the NBPs sampled by the Hα blue wing, confirming the alignment. These data were collected at 14:51 UT.

true magnetic-field intensity (Gauss) have been achieved with Hinode/SOT data (see, for example, Lites and Ichimoto 2013) in the past, however, in this Chapter no such conversion is attempted. This can be justified by the fact that a linear factor can be applied to Stokes V/I data in the non-umbral and non-penumbral pixels to return magnetic field strength. As these data are considered only for their spatial positions and proportional cancellation rates, a possibly erroneous conversion to magnetic-field intensity would provide no benefit here.

In Fig. 4.4, the FOV analysed in this Chapter is presented for five wavelengths. In a similar manner to Chapter 3, this FOV contains a sunspot which is surrounded by a number of smaller-scale magnetic elements indicative of line-of-sight magnetic fields. In the top row of Fig. 4.4, Hinode/SOT Stokes V/I data (left frame) and the Hα blue wing (right frame) are plotted. The middle row plots both the Fe I 6302.5 Å line core (left frame) and the Hα line core (right frame). It is clear that neither the sunspot nor the small-scale magnetic elements are observable in the Hα line wing. The bottom frame of Fig. 4.4 depicts a larger FOV sampled by the SDO/AIA 1700 Å filter, outlining the wider structure surrounding this sunspot. A black box and black contours outline the network elements visible in the Hα blue wing and confirm the alignment of these instruments.

4.4 Data Analysis

4.4.1 Ellerman Bomb Identification

Within these data, a number of Ellerman bombs are immediately obvious even through a brief visual inspection of the Hα line profiles. These features exhibit intensity enhancements and show evidence of 'flaring' (as discussed by Watanabe et al. 2011), or an explosive nature, during their lifetimes. In Fig. 4.5, a zoomed region of the FOV analysed in this Chapter is plotted for a number of wavelengths, highlighting a typical Ellerman bomb event (during its formation period) identified by an increase in brightness in the Hα line wings. The

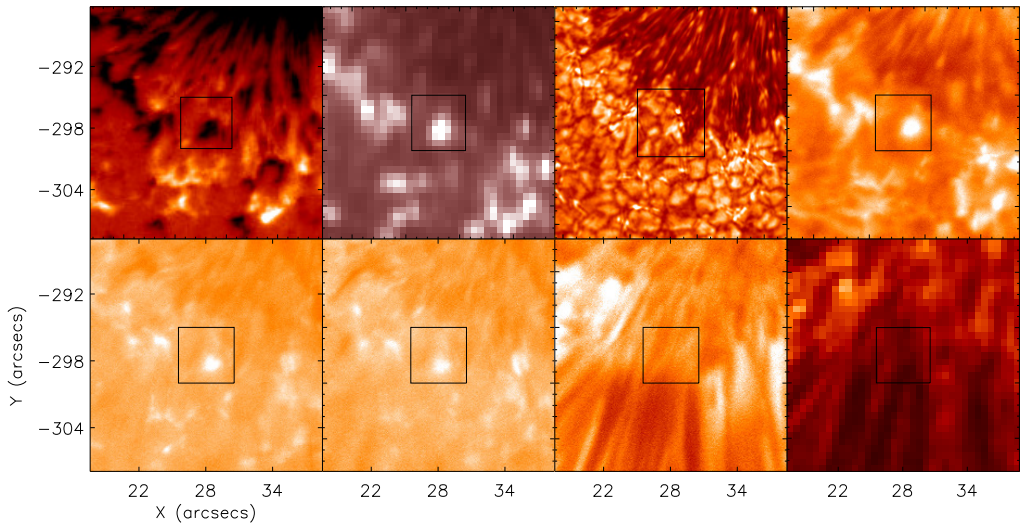

Figure 4.5: In the top row, (left to right) coaligned Hinode/SOT Stokes V/I, SDO/AIA 1700 Å, DST/ROSA *G*-band, and DST/IBIS Fe I 6302.5 Å line core images are plotted. The bottom row (left to right) depicts the same FOV sampled at the DST/IBIS Hα blue and red wings (approximately $\pm$0.75 Å), DST/IBIS Hα line core, and SDO/AIA 304 Å. The black box highlights an example Ellerman bomb event. This FOV is plotted at the temporally closest image for each wavelength to 15:02:30 UT.

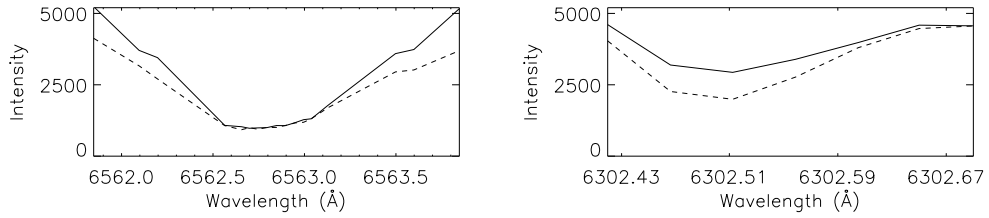

Figure 4.6: (a) Hα line profile for two spatial positions within the box in Fig. 4.5. The bold and dashed lines correspond to the Ellerman bomb event and quiet Sun, respectively. (b) Co-spatial Fe I line profiles.

lower photosphere shows evidence of a brightening co-spatial to the Ellerman bomb, with intensity increases being observed in the SDO/AIA 1700 Å and DST/ROSA *G*-band images (as has been discussed by, *e.g.*: Qiu et al. 2000, Jess et al. 2010a, Nelson et al. 2013a). In the Fe I 6302.5 Å line core, a co-spatial brightening event is also observable; however, no signal of this event is observed in the SDO/AIA 304 Å images. These observations are typical of Ellerman bombs and support the hypotheses of a number of authors such as Matsumoto et al. (2008b), who found evidence that these events were excited in the upper-photosphere. The top row of Fig. 4.5 plots (from left to right) the Hinode/SOT Stokes V/I, SDO/AIA 1700 Å, DST/ROSA *G*-band, and DST/IBIS Fe I 6302.5 Å line core images. The bottom row (from left to right) depicts the DST/IBIS Hα blue wing, red wing, and line core images as well as the SDO/AIA 304 Å filter.

In Fig. 4.6, the Hα and Fe I 6302.5 Å line profiles for the Ellerman bomb depicted in Fig. 4.5 are plotted such that the simulations defined in Section 4.2 can be compared. It should be noted that no events have sustained intensities brighter than 150 % of the background intensity during the course of these data (possibly due to effects of seeing and the lack of data reduction techniques) and, hence, 140 % of the background emission is used as a rough guide for identification of these features. Due to this, the current analysis is limited to large Ellerman bomb events, which show sustained brightening and flaring. The line profiles observed in Fig. 4.6 agree with both the definition of Ellerman bombs within the literature (originally put forward by Ellerman 1917 and later confirmed by, for example, Georgoulis et al. 2002, Matsumoto et al. 2008b, Watanabe et al. 2011) and, interestingly, the MURaM simulations considered in this Chapter. Due to the co-spatial formation of these features with bi-poles identified in Stokes V/I data, it is compelling to suggest that the observed and simulated features are comparable and should be analysed further in detail. Overall, seven potential features were identified for further analysis, each of which was co-spatial to a bi-pole as inferred by the Hinode/SOT Stokes V/I

data. Four of these events were comparable in size and lifetime to typical Ellerman bombs within the literature, however, three of these features were much smaller (less than 0.5″ in diameter).

4.4.2 Temporal Evolution of Ellerman Bombs

As has been previously discussed in the earlier Chapters of this thesis, data collected through fast line scans often exhibit significant stretching and jitter which are difficult to remove from science images. These motions (introduced by the Earth's atmosphere) add complexities to the interpretation of signals such as oscillations in area or short-lived intensity enhancements which are evident in time series. The influence of such stretching is particularly telling when analysing small-scale features like Ellerman bombs, with circular diameters less than 0.5″ and lifetimes of the order minutes. The longer time-scale evolutions of Ellerman bombs in these observations were, however, studied. Results were achieved by producing a sequence of images for each Ellerman bomb for investigation. In Fig. 4.7 a sample of these images are plotted through time for the event depicted in Fig. 4.5. It is of interest to note the Hα line wing (blue and red wings are plotted in the top and second rows, respectively) and the Fe I 6302.5 Å line core (third row) display brightenings which are co-spatial to a bi-polar region (inferred from the Hinode/SOT Stokes V/I image in the bottom row). Through time, this Ellerman bomb clearly evolves in both area and intensity similar to traditional Ellerman ombs (as discussed by, for example, Georgoulis et al. 2002, Watanabe et al. 2011, Rutten et al. 2013).

All of the seven features identified in this Chapter displayed co-temporal brightness and area enhancements in both the Hα line wings and the Fe I 6302.5 Å line core (as represented by the feature plotted in Fig. 4.7). As the predicted formation heights of the Hα line wings and Fe I 6302.5 Å line core are similar, this co-temporal behaviour is unsurprising. Interestingly, each of the smaller features discussed here exhibited similar flaring behaviour to the larger events (except on a smaller scale), allowing for the possibility that these features are

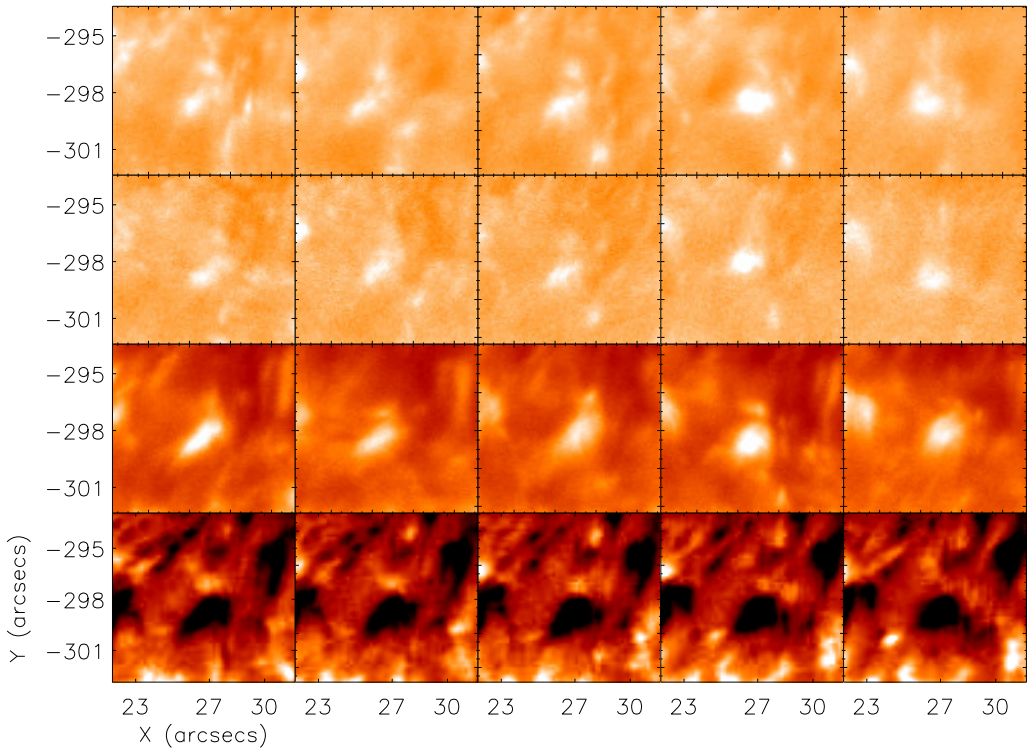

Figure 4.7: A zoomed FOV of a representative bi-polar region and a corresponding Ellerman bomb event in the Hα blue wing (top row), Hα red wing (second row), Fe I line core (third row), and Hinode/SOT Stokes V/I (bottom row) over time. Each column is the temporally closest frame for each wavelength to 14:52:36 UT, 14:55:38 UT, 14:58:39 UT, 15:01:39 UT, and 15:04:45 UT, respectively. Lightcurves for the full observational period are plotted in Fig. 4.8.

Event	Bi-pole	Cancellation	Emergence	Size
1	Yes	Yes	No	Typical
2	Yes	No	No	Typical
3	Yes	Yes	No	Typical
4	Yes	No	Yes	Typical
5	Yes	Yes	No	Small
6	Yes	Yes	No	Small
7	Yes	Yes	No	Small

Table 4.1: Properties of the seven events analysed in this Chapter, including the links to the photospheric magnetic field and its evolution.

driven by the same mechanism. When the co-temporal evolutions of these events are used as a base such that the simulated profiles presented in Fig. 4.3 can be compared, analogous evolutions are found at these line positions. However, at the simulated reconnection sites, a propagation of a reconnection is observed down through the solar atmosphere. This is hypothesised to occur due to expansion of the magnetic field concentrations towards the upper layers of the numerical box. The decreasing gas pressure allows reconnection to occur earlier in the upper-simulated photosphere than in the lower regions. It could be expected, therefore, that the thermal effect of reconnection would first be seen in the parts of the Hα line profile sensitive to the higher solar atmosphere, followed by intensity increases in the Hα wings and reduced opacity in the Fe I 6302.5 Å line core. As has been widely discussed, this is not the case, with no signal being observed in the Hα line core (see Chapter 3). Future analysis of simulations with a larger height would be required to understand whether this simulated reconnection is also limited to the lower solar atmosphere and, if so, why.

4.4.3 Links to the Photospheric Magnetic Field

The flaring properties of Ellerman bombs has previously been attributed to the impulsive nature of the hypothesised driver of these features, namely magnetic reconnection. In a similar manner to the analysis presented in the previous Section, it was possible to analyse the photospheric line-of-sight magnetic field component through time to detect evolutions in the localised structuring. In Table 4.1, the properties of each of the Ellerman bombs discussed in this Chapter are presented. Notice that all of these events form co-spatially with a magnetic bi-pole. Further to this, six of these bi-poles evolve visibly through time with five appearing to cancel and one appearing to be a site of flux emergence. This supports the validity of the aim of this Chapter which is to compare the output from realistic solar simultations to observational data. A brief discussion of the event which does not form co-spatially with cancellation or emergence should be included here. It is possible that magnetic field dynamics are occurring on sub-resolution levels (for example a cancellation rate comparable with the emergence of new flux in the region) or that this event is a pseudo-Ellerman bomb, *i.e.*, it is a region of raised intensity due to strong magnetic concentrations. With these current data is would be difficult to conclude firmly either way, however, due to the spectral properties of this event being comparable to the other six features observed in these data, this event will be considered as an Ellerman bomb for the remainder of this Chapter.

Lightcurves for the event depicted in Fig. 4.7 are plotted in Fig. 4.8. These lightcurves were made by focusing the image used in Fig. 4.7 onto the opposite polarity region such that no new, strong flux appears within the FOV in the lifetime of these observations. The total positive flux was then calculated by summing all positive values within the box (*vice versa* for the negative polarity) for each frame before plotting the normalised total flux over time. In Fig. 4.8(a), the smoothed Hα line wing (black and maroon for $\pm$ 0.75 Å, respectively) and the Fe I 6302.5 Å line core (orange) intensities are plotted through time for the same box. In Fig. 4.8(b) the negative polarity (black), positive polarity (orange)

and total flux (maroon) are also plotted. Over the period of these observations, there is a significant decrease in the flux of this small bi-polar region, dropping to around 68 % of the original flux, and only 30 % of the negative polarity flux. This decrease in flux is easily observed through the sequence of images presented in Fig. 4.7. Within a 15 minute period, a decrease of this order due to magnetic reconnection would suggest that any corresponding energy release must be strong, and could produce large temperature increases in the surrounding atmosphere.

The IBIS data (in Fig. 4.8 [top]) reaches a maximum intensity for each of these lines at approximately 15:02 UT, maintaining a peak for around two to four minutes. This peak is identified as 'flaring' within this Ellerman bomb, associated with both increased intensity and area. The short-lived peak is more evident within the Fe I 6302.5 Å line core, where an eight percent increase in intensity is observed within around one minute. Co-temporally, a rapid decrease in negative (and total) polarity flux in Fig. 4.8 (bottom), which continues until the end of these data, is observed. A second, smaller peak is observable at approximately 14:54 UT and corresponds to a large drop in both negative polarity and total flux within this FOV. Although this co-temporal brightening and flux cancellation occurs for several examples within this dataset, the cadence and spatial resolution of the Hinode/SOT data analysed in this Chapter are insufficient to accurately isolate and measure the magnetic evolution of these bi-poles, or MMFs. In Chapter 6, a larger dataset of magnetograms will be analysed in conjunction with high-resolution spectral data to further this research.

Hα wing brightening events co-spatial to uni-polar regions, such as the strong field at (33, -302) in Fig. 4.5, were also studied within these data. The average area of brightenings over uni-polar fields appeared to be larger than bi-polar Ellerman bombs. Smaller, shorter-lived intensity variations (comparable to changes in seeing level) were also common implying that rapid, high-energy releases may not be leading to these brightenings and, hence, that the increase in intensity in the Hα line wings and Fe I 6302.5 Å line core may be due to

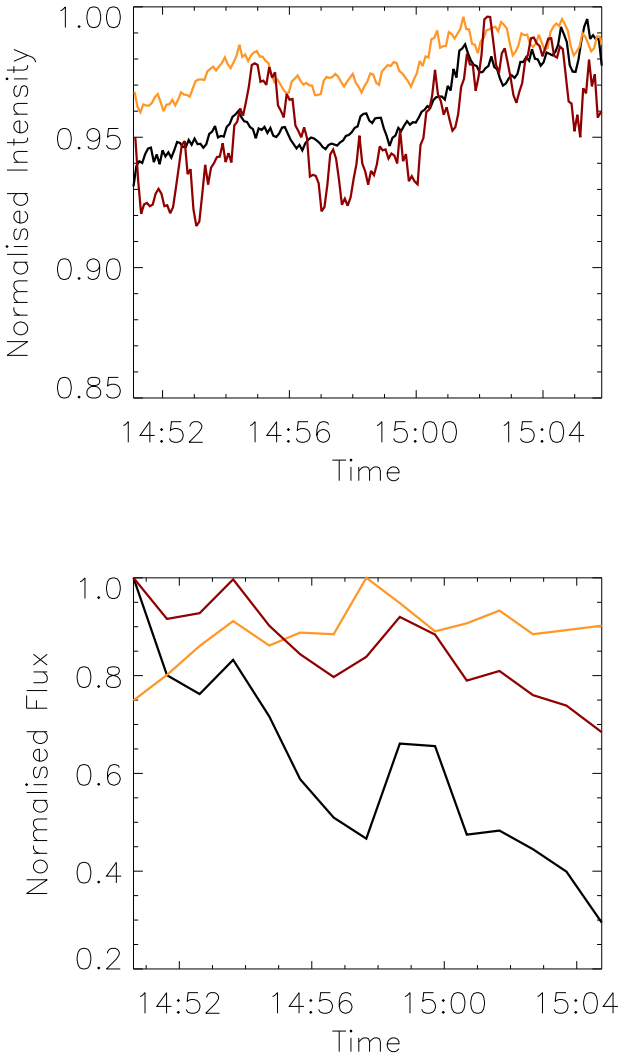

Figure 4.8: The intensity evolution of the DST/IBIS data over time (top row) plotting the Hα blue wing (black), the Hα red wing (orange), and the Fe I 6302.5 Å line core (maroon). Each line represents the average intensity within a small box, focused on the potential Ellerman bomb which contains no other localised intensity increases above the background level. The bottom frame plots the evolution of the estimated magnetic field (using Hinode/SOT Stokes V/I data) over time. The negative-polarity flux (black line), the positive-polarity flux (orange line), and total unsigned flux (maroon line) are plotted. As flux strengths are not considered here, each individual line is normalised to itself in order to highlight the general property of flux cancellation. A decrease of flux to around 68 % of the original strength is measured. Such cancellation will be discussed further in Chapter 6.

the strength of the magnetic field (analogous to the pseudo-Ellerman bombs discussed by Rutten et al. 2013 and the reduced opacity simulated by Shelyag et al. 2007, respectively). Within such events, the shape of the intensity enhancement is often different between the imaged Hα wings (which is not true of the bi-polar Ellerman bombs, such as the event presented in Fig. 4.7). It is found that brightenings occurring over uni-polar regions still show significant intensity increases (often above thresholds currently applied within automated Ellerman bomb tracking, such as 130 % or 150 % of the background intensity) within the Hα line wings, however, the line profiles frequently show excess intensity in one wing over the other.

The event at (35, -298) in Fig. 4.5, for example, displays co-spatial intensity increases for short periods during these observations and would, using thresholds alone, be classified as an Ellerman bomb for these times; however, for the majority of these observations, the line wings do not evolve asymmetrically (as can be seen in Fig. 4.5). It can be suggested that comparable temporal and morphological evolutions between the Hα line wings are an important factor in Ellerman bomb identification (similar to that shown in Fig. 4.7) and that any events which show non-comparable spatial evolutions (*e.g.*, one large lobe with moderately increased intensity and an area of around $1''^2$ in the red wing and a small, extremely intense $0.3''^2$ brightening in the blue wing) between the wings are, in fact, pseudo-Ellerman bombs.

4.5 Discussion

In this Chapter, analysis of multi-instrument, multi-wavelength observations and numerical simulations has been conducted to investigate the formation mechanism of Ellerman bombs as small-scale brightening events in the Hα line wings, commonly found to occur in emerging ARs. Numerous possible Ellerman bomb events were found within these data through a rigorous inspection of the 162 DST/IBIS Hα line profiles. The evolution of seven events which were

deemed as candidate Ellerman bombs was then studied in order to identify whether these features showed instances of flaring (rapid changes in morphology attributed to an energetic driver by Watanabe et al. 2011). In order to investigate the link between Ellerman bombs and magnetic fields, co-spatial Stokes V/I data collected by the Hinode/SOT instrument were also analysed. Any small opposite polarity flux regions observed to be co-spatial with Ellerman bombs and isolated from other strong fields were recorded. Morphologically, these small-scale flux regions were observed to change on the order of minutes, with six of the seven bi-poles showing some evidence of cancellation or emergence. The evolution of a large, flaring Ellerman bomb event and the corresponding flux region is shown over the 15 minute observational period studied in this Chapter in Fig. 4.7.

This research has also focused on the signatures of Ellerman bombs observable in the Fe I 6302.5 Å line profile. It was found that each Ellerman bomb within these data corresponded to a brightening in the line core of the Fe I 6302.5 Å absorption line. A representative example of the co-spatial, co-temporal profiles is plotted in Fig. 4.6, with an imaging representation of this relationship being depicted in Fig. 4.7 through time. The bright features within the Fe I 6302.5 Å line core were observed to exhibit rapid morphological changes reminiscent of the flaring properties identified within the Hα line wings. Overall, four of the Ellerman bombs and the brightenings in the line core of the Fe I 6302.5 Å line profile have lifetimes of the order minutes and diameters of around $1''$, close to values found in previous researches (see, for example, Georgoulis et al. 2002, Watanabe et al. 2011). Three other features exhibit similar morphological traits but with smaller diameters of around $0.5''$.

In Fig. 4.8, the evolution of one example Ellerman bomb co-spatial to a bi-pole identified in Hinode/SOT data is considered. Unfortunately during this time interval, only this single event was suitably isolated such that accurate estimation of its magnetic flux through time could be considered. Considering a zoomed region in which no other magnetic field elements were evident during

these observations, the magnetic flux of both polarities of this bi-pole through time were measured, as well as the average intensity of the Ellerman bomb in the spectral observations (calculated using a similar box). When plotted, this Stokes V/I signal through time exhibits a decrease in total flux by approximately 32 %. The co-temporal and co-spatial link between this rapid cancellation of flux and the bright regions in the photospheric wavelengths potentially implies that a release of magnetic energy into the surrounding plasma by a small-scale magnetic reconnection event is the driver of this feature. However, it should be firmly noted that other explanations (such as flux submergence) could also explain the observed cancellation. Unfortunately, even relatively high-cadence, high-resolution magnetograms, such as those studied here, are unable to detect the difference between these two scenarios.

The influence of the magnetic field on the Fe I 6302.5 Å line has been discussed in previous researches (see, *e.g.*, Shelyag et al. 2007, Danilovič 2009). Shelyag et al. (2007) suggested that regions of strong flux, especially close to magnetic inversion lines, where opposite polarites converge, could lead to a reduction in absorption in the line core, as well as splitting (where two intensity minima are observed within the line profile). Danilovič (2009) found that abnormal (non-rotationally symmetric) Fe I 6302.5 Å Stokes V profiles were co-spatial with both strong magnetic fields and magnetic reconnection in the photosphere. It has, therefore, been suggested that the formation of the Fe I 6302.5 Å line profile is intrinsically influenced by the magnetic field. A combination of these results could be used to intuitively expect coaligned Ellerman bomb and Fe I 6302.5 Å brightenings as were found here; however, as the ground-based observations used in this research could not be used to measure the Stokes V profile and, due to both the spatial and spectral resolutions, did not exhibit evidence of splitting within the Fe I 6302.5 Å line core, it is suggested that further research be carried out when sufficiently high-resolution data are available.

In order to further understand these observations, a model box was constructed to simulate the solar photosphere using the MURaM code of radiative

magnetoconvection by Dr. Sergiy Shelyag. Within the model box, the line profiles from small bi-polar regions, similar to the representative example presented within this Chapter were inferred. Interestingly, these simulated cancellation features exhibited similar traits to Ellerman bombs forming over bi-polar regions. Further study of the evolution of these small-scale events over time in the simulations was undertaken, showing temperature increases co-spatially with magnetic inversion lines at bi-polar regions. Interestingly, the relationship noted in the observations between the Hα and Fe I 6302.5 Å line profiles also appeared in the simulations, which showed increased intensity in the line wings and line core, respectively. The reconnection events analysed in this article appear to be of Sweet-Parker type, however, a more in-depth study of the MURaM code itself and the physics which is occurring at the potential reconnection site is required to fully understand the mechanism which is occuring within the simulations.

Overall, the observed and simulated photospheres analysed in this article, exhibit analogous line profiles co-spatial to bi-polar regions, namely brightenings within the Hα line wings and an increase in intensity in the Fe I 6302.5 Å line core. It can be suggested that this analysis has presented the clearest evidence to date, that the sub-class of brightening events known as Ellerman bombs in the Hα line wings are formed by magnetic reconnection in the solar photosphere. However, it should be noted, that improved temporal, spatial and spectral resolution when inferring both photospheric imaging lines and magnetic field is required before observations are capable of definitively supporting magnetic reconnection.

Chapter 5

Morphological Traits of Ellerman Bombs at the Limb

5.1 Overview

The physical properties of Ellerman bombs and their relationship to the photospheric line-of-sight magnetic field have been extensively discussed in the previous Chapters of this thesis (as well as in this comprehensive literature written about these phenomena since their discovery by Ellerman 1917). It has recently become popular to research the formation and morphology of these small-scale phenomena at the solar limb, where any vertical motions are be immediately evident without the ambiguity associated with Doppler measurements. Through an analysis of two ARs observed at different viewing angles (one near the disc centre and one at the limb), Roy (1973) were the first to attempt to quantify the vertical properties of these features, inferring that Ellerman bombs exhibited extensions away from the surface of the Sun. These results were later corroborated by Kurokawa et al. (1982), who provided the first measurements of lengths and widths of Ellerman bombs at the limb, finding values of approximately 800 km and 450 km, respectively. More recently, Watanabe et al. (2011) presented further research on these features at a viewing angle of μ=0.67 (close to the

solar limb), returning similar size estimates as Kurokawa et al. (1982) but also measuring upward flows with speeds which averaged at approximately 8 km s^{-1}.

In order to further the understanding of the community about the Ellerman bomb phenomena, specifically with respect to their manifestation at the solar limb, this Chapter has two separate aims. Initially, the evolution and morphology of Ellerman bombs observed at the solar limb in a high-resolution, high-cadence, Hα line profile dataset (collected using the CRISP instrument at the SST in La Palma and supplemented by images sampled by SDO/AIA) will be analysed. By providing estimates of the widths, vertical extensions, and speeds of any Ellerman bombs observed in this dataset, this study cements the results of previous researches that these phenomena are small-scale apparent explosive events in the Hα line wings that appear to have no influence on the upper solar atmosphere. Secondly, this Chapter presents two case studies which demonstrate the complex nature of Ellerman bomb events (again, observed at the solar limb). Both analysed features display distinct, previously unseen characteristics which offer further in-sight into the formation mechansism and physical properties of Ellerman bombs.

Overall, this Chapter is structured as follows: In Section 2, the observations analysed in this Chapter are described. Section 3 outlines the data analysis which forms the core of this research. A discussion about the relevance of these results with regards to the current understanding of the community is then included in Section 4. The results obtained through conducting this research are published in: **C. J. Nelson**, E. M. Scullion, N. Freij, J. G. Doyle, & R. Erdélyi, 'Small-Scale Structuring of Ellerman Bombs at Solar Limb', *The Astrophysical Journal, Volume 798 (2015), Page 19*,

5.2 Observations

The ground-based data analysed in this Chapter were collected using the SST/CRISP instrument during a period of good seeing on the 21st June 2012. Data appro-

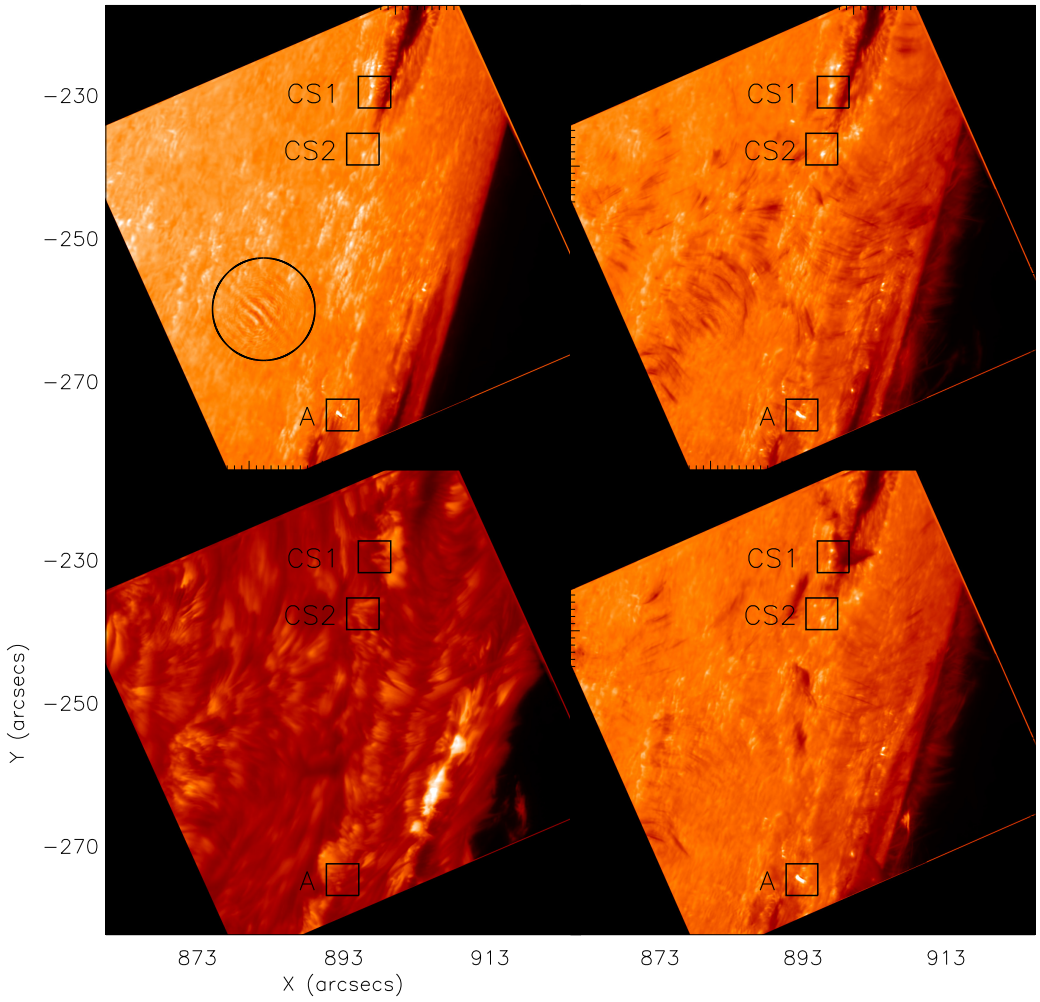

Figure 5.1: The FOV of AR 11506 analysed within this Chapter, sampled at four positions within the Hα line scan: The far blue wing (approximately -1.8 Å; top left); the near blue wing (-0.95 Å; top right); the Hα line core (0 Å; bottom left); and the red wing ($+0.95$ Å; bottom right). The black boxes in each image indicate three regions of interest analysed in detail later in this Chapter. A known fringing artifact of the image reconstruction process is visible in the black circle in the far blue wing image at approximately (883, -260).

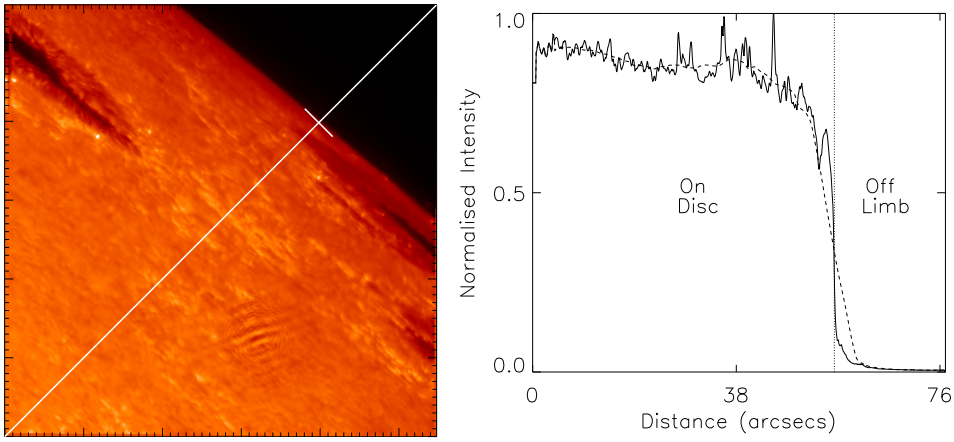

Figure 5.2: The FOV analysed in this Chapter in the far blue wing (left hand frame). The diagonal line highlights the pixels used to make the intensity by distance plot (right hand frame). A small white line in the left hand image indicates the approximate position of the solar limb in the image corresponding to the dashed, vertical line in the right hand frame.

priate for this study were collected by sampling a large FOV at the solar limb, centred at x_c=893″, y_c=-250″ (with respect to the disc centre) between 7:15:09 UT and 7:48:25 UT. This FOV contained three sunspots from AR 11506. Hα line scans, sampling 35 evenly spaced spectral positions (each sampled eight times per sequence) between -2 Å and $+1.2$ Å from the line core (situated at 6562.8 Å) were obtained, and processed using the MOMFBD (see van Noort et al. 2005 for details) image restoration method. This followed the standard procedures in the reduction pipeline for CRISP data (de la Cruz Rodríguez et al. 2015) and preceeded the post-MOMFBD correction for differential stretching suggested by Henriques (2012) (also see Sekse et al. 2012 for more details). Overall, the pixel size of these data are 0.059″ (which corresponds to approximately 43 km in a transverse scale) and the temporal cadence is approximately 7.7 seconds. In the following sections of this Chapter, all measurements will be given in terms of the transverse scale and not with respect to the pixel size. Co-temporal and co-spatial data sampled by the SDO/AIA (see Lemen et al. 2012)

instrument are included in this analysis in order to assess whether the vertical components of Ellerman bombs can influence the upper solar atmosphere.

In Fig. 5.1, an overview of the FOV analysed within this Chapter is plotted for four separate positions within the Hα line wings. Clockwise from the top left image, data sampled by narrow-band filters at -1.8 Å, -0.95 Å, $+0.95$ Å, and 0 Å are represented. These data were collected at approximately 7:36:20 UT during a single sequence conducted by the SST/CRISP instrument. Within this FOV, portions of three sunspots (two in the southern part of the FOV and one in the northern section) are observable, as well as a large plage region in the centre of the line wing images. All Ellerman bombs suitable for analysis in this Chapter occur close to these sunspots. The absorption which occurs in the Hα line core is immediately obvious when comparing the line wing images to the line core. The underlying photosphere is obscured by the chromospheric material in the Hα line core (in the bottom left image), including the apparently horizontal fibril structures which form an apparent canopy. It is possible that these features could act as a barrier to limit mass flow from the lower atmosphere into the upper atmosphere, hence, acting as an upper limit for Ellerman bomb lengths. Three boxes with labels 'A', 'CS1', and 'CS2' are overlaid on each of the images, highlighting the three Ellerman bombs discussed in later sections of this Chapter (represented in Fig. 5.6, Fig. 5.7, and Fig. 5.8, respectively).

5.3 Data Analysis

5.3.1 Ellerman Bomb Statistics

Within the Hα line profile data analysed here, Ellerman bombs were easily identified as significant increases in intensity, apparent from around 0.5 Å either side of the line core. As was stated in Chapter 3, the appropriate threshold for identifying Ellerman bombs must be considered for each individual dataset. As these data sample a FOV at the solar limb, the background intensity across an representative image was not constant (as can be seen in Fig. 5.2) meaning a

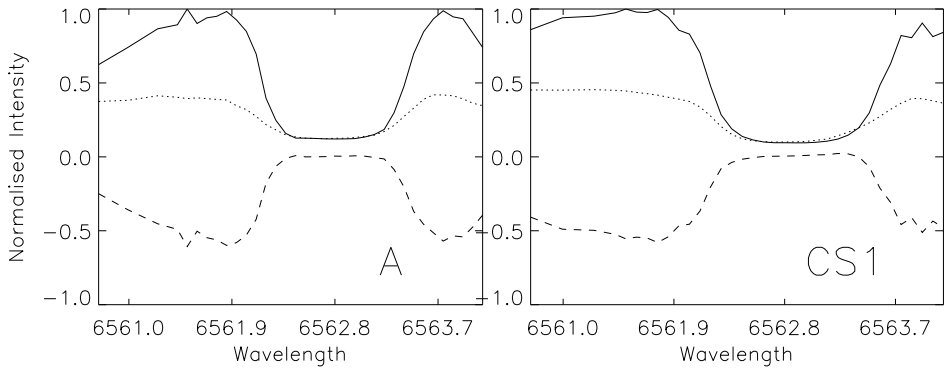

Figure 5.3: Normalised line profiles of two representative Ellerman bombs compared to the background intensity of the nearby quiet Sun. The Ellerman bomb line profiles (solid lines) for box 'A' (left) and box 'CS1' (right) in Fig. 5.1 compared to the local quiet Sun (dotted line in both frames). The dashed lines shows the inverted (for clarity) difference in intensity (normalised against the peak Ellerman bomb intensity) between the quiet Sun and Ellerman bomb line profiles.

more pragmatic Ellerman bomb identification technique than a general threshold was required. In this Chapter, therefore, Ellerman bombs are defined as events which have intensity increases of greater than 1.5 times the background intensity from the nearby quiet Sun in the wings of the Hα line profile and also a dynamic, explosive nature through time (evidenced by visually inspecting imaging data). As well as this, fragmenting Ellerman bombs observed within these data were classified as being a single event, with all fragments being tracked and contributing to the total lifetime. If an event became completely unobservable and did not recur for five frames, any new co-spatial brightening was then classified as a new Ellerman bomb event. By employing these guidelines, any potential influence of NBPs (such as those situated in the centre of the far blue wing FOV in Fig. 5.1 at x_c=893″, y_c=-250″), that have a smaller increase in line wing intensity within these observations when compared to the Ellerman bomb excess emissions, on this analysis was removed. Overall, 22 Ellerman bomb events were confidently identified within these observations for further analysis.

Three regions in which Ellerman bombs occur during these observations are highlighted for reference in Fig. 5.1 by black boxes. Each of these events is analysed in detail in the following Sections.

In Fig. 5.3, normalised line profiles for two of the representative Ellerman bomb events highlighted in Fig. 5.1 (solid lines; scaled to the maximum intensity of the Ellerman bomb profile) are plotted. The significant intensity increases of these events are immediately evident when compared to the local quiet Sun (the dotted lines which are also scaled to the maximum intensity of the Ellerman bomb profile). To highlight the percentage increase in intensity, the inverted (for visual ease) difference between the quiet Sun and the Ellerman bomb events (dashed lines) is also plotted. The difference between the line-wing intensities of the Ellerman bombs and the quiet Sun peaks at over -0.5 indicating a doubling of the intensity within the explosive Ellerman bomb structure. Such high gradients between Ellerman bombs and the background atmosphere are not observed in every frame through the lifetime of an event as the intensity of individual features appears to vary on timescales of seconds (similar to the behaviour discussed by Qiu et al. 2000). Whether this is an artifact of changes in seeing conditions over short time-scales or a physical property of the observed Ellerman bombs remains to be seen and should be analysed in future research. It should again be stressed, therefore, that an acceptable thresholding value to be used by an automated tracking algorithm (as used in earlier Chapters of this thesis) or in Ellerman bomb identification (such as in this Chapter) is highly dependent on a number of factors such as the instrumentation, data processing techniques, and the seeing at the time of the observations.

After the identification of all observed Ellerman bombs in these data, each event was carefully analysed to determine its lifetime and area. As the definitions between Ellerman bombs and the background are strong in these data (as is shown in Fig. 5.3), the estimation of the lifetime was easily completed by creating a movie of the evolution of each event through time. The start and end frames of each feature were identified as the initial and final frames

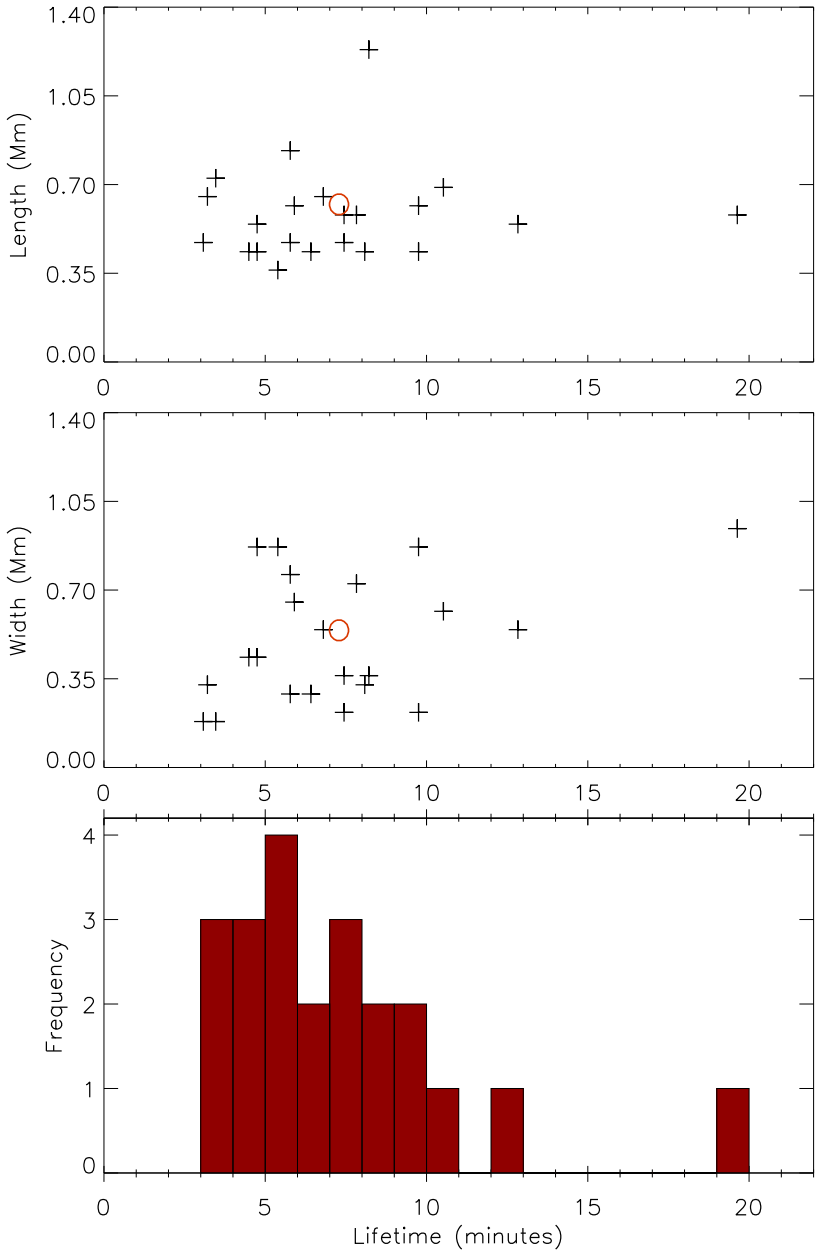

Figure 5.4: Basic statistical properties of the Ellerman bombs observed in these data. (Top) Scatter plot of peak Ellerman bomb length vs lifetime. (Middle) Scatter plot of Ellerman bomb width against lifetime. (Bottom) Lifetime distribution of the 22 identified Ellerman bombs, with all but three events existing for less than 10 minutes. The red circles indicate the mean of both variables for each of the scatter plots.

in which a structure (systematically identified through visual inspection) with intensity over the threshold value of 1.5 times the local background intensity (corroborated in each frame using the CRISPEX tool; see Vissers and Rouppe van der Voort 2012) was observable. Overall, the average lifetime of Ellerman bombs in these data can be estimated as approximately 7 minutes (with a standard deviation of around 4 minutes), comparable to previous researches by, *e.g.*, Roy (1973), Watanabe et al. (2011), and in Chapter 3. The shortest and longest-lived events observed in this dataset had lifetimes of 3 and 20 minutes, respectively; however, it should be noted that a number of shorter-lived brightenings which exhibited similar traits to the identified Ellerman bombs but did not quite achieve the required intensity threshold, did exist meaning it is not possible to suggest that these data reveal a lower limit for Ellerman bomb lifetimes. The distribution of lifetimes within these data is plotted as a histogram in Fig. 5.4c. In their research on Ellerman bombs at the solar limb, Roy (1973) inferred that limb events had a shorter lifetime than those observed on the solar disc. Our results do not support this assertion, however, a larger statistical sample of Ellerman bombs would be required to actively negate this hypothesis.

The relationship between the peak lengths and lifetime and the peak widths and lifetime of the Ellerman bombs observed in this dataset are plotted in Fig. 5.4a and Fig. 5.4b, respectively. A general trend appears to exist within these data that longer lived Ellerman bombs have larger lengths and widths (as previously discussed by Roy 1973), however, the small sample size considered in this Chapter is insufficient to understand whether this apparent relationship is statistically significant. It is of more interest in this Chapter to understand the profile of the evolution of the vertical motions of these events through time. In Fig. 5.5, three Ellerman bombs are presented in the top row (including event 'A' in the far column and two further representative events) before a time-distance diagram of each feature is plotted below, including the on-set and fading of each event. Each of the distance-time plots appear to depict a parabolic tra-

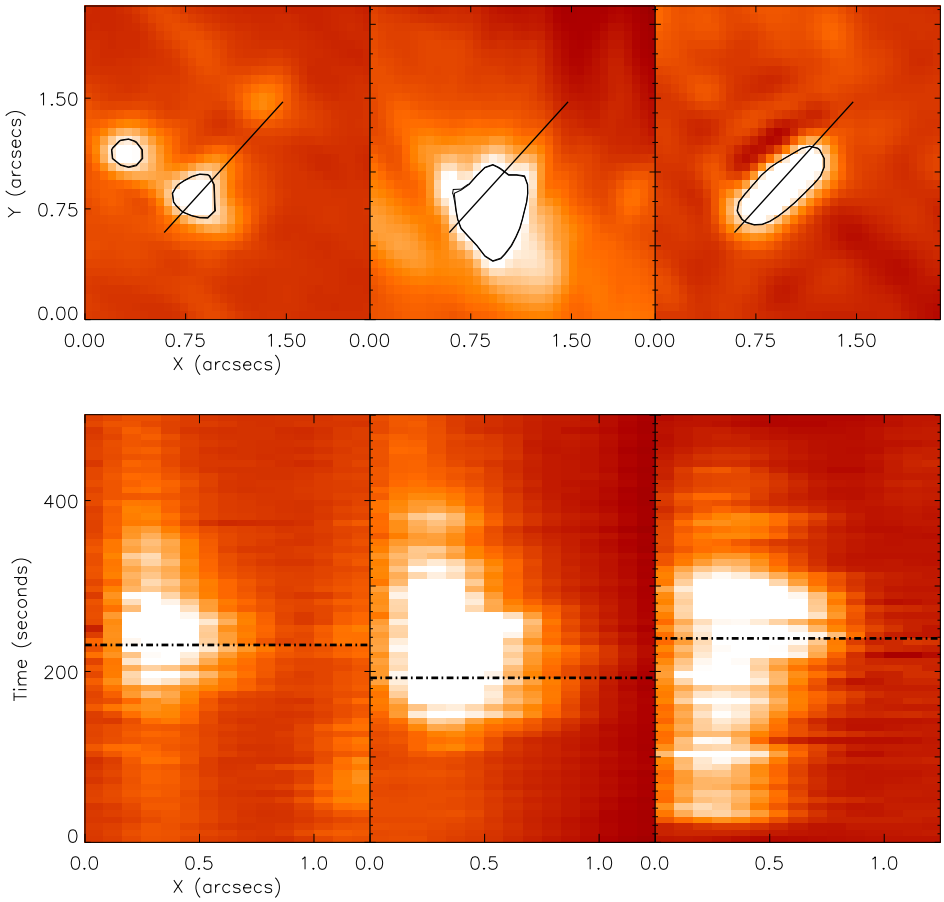

Figure 5.5: Three representative Ellerman bomb (top row) with Ellerman bomb 'A' (highlighted in Fig. 5.1) plotted in the right hand column. Black contours outline the regions with intensity over 1.5 times the average background intensity and the black lines indicated the pixels selected to produce the distance-time diagrams (bottom row). These distance-time diagrams depict the rise and fall phases of these Ellerman bombs. The horizontal dashed lines indicate the frames plotted in the top row for each Ellerman bomb, respectively.

jectory (whereby the tip of the Ellerman bomb appears to extend away from the footpoint before slowing and then falling back down) for the intensity increases through time with these Ellerman bombs exhibiting obvious rise and fall phases. Although the morphological traits of these features are nicely portrayed in Fig. 5.5, it is important to note that the calculation of upward flow speeds was conducted using measurements of the peak height of the event from frame-to-frame and not using distance-time diagrams. This was due to the horizontal motions of Ellerman bombs through time, which meant that no slit accurately tracked the tip of the feature through time.

In Fig. 5.6, Ellerman bomb event 'A' is plotted through time to highlight the parabolic trajectory using imaging observations. The two left hand columns plot the Hα line wings (at approximately $\pm$1 Å), the right central column plots the Hα line core, and the far right column plots the co-spatial plasma inferred by the SDO/AIA 304 Å filter. The Ellerman bomb appears simultaneously and co-spatially in both wings before extending away along a constant trajectory (indicated by the black lines in the Hα line wings). Overall, 20 of the 22 Ellerman bombs analysed in this Chapter appear to have tips which extend and contract with similar parabolic trajectories to the event plotted in Fig. 5.6. For the 20 Ellerman bombs which evolved with a parabolic trajectory, an average vertical speed of around 8.9 km s^{-1} was measured (from onset to peak extension) with a standard deviation of approximately 3.2 km s^{-1}. Most events attain even higher velocities during their most explosive periods. It was also found that 12 of the Ellerman bomb events analysed here also displayed obvious transverse motions, averaging at 1.7 km s^{-1} (and a standard deviation of 1.4 km s^{-1}). The average horizontal speed measured for these events is slightly higher than previous estimates (by, *e.g*, Georgoulis et al. 2002, Watanabe et al. 2011, Nelson et al. 2013a). This can be accounted for due to the influence of several extremely dynamic Ellerman bombs which had apparent motions over 3 km s^{-1}. Two of these events will be examined in case studies later in this Chapter.

Co-spatial EUV data inferred by the SDO/AIA instrument were also ex-

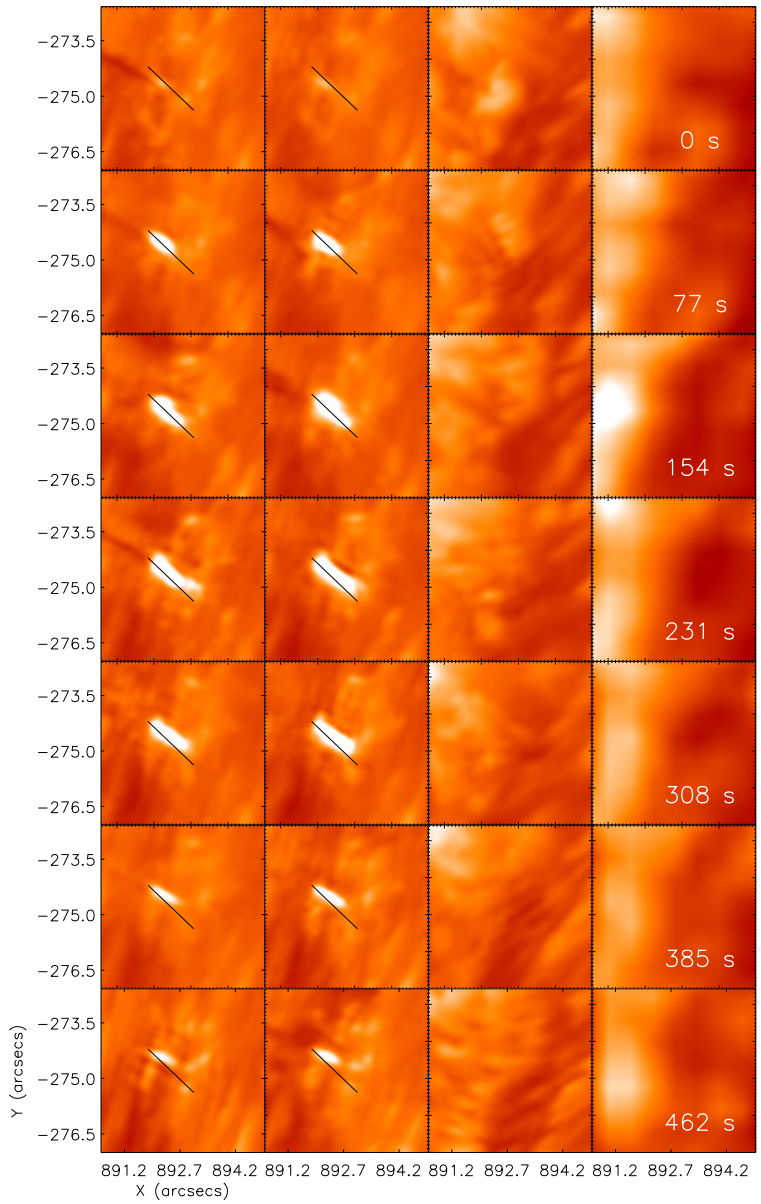

Figure 5.6: The evolution of Ellerman bomb event 'A' (from Fig. 5.1) in the blue (left) and red (middle left) wings of the Hα line profile (with wavelengths at approximately $\pm$1 Å), the co-spatial Hα line core (middle right), and SDO/AIA 304 Å filter (right). The black line of length 1200 km in the Hα line wings shows the approximate path of the Ellerman bomb for reference. The images in the top row were taken at 17:32:30 UT.

amined for each Ellerman bomb. As Ellerman bombs consist of a vertical extension, it is important to assert whether a signature is observed in the upper atmosphere. The majority of previous studies have found no signal even within the Hα line core (see, for example, Zachariadis et al. 1987, Watanabe et al. 2011, Vissers et al. 2013), despite recent work by Bello González et al. (2013) suggesting that some Ellerman bombs may penetrate into the chromosphere. The Ellerman bombs analysed in this Chapter show no influence in the upper atmosphere, sampled by both the Hα line core (plotted in the third column of Fig. 5.6) and the EUV SDO/AIA filters (plotted in the fourth column of Fig. 5.6). As these data were collected at the solar limb and the majority of previous researches of the Ellerman bomb phenomenon have revealed no coronal response (see, for example, Schmieder et al. 2004), this is unsurprising as the large optical depth (the amount of plasma through which the light must travel) would cause any localised intensity changes which might occur to be obscured.

The recent launch of the Interface Region Imaging Spectrograph (IRIS; De Pontieu et al. 2014) satellite has provided high-resolution co-spatial observations of the Transition Region for research, and has, to date, driven interesting results with regards to Ellerman bombs. Initial analysis of IRIS data around ARs by Peter et al. (2014) indicated the existence of small-scale transient explosive features co-spatial to bi-polar structures observed in photospheric line-of-sight magnetograms. These authors hypothesised that such brightening features, observed in plasmas with temperatures up to 10^5 K could be the response of the upper-atmosphere to Ellerman bombs, however, no Hα or other lower atmospheric diagnostic was available for their study. Vissers et al. (2015) continued research into the link between Ellerman bombs and such IRIS 'bombs' finding that a subset of the IRIS transients did appear co-spatially with Ellerman bombs. These authors did suggest, though, that smaller temperature enhancements of around 2×10^4 K (still much higher than the 1.5×10^3 K predicted by semi-empirical modelling) could be the reason for the observed signal.

One of the most interesting questions which is now open with regards the

links between Ellerman bombs and these IRIS 'bombs' is the lack of response from the Hα line core to the supposedly high-temperature plasma. Potentially, material within the Ellerman bombs themselves is being heated to Transition Region temperatures but is still not reaching the heights of the chromosphere meaning increased emission from Ellerman bomb at wavelengths corresponding to the Hα line core is scattered by the chromospheric canopy, leading to no signature being observed. It will be interesting to further study this relationship in future work, particularly with the upcoming Daniel K. Inouye Solar Telescope (DKIST) which should provide incredible spatial resolutions and, hence, allow detailed comparison of Hα line profiles to semi-empirical models of the solar atmosphere to understand whether the potential temperature increases within Ellerman bombs are formed in only some small region of the overall structure or only occur in a small number of events.

As the intensity enhancements indicative of Ellerman bombs occur in both wings of the Hα line profile simultaneously and exhibit parabolic trajectories (as found in this Chapter), it is possible that these observables are a result of increased temperature and density in localised regions. Simulations of Ellerman bombs within the lower solar atmosphere (by, *e.g.*, Archontis and Hood 2009; Nelson et al. 2013b) have associated these traits with the process of magnetic reconnection in the photosphere. The observations presented within this Chapter corroborate the hypothesis that magnetic reconnection in the photosphere could lead to the flow of plasma within the lower solar atmosphere, hence creating density increases in the local atmosphere similar to those observed here; however, it should be noted that no magnetic field data of sufficient resolution comparable to Ellerman bomb cross-sections are available for comparison to the SST/CRISP data analysed in this Chapter.

5.3.2 Case Study: I

As has been previously discussed in this Chapter, it is common that large, apparent horizontal motions are observed within Ellerman bombs during their

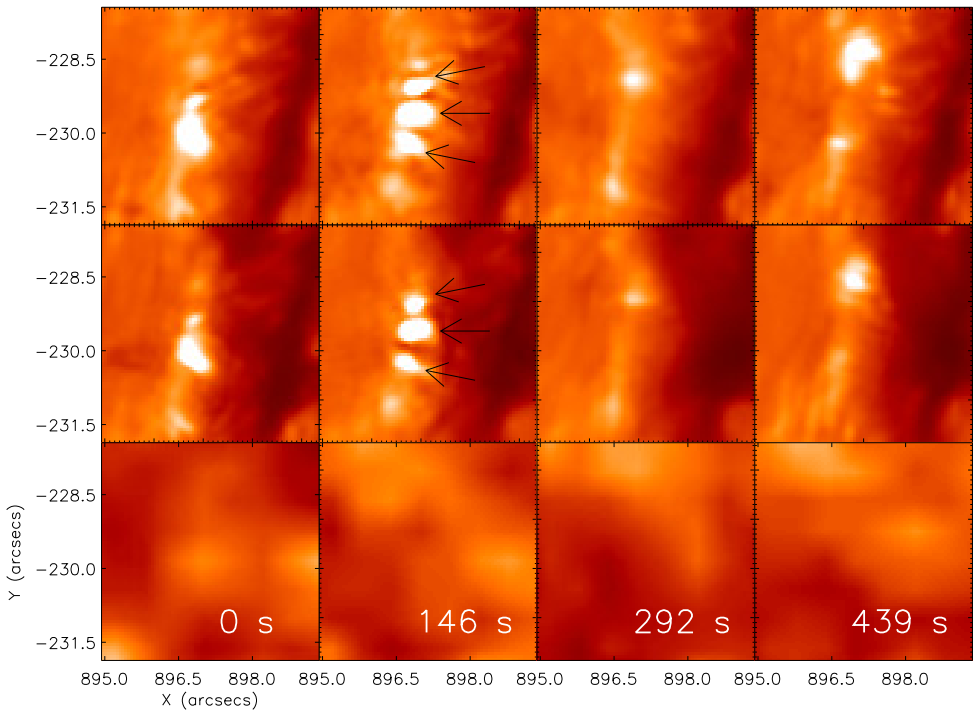

Figure 5.7: An illustration of the propagation of the Ellerman bomb analysed in Case Study I for both the blue (−1 Å; top) and red (+1 Å; middle) wings of the Hα line profile, as well as the SDO/AIA 304 Å filter (bottom). The almost northward propagation of this event appears to be parallel to the nearby penumbra and follows the bright track evident in the third frame. In the second frame for each wavelength, three small sub-structures are highlighted with arrows. The line wings are originally sampled at 7:29:54 UT and each subsequent image is separated by 146.3 seconds.

lifetimes within these data. How these horizontal motions lead to interactions with plasma in the wider atmosphere is of specific interest and could prove key in assessing the potential influence of Ellerman bombs within the solar photosphere. In previous studies, it has proved difficult to accurately link Ellerman bomb events with any other solar phenomena and, hence, they have been analysed as localised events. Here, one specific example of a region which appears to be susceptible to the formation of a number of Ellerman bombs in a structured manner is presented. Ellerman bomb events within this region display strong horizontal motions and appear to trigger other, similar events in different spatial locations as if through a 'train' of energy release.

In Fig. 5.7, the evolution of the northern event emphasised in Fig 5.1 with the label 'CS1' is plotted, with respect to time for both -1.1 Å (top row), $+1.03$ Å (middle row), and the SDO/AIA 304 Å filter. The first column depicts the original Ellerman bomb early in its lifetime, before the fracturing of this event into three separate sub-features is evident in the second column (with each substructure indicated by arrows). Each independent fracture appears to slowly propagate away from the original footpoint along the bright trail evident in the Hα wing images in the third column. After the original Ellerman bomb fades for long enough such that it is deemed to have ended, a second large Ellerman bomb event occurs, as evidenced in the final column. This rapid morphology is reminiscent of the evolution of the magnetic field simulated by Archontis and Hood (2009) where an emerging flux rope formed in a 'sea-serpent'-like manner, reconnecting at a number of individual $\cup$s to form a larger over-lying loop. It would be of interest, in future studies, to continue the work of Pariat et al. (2004) (who analysed Flare Genesis Experiment magnetic field measurements) to understand whether evidence of such small-scale flux emergence (on scales of a few arcseconds) is apparent co-spatially with events within high-spatial and temporal resolution magnetic field data collected by the SST/CRISP instrument. Unfortunately, due to the nature of the observing sequence analysed here, no such magnetic field measurements are available for analysis in this

Chapter.

In previous researches, Ellerman bombs have been shown to occur co-spatially with inter-granular lanes (see, for example, Denker et al. 1995, Nelson et al. 2013a). It is possible that the bright trail which appears to guide the Ellerman bombs is evidence of a localised network structure, or an inter-granular lane. On-disc observations of the Hα line wings often include weak intensity increases, reminiscent of this trail, co-spatial to strong magnetic fields inferred using magnetograms or G-band data. It is, therefore, possible that these Ellerman bombs are propagating along a defined structure and, hence, that further information could be derived by analysing on-disc examples of such events. High-resolution, multi-wavelength observations close to the disc centre should be further investigated in future work to infer whether these events are indeed guided by the magnetic field and, specifically, whether this splitting and small-scale explosive nature is evidence of the sustained cancellation of magnetic fields (which would further support the magnetic reconnection hypothesis).

It has been widely reported that Ellerman bombs both migrate (for example, Denker et al. 1995, Nindos and Zirin 1998) and appear to recur, but what has not been presented yet in the detail included in this Chapter, is a direct link between two apparently separate, and highly structured, events. This does pose several important questions which can be discussed here. For example, what process is leading to the creation of multiple ejections (which all follow similar parabolic trajectories) within this individual Ellerman bomb? If magnetic reconnection is indeed the driver of Ellerman bombs, then, are we observing a 'train' of reconnection through a 'sea-serpentine' morphology as simulated by Archontis and Hood (2009)? Thus, are sequential and apparently connected Ellerman bombs a signature of multiple stages of small-scale flux emergence leading to the emergence of a larger flux rope, which could potentially extend into the outer layers of the atmosphere? The spatial separation between the initial and final Ellerman bomb event is around 2200 km, hence, this would suggest that a single reconnection event in a unstable region could lead to a sustained energy

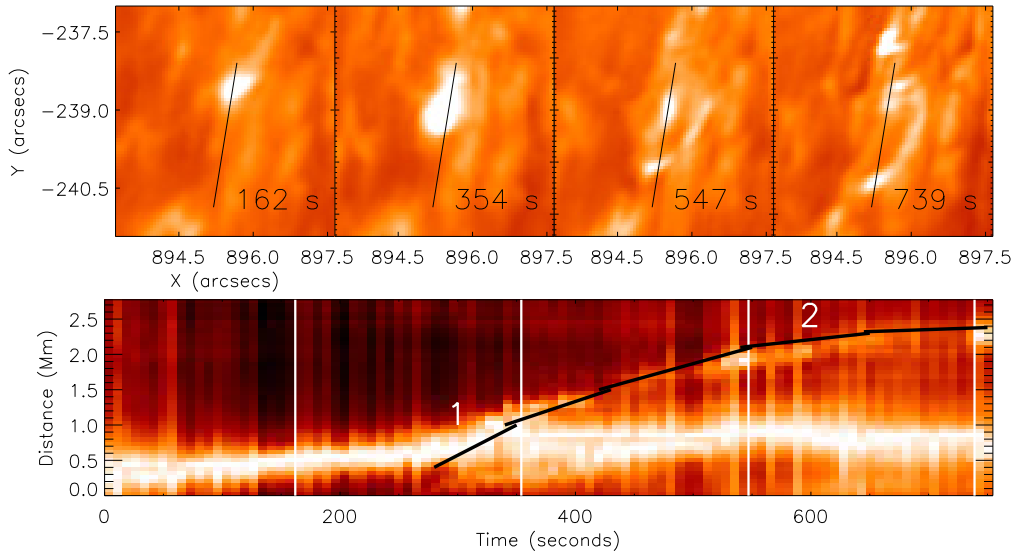

Figure 5.8: The evolution of the Ellerman bomb analysed in Case Study II at +1 Å. In the top row, four frames are plotted starting at 7:40:49 UT and separated by 146.3 seconds. The initial Ellerman bomb event is easily observed in the left-hand frame. The most 'explosive' period of this event is shown in the second frame, before the generation of the apparent loop is depicted in the third and fourth frames. The bottom row plots a time-distance diagram calculated using the black slit overlaid on the top row (with intensity normalised at each time-step to remove the influence of changes in seeing). The black line indicates the apparent speed of the event through time. The apparent speeds of the event at the times marked by 1 and 2 are 6.2 km s^{-1} and 0.6 km s^{-1}, respectively. White vertical lines depict the temporal position of each of the four top row plots.

release within the local plasma (of course, this statement also applies if another driver is the cause of these events). For a full analysis of events such as this to be completed, high-resolution magnetic field data would be required, collected by, for example, the SST/CRISP instrument. It is imperative that further research be carried out using both imaging observations and state-of-the-art computational modelling to understand this process in more detail.

The second important result which can be drawn from this event is that small-scale Ellerman bomb dynamics, as discussed by Nelson et al. (2013a), are conspicuous within these data. It is inherently clear that higher-resolution data may allow further insight into the dependence, or indeed independence, of these small-scale events to close-by larger Ellerman bomb events. The individual parabolic trajectories evident in each of the smaller-scale structures (highlighted in Fig. 5.7) analysed in this Section adds weight to the argument that each fragment may be formed by a separate (or a single repetitive migrating) driver. Overall, future analysis of Ellerman bombs in a wide range of datasets should be conducted to assess whether a minimum Ellerman bomb size is determinable using modern instrumentation.

5.3.3 Case Study: II

The final case study included within this Chapter focuses on the event highlighted in Fig. 5.1 by the box labeled 'CS2'. A number of interesting morphological features are observed during the evolution of this event which further evidence the dynamical nature of Ellerman bombs. This Ellerman bomb exhibits the most rapid apparent horizontal motions observed in this dataset with speeds reaching around 6 km s^{-1}. These high speeds occur during the splitting of the event into two distinct parts, one of which remains in an almost constant spatial position and the other appears to separate to a distance of around 2 Mm. Such dynamics have yet to be studied in the literature and provide a potentially excellent diagnostic tool for future analysis of the driver of Ellerman bombs.

The evolution of the event is depicted by the top row of Fig. 5.8 which plots

information sampled at +1 Å. The original Ellerman bomb, initial splitting, fading, and then loop formation are visualised in the first, second, third, and fourth frames, respectively. The bottom row of Fig. 5.8 depicts a time-distance diagram for the spatial positioning indicated by the black line in each of frames in the top row. The initial off-shoot appears to be as bright as the original Ellerman bomb event and propagates away from the initial Ellerman bomb formation site at a speed of 6.2 km s^{-1}. This is over four times the average apparent horizontal motion speed of Ellerman bombs within these data. The off-shoot continues to move away from the large Ellerman bomb and decelerates until it reaches a speed of around 0.6 km s^{-1}. A thick black line is overlaid on the time-distance plot to emphasise the path of the off-shoot through time.

Of particular interest in this Chapter is the similarity of this evolution to magnetic flux emergence events. Comparable morphological traits to these were reported by both Otsuji et al. (2007) and Ortiz et al. (2014). These researches analysed events which had initial separation, or splitting, speeds of around 5 km s^{-1} which dropped through time to around 1 km s^{-1}. The final footpoint separation was reported to be on the order of 2200 km - 3000 km, comparable to the separation observed here. Flux emergence models also commonly discuss the occurrence of bright regions at the footpoints of formed loops (see, for example, such authors as Guglielmino et al. 2008), as observed here in the form of an Ellerman bomb. These brightenings have been linked to reconnection between the emerging and existing fields and could facilitate the transport of energy from the lower solar atmosphere into the corona (as found to be, for example, by Isobe et al. 2008). Unfortunately, as this event occurs during the final sequences of the collection of this dataset, we are unable to establish whether this brightening and loop structure displays the complete set of traits linked to flux emergence models in previous studies; however, the hints discussed in this Section are compelling. Interestingly, Zachariadis et al. (1987) observed that Ellerman bombs often formed as pairs, seperated by around 3″. It is plausible that such pairs were formed in a comparable method to that described in this

Section.

In terms of Ellerman bombs, this apparent link to a spectral signature of small-scale flux emergence (with properties similar to those discussed by, *e.g.*, Otsuji et al. 2007) could prove exciting and could drive future studies using high-spatial and temporal resolution observations. Magnetic flux emergence has long been discussed as a potential driver of magnetic reconnection (see, for example, Heyvaerts et al. 1977, Shibata et al. 1992, Guglielmino et al. 2008) and, in particular, as a driver for Ellerman bombs (suggested by, *e.g.*, Georgoulis et al. 2002, Pariat et al. 2004, Archontis and Hood 2009). Therefore, future studies utilising high-resolution SST/CRISP magnetograms could attempt to quantify key dynamical properties of flux emergence required for Ellerman bomb formation (for example, the quantity of flux which must emerge or the rate of emergence). It must be acknowledged that no co-spatial magnetic field data is available for this study and, as such, we are unable to conclusively link this event with flux emergence, however, the similarities presented here are intruiging. It should be noted by the reader that other alternatives exist to the flux emergence scenario, such as mass loading of an already existing loop. A larger-scale study of such events would be required to definitely solve this issue. It is also unfortunate that these observations end co-temporally with the fourth frame of Fig. 5.8, meaning that a complete analysis of this event is impossible. A variety of datasets should be analysed in the near future to further test these findings, specifically in terms of how many Ellerman bombs are actually linked to examples of flux emergence.

5.4 Discussion

The results presented in this Chapter support the conclusions of earlier investigations, where it has been suggested that Ellerman bombs are energetic explosive events emanating from the lower solar atmosphere (see, for example, Georgoulis et al. 2002, Watanabe et al. 2011, Nelson et al. 2013b). The average

lifetime and spatial properties of brightenings analysed in this article (7 ± 4 minutes and widths around $0.65''$) are comparable to values reported by a number of authors as properties of Ellerman bombs, therefore, allowing us to confidently link these near-limb events to on-disc Ellerman bombs. However, we present the first limb measurements of Ellerman bomb lengths using state-of-the-art ground based instrumentation, finding the average height of these events to be 600 km (which is well below the believed height of formation for the Hα line core of 2000 km). This is slightly shorter than previous estimates by Kurokawa et al. (1982). It should be noted that a plethora of highly dynamic events within our data were observed which did not eventually reach the required intensity threshold for identification as an Ellerman bomb, possibly due to a mixing of events within the line-of-sight resulting in a single less intense line profile.

Strong evidence of flows associated with Ellerman bombs are also found, agreeing with previous observations by, for example, Roy (1973) at the limb and Matsumoto et al. (2008b) on the disc. The tips of 20 out of 22 events appeared to follow a parabolic trajectory through time suggesting the occurrence of a displacement of plasma, increasing the density and temperature within a localised region, hence, leading to the enhancement of the intensity in the wings of the Hα line profile (similar to the semi-empirical models of, for example, Fang et al. 2006). Potentially, this propagation of plasma could be considered analogous to the flows observed by Nelson et al. (2013b) at a simulated reconnection site where rapid cancellation of opposite polarity field occured. Unfortunately, no co-spatial magnetic field data were available for analysis in this Chapter. It should be noted, however, that no evidence of Ellerman bombs within the Hα line core or the SDO/AIA EUV filters was found during this research, agreeing with previous studies (*e.g.*, Schmieder et al. 2004) which have concluded that the vertical extensions of these events may not be sufficient to penetrate into the chromosphere and lower corona.

As has been discussed previously in this Chapter, the recent work of Peter et al. (2014) and Vissers et al. (2015) presents an interesting conundrum.

Both of these researches found high-temperature signals ($\sim 10^5$ K) co-spatial to inferred and observed Ellerman bombs, respectively, disagreeing with previous work which found temperature enhancements of 1.5×10^3 K could account for the spectral signatures of these features (see, for example, Fang et al. 2006). Initial work (continuing that of Vissers et al. 2015) should aim to understand whether the co-spatial relationship between Ellerman bombs and transition region signals is more than just coincidence, before attempts to model how such high-temperature plasma can be formed within Ellerman bomb structures (*e.g.*, through reconnection processes or through micro-turbulence developing between the moving Ellerman bomb plasma and the approximately stationary background atmosphere) should be attempted. It will be of interest to discover how the spectral signatures in the Hα line wings and Transition Region filters can be reconciled with the lack of signal in the Hα line core and SDO/AIA 304 Å filter.

The two individual case studies included in this Chapter highlight the small-scale dynamics associated with Ellerman bombs which had not previously been observed. Within the first case study, the influence of an Ellerman bomb on the surrounding atmosphere was analysed. A large Ellerman bomb event appeared (by visual inspection) to fragment, with the small-scale pieces propagating north, away from the formation site. Each of the small-scale fragments were only around 230 km in diameter, similar in size to the events analysed by Nelson et al. (2013a). The northern-most fragment drifted to around 1500 km from the initial position before reducing dramatically in size and fading below the threshold of 1.5 times the local background intensity. A second large Ellerman bomb event was then observed to occur at the same spatial position.

The second case study discussed a rapid splitting of a large Ellerman bomb event close to a large sunspot. The main body of the ejection appeared to propagate south, away from the initial event, and continued until the end of these observations, decelerating from around 6.2 km s^{-1} to approximately 0.6 km s^{-1}. Possibly, the most interesting aspect of this example is the apparent

loop formation between the two main bodies in the Hα line wings, potentially indicating a flux emergence region (see, for example, Otsuji et al. 2007, Ortiz et al. 2014). Despite a significant apparent vertical extension of this loop, no evidence of any such structure within the Hα line core was found (possibly due to the dense foreground structures in the Hα line core obscuring any signal) suggesting that even a dynamic event, such as this example, has no initial influence on the upper chromosphere. Unfortunately, these observations ended before the loop faded and, as such, it is impossible to discuss the full evolution of this event. It is strongly encouraged that further work be carried out continuing the analysis presented by Pariat et al. (2004), to fully understand and quantify the role of small-scale (spatial scales of the order a few arcseconds) in driving Ellerman bombs. Modern data available with the SST/CRISP instrument and soon to be available from the DKIST's Visual Tunable Filter (VTF) instrument would be excellent for conducting such a study.

Overall, this analysis highlights both the small-scale structuring and dynamic nature of Ellerman bombs when observed at the solar limb. An investigation of a wide variety of these events at a range of spatial positions over the Sun would be required to fully understand how many Ellerman bombs display morphologies similar to those discussed within the presented case studies; however, the importance of investigating the sub-structures of small-scale, explosive phenomena in the lower solar atmosphere which can act as important agents in triggering local instabilities in the magnetic environment of the solar surface has been highlighted by this study.

Chapter 6

On The Ability Of MMFs To Drive Ellerman Bombs

6.1 Overview

So far in this thesis, the Ellerman bomb (see, for example, Ellerman 1917, Severny 1956, Georgoulis et al. 2002) phenomenon has been introduced and analysed in a number of datasets. In general, this work has aimed to test the hypothesis that Ellerman bombs are formed by magnetic reconnection close to the photosphere. Specifically, in Chapter 4, a cancellation event in the moat region surrounding a sunspot was presented; however, the measurement of magnetic field strengths was not possible as no inversions from Stokes profiles were attempted. Following on from this, Case Study 1 in Chapter 5 detailed the development of multiple small-scale dynamic events within a larger Ellerman bomb, potentially indicating a repetitive impulsive driver was responsible for their formation. In this Chapter, a selection of high-resolution ground-based datasets, collected by the IBIS instrument over a period of two hours, are combined with measurements of the vertical magnetic field inferred by the SDO/HMI instrument in order to identify potential Ellerman bombs with clear links to cancelling regions (for example, MMFs as discussed by Sheeley 1969, Vrabec 1971, Harvey

and Harvey 1973).

A potential link between a sub-section of Ellerman bombs and MMFs was originally presented by Nindos and Zirin (1998); however, these authors were only able to infer that a spatial correlation between portions of both features existed. With respect to opposite polarity MMFs, Nindos and Zirin (1998) noted that the Ellerman bombs in their study '...were not associated with approaching opposite polarity features nor did they occur above magnetic field reconnection neutral points.' In more recent studies, though, specific links between Ellerman bombs and bi-poles have been presented (see, for example, Georgoulis et al. 2002, Watanabe et al. 2011, Nelson et al. 2013b) meaning further research is essential to fully understand any potential link between Ellerman bombs and MMFs. By implementing the Yet Another Feature Tracking Algorithm (YAFTA; Welsch and Longcope 2003) in this Chapter, isolated MMFs can be studied in detail, allowing measurements of parameters such as cancellation rates to be made. Unfortunately, in an AR, where strong magnetic fields are common, it is difficult to easily isolate specific bi-polar interactions within the YAFTA output from which accurate magnetic field strength measurements can be obtained through time. Therefore, this research is focused on thoroughly analysing a small-number of relevant events.

After a comprehensive inspection of these data, two isolated MMFs (both spatially correlated to Hα line wing brightenings which can potentially be interpreted as Ellerman bombs) were found for analysis. Accurate measurements of the magnetic field strengths of these MMFs were made from the YAFTA output (with an input from SDO/HMI data) through time meaning any cancellation, or reduction in flux through time, within these events could be inferred. These cancellation rates were then applied to the basic algebraic model of photospheric magnetic reconnection initially discussed by Litvinenko (1999) (and further implemented by, for example, Litvinenko and Martin 1999, Chae et al. 2003, Litvinenko et al. 2007) which gave outputs which could be compared to observable parameters such as the upward flow velocity (comparable to the re-

sults given in Chapter 5) and the upward mass flux (which could be compared to the estimated properties of surges which have been potentially linked to Ellerman bombs by, for example, Rust 1968, Roy 1973, Madjarska et al. 2009). Recent work by Filippov et al. (2007) has suggested a link between rapid flux emergence (increases by a factor of 25 within 5 minutes) and surge formation, potentially defining physical conditions in the solar atmosphere which would be conducive to both surges and Ellerman bombs. Although no bi-polar regions which exhibit such behaviour existed in this study, the implementation of techniques to understand whether cancellation rates observed within MMFs co-spatial to Ellerman bombs are sufficient to drive enough mass to fill surges could provide a basis from which a larger sample of such events can be analysed in detail in the future.

The uniqueness and importance of this study lie in the combined use of a variety of techniques to comprehensively analyse a small-number of confidently identified bi-polar MMFs linked to Hα brightenings with properties similar to Ellerman bombs. Specifically, it is of interest to understand whether the cancellation rates observed within bi-polar MMFs, when used as an input for the model of Litvinenko (1999), are sufficient to explain the morphological evolution of Ellerman bombs and to supply the required mass for solar surges. This research could potentially provide a basis from which a larger statistical sample of Ellerman bombs, surges, and MMFs can be conducted. This Chapter is structured as follows: In Section 2, the observations analysed in this Chapter are presented. Section 3 details the in-depth data analysis of the two potential Ellerman bomb-MMF pairs (including the estimation of the reconnection rates) before the model presented in Litvinenko (1999) and Litvinenko et al. (2007) is briefly introduced in Section 4. Finally, output from this model is analysed in Section 5 before a discussion about the relevance of this study is included in Section 6. The research presented in this Chapter makes up part of the project submitted for publication in the Monthly Notices of the Royal Astronomical Society.

6.2 Observations

The ground-based data analysed in this Chapter were collected using the IBIS instrument at the NSO/DST. Three distinct observational routines (which shall be denoted as 'A', 'B', and 'C' for ease) were employed over a two hour period on the 30th September 2012 between 14:34:19 UT and 16:32:50 UT. The seeing conditions were variable through time, however, the quality was generally high between 15:00 UT and 16:15 UT. Routine 'A' comprised a 17-point Hα line scan and a 9-point Fe I 6302.5 Å line scan, neither of which sampled with even spacing through the profiles. The minimum and maximum wavelengths of the observed Hα line profile were -0.99 Å and $+1.01$ Å from 6562.8 Å, respectively. As in other Chapters, all Hα wavelength measurements from this point will be given relative to the line core wavelength of 6562.8 Å. The Fe I 6302.5 Å data are not analysed in this Chapter and so will not be discussed further. In total, 26 images were taken per sequence repetition with a cadence of approximately 5.4 seconds. Routine 'B' imaged the wings of the Hα line profile at only -0.74 Å and $+0.76$ Å, acquiring 30 frames at each line position, totalling 60 frames per repetition. Each set of 30 frames was then reduced using the speckle method (see, for example, Wöger et al. 2008) returning data with a total cadence of around 6.8 seconds. Finally, routine 'C' was similar to routine 'B' except that each line position was only sampled 10 times, giving a total of 20 frames per repetition at a cadence of 2.4 seconds. Once again, these data were reduced using the speckle method. Each of these datasets has a pixel size of around $0.097''$ and samples a circular FOV with a diameter of approximately $80''$. These data are, therefore, perfect for analysing the small-scale phenomena in the lower solar atmosphere of interest in this study. A summary of the two hour period of observations can be found in Table 6.1.

The FOV of the IBIS observations discussed here was centred on the leading sunspot of NOAA AR 11579. This sunspot was situated at approximate co-ordinates of x_c=$50''$ and y_c=$-275''$ (with respect to the disc centre), meaning it is an excellent candidate for observing the vertical magnetic field in the pho-

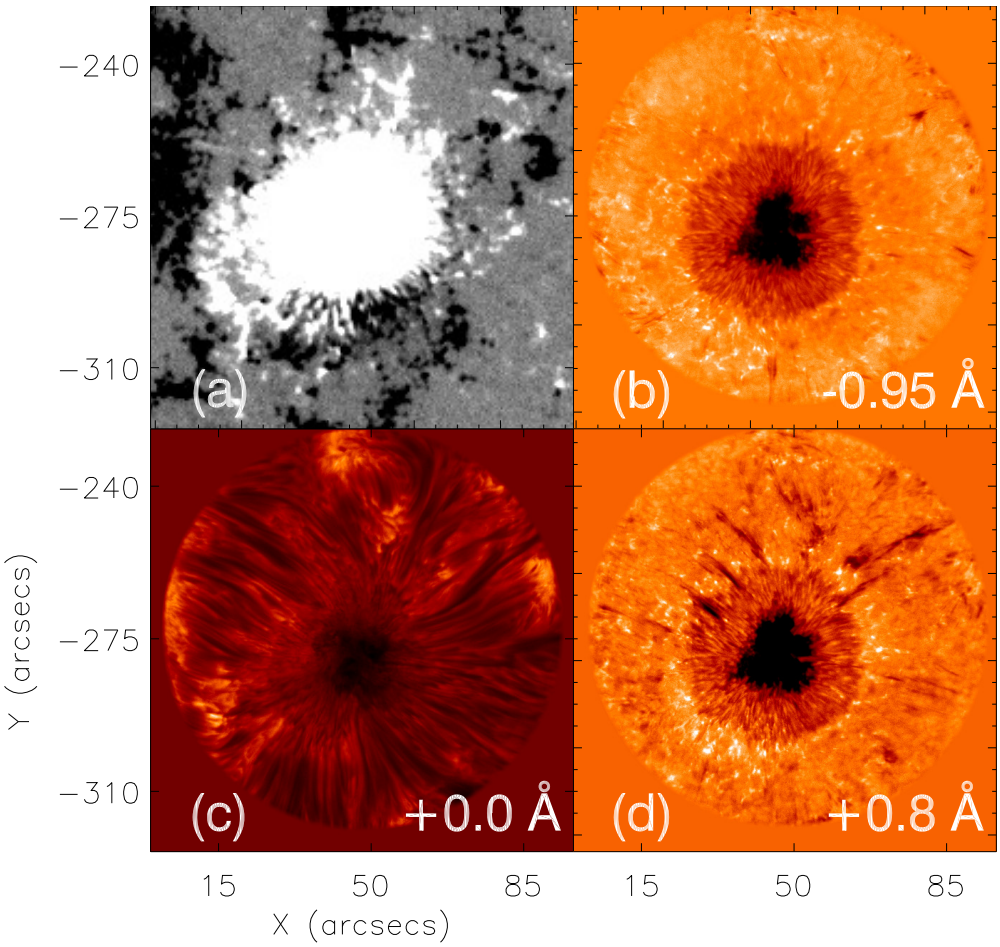

Figure 6.1: The FOV analysed in this Chapter at approximately 15:41 UT on 30th September 2012 showing: (a) the vertical magnetic field measured in the photosphere by the SDO/HMI instrument (to emphasise the opposite polarity nature of the region, the minimum and maximum thresholds of the plot have been set to −100 G and 100 G, respectively); and (b)-(d) the IBIS FOV for three wavelengths (indicated in each individual sub-plot) in the Hα line scan.

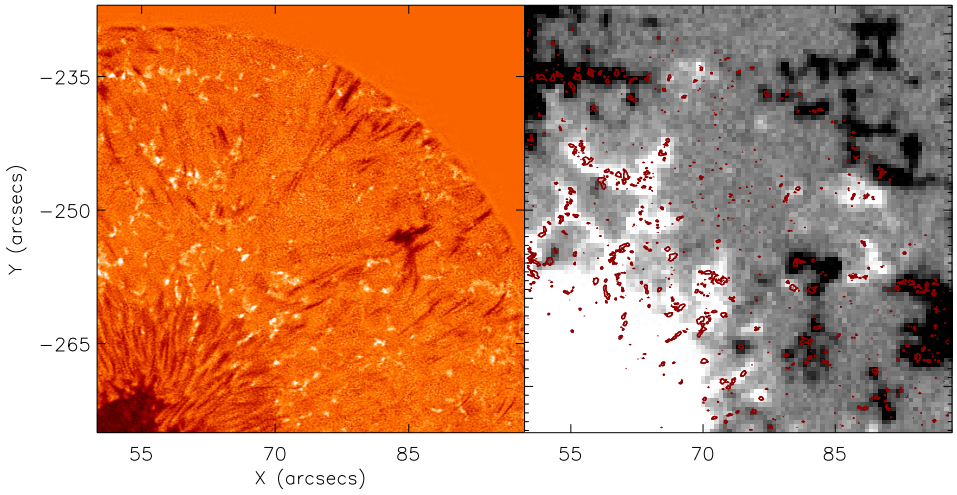

Figure 6.2: A region from the FOV plotted in Fig. 6.1. The left panel depicts the Hα blue wing and the right panel shows the co-spatial vertical magnetic field as inferred by the SDO/HMI instrument. The red contours overlaid on the photospheric magnetic field image outline the obvious network features from the Hα image and confirm the accuracy of the alignment.

tosphere. In this study, vertical magnetic fields are inferred through analysis of data collected by the SDO/HMI instrument, which were downloaded, reduced, and cropped to the IBIS FOV using standard *SolarSoft* routines. Co-alignment was achieved by matching bright regions in the Hα line wing (hypothesised to be a good proxy of the vertical magnetic field by Rutten et al. 2013) at +0.76 Å with small-scale magnetic field structures in the SDO/HMI images. In Fig. 6.1, the co-aligned vertical magnetic field data (scaled with minima and maxima of −100 G and 100 G, respectively) are plotted along with three wavelengths from the Hα scan sequence (specifically −0.95 Å, 0.0 Å, and +0.8 Å). The central sunspot, as well as more small-scale network structures, is easily observed in the two Hα line wing images, however, it is masked somewhat in the complex Hα core by overlying fibril structures. The co-alignment between the instruments is plotted in Fig. 6.2, where the left hand frame depicts the Hα blue wing intensity and the right frame maps the co-spatial vertical magnetic field structuring with

Start time (UT)	End time (UT)	Routine	Frames	Cadence
14:34:19	14:49:20	B	133	6.8 seconds
14:51:04	15:05:55	A	162	5.4 seconds
15:07:35	15:22:32	C	377	2.4 seconds
15:24:12	15:39:13	B	133	6.8 seconds
15:41:00	15:59:59	A	207	5.4 seconds
16:01:53	16:15:17	C	338	2.4 seconds
16:17:49	16:32:50	B	133	6.8 seconds

Table 6.1: Summary of the observations analysed in this Chapter with routines 'A', 'B', and 'C' defined as the Hα line scan, 30-frame speckle, and 10-frame speckle sequences, respectively. Each of these sequences returned data with high-spatial ($\sim 0.2''$) and temporal (> 10 seconds) resolution data of the Hα line. These routines are described in detail in the first paragraph of the Observations Section of this Chapter.

contours of Hα bright points overlaid.

6.3 Data Analysis

Through a brief analysis of Fig. 6.1, it is obvious that there is a sizeable positive polarity sunspot in the centre of the FOV, surrounded almost ubiquitously by magnetic elements, with sizes encompassing varying scales, of both positive and negative polarity. The sunspot, as well as a large proportion of the plage region situated in the top left of the image, remain relatively unchanged throughout the course of these observations both morphologically and with regard to the magnetic field strength. However, numerous smaller-scale flux regions, identified as MMFs (see, for example, Sheeley 1969, Harvey and Harvey 1973), are evident in this FOV. These small-scale bi-polar flux regions appear to flow away from the sunspot, approaching each other before cancelling away. This behaviour within MMFs was first noted in spectroscopic data by Sheeley (1969) and within magnetic field data by Harvey and Harvey (1973). In this Chapter, it is these small-scale flux elements, and their potential ability to drive the Ellerman bomb

phenomena, that shall be analysed.

In order to successfully analyse these small-scale, magnetic events, it was first necessary to visually identify small-scale, bi-polar MMFs which did not interact with any large-scale flux throughout their lifetime. Within these data, two suitable MMFs were found. As has been previously mentioned, tracking of magnetic features within these data was conducted using the YAFTA code, which requires minimum thresholding of both magnetic field strength and area to track features through frames. In this study, these thresholds are set at 40 G and 2 pixels, respectively. Other thresholds were tested but either over-estimated the area of the magnetic features (through a visual inspection) or were unable to track the feature consistently through time. The total magnetic field strength and area of each of the individual polarities through time were included in the YAFTA output for easy extraction and study. Following this, the co-spatial Hα data available at the time of the cancellation was checked in order to identify if any Hα line wing intensity enhancement, with comparable properties to Ellerman bombs, was present.

It is important to note that further cancelling bi-poles were evident in these data, however, often these consisted of one small-scale single polarity flux region 'disappearing', whilst approaching a large-scale opposite polarity 'standing' region of flux which did not evolve over the course of these observations. By testing the YAFTA algorithm on such regions it was found that no cancellation or emergence signal could be detected, most likely due to the links to the larger-scale flux concentrations. It appeared that the YAFTA algorithm sporadically detected larger and smaller regions of field, due to changes in the observed magnetic structure, therefore, adding and removing flux from the output as noise which reduced the effectiveness of this study. Additionally, it proved difficult to identify where the observed cancellation occurs and, hence, accurately estimate the cancellation rate and length of the current sheet (both of which are required as inputs for the model presented by Litvinenko 1999).

6.3.1 Cancelling Event '1'

The first bi-polar MMF event analysed in this Chapter was observed to propagate away from the penumbra of the sunspot between 14:45 UT and 16:00 UT. The evolution of this event is plotted within the 4″ diameter black circle in the left hand column of Fig. 6.3. Prior to the measured cancellation, a large region of positive polarity flux appeared to fragment, before one of the fragments interacted with a region of emerging negative polarity flux. Both of the bi-poles cancelled sufficiently through this period of time such that they were no longer observable in magnetogram data. Through inspection of Hα line wing images co-spatial and co-temporal to the cancellation, it was possible to establish that a brightening, potentially comparable to an Ellerman bomb, occurred at this position during this time (depicted in the second row of the right hand column of Fig. 6.3), possibly linked to the evolving magnetic field topologies. The YAFTA output for this MMF was then visually inspected and the event numbers corresponding to the opposite polarity regions were noted. The magnetic field strength and area were then calculated for each frame allowing for the accurate computation of R, the cancellation rate, and an estimation of l, the length of the reconnecting current sheet.

This MMF exhibits significant horizontal motions through its observable lifetime, similar to those noted in previous research (see, *e.g.*, Harvey and Harvey 1973, Lim et al. 2012), which can easily be inferred from Fig. 6.3. In Fig. 6.4, representative frames of the MMF and potential Ellerman bomb analysed in this Section are plotted (top row). The estimate of the length of the current sheet is indicated with a white line and an arrow in the left hand image and the Hα intensity enhancement is highlighted by the arrow in the right hand frame. In the left hand frame on the bottom row, the total positive flux of the MMF is plotted through time between approximately 14:50 UT and 16:00 UT. An obvious decrease in flux of this MMF through time is immediately evident with a linear fit of this gradient overlaid with the dashed line. Overall, the cancellation rate and the current sheet length of this MMF can be estimated to

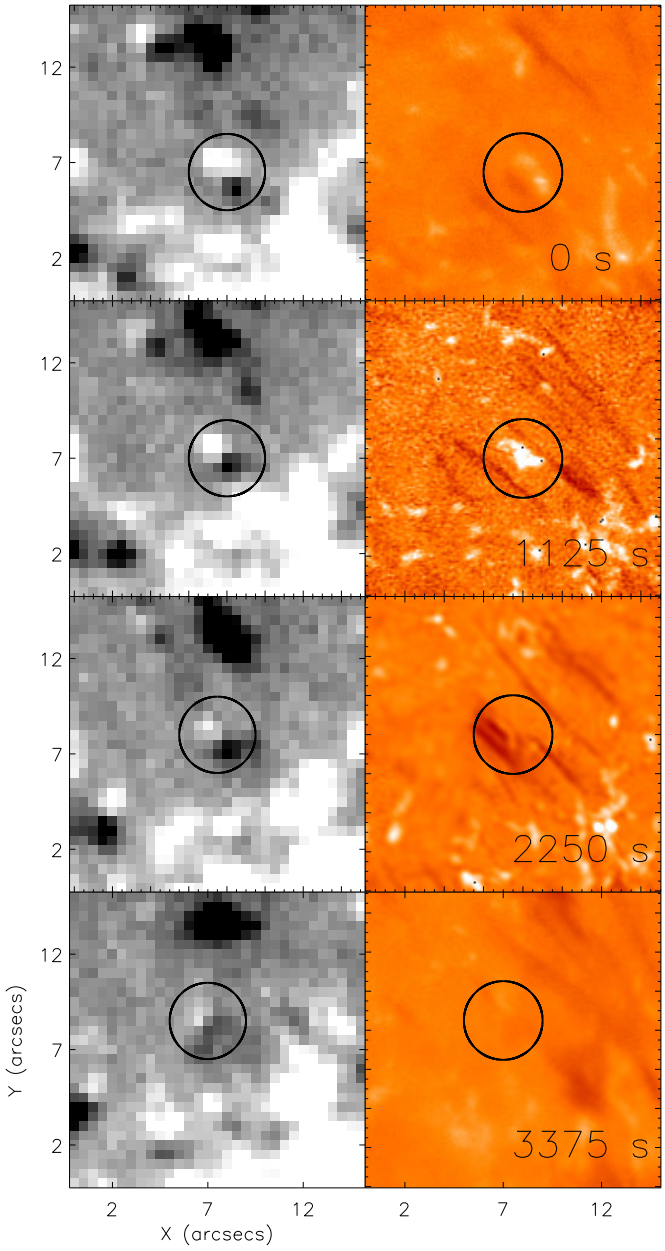

Figure 6.3: The evolution of Cancelling Event '1' through time for both SDO/HMI photospheric line-of-sight magnetograms (left column) and the Hα blue wing (right column). Despite the relatively long life of the MMF, it is simple to see that the Hα brightening, possibly interpreted as an Ellerman bomb, is only observable in one frame (due to the lifetime of this event being around 10 minutes).

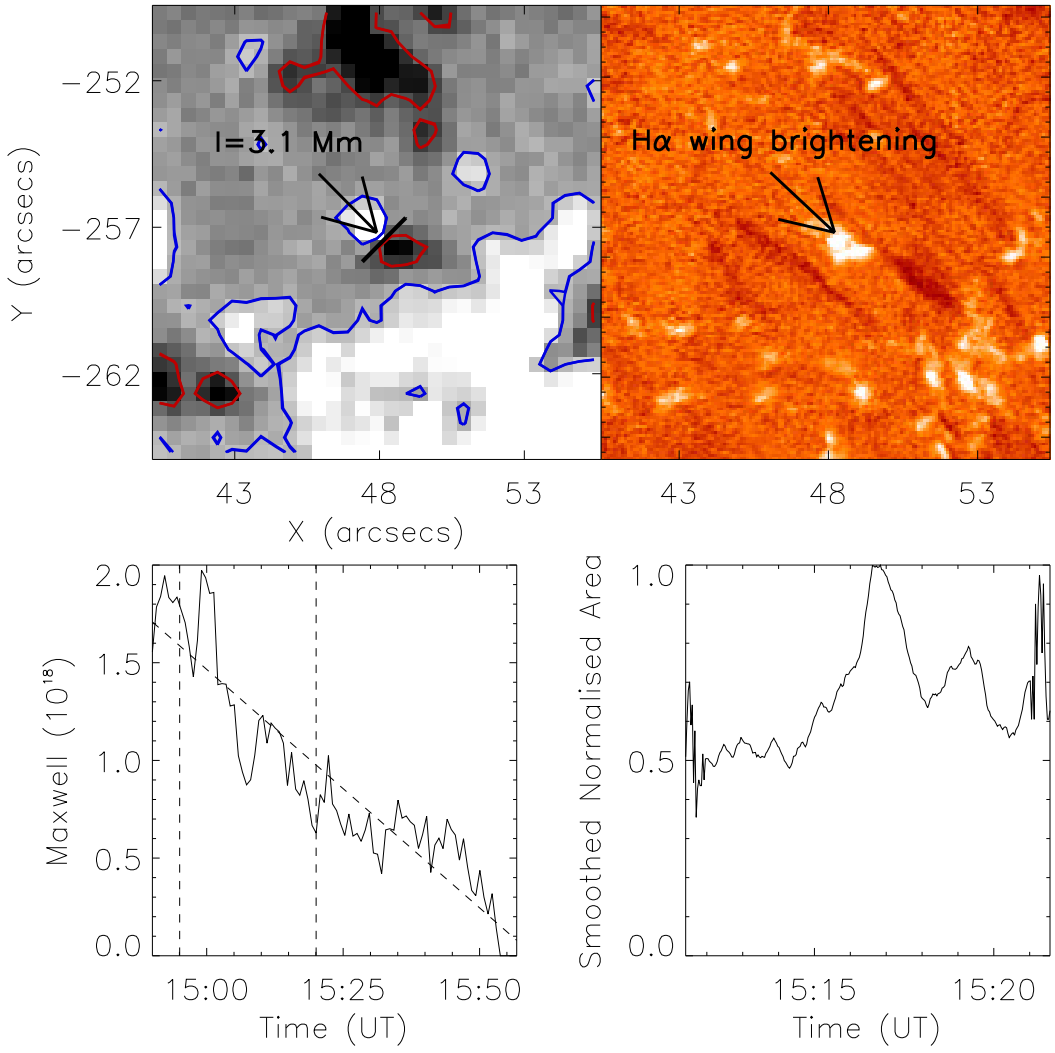

Figure 6.4: The FOV surrounding Cancelling Event "1" at 15:15:33 UT. The vertical magnetic field topology (top left) is plotted with minima and maxima of −100 G and 100 G, respectively. The length of the current sheet is indicated by the white line and black arrow and is estimated to be approximately 3.1 Mm. Co-temporal Hα blue wing image (−0.74 Å) depicting the potential Ellerman bomb (top right). The positive magnetic flux through time (bottom left) shows a steady decrease over the course of one hour at a rate of approximately 4.1×10^{14} Mx s^{-1}. The mean area of the Hα brightening (bottom right) shows a peak at approximately 15:15 UT associated with 'flaring'. Noise in the measurements of the area is evident at both edges of the time interval.

be 4.1×10^{14} Mx s^{-1} and 3.1 Mm, respectively.

The Hα line wing intensity enhancement co-spatial to this cancellation could be considered, in many ways, a standard example of an Ellerman bomb. With a width and length of around 1″ and a lifetime of approximately 10 minutes, this potential Ellerman bomb formed with properties typical of those analysed in previous Chapters. The event formed in the final frames of the first implementation of routine 'A', before evolving through the following routine. The morphology of this event began as a relatively small brightening in the Hα line wings, before behaviour indicative of flaring (as discussed in previous Chapters and by, for example, Watanabe et al. 2011) was evident (shown in the bottom right panel of Fig. 6.4). After this flaring, the brightening decreased in size before fading from view entirely (as can be seen in the final two rows of Fig. 6.3). The area and intensity of the event peaked at around 15:15 UT (close to the frame plotted in Fig. 6.4) which was after significant cancellation had already occurred. Why this delay between the initial cancellation measured within the MMF and the occurrence of the brightening is a question which cannot be answered within this study. Future research combining the methods presented here with state-of-the-art simulations could potentially offer in-sight into whether a process such as flux-pile up is required to reach a threshold value before any potential reconnection can occur.

6.3.2 Cancelling Event '2'

The morphological properties of the second bi-polar event (identifiable between 15:50 UT and 16:40 UT) analysed in this Chapter were similar to the first. Initially, a region of positive polarity flux was observed to fragment from a larger body close to the sunspot, before interacting with an emerging negative polarity flux segment (as plotted in the left hand column of Fig. 6.5). The response of the Hα line wings to this MMF is plotted in the right column of Fig. 6.5. In a similar way to Cancellation Event '1', the photospheric line-of-sight magnetic field and Hα blue wing spectroscopic image are plotted in the

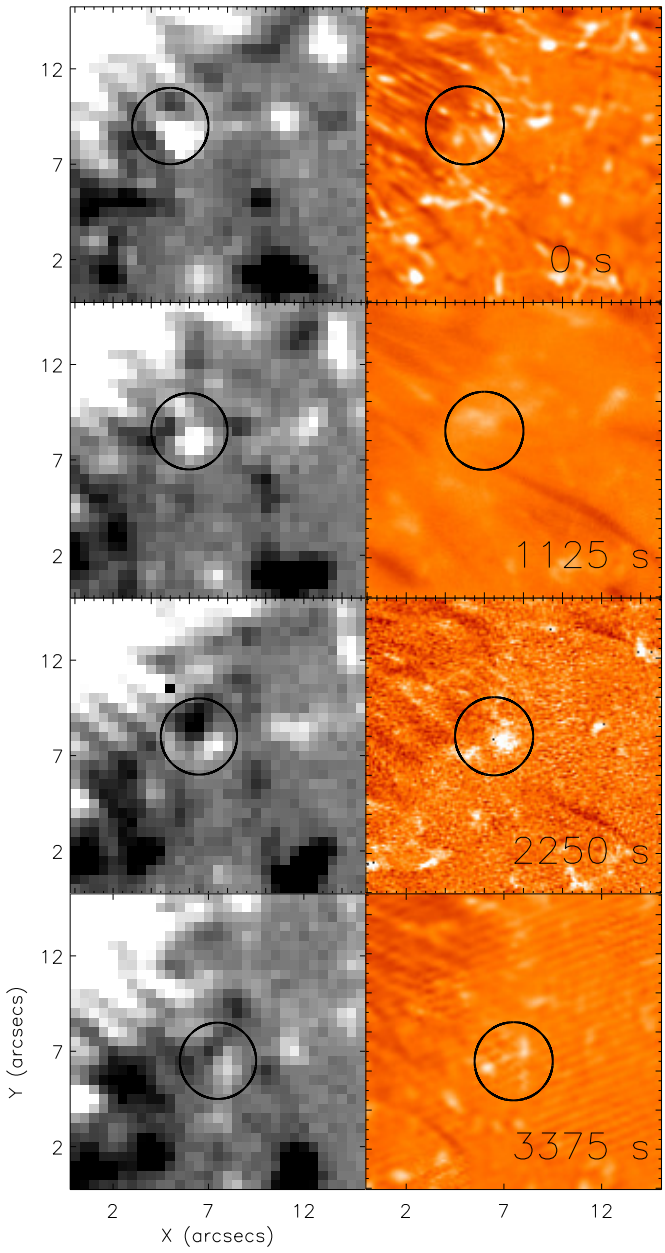

Figure 6.5: The same as Fig. 6.3 but for Cancelling Event '2'. Again, note the relatively short lifetime of the potential Ellerman bomb compared to the MMF.

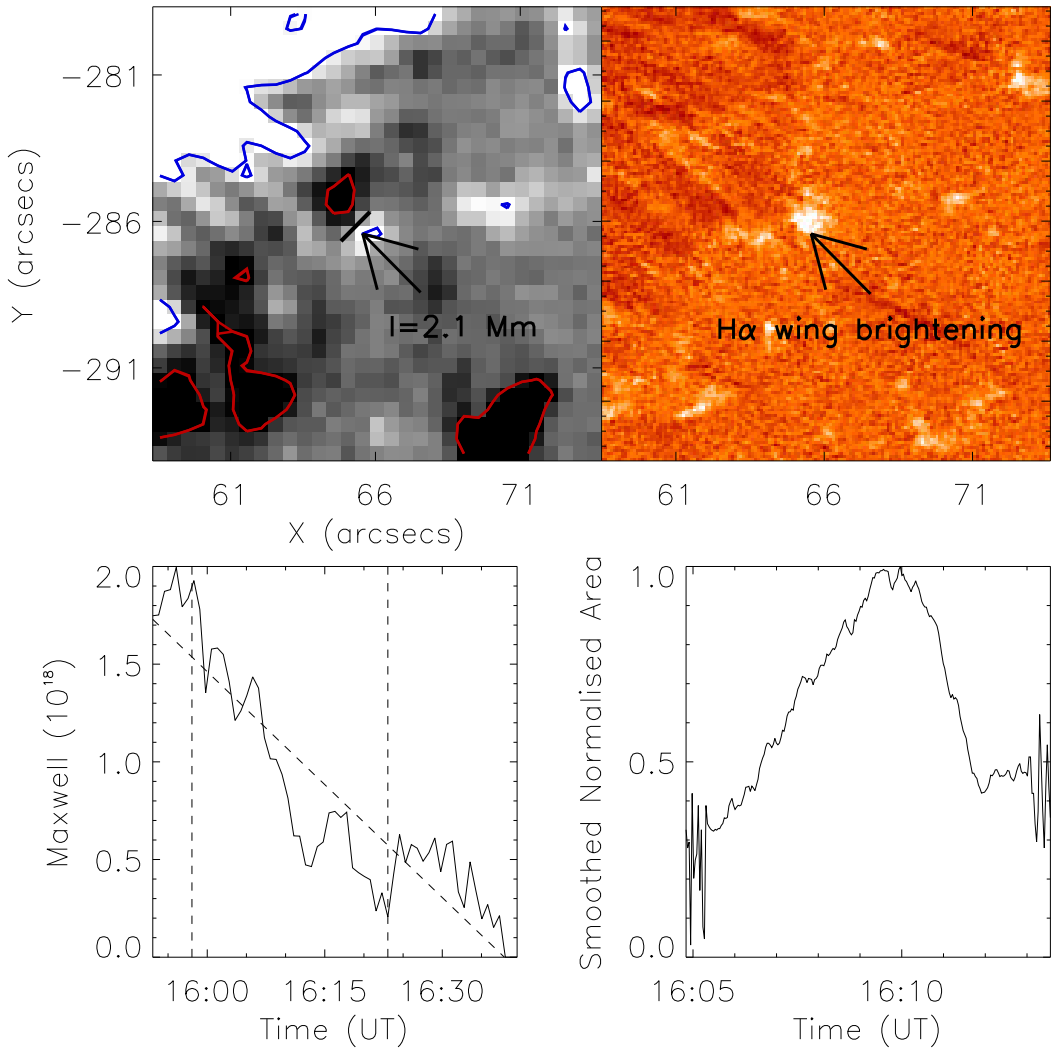

Figure 6.6: The same as Fig. 6.4 but for Cancelling Event '2'. This FOV is observed at 16:10:18 UT. The positive magnetic flux decreases with a cancellation rate of approximately 6.4×10^{14} Mx s^{-1} over a length of 2.1 Mm.

top row of Fig. 6.6 (left and right frames, respectively), before the cancellation rate (with linear fit) and the area of this event through time are depicted in the bottom row. For this event, a cancellation rate of 6.4×10^{14} Mx s^{-1}, and a current sheet length of 2.1 Mm are found, comparable to Cancellation Event '1'.

The potential Ellerman bomb at this spatial position displayed similar properties to that studied in Cancelling Event '1' with a diameter close to 1″ and a lifetime on the order minutes. Again, this event began as a relatively small brightening in the Hα line wings before it rapidly expanded in area and intensity until around 16:10 UT. From there, it began to recede from view (depicted in the right hand frame on the bottom row of Fig. 6.6). Again, cancellation occurred before the occurrence of the brightening potentially hinting that some form of sub-process (such as flux build-up) is required for the formation of these phenomena. Interestingly, the rise to the peak area and intensity of this event corresponded to the period of greatest cancellation. It would be of interest to analyse high-resolution, co-temporal photospheric magnetic field measurements and Hα line profile spectroscopic observations collected by the SST/CRISP instrument in future research.

6.4 Litvinenko (1999) Model

6.4.1 Isothermal Model

This Chapter discusses the analytical model of photospheric magnetic reconnection originally proposed by Litvinenko (1999), with specific attention paid to whether the cancellation co-spatial to MMFs is sufficient to drive the Ellerman bomb phenomena. This model has been used in a number of past researches (including, for example, Litvinenko and Martin 1999, Chae et al. 2003, Litvinenko et al. 2007) and appears to account for a number of observed properties of flux cancellation, such as upward propagation of material from the reconnection site and potential mass supply to filaments. As Ellerman bombs have been linked

to the formation of surges in previous work (see, for example, Rust 1968, Roy 1973, Madjarska et al. 2009), it is of interest to analyse whether including the observed properties of cancellation regions, some of which are associated with regions of increased intensity in the Hα line wings, into this model returns realistic comparisons with Ellerman bomb characteristics (for example, the upward flow velocity of 9 km s^{-1} found in the previous Chapter and in Nelson et al. 2015).

The overall model initially presented by Litvinenko 1999 is relatively simple yet it will be included here for completeness. Consider a vertical current sheet which has formed between two opposite polarity regions in the photosphere. The physical parameters are written as follows: the length (x co-ordinate), thickness (y co-ordinate), and height (z co-ordinate) of the current sheet are defined as l, $2a$, and $2b$; the plasma densities at the entrance to the current sheet and within the current sheet are $n_{\rm c}$ and n; the corresponding temperatures are $T_{\rm c}$ and T; $B_{\rm c}$ and $v_{\rm c}$ are the magnetic field and in-flow speed at the entrance to the current sheet; v is the out-flow speed; and finally c, $k_{\rm B}$, σ, and $m_{\rm p}$ are the speed of light, Boltzmann constant, electrical conductivity, and the proton mass, respectively. The influence of magnetic flux pile-up (see Litvinenko et al. 2007) adds two further parameters, namely the external in-flow speed, $v_{\rm i}$, and the external magnetic field strength $B_{\rm i}$.

The Sweet-Parker reconnection model (Parker 1957; Sweet 1958), modified into a set of order-of-magnitude equations for the compressible case by Syrovatskii (1976), is used to formulate the equations of this system. As in Litvinenko (1999), the mass balance equation at the sheet can be written as:

$$n_{\rm c} v_{\rm c} b = n v a, \tag{6.1}$$

and the in-flow speed can be described by:

$$v_{\rm c} = \frac{c^2}{4\pi\sigma a}. \tag{6.2}$$

The sub-Alfvénic in-flow speeds mean that the momentum equation across the sheet can be written as:

$$n_{\rm c}kT_{\rm c} + \frac{1}{8\pi}B_{\rm c}^2 = nkT \tag{6.3}$$

and the momentum equation along the sheet is:

$$\frac{1}{2}m_{\rm p}nv^2 + n_{\rm c}kT_{\rm c} = nkT. \tag{6.4}$$

Finally, Litvinenko et al. (2007) argued that the balance equation for magnetic flux outside the sheet can be written as:

$$r = v_{\rm c}B_{\rm c} = v_{\rm i}B_{\rm i}, \tag{6.5}$$

where $r = R/l$, and R is the observed flux cancellation rate for either magnetic polarity (as measured for the MMFs analysed in this Chapter in the previous Section). Litvinenko (1999) also assumed that $b = \Lambda(z)$ (the atmospheric scale height) and $T = T_{\rm c}$ (*i.e.*, that the reconnection is iso-thermal).

The atmospheric scale height (Λ), temperature ($T_{\rm c}$), electrical conductivity (σ), and density ($n_{\rm c}$) can be estimated for various heights from atmospheric models. In this Chapter, the VAL-C model is used (Vernazza et al. 1981). Further parameters ($v_{\rm i}$ and r) can be inferred from magnetic field data, however, in this study, the average in-flow speed of 300 m $^{-1}$ measured by Litvinenko et al. (2007) is used. This value must be assumed in this research due to the relatively low-resolution nature of SDO/HMI magnetograms. Approximately 27 frames would be required for a convergence of one pixel to occur between the opposite polarity regions at 300 m s^{-1} making this value impossible to accurately measure within one hour (or 80 SDO/HMI frames). Future research, potentially exploiting high-resolution ground-based magnetograms (potentially from the SST/CRISP instrument) should be conducted to better quantify these velocities within MMFs.

This leaves six variables (n, $v_{\rm c}$, $B_{\rm i}$, $B_{\rm c}$, a, and v) to be calculated from

Equations (6.1)-(6.5). Simple algebraic manipulation, however, allows Equations (6.1)-(6.5) to be combined to give:

$$v_{\rm c}^3 = \frac{c^2 r}{4\pi\Lambda\sigma\left(4\pi m_{\rm p} n_{\rm c}\right)^{\frac{1}{2}}}\left(1+\frac{r^2}{8\pi k n_{\rm c} T_{\rm c} v_{\rm c}^2}\right)^{\frac{1}{2}}, \tag{6.6}$$

leaving only five variables from five equations. The remaining parameters can finally be written as:

$$B_{\rm i} = \frac{r}{v_{\rm i}}, \tag{6.7}$$

$$B_{\rm c} = \frac{r}{v_{\rm c}}, \tag{6.8}$$

$$a = \frac{c^2}{4\pi\sigma v_{\rm c}}, \tag{6.9}$$

$$n = n_{\rm c} + \frac{B_{\rm c}^2}{8\pi k T_{\rm c}}, \tag{6.10}$$

and

$$v = \frac{B_{\rm c}}{\left(4\pi m_{\rm p} n\right)^{\frac{1}{2}}}. \tag{6.11}$$

Finally, it was also noted by Litvinenko and Martin (1999) and Litvinenko et al. (2007) that the upward mass flux, F, associated with the reconnection region could be written as:

$$F = 2 m_{\rm p} a n l v. \tag{6.12}$$

In addition to the system of equations presented by Litvinenko (1999), two further equations can be studied in order to compare the outputs from the model to previous results assertained with respect to the Ellerman bomb phenomena. Firstly, Takasao et al. (2013) suggested that the maximum height of a jet which could be ejected from the photosphere could be estimated using the basic formula:

$$H_{\rm jet} = \frac{\Lambda}{\beta} \tag{6.13}$$

where β is the plasma beta, calculated at the current sheet as:

$$\beta = \frac{nkT}{B_{\rm c}^2/(2\mu)}, \tag{6.14}$$

where μ is the magnetic permeability. Secondly, it is possible to calculate the total magnetic energy within the current sheet which could be converted into both radiation (to compare to the estimates put forward in Chapter 3 and Georgoulis et al. 2002, Nelson et al. 2013a) and kinetic energy (driving the mass motion). Here, the magnetic energy is calculated as:

$$E_{\rm mag} = \frac{B_{\rm c}^2}{2\mu} \times V \tag{6.15}$$

where V is the volume of the current sheet.

In order to begin this study, let us present specific values that will be used in this Chapter. Three required values are well defined in physics, namely the speed of light ($c = 299792458$ m/s), the proton mass ($m_{\rm p} = 1.67262178 \times 10^{-24}$ g), and Boltzmann's constant ($k = 1.3806488 \times 10^{16}$ g cm^2 s^{-2} K^{-1}). Three further values are taken from the VAL-C model (see Vernazza et al. 1981) at the temperature minimum region (around a height of 500 km). These are the electrical conductivity which is assumed to be 9.9×10^{10} s^{-1}, the number density at 2.1×10^{15} cm^{-3}, and the background temperature of 4200 K. Finally, the height of the current sheet is assumed to be the scale height in the solar photosphere, which is estimated here as 100 km.

6.4.2 Non-isothermal model

Numerous observations and theoretical predictions of Ellerman bombs have suggested that a temperature enhancement occurs at the potential reconnection site (see, for example, Kitai 1983, Fang et al. 2006, Nelson et al. 2013b). In this Chapter, therefore, a basic modification to the model presented by Litvinenko (1999) is considered. This modification is based around the assumption that

$T \neq T_{\rm c}$ (*i.e.*, that the reconnection site is not isothermal). This means Eq. (6.6) must be rewritten as:

$$v_{\rm c}^3 = \frac{c^2 r}{4\pi\Lambda\sigma\left(4\pi m_{\rm p} n_{\rm c}\right)^{\frac{1}{2}}}\left(\frac{T_{\rm c}}{T} + \frac{r^2}{8\pi k_{\rm B} n_{\rm c} T v_{\rm c}^2}\right)^{\frac{1}{2}} \tag{6.16}$$

Further to this, Equation (6.10) must now be modified to:

$$n = \frac{n_{\rm c} T_{\rm c}}{T} + \frac{B_{\rm c}^2}{8\pi k T}. \tag{6.17}$$

It is important to note that six variables must now be solved by five equations and that a relationship between T and $T_{\rm c}$ must be included to counter this problem. It is, therefore, assumed that:

$$T = T_{\rm c} + \Gamma, \tag{6.18}$$

where Γ is a non-zero, positive constant which can be iterated through to compare a range of values.

6.5 Results

6.5.1 Cancelling Event '1'

At this point in the Chapter, it is possible to include the input values estimated for each of the MMF-Hα brightening pairs into the Litvinenko (1999) model. For Cancelling Event '1', the measured parameters are $R = 4.1 \times 10^{14}$ Mx s^{-1} and $l = 3.1 \times 10^{8}$ cm which, when included in the isothermal ($T = 4200$ K) Equations (6.7)-(6.12), output values of $v_{\rm c} \approx 0.085$ km s^{-1}, $B_{\rm i} \approx 44$ G, $B_{\rm c} \approx 156$ G, $n_{\rm c} \approx 3.8 \times 10^{15}$ cm^{-3}, $v \approx 5.6$ km s^{-1}, $a \approx 0.852$ km, and $F \approx 6.6 \times 10^{14}$ g hr^{-1}. A partial summary of this event is included in the appropriate row of Table 6.2. Each of the output values estimated for this event are comparable to the values calculated by Litvinenko et al. (2007), therefore, implying that the

	Measured Variables		Calculated Variables		
Event	R (Mx s^{-1})	l (cm)	B_c (G)	v (km s^{-1})	F (g hr^{-1})
1	4.1×10^{14}	3.1×10^{8}	156	5.6	6.6×10^{14}
2	6.4×10^{14}	2.1×10^{8}	249	6.8	6.5×10^{14}

Table 6.2: The measured input values and selected computed output values for each of the cancellation events analysed in this Chapter for the isothermal (4200 K) model.

application of this model may be relevant here. The initial check of this model to observables can be conducted using the estimated up-flow velocity of 5.6 km s^{-1}, which is around one standard deviation lower than the mean velocity measured at the limb in the previous Chapter (and by Nelson et al. 2015). In addition to this, the predicted magnetic field strengths are comparable to those measured by the SDO/HMI instrument for this MMF, suggesting that the output from this model is, indeed, reasonable when compared to observations.

By applying the outputs from the model to Equations (6.13)-(6.15), estimates of the maximum jet extension from the reconnection site and the upper-limit of magnetic energy conversion can be inferred. The local plasma-β can be calculated within the current sheet and the atmospheric scale height, Λ, is kept as 100 km. From these values, the maximum jet extension is found to be 443 km. This value is slightly shorter than the majority of Ellerman bombs observed at the limb (see, for example, Watanabe et al. 2011, Nelson et al. 2015, Chapter 5) but it is still within a reasonable range for comparison. It could, therefore, be suggested that if the co-spatial Hα brightening event were an Ellerman bomb, it would be a weak example of such an feature. Finally, the total magnetic field energy within the current sheet (using the output magnetic field strength and the estimated current sheet volume) can be estimated at 1.02×10^{26} ergs, which if converted at a steady rate over the course of the hour during which this MMF was observable would give an energy release rate of 2.84×10^{22} ergs s^{-1}. Assuming a lifetime of 10 minutes for an Ellerman bomb, this would allow

1.7×10^{25} ergs of magnetic energy to be converted to either radiative or kinetic energy. This value is comparable to radiative energy estimates presented by Nelson et al. (2013a) and in Chapter 3 but two orders of magnitude lower than those discussed by Georgoulis et al. (2002). A larger range of cancellation rates will be studied in future work (and included in the article on which this Chapter is based) in order to test whether this value is typical of such MMFs.

In Fig. 6.7, a number of parameters are plotted with respect to temperature at the current sheet. It is immediately apparent that both the in-flow velocity and mass flux rate decrease with increased temperature at the current sheet, whereas the ratio of the current sheet magnetic field to the incoming magnetic field and the out-flow velocity both increase at higher temperatures. Interestingly, even if a large increase in temperature at the site of the current sheet is considered, the out-flow velocity for this cancellation feature does not reach the average vertical propagation speed of Ellerman bombs observed at the limb in the previous Chapter (or in Nelson et al. 2015). The upward mass flux predicted for this event is an order of magnitude smaller than that predicted by both Litvinenko and Martin (1999) and Litvinenko et al. (2007) and the time required to fill a filament with typical mass around 5×10^{16} g (suggested by, for example, Litvinenko et al. 2007) is on the order of 100 hours (around two orders of magnitude longer than the cancellation observed in this event). Of course, small-scale cancellation features with lifetimes of less than one hour are unlikely to prove essential for the formation of filaments, however, smaller-scale events such as surges are of more interest in this Chapter, due to the potential links between these phenomena and Ellerman bombs. The feasibility of this model to describe this relation shall be discussed further in the Discussion of this Chapter.

6.5.2 Cancelling Event '2'

Finally, the input values of $R = 6.4 \times 10^{14}$ Mx s^{-1} and $l = 2.1 \times 10^{8}$ cm calculated for Cancelling Event '2' will be considered. Including these values in

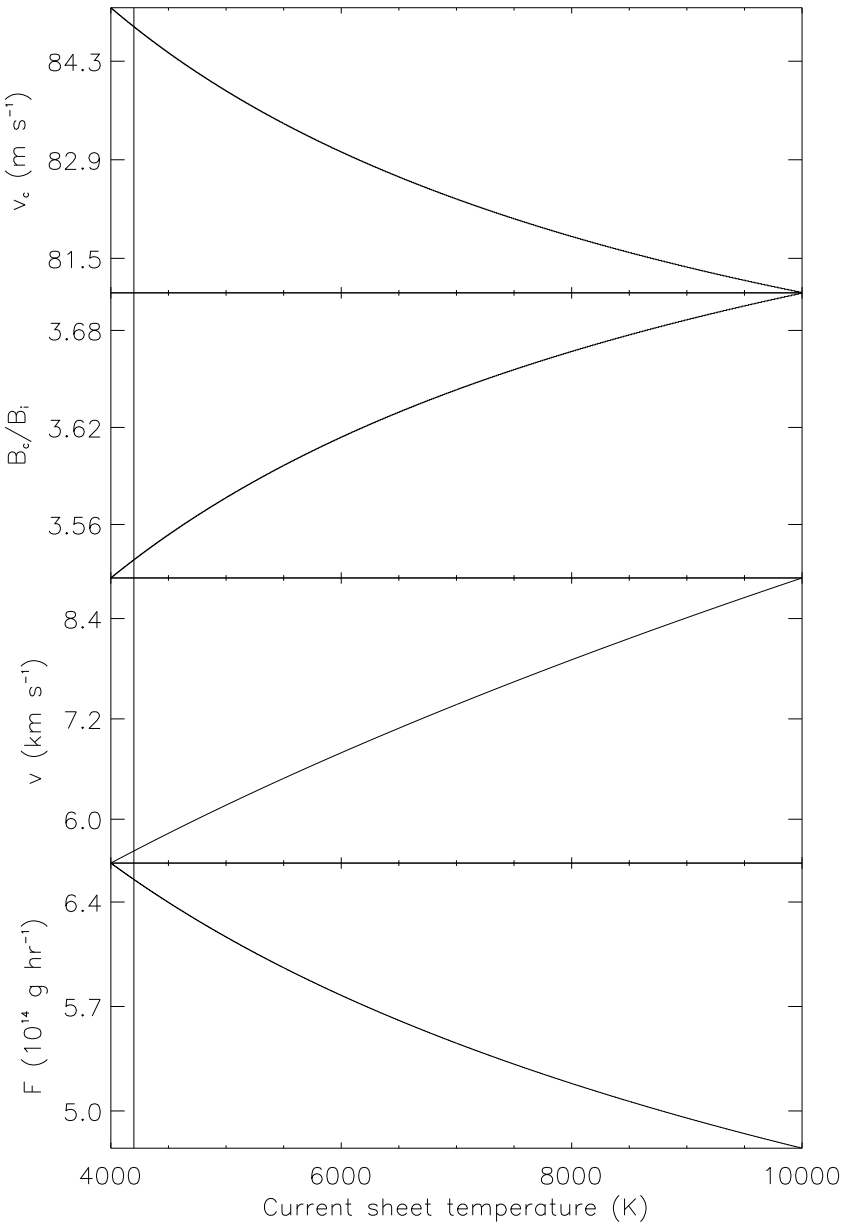

Figure 6.7: The dependence of the in-flow velocity, ratio of current sheet magnetic field to external magnetic field, out-flow velocity and mass flux rate with current sheet temperature for Cancelling Event '1'. The background temperature of 4200 K is depicted by the vertical line.

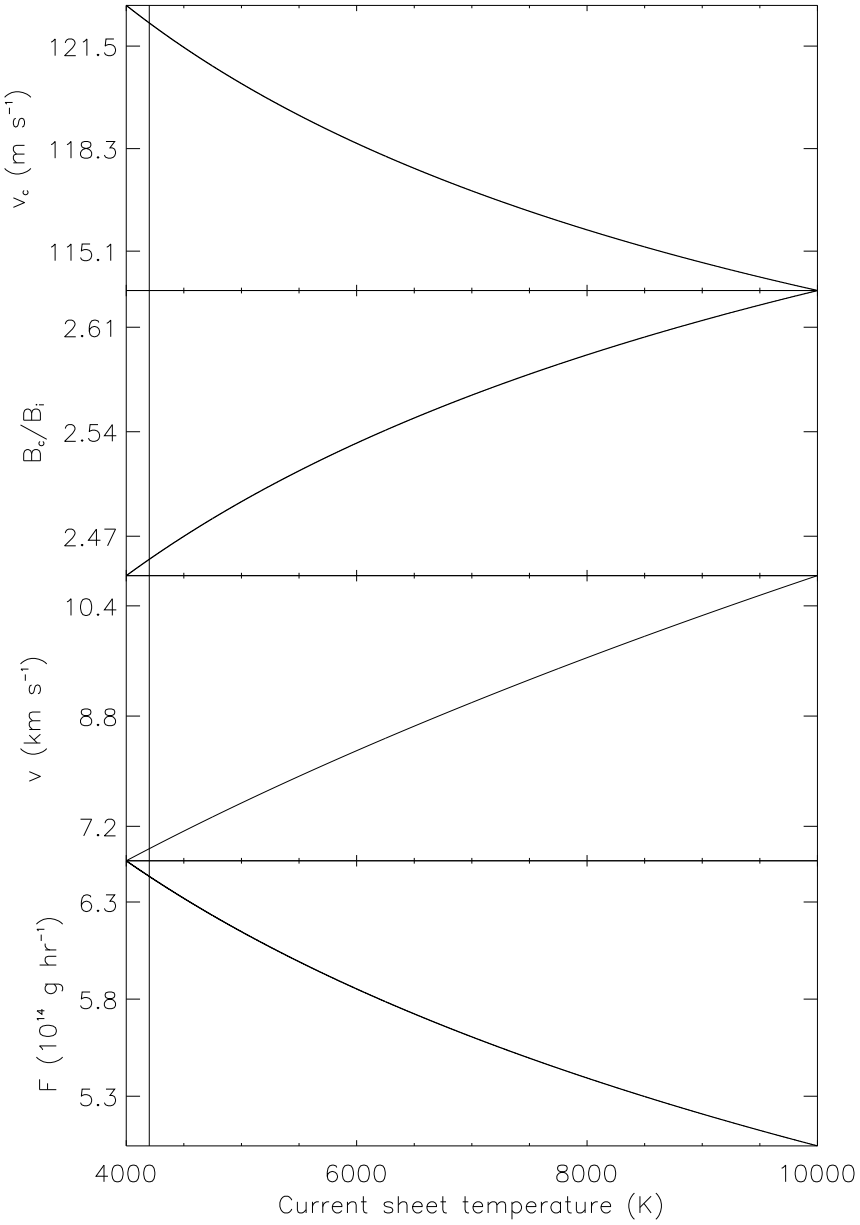

Figure 6.8: Same as Fig. 6.7 for Cancelling Event '2'.

the isothermal model (again with $T = 4200$ K), values of $v_c \approx 122$ m s^{-1}, $B_i \approx 101$ G, $B_c \approx 249$ G, $n_c \approx 6.4 \times 10^{15}$ cm^{-3}, $v \approx 6.8$ km s^{-1}, and $F \approx 6.5 \times 10^{14}$ g hr^{-1} are obtained. These values, as expected, are comparable to those of Cancelling Event '1' and those estimated by Litvinenko et al. (2007). Several parameters are included for easy reference and comparison in the appropriate row of Table 6.2. Interestingly, the up-flow velocity predicted for this event is higher and closer to the mean upward velocity found in the previous Chapter (and by Nelson et al. 2015), however, the mass flux is almost exactly the same between the two features. It is possible that the Hα brightening co-spatial to this event is more likely to be a traditional Ellerman bomb with more typical properties when compared to the literature.

In order to further test the potential capabilities of this MMF to drive Ellerman bombs, it is also of interest to calculated the upward extension and total energy within the current sheet available for conversion to radiative and kinetic processes. It is immediately obvious that the estimated magnetic field strength within the current sheet is higher for this event leading to an increased extension length (when compared to Cancellation Event '1') of 670 km. This value is extremely reasonable when compared to statistical properties of Ellerman bombs (Watanabe et al. 2011, Nelson et al. 2015). In addition to this, the total magnetic energy within the current sheet initially is slightly higher at 1.22×10^{26} ergs, which if steadily released into radiative and kinetic energy over the course of one hour would give a conversion rate of 3.41×10^{22} ergs s^{-1}. Again, assuming a lifetime of 10 minutes for a typical Ellerman bomb allows us to calculate the total energy available as 2.05×10^{25} ergs, which once again, lies between the values estimated by Nelson et al. (2013a) and Georgoulis et al. (2002).

In Fig. 6.8, the output plotted and described in Fig. 6.7 are depicted for this event. Again, the in-flow velocity and upward mass flux both decrease with temperature at the current sheet. For this feature, only a relatively small temperature enhancement (of around 2000-3000 K) is required for the upward flow speed to match the average velocity at the limb presented in the previous

Chapter. The upward mass flux for this event is, once again, relatively small when compared to results obtained with respect to larger cancelling features as presented by, for example, Litvinenko et al. (2007). It should be noted that the in-flow speeds estimated by this method (which, for Cancelling Event '2' are around 120 m s^{-1}) can not be measured for such short lived events using the SDO/HMI instrument. The pixel size of data collected by this instrument is approximately 362500 m, meaning displacements of 5400 m (the in-flow speed multiplied by the cadence) are negligible from frame-to-frame.

6.6 Discussion

In this Chapter, the relationship between two MMFs and Hα brightening pairs in the moat region surrounding a sunspot have been analysed. This research aimed to further analyse the potential relationship between Ellerman bombs and MMFs (originally discussed by Nindos and Zirin 1998) with specific interest paid to the potential role of cancellation in Ellerman bomb formation. Initially, magnetic flux elements, within a FOV co-spatial to high-resolution spectral observations collected by the IBIS instrument, were tracked within SDO/HMI data before two isolated, bi-polar MMFs were identified for further analysis. The co-aligned regions sampled in the Hα line wings were then visually inspected to confirm or deny the formation of any Hα brightening (comparable to Ellerman bombs). The evolution of both the SDO/HMI magnetograms and the co-spatial Hα blue wing are plotted in Fig. 6.3 and Fig. 6.5. The total magnetic flux strength of each of the opposite polarity regions were read-out from the YAFTA output and plotted through time (see the bottom left frames of Fig. 6.4 and Fig. 6.6) in order to interpret whether any cancellation was apparent. Both of the events analysed in this Chapter exhibited significant cancellation through their lifetimes, with each bi-pole being observable for little over one hour.

The Hα brightenings co-spatial to the MMFs had typical properties associated with Ellerman bombs, including excess emissions in the wings of the Hα

Event	Density (g km^{-3})	Height (km)	Radius (km)	Time (s)
Spicule	3×10^2	10000	250	3.3
Surge	5	39000	4000	54.4

Table 6.3: The estimated physical parameters of spicules (taken from Sterling 2000) and surges (estimates reported by, *e.g.*, Bong et al. 2014). The time required to provide the estimated mass to a cylindrical feature with the noted height and radius, given a flux of 6.5×10^{14} g hr^{-1}, is also included.

line profile, areas close to $1'' \times 1''$, and lifetimes on the order of minutes (see, for example, Georgoulis et al. 2002, Watanabe et al. 2011, Chapter 3). Both potential Ellerman bomb features exhibited obvious rise and fade phases (in terms of intensity and area), potentially corresponding to the upward propagation of material as presented in Chapter 5, with peaks of both quantities occurring after significant cancellation had already been measured (see the bottom right frames of Fig. 6.4 and Fig. 6.6). Interestingly, the peaks of both of these parameters for Cancelling Event '2' were co-temporal to the greatest measured cancellation (as plotted in Fig. 6.6). Determining whether the increased cancellation rate at that time contributed to the formation of the potential Ellerman bomb or not is beyond the capabilities of this dataset (due to the potential noise in the measurements) and would require a larger statistical sample from a higher-resolution instrument such as the SST/CRISP. Future work should aim to complete such a study.

The measured properties of each of the MMFs were then used as inputs in the magnetic reconnection model of Litvinenko (1999) in order that outputs testable against observations of Ellerman bombs could be found. Specifically of interest in this Thesis is the upward flow velocity at the site of the hypothesised reconnection which can be directly compared to the measurements obtained at the solar limb in the previous Chapter and in Nelson et al. (2015). The two features analysed here (Cancellation Events '1' and '2') resulted in upflow velocities of 5.6 km s^{-1} and 6.8 km s^{-1}, respectively, both of which are within one

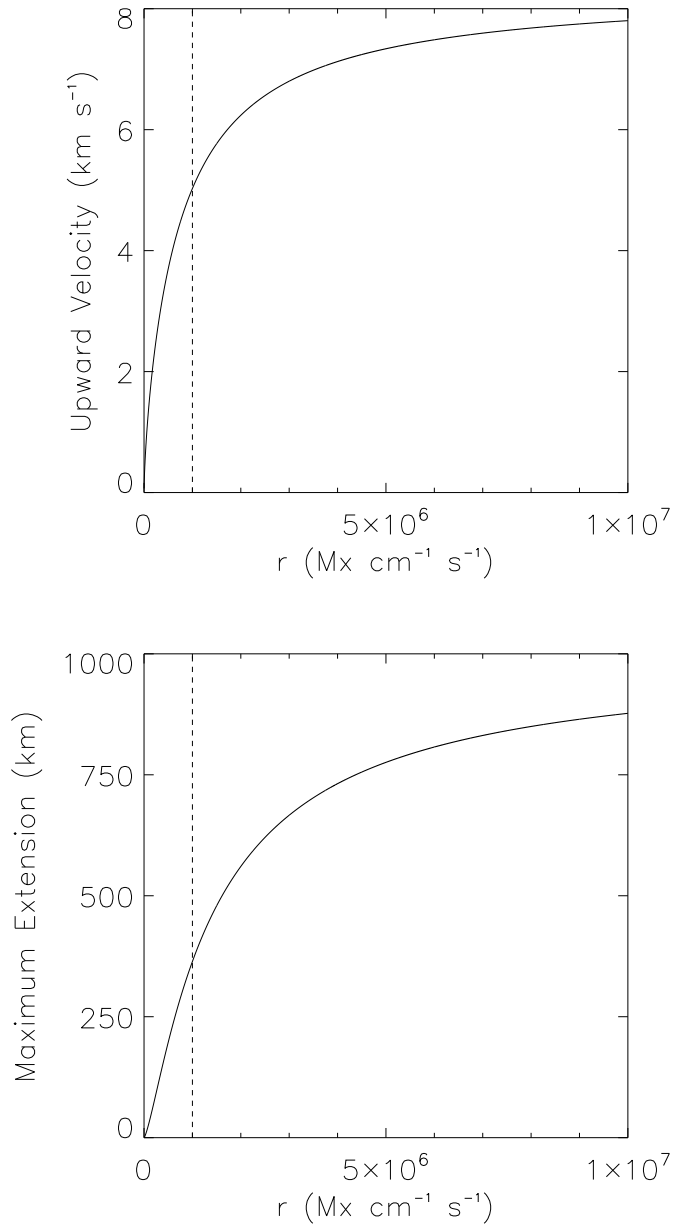

Figure 6.9: The upward velocity (top frame) and upward extension (bottom frame) as a function of r. It should be noted that even with extremely large values of r, the maximum upward extension does not exceed 1 Mm, unlike some Ellerman bombs. An r value of 10^6 Mx cm^{-1} s^{-1} is overlaid for reference.

standard deviation of the mean estimated in Nelson et al. (2015). The maximum upward extensions, estimated using the technique discussed by Takasao et al. (2013), were also calculated and gave values of 443 km and 670 km for the MMFs, respectively. The upward extension length predicted for Cancellation Event '2' is comparable to the mean value calculated in Chapter 5 (and by Watanabe et al. 2011, Nelson et al. 2015), however, the value estimated for Cancellation Event '1' is towards the lower limit of heights previously found for Ellerman bombs. A larger statistical sample of such features will be analysed in future work and included in the article based on this Chapter.

As well as the measured cancellation rates discussed here, it is also possible to analyse the influence of a range of r values on quantities of interest. In Fig. 6.9, the upward velocity (top frame) and the maximum extension (bottom frame) are plotted for r values ranging from zero to 10^7 Mx cm^{-1} s^{-1}. It is immediately evident that both quantities increase smoothly throughout this range, with a decreasing gradient at higher r values. Values of r exceeding 10^6 Mx cm^{-1} s^{-1} appear to return comparable lengths and velocities to the majority of Ellerman bomb events. However, it can be observed that the maximum upward velocity and maximum extension length do not exceed 10 km s^{-1} and 1000 km, respectively, within a realistic range of r values (as quoted in the literature and previously in this Chapter). As neither of these predictions are greater than the largest observed upward velocities and extension lengths (by, for example, Watanabe et al. 2011, Nelson et al. 2015), it would be of interest in future work to understand the role of the initial VAL-C model in limiting these quantities. It is possible that a background model taken from a plage region would increase these outputs and exceed Ellerman bomb measurements allowing a maximum r value to be suggested.

In addition to the upward extensions and velocities, the estimated magnetic field strengths from this model are comparable to the strengths of the MMFs as measured by the SDO/HMI magnetograms (of the order 10^2 G). Calculating the magnetic energy within the current sheet at the start of the cancellation period

also allowed a potential energy release rate to be estimated. The properties of both MMFs returned values of the order 10^{26} ergs, giving cancellation rates of around 3×10^{22} ergs s^{-1}. By assuming a lifetime of 10 minutes for the potential Ellerman bombs co-spatial to these MMFs would allow around 2×10^{25} ergs to be released during their existance. This value is on the upper limit of those presented in Chapter 3 and on the lower limit of those discussed by Georgoulis et al. (2002) and in the wider literature. It would be interesting to assess how this energy release rate changes with larger cancellation rates. Overall, this model appears to accurately return the properties of Ellerman bombs as detailed by the literature, providing further evidence that the hypothesis of photospheric magnetic reconnection as a driver for these events could hold.

It is important, however, to acknowledge two of the issues which constrict this analysis. Firstly, the observed cancellation could, instead of the hypothesised magnetic reconnection, be formed by another process, such as flux submergence, potentially limiting the usefulness of this research. Secondly, the basic nature of the analytical model applied here certainly over-simplifies any reconnection which might exist. However, a number of other researches have exploited this model, returning reasonable upward mass fluxes and filling times for phenomena such as filaments (Litvinenko and Martin 1999, Litvinenko et al. 2007), implying that there could be some usefulness to analysis as presented in this Chapter. It is important to further this research in the future, potentially by combining the methods presented here with realistic numerical simulations (similar to the method applied in Chapter 4).

With the limitations of this model considered, it is now of interest to put into context the estimates of the mass flux given by this model. In Table 6.3, the densities and physical basic parameters of both spicules (see, Sterling 2000) and surges (from Bong et al. 2014) are included. Using these parameters, and assuming a cylindrical feature with volume equal to $\pi r^2 h$ (where r and h are the radius and height of the event, respectively), it is possible to calculate the time (right hand column) which would be required to provide enough mass

given an upward mass flux of 6.5×10^{14} g hr^{-1}. The times of 3.3 seconds and 54.4 seconds for spicules and surges, respectively, are relatively small compared to the observed formation times of these events. Indeed, if the kinetic energy is taken as $E_{\rm kin} = \frac{1}{2}mv^2$ and the mass moved every second is constant (at 1.81×10^{11} g s^{-1}) with a velocity of 5600 m s^{-1} (the same as predicted for Cancellation Event '1'), a required kinetic energy of 2.83×10^{22} ergs s^{-1} would be required. This value is only 0.01 ergs s^{-1} lower than the estimated energy release rate for this MMF. It is interesting, however, that this model does not exclude the possibility that cancellation co-spatial to Ellerman bombs could also drive surges.

It is important to note, though, that the underlying processes which lead to surge formation are currently unknown and, hence, cancellation in the photosphere may not be of direct (but may be of indirect) importance for driving these events. Some authors have suggested that photospheric reconnection, for example, at the sites of Ellerman bombs in ARs could lead to the propagation of a shock wave upwards towards the chromosphere, raising the chromospheric canopy to heights comparable to surges (see, for example, Suematsu et al. 1982, Shibata et al. 1982, Takasao et al. 2013). In this scenario, it is not mass ejection from the reconnection site as encompassed by the model analysed in this Chapter which leads to the outflow. Therefore, due to the limitations of this model, we do not firmly rely on the mass out-flows calculated here, nor the estimated energies required to drive these surges. It is important that future high-resolution observations be compared to numerical simulations which include accurate diagnostics of both the photosphere and the chromosphere in order to fully understand the physics associated with the potential link between these events.

The apparently sporadic relationship between Ellerman bombs, surges, and MMFs is both confusing and intriguing. Within the literature, numerous authors have discussed the potential relationship between Ellerman bombs and surges (see, for example, Rust 1968, Roy 1973, Madjarska et al. 2009), how-

ever, numerous datasets have also been analysed showing no link between these features (such as all data analysed in this thesis). Whether specific conditions must be achieved within a multi-stage process for an Ellerman bomb to drive a surge or whether these events are unrelated other than by an occasional co-spatial occurrence is still to be understood. In a recent article, Filippov et al. (2007) suggested that a rapid increase in the strength of a bi-polar region (up to a factor of 25) would be required within 5 minutes in order for a surge to form. The two MMF events analysed in this Chapter neither show such rapid increase in flux quantity over a short amount of time, nor a link to a surge. Combining the techniques employed to conduct this research with a larger sample size of Ellerman bomb-MMF pairs to fully understand whether some correlation between rapid growth of bi-poles and the co-spatial formation of Ellerman bombs and surges exists would be of great interest to the community.

Chapter 7

Relationship between an Hα Surge and an EUV Brightening

7.1 Overview

In the previous Chapters of this thesis, high-resolution ground- (*e.g.*, from the DST) and space-based (for example, from the SDO satellite) data have been analysed with the specific aim of furthering the knowledge of the community about the Ellerman bomb phenomena. In this Chapter, however, the focus of study is shifted. During observations of a plage region (collected by the DST/IBIS instrument) trailing a sunspot in AR 11579, a small-scale surge (discussed by, *e.g.*, Roy 1973, Roy and Leparskas 1973) was apparent within the Hα line wings. This feature first evolved in the blue wing before fading and appearing in the red wing, potentially indicating, if the decreased emission at these wavelengths is a result of motions or Doppler shifts, the tip of the feature followed a parabolic evolution profile (similar to the path of a ball during flight after being thrown). In order to analyse this feature, the DST/IBIS observations were combined with data sampled by both the SDO/HMI and SDO/AIA instruments in order to infer information about the photospheric line-of-sight magnetic field and the coronal response to the surge. This research is of inter-

est due to the potential link between the blinker phenomena (see, for example, Harrison 1997) and surges as discussed by Subramanian et al. (2012). This hypothesis was considered to be one of the two most likely formation mechanisms of blinkers (with the other comprising transition region dynamical motions).

This Chapter will be structured as follows: In Section 2, the observations analysed will be set out. Section 3 will detail the data analysis conducted on the isolated surge event, including analysing small-scale structuring and influence on the upper solar atmosphere, before a discussion of this research is presented in Section 4. Credit: **C. J. Nelson** & J. G. Doyle, 'Excitation of an outflow from the lower solar atmopshere and a co-temporal EUV transient brightening', *Astronomy & Astrophysics, Volume 560 (2013), Page A31*, reproduced with permission,

7.2 Observations

The data analysed in this Chapter include ground-based observations collected using the DST/IBIS instrument during a period of good seeing on the 30th September 2012 between 17:22 UT and 17:37 UT. A total of 377 images in both the blue and red wings of the Hα line profile (each comprising of the speckle, see Wöger et al. 2008, output from 10 input frames) with spectral positions at approximately $\pm$0.8 Å from the line core were sampled. The FOV of these data was centred on a large plage region trailing AR 11579, with co-ordinates of x_c=10″, y_c=−225″, with respect to the disc centre. After reduction of these data, each science-ready image had a cadence of 2.4 seconds with pixel sizes of around 0.097″. This FOV was selected for observations as it contained a small, dynamic pore (as well as obvious network structuring that was later found to be co-spatial with a uni-polar region of magnetic flux). The large-scale structuring of this plage region remained relatively stable throughout these observations.

Space-borne data from both the SDO/AIA and SDO/HMI instruments are also analysed in this Chapter. As was discussed in Chapter 2, the 1700 Å

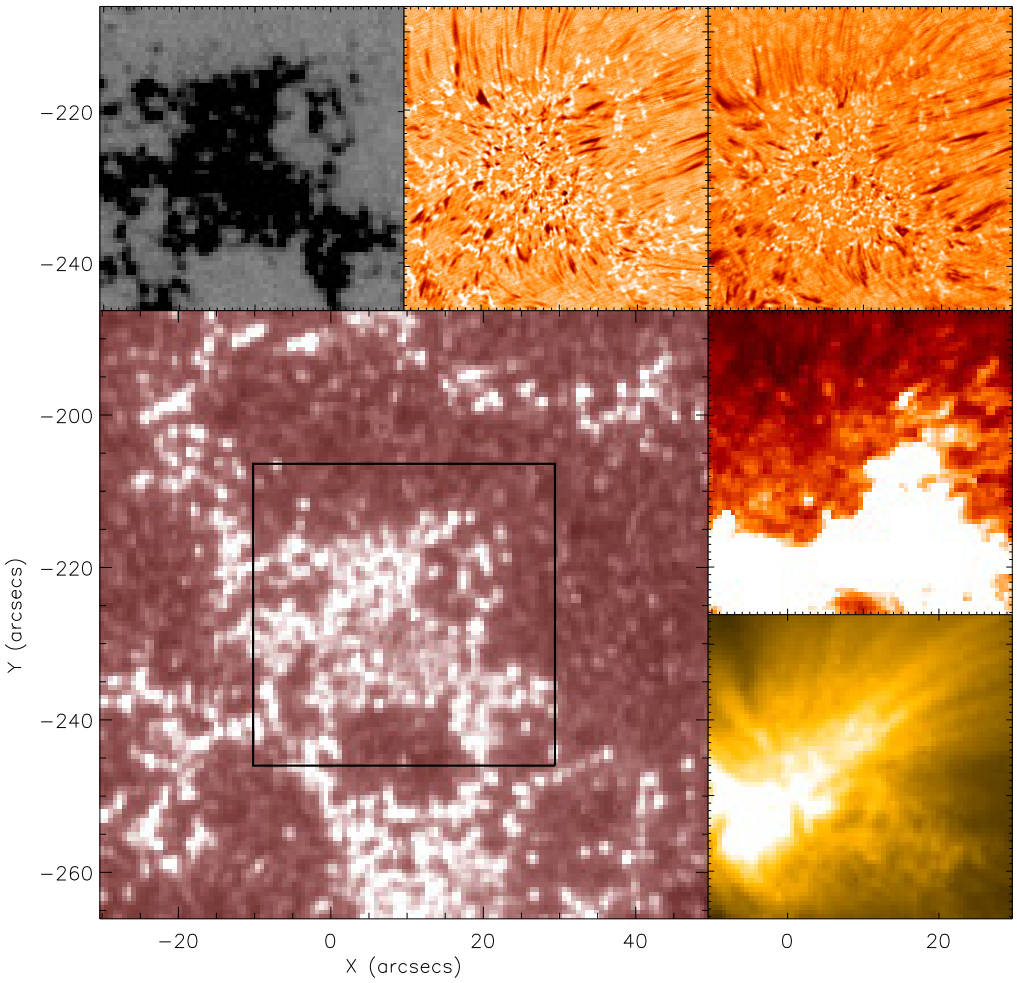

Figure 7.1: Snapshot of data analysed within this Chapter sampled at the closest frame to 17:24 UT for each instrument. Data from the SDO/AIA 1700 Å filter (bottom left frame) depict the entire FOV of these observations. The black box outlines the zoomed FOV considered in this Chapter and plotted in the remaining frames. Clockwise from the top left frame, these images consist of: An SDO/HMI magnetogram; a DST/IBIS Hα blue wing image; a DST/IBIS Hα red wing image; the SDO/AIA 304 Å filter; and the SDO/AIA 171 Å filter.

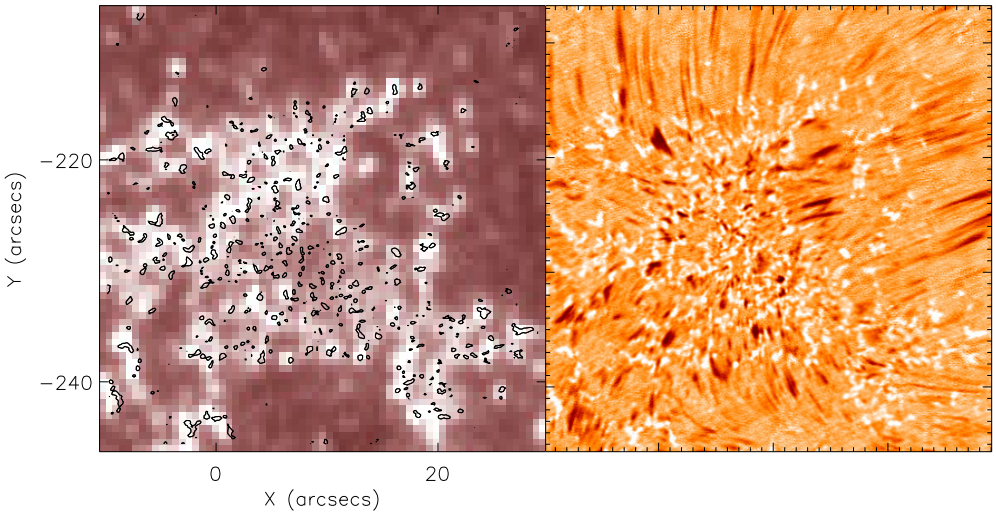

Figure 7.2: The zoomed FOV indicated in Fig. 7.1 for both the 1700 Å SDO/AIA filter (left hand frame) and a DST/IBIS blue wing image (right hand frame). The contours overlaid on the left hand frame outline the bright NBPs visible in the Hα blue wing, accurately mapping SDO/AIA 1700 Å bright points. This technique is used to confirm the co-alignment between these instruments, as well as the SDO/HMI data.

SDO/AIA wavelength has a cadence of 24 seconds, whereas all other SDO/AIA filters have a cadence of 12 seconds. The pixel size of data collected by the SDO/AIA instrument is 0.6″. The use of the SDO/HMI instrument also allows for line-of-sight photospheric magnetic-field inferences. These data have a pixel size of 0.5″ and a cadence of 45 seconds. Finally, each SDO/AIA and SDO/HMI was cropped, aligned, and de-rotated to follow the DST/IBIS FOV through time. In Fig. 7.1, the bottom left panel plots the total FOV of these data as observed by the SDO/AIA 1700 Å filter. A black box in this frame depicts the FOV of the other panels in Fig. 7.1 which, clockwise from top left, plot: The photospheric line-of-sight magnetic field inferred by SDO/HMI; the Hα blue wing; the Hα red wing; the SDO/AIA 304 Å filter; and the SDO/AIA 171 Å filter. Each image was sampled at approximately 15:24 UT.

To facilitate the research presented in this Chapter, bright points observed in the 1700 Å photospheric continuum are used to align the instruments, before the co-spatial nature of all SDO/AIA wavelengths is exploited to align the transition region and coronal filters. In Fig. 7.2, the zoomed FOV outlined by the black box in Fig. 7.1 is plotted for both the SDO/AIA 1700 Å filter (left hand frame) and the Hα blue wing (right hand frame). Black contours in the left hand frame outline the NBPs evident in the right hand frame confirming the accuracy of the co-alignment of these data. As the aim of this Chapter is to consider the influence of the surge event from the lower atmosphere on the SDO/AIA coronal filters, such an accurate co-alignment is important to negate the return of spurious results.

7.3 Data Analysis

7.3.1 Evolution within the Hα Wings

The event studied in this Chapter was first observed in the Hα blue wing as a medium-sized ejection emanating from the edge of a large region of network (indicated by the white arrow in Fig. 7.3). In Fig. 7.4, the evolution of this event

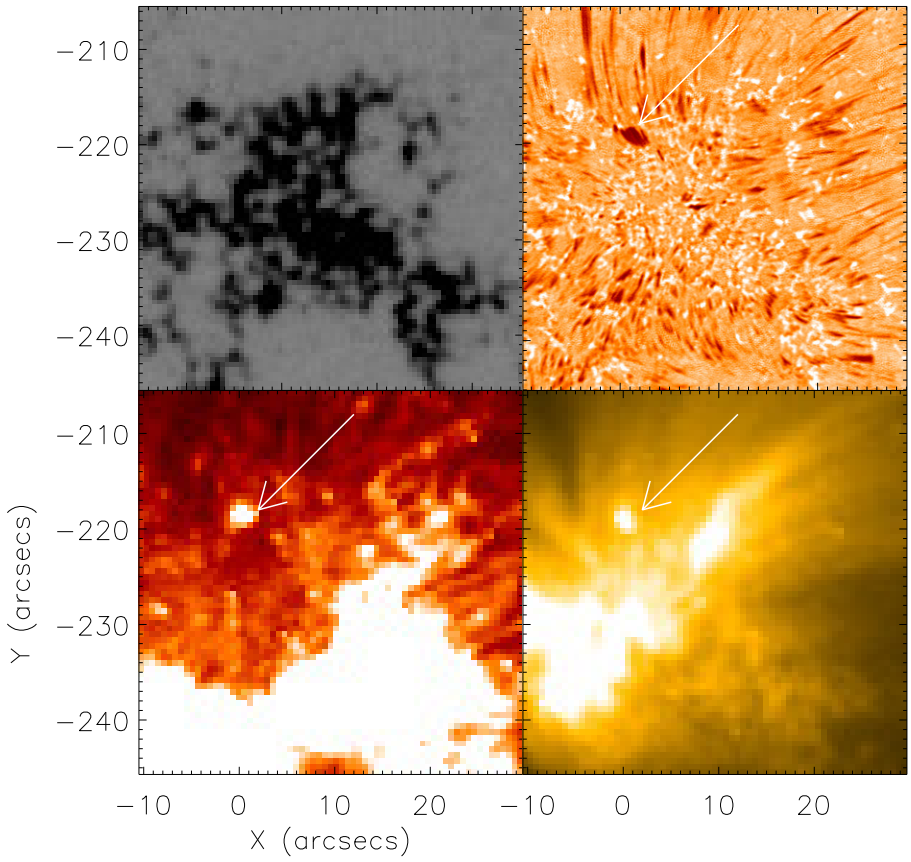

Figure 7.3: Data sampled at the closest frame to 17:30:01 UT for each instrument highlighting the surge-bright point pair analysed in this Chapter. Clockwise from the top left image, the vertical magnetic field inferred by the SDO/HMI instrument, a DST/IBIS Hα blue wing image, the SDO/AIA 171 Å filter, and the SDO/AIA 304 Å filter. The arrow plotted in all but the top left panel indicates the event discussed in this Chapter.

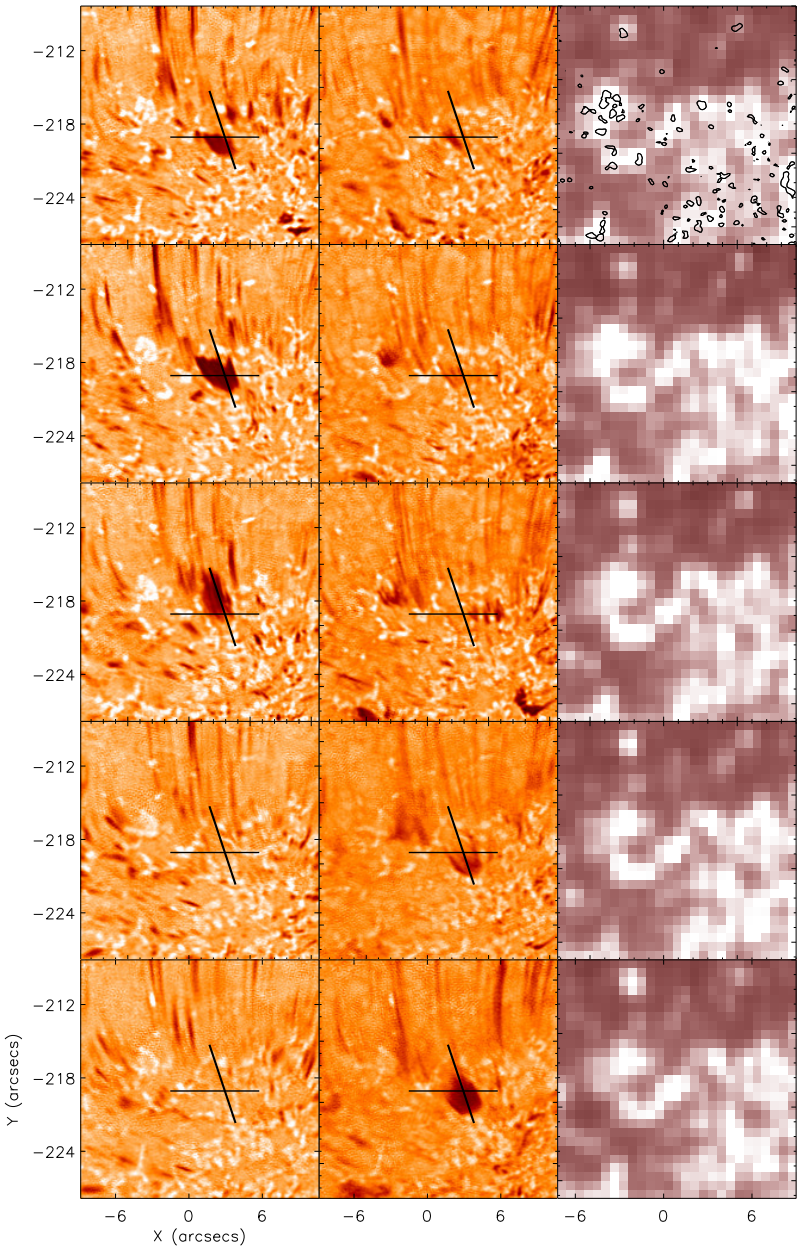

Figure 7.4: The temporal evolution of this feature in the blue wing (left column), red wing (middle column), and SDO/AIA 1700 Å (right column). The top row was sampled at 17:29:42 UT and each subsequent row was separated by 70 seconds. The alignment of these data is confirmed with the contours on the initial SDO/AIA image. The black lines in the Hα images plot the slits used to produce Fig. 7.5 and Fig. 7.6 (with the horizontal line corresponding to Fig. 7.6).

through time for the blue (left hand column) and the red (middle column) wings of the Hα line are plotted where each column is separated by approximately 70 seconds. The right hand column plots co-spatial, co-temporal SDO/AIA 1700 Å data. If one were to consider the observed absorption in the Hα line wings in terms of motions, an apparent parabolic shape of the event would be evident. Strong absorption firstly occurs in the blue wing, indicating an upward motion of the plasma, before this fades and reappears in the red wing, hinting at a downflow. Although these data only cover a period of 15 minutes, the full evolution of the event in the blue wing is observable; however, absorption in red wing data still covers a significant area in the final frame. Estimating the lifetime in the red wing to be comparable to the lifetime in the blue wing, it is possible to infer a total lifetime of around 10 minutes. In order to assert whether the continued absorption past the final frame of these data could influence the results discussed in this Chapter, emissions in the SDO/AIA lines were visually inspected. It was found that the signatures of this event in SDO/AIA data had diminished well before the end of these DST/IBIS data and, therefore, assumed that the lack of photospheric sampling of the end of this event would not interfere with any conclusions regarding the coupling of this feature to the upper-atmosphere.

The apparent morphology of this event, in the Hα blue wing, shows rapid changes in both length and width over time. The event begins as a small number of fine threads, analogous to the near ubiquitous fibrils observed at the right of the FOV in Fig. 7.2, being emitted from co-spatial footpoints before a small 'blob' is formed (around 1″ by 1″ in area) as seen in the initial frame of Fig. 7.4. This 'blob' then expands in width and length to nearly 4″ by 4″ at its peak, before the absorption reduces. Interestingly, once the event reaches a peak length, it appears to propagate away from its footpoint, as can be observed in the third Hα blue wing frame in Fig. 7.4, suggesting an ejection of a finite amount of mass away from a potential source over time. The black lines over-plotted on the IBIS line wing images in Fig. 7.4 indicate the axis parallel to the

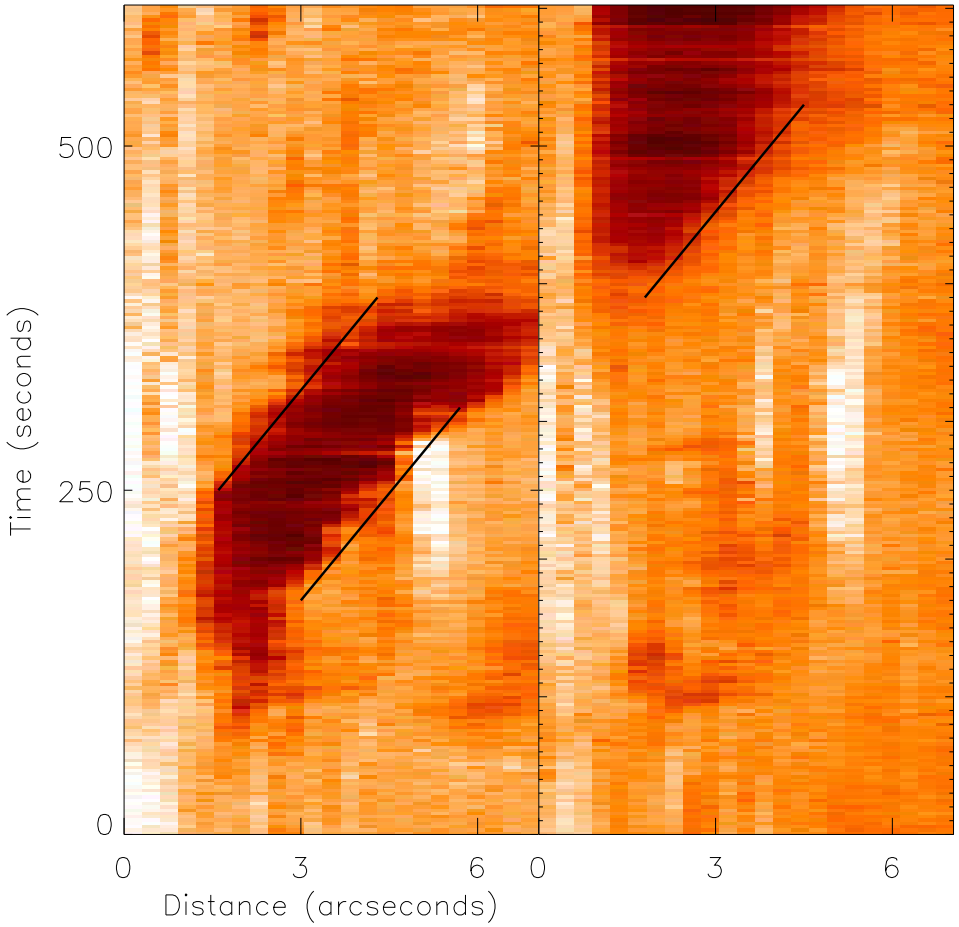

Figure 7.5: Two distance-time diagrams depicting the morphology of the event analysed in this Chapter along a slit parallel to the apparent propagation of material for the Hα blue wing (left frame) and red wing (right frame). The overlaid black lines indicate the gradient of the motion and, hence, the apparent speed within the Hα line wings. The slit position is shown in Fig. 7.4 (as the near vertical black line).

direction of propagation of this surge and a representative cross-cut analysed in the following sections of this Chapter.

In Fig. 7.5, two time-distance diagrams for the slit taken parallel to the axis of propagation in Fig. 7.4 are plotted for both wings of the Hα line. Over time, absorption in the blue wing (left hand panel) is observed to propagate outwards from a footpoint at a steady speed (indicated by the lower black line), estimated to be around 14 km s^{-1}, which is slightly higher than the sound speed in the photosphere and lower chromosphere (estimated by Judge and Peter 1998). It is interesting to note that as the absorption feature fades away from the footpoint, approximately the same speed can be measured (indicated by the upper black line). Following the end of the absorption in the Hα blue wing, the intensity lowers in the red wing. Interestingly, this absorption appears to fill with a similar speed to the blue wing. The vertical component of any motion would be required to calculate an accurate total velocity for this event. Using basic trigonometry, however, it is possible to calculate estimates of the total velocity. For example, a 30° angle of propagation would be required for an increase to a total velocity of 16 km s^{-1}. Larger angles such as 60° or 85° would lead to velocities of 28 km s^{-1} and 163 km s^{-1}, respectively (which is within the range measured by Roy and Leparskas 1973).

7.3.2 Small-Scale Structuring

Throughout the lifetime of this event, as depicted in Fig. 7.4, small thread-like structures can be observed within the larger 'blob'. These threads are reminiscent of the common fibrils which are easily seen in Fig. 7.2, however, their apparent length is shorter. Unfortunately, it is impossible to infer whether the difference in length is a morphological trait or a line-of-sight issue and, therefore, it is not discussed further. In Fig. 7.6, a time-distance plot taken for a co-spatial slit in the blue (left) and red (right) wings of the Hα line is presented to highlight the existence of small-scale structures across the event. Each time-distance diagram is calculated for the slit perpendicular to the propagation of

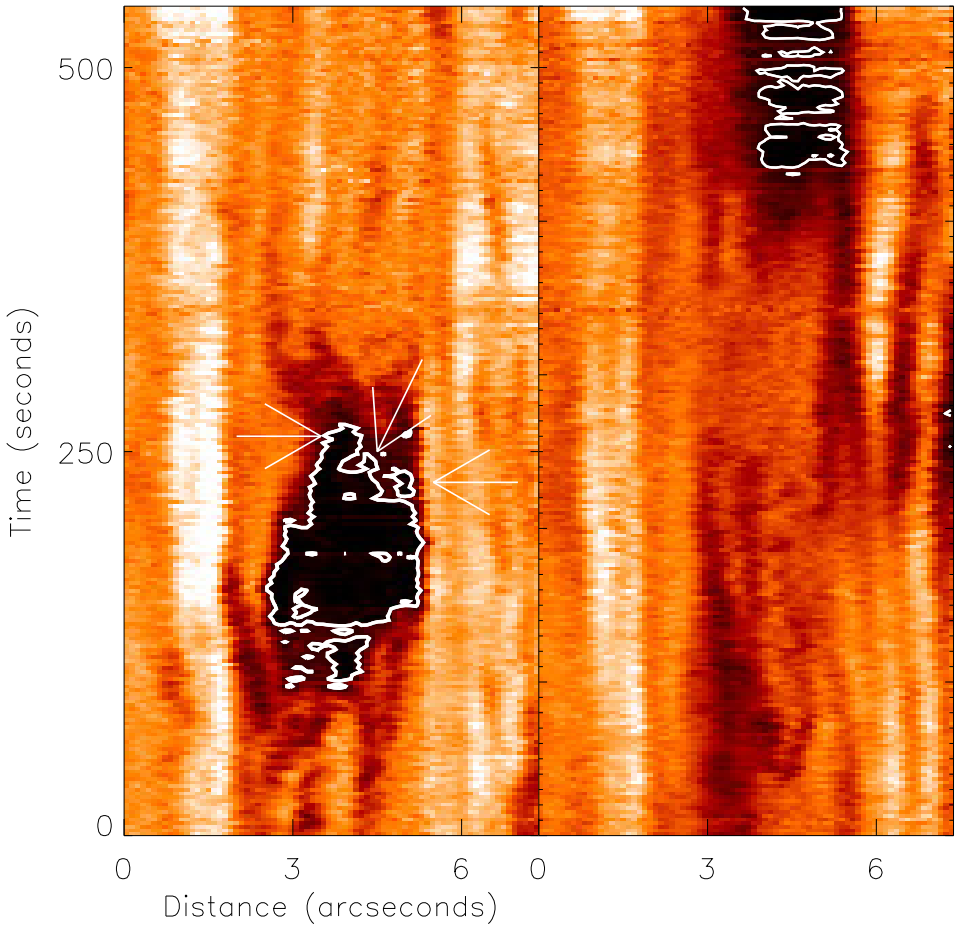

Figure 7.6: Two time-distance diagrams sampled using the slit perpendicular to the surge event in Fig. 7.4 for the Hα blue wing (left hand panel) and red wing (right hand panel). The white contours in both panels outline the small-scale structuring apparent within this event. For example, three individual 'fingers' of this surge are highlighted using white arrows.

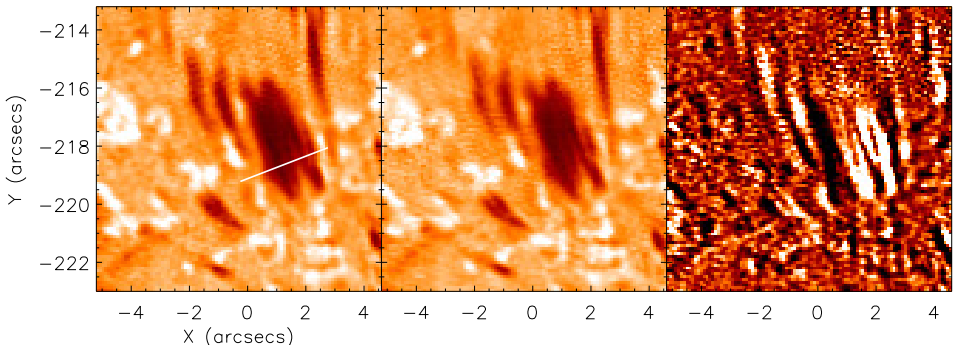

Figure 7.7: Evolution of the event analysed in this Chapter through time highlighting the fine structured nature of this event. (Left frame) Hα blue wing emission at 17:32:25 UT ; the white line indicates the slit selected for analysis in Fig. 7.6. (Centre frame) The Hα blue wing emission at 17:32:27 UT (*i.e.*, the consecutive frame). (Right frame) Difference image between the frames depicting the multiple fine structures within this event.

the 'blob' in Fig. 7.4 through time.

The white contours in Fig. 7.6 outline several small-scale structures within the larger-scale surge. To further highlight these smaller structures, difference images were analysed frame-by-frame. A running difference technique, whereby $Diff[x, y, t + 1] = Frame[x, y, t + 1] - Frame[x, y, t]$, was implemented to identify changes in intensity between consecutive frames. In Fig. 7.7, a representative example of the output of such an analysis is plotted. Within the imaging data, it is difficult to see the rapid changes in intensity between the individual fibril events through time, however, the difference image clearly shows the existence of the small-scale structures within the larger-scale 'blob'. The lifetimes and evolutions of these structures are similar to those observed for Type I spicules, however, these properties do not discount either p-mode buffeting (De Pontieu et al. 2004) or magnetic reconnection (Yokoyama and Shibata 1996) as the driver of this surge.

7.3.3 Links to the Photospheric Magnetic Field

The relationship between surges and strong, vertical photospheric magnetic fields has been well documented in recent years (see, for example, Roy and Leparskas 1973, Madjarska et al. 2009, Kayshap et al. 2013). As has been discussed in previous Chapters of this thesis, Ellerman bombs are sometimes observed at the footpoints of surges and have been interpreted as potential evidence of magnetic reconnection co-spatial to the apparent footpoint of these events (for example, Roy 1973). More recently, links between surges and flux cancellation within an AR have been presented (by, for example Chae et al. 1999, Brooks et al. 2007, Chen et al. 2009) who suggested that the observed reduction in magnetic field was evidence supporting reconnection as a driver for the ejection of plasma from the lower chromosphere.

The surge identified in this Chapter, however, forms co-spatially with a large uni-polar plage region (as is easily seen in the top left frame of Fig. 7.1 and Fig. 7.3). The large-scale magnetic field within this FOV appears to be stable throughout the course of these data, providing no evidence of flux emergence or cancellation co-spatial to the surge. Indeed, these data depict a constant magnetic field structure through time. Despite small-scale restructuring of the magnetic field within the plage region that is co-temporal to the beginning of the absorption feature, it is difficult to quantify how much influence, if any, this has on the ejection.

Therefore, the magnetic evolution of this FOV over the course of a two-hour period surrounding the data was analysed to infer whether large-scale morphological changes occurred before the surge. These data confirmed that no observed bi-polar fields interact to form this event and that only small-scale restructuring occurs within the large uni-polar plage region. No evidence of magnetic cancellation, or reconnection, leading to the formation of this event is found. It should be noted that although there are few dynamic changes within this FOV, complexity of the magnetic field can be inferred through the number and frequency of network bright points, which are often used as a proxy

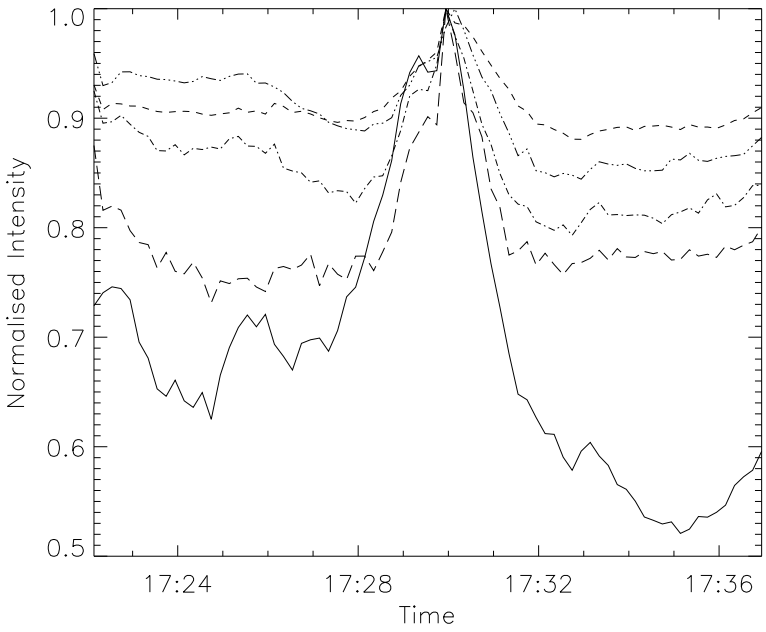

Figure 7.8: Lightcurves showing the evolution of the intensity recorded by a sample of SDO/AIA filters (sampling the upper-atmosphere) during the course of this event. From the bottom to the top on the left hand side of the image, the SDO/AIA 304 Å (solid line), 131 Å (long-dashed), 211 Å (dot-dashed), 171 Å (short-dashed), and 193 Å (dot-dot-dot-dashed) filters are plotted.

for the vertical magnetic field (see, *e.g.*, Leenaarts et al. 2006, Rutten et al. 2013). It is, therefore, possible that magnetic structuring on scales smaller than those currently resolvable using the SDO/HMI instrument is occuring during this period, leading to reconnection of complex topologies. However, no such evidence is apparent in the data analysed here.

7.3.4 Signatures in the Transition Region and Corona

The final Section within this Chapter assesses the apparent influence this event has on the upper atmosphere through an analysis of the SDO/AIA EUV filters.

It can be easily inferred from Fig. 7.3, that a co-spatial brightening event exists within the AIA 304 Å and 171 Å filters during a period of strong absorption within the Hα blue wing. Within the 304 Å filter, the peak area of this brightening is approximately 4″ by 4″, consistent with the area of a small blinker event (as discussed by, *e.g.*, Chae et al. 2000, Parnell et al. 2002, Madjarska and Doyle 2003) and the area of the event in the IBIS data. It is, therefore, considered that this event is a blinker in the upper-atmosphere.

The evolution of the area of this brightening within the 304 Å filter is roughly parabolic, showing a steady rise to the peak area, before dropping off once again to the background intensity. This parabolic evolution is also apparent within all other SDO/AIA upper atmospheric filters co-temporally, implying that this brightening is formed as a result of increased density or filling factor in the transition region and corona (as has been suggested in previous researches by, *e.g.*, Priest et al. 2002, Subramanian et al. 2012). Therefore, the research presented in the previous sections of this Chapter could relate to the supply of mass from the lower atmosphere into the upper atmosphere. Due to the small-scale structuring observed within this event, an open question which is not answered by this Chapter is posed (in addition to the question of what causes the surge initially): Do smaller fibril structures which are observed within the line wings have a similar, albeit smaller, influence on the upper atmosphere? This question could potentially be solved in the future through analysis of co-spatial ground-based data and the higher resolution (with respect to the SDO/AIA instrument) data available from the IRIS satellite.

The temporal evolution of the intensity of this event is plotted in Fig. 7.8 for a number of SDO/AIA filters. A 7″ by 6″ box was selected around this small-scale blinker such that no other localized brightening events occurred within the FOV during this period. The average intensity of this box was then calculated for each frame during these observations and plotted for each of five EUV SDO/AIA filters (from bottom to top in the original frame: 304 Å; 131 Å; 211 Å; 171 Å; and 193 Å). The localized brightening event occurs

for approximately four minutes. It is interesting, and worthy of future study, to understand whether the lifetime and area of this event (which are both on the lower limit of statistics of blinkers as discussed in the literature by, for example, Madjarska and Doyle 2003) are related to the size of the original ejection observed within the Hα line wings.

It is worthy to note, that the original brightening in the SDO/AIA filters occurs co-temporally with the initial stages of the formation of the Hα event (similar to the numerical results of Yokoyama and Shibata 1996), before fading entirely whilst there is still strong absorption in the blue wing. In Fig. 7.9, a visualization of this process is depicted. The second frame of Fig. 7.9 highlights the delay of absorption in the Hα blue wing. Only the initial stages of development within the Hα blue wing are observed in this column compared to the near peak emission in the SDO/AIA 304 Å data. One possible reason for the time lag within these data could be that only one specific spectral position in each wing within the Hα line is observed and that, therefore, only a snapshot of the whole physical process which is occurring is sampled. If full Hα line scan data were available to analyse during this event, a better picture of the observed coupling may have been inferred. The evidence that this strong absorption feature in the Hα line wings is intrinsically linked to the possible blinker event observed within the SDO/AIA images is intriguing and will be discussed further in the final Discussion section of this Chapter.

7.4 Discussion

In a recent article, Subramanian et al. (2012) suggested two possible formation mechanisms for blinkers, namely the injection of plasma from the chromosphere or transition region dynamics (such as flows in existing loop structures). The research presented in this Chapter offers the first evidence that at least a sub-set of the transition region brightenings known as blinkers are formed due to an in-flux of mass from the lower solar atmosphere. It remains to be seen, however,

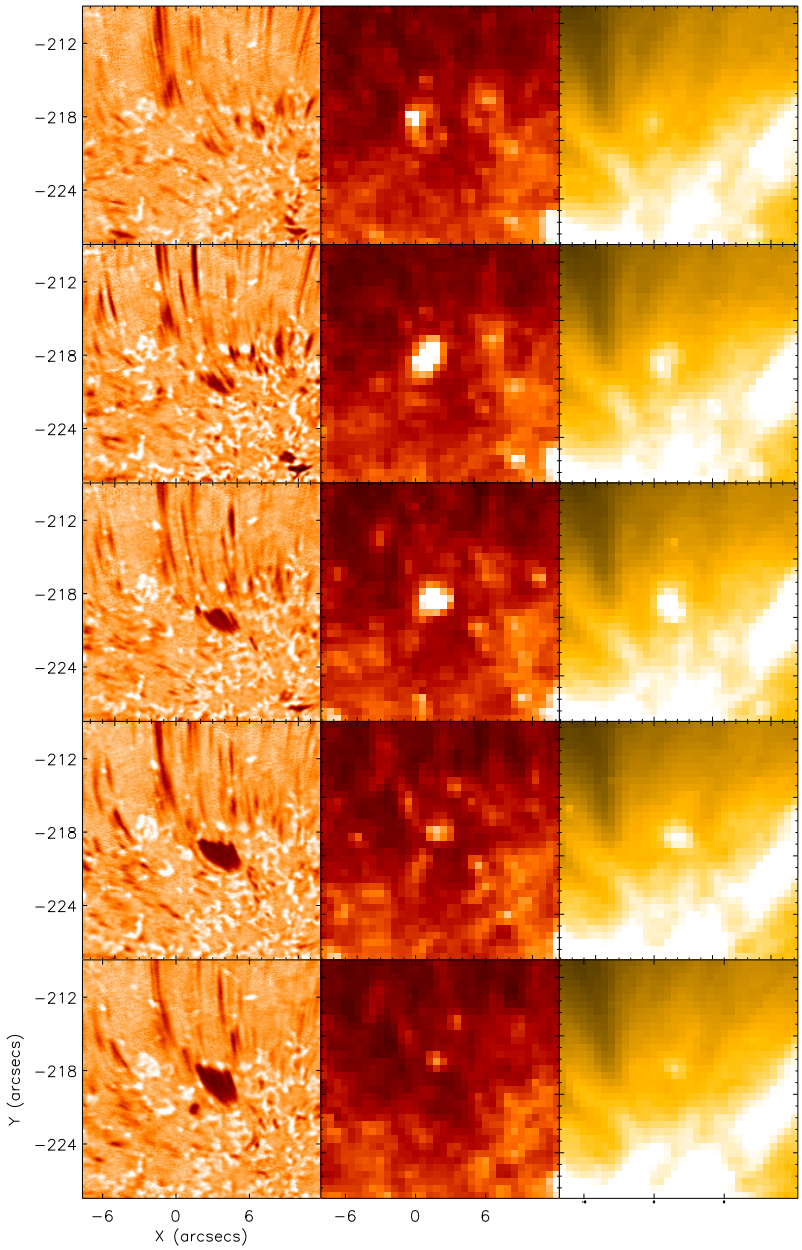

Figure 7.9: The evolution of the event analysed in this Chapter in the Hα blue wing (left hand column) and the SDO/AIA 304 Å (middle column) and 171 Å (right hand column) filters. The difference between each frame is approximately 48 seconds (starting at 17:28:26 UT and ending at 17:31:37 UT). The temporal difference between each wavelength in an individual row is below 10 seconds.

what quantity of blinkers are formed in this way. Doyle et al. (2004) discussed blinker phenomena being associated with brightenings in pre-existing coronal loops. The observed features appeared to occur during the emergence of magnetic flux into the photosphere which, it was hypothesised, caused interchange reconnection in the loops. The temperature interfaces (created by the reconnection process) between the cool plasma of the newly emerging loop and the hot plasma of the existing loop was believed to cause the observed activity. Doyle et al. (2004) suggested that the temperature interfaces propagated with the characteristic speed of a conduction front, heating up the cool chromospheric plasma to coronal temperatures and increasing the volume and brightening to transition region temperatures.

In a more recent study, Subramanian et al. (2012) classified blinkers into two categories, one associated with coronal counterparts and the other with no coronal counterparts. Around two-thirds of the blinkers showed coronal counterparts and corresponded to various events like EUV/X-ray jets, brightenings in coronal bright points, or foot-point brightenings of larger loops. The present event fits into those showing a coronal component and matches the slow-shock model presented by Yokoyama and Shibata (1996) suggesting that magnetic reconnection in the photosphere may be the driver of this event. However, it should be noted that no evidence of magnetic reconnection was evident in SDO/HMI data and this blinker did not occur co-spatially with any apparent loop structures in SDO/AIA data. These results are, therefore, inconclusive (which is unsurprising given the analysis of a single event) with respect to discovering a general formation mechanism of all blinkers.

Overall, it can be suggested that the brightening observed within these SDO/AIA data is analogous to a blinker. Although the spatial and temporal scales of this event are on the lower limit of previously observed blinkers (such as those observed by, for example, Harrison 1997, Harrison et al. 1999, Bewsher et al. 2002), either the improved spatial and temporal resolutions of the data used within this Chapter or the fact that this is potentially a single,

relatively weak event may account for this. Combining this result with the large absorption feature within the Hα line wings, interpreted as an on-disc surge, presents additional evidence that at least a sub-set of transient brightening features within the transition region and corona are linked to mass supply from the lower atmosphere (as was suggested by Priest et al. 2002). Due to the co-temporal reaction of the Hα line wings and the EUV filters, it is possible that the increased filling factor in the upper atmosphere is caused by a slow shock, propagating away from a reconnection site in the lower atmosphere, analogous to the process described by Yokoyama and Shibata (1996). However, the final picture is inconclusive and, therefore, no strong assertions should be made about the formation mechanism of the surge itself.

Chapter 8

Conclusions and Future Work

8.1 Overview of this Thesis

This thesis contains research into small-scale dynamics in the lower solar atmosphere, specifically with respect to the Ellerman bomb phenomenon. High-resolution, high-cadence ground-based Hα data have been studied in each Chapter, often supplemented by measurements of the photospheric line-of-sight magnetic field and upper atmospheric intensity. The majority of the work conducted here, has focused on understanding the formation mechanism responsible for Ellerman bombs (hypothesised to be magnetic reconnection by authors such as Georgoulis et al. 2002, Pariat et al. 2004, Watanabe et al. 2011). Largely, the aims of this thesis have been achieved through observational data analysis; however, comparisons with state-of-the-art simulations and novel analytical models have also been conducted.

8.2 Summary of Results

8.2.1 Statistical Analysis of Ellerman Bombs

In Chapter 3, the possibility that small-scale brightenings close to the spatial resolution of the DST/IBIS instrument are related to the Ellerman bomb phenomena was explored. An automated detection algorithm was applied to 90 minutes of Hα line profile and speckle data collected on the 18th November 2010, selecting regions with brightness over 130 % of the average background intensity (the same threshold value applied by Georgoulis et al. 2002). This algorithm was tested by isolating features with spatial scales over $0.64''^2$ (which is close to the capabilities of the Flare Genesis Experiment) and then comparing basic statistics of these events to Ellerman bombs within the literature. An average lifetime of this null set of events was found to be 7.2 minutes. Due to the proximity of this value to other estimates of Ellerman bomb lifetimes (including Kurokawa et al. 1982, Zachariadis et al. 1987, Watanabe et al. 2011), it was concluded that the selection criteria of the algorithm were suitable.

Overall, 3570 features were selected by the algorithm within these data. Many of these events were short-lived, with the average lifetime being close to 2.6 minutes, with many of these brightening events having lifetimes below 2 minutes. It is interesting to note, that many of these features appeared and disappeared within 3.5 minutes, which was the cadence of the Flare Genesis Experiment (discussed by Georgoulis et al. 2002, Pariat et al. 2004). In addition to these short lifetimes, the average area of these features was measured to be $0.11''^2$ (comparable to a 240 km to 240 km box) indicating that small-scale structuring can occur on scales close to the spatial resolution of the DST/IBIS instrument. It remains to be seen how many of these small features are Ellerman bombs, however, it can not be discounted that structuring is occurring below the spatial resolution of these data (similar to the discussions of De Wijn et al. 2009). The behaviour of such small-scale features could provide further exciting opportunities for research in the coming years.

The energetics of the selected features was also discussed. A technique described by Georgoulis et al. (2002) (who used methods introduced by Nagai 1980) was applied to these data to estimate the total energy release of all events returned by the algorithm assuming only radiative losses. The values found by this analysis were around two to three orders of magnitude smaller than those presented by both Bruzek (1972) and Georgoulis et al. (2002), however, this discrepancy can be explained by the small-scale (one order of magnitude smaller on average) and short-lived (one order of magnitude shorter-lived on average) features discussed in this Chapter. Power laws calculated for these data gave low indexes (from -0.18 to -2.09) for the occurrence of these events, potentially due to their formation close to the limitations of these data. It would be interesting to revisit such an analysis when data from the Daniel K. Inouye Solar Telescope (DKIST; formerly known as the Advanced Technology Solar Telescope) is available.

Finally, the temporal evolution and spatial positioning of selected features was discussed. A thorough inspection of these data highlighted three distinct traits which were exhibited by brightenings selected by the algorithm. The first case involved completely isolated brightenings which appeared to have no links to other events in time or space. The second class of features involved multiple events occurring from the same spatial position, either after the initial brightening had faded or had propagated away from its source in the moat flows (see Sheeley 1969). The final class can be descibed in three stages: 1) An event was detected by the algorithm which then; 2) decreases in intensity and is dropped by the algorithm before propagating away from its initial position before; 3) increasing in intensity once again and being re-selected by the algorithm. Many of the selected features occurred co-spatially with *G*-band MBPs (as has been previously discussed by Jess et al. 2010a to a limit extent); however, some bright potential Ellerman bomb features were observed to form apparently away from any MBPs. This relationship should be explored in more detail in future work.

8.2.2 Comparison of Numerical Signatures to Observational Evidence of Ellerman Bombs

In Chapter 4, comparisons of numerical simulations of magnetic reconnection to observations of Ellerman bombs were made. Observational data of the Hα and Fe I 6302.5 Å line profiles were collected by the DST/IBIS system on the 30th September 2012 whilst co-temporal sampling of the G-band continuum was conducted by the DST/ROSA instrument. These data were supplemented by Stokes V/I measurements collected by the Hinode/SOT and images of the upper atmosphere sampled by the SDO/AIA. Data from both of these instruments were reduced using standard *SolarSoft* routines before being co-aligned and de-rotated through time. In total 15 minutes of data were collected by the ground-based instruments with a cadence of around 5.6 seconds.

Potential Ellerman bombs were identified within DST/IBIS Hα line wing images as regions of brightness which induced no discernible signal in the line core. Within these data, seven such features were confidently selected. Following this, profiles of the Hα and Fe I 6302.5 Å lines were plotted for each event highlighting the common trait of reduced absorption in the Fe I 6302.5 Å line core co-spatial with the Ellerman bomb. These results were then compared to the numerical simulations in an attempt to further understand the physical processes which were being observed. It was found that the identified behaviour of Ellerman bombs in these two line profiles was comparable to the simulated line profiles at sites of magnetic reconnection within the numerical solar photosphere. This result agreed well with previous researches of Ellerman bombs (for example, Georgoulis et al. 2002, Isobe et al. 2007, Archontis and Hood 2009) indicating that a more thorough analysis should be conducted.

Next, the temporal evolution of these features was discussed. Specific attention was paid to the evolution in the Hα line wings in comparison to the Fe I 6302.5 Å line core. A similar evolution in both intensity and area was found for both wavelengths. As the estimated formation heights of the Hα line wings and the Fe I 6302.5 Å line core are similar, this result is unsurprising. This

co-temporal evolution agrees well with the simulated profiles at the numerical magnetic reconnection site. Interestingly, the simulated profiles do depict some form of narrowing of the Hα line profile at the reconnection site; however, as the simulation box does not reach high enough into the atmosphere to accurately model the Hα line core, this is most likely a numerical error. It would be of great interest to understand the signals of such reconnection sites in numerical boxes with larger vertical domains.

Overall, the seven Ellerman bombs analysed in this Chapter could be split into two distinct groups, namely typical Ellerman Bombs and small Ellerman hombs. Each of these features exhibited some form of 'flaring' through time, with increases in intensity and area evident. In order to further understand the role of the magnetic field with respect to the Ellerman bomb phenomena, co-spatial Stokes V/I data (sampled by the Hinode/SOT instrument) were observed through time. In total, five of the seven features occurred co-spatially with regions of flux cancellation and a single further event occurred co-spatially with apparent flux emergence. These complicated and evolving regions are indicative of typical magnetic field structuring (such as that suggested by Georgoulis et al. 2002) expected to lead to the formation of Ellerman bombs and agree well with the simulated bi-pole. In order to attempt to quantify any cancellation, a single isolated feature was analysed by placing a box around the bi-pole such that no other flux was apparent and then measuring the field strength through time. In only 15 minutes, a decline in total flux in the region to 68 % of the original value was observed. Further attempts to understand such cancellation were attempted in Chapter 6.

8.2.3 Ellerman Bombs at the Solar Limb

The properties of Ellerman bombs at the solar limb were discussed in Chapter 5. Line profiles sampling the Hα wavelength were collected by the SST/CRISP instrument on the 21st June 2012 with a FOV containing three sunspots within AR 11506. Ellerman bombs were then identified within these data by using a

threshold value of 150 % of the local background intensity before each feature was visually inspected through time returning basic properties such as lifetimes, widths, and lengths. These values (at 7 minutes, 500 km, and 600 km, respectively) are comparable to Ellerman bombs within the literature, especially in studies at the solar limb (see, for example, Kurokawa et al. 1982, Watanabe et al. 2011) confirming the accuracy of the selection criteria.

Further to the basic physical properties, the evolution of the Ellerman bombs through time was also of interest in this Chapter. Each selected feature was tracked through time and the peak height measured for each frame. In this way, it was possible to identify that all but two Ellerman bombs in these data appeared to follow a parabolic path through time with an average up-ward velocity of approximately 8.9 km s^{-1}. This value is close to those measured by Watanabe et al. (2011) and is also close to the sound speed estimated for the photosphere and chromosphere by Judge and Peter (1998). These profiles suggest that Ellerman bombs could be the signature of temperature and density enhancements in a localised region (as has been discussed by Fang et al. 2006). Two case studies were then presented which detailed the small-scale dynamical nature of Ellerman bombs.

The first case study discussed the morphology of a large Ellerman bomb close to a sunspot, which split into three extremely small-scale segments that propagated away from the initial feature. Each segment appeared to follow a bright 'trail' in a manner similar to that recently discussed by Reid et al. (2015), before another large Ellerman bomb was formed at the furthest distance reached by the segments (around 2200 km from the initial feature). The apparent connection between these two features offers evidence (agreeing with the time-distance analysis conducted in Chapter 3 and since corroborated by Reid et al. 2015) that photospheric motions (such as moat flows or convective motions) could cause consecutive reconnection events in different spatial positions. Interestingly, each of the segments of the original Ellerman bomb exhibited similar intensity enhancements and evolution profiles to the initial event potentially supporting the

assertions of Chapter 3 that Ellerman bombs can form on spatial scales close to the spatial resolution of ground-based instruments.

The second case study presented in this Chapter analysed an Ellerman bomb which was observed to split, seemingly violently. One segment propagated away from the initial spatial position of the Ellerman bomb at a speed of around 6.2 km s^{-1}, with the speed then decreasing to around 0.6 km s^{-1}. The other segment remained stationary through these observations. Once an approximate separation distance of 2 Mm was reached, a loop could be observed to connect the two segments. Interestingly, the morphology of this feature was comparable to the evolution of flux emergence events in observations (see, *e.g.*, Otsuji et al. 2007, Ortiz et al. 2014). This research offers an excellent channel for future study with regards to flux emergence, potentially using high-resolution magnetic field measurements collected by the SST/CRISP instrument.

8.2.4 On The Ability Of MMFs To Drive Ellerman Bombs

Chapter 6 detailed further research into the potential relationship between Ellerman bombs and MMFs (as has been previously been discussed by authors such as Nindos and Zirin 1998). Two hours of Hα line wing observations collected by the DST/IBIS instrument on the 30th September 2012 were reduced and destretched through time before line-of-sight photospheric magnetic field measurements sampled by the SDO/HMI were aligned and de-rotated to track the same FOV. Within these Hα data, numerous wing intensity enhancements (with morphological properties comparable to Ellerman bombs) were evident, often forming co-spatially with magnetic bi-poles (where reconnection is hypothesised to occur). In order to complete a thorough measurement of the role of any potential flux cancellation (or emergence) exhibited by the MMFs, however, it was neccesary to identify isolated events using YAFTA. Two such isolated MMFs suitable for analysis were evident during these observations.

Initially, magnetic field measurements of both the positive and negative sections of the bi-poles were computed through time using the YAFTA output.

An inspection was then conducted to identify the initial frames at which the two magnetic field elements began to interact and the final frame in which the bi-pole was evident. A linear fit was applied between these frames to the magnetic field strength through time allowing for the estimation of a cancellation rate for both bi-poles. This cancellation rate was calculated to be around 10^{14} Mx s^{-1} for both features. Interestingly, both MMFs appeared to have initial total fluxes on the order of 10^{18} Mx, diameters of around 1500 km and lifetimes on the order of one hour which is typical for these features (see, for example, Li and Zhang 2013). Calculating the initial magnetic energy, and assuming this energy was converted to radiative or kinetic energy during the cancellation, allowed an estimate of the energy available during the lifetime of the Hα brightening. The returned value was between the maximum energy returned in Chapter 3 and those estimated by Georgoulis et al. (2002). It is, therefore, possible that an Ellerman bomb did occur at this location.

Finally, these observed properties of these MMFs were used as an input into the basic analytical model of Sweet-Parker magnetic reconnection developed by Litvinenko (1999) and Litvinenko et al. (2007). This model was able to estimate upward flow velocities at reconnection sites using the measured cancellation rates. The obtained upward flow velocities were 5.6 km s^{-1} and 6.8 km s^{-1} which are both within one standard deviation of the mean vertical propagation rate measured in Chapter 5. As well as this, an increase in number density at the reconnection site is predicted agreeing with the results presented in Chapter 4 and within the literature (see, for example, Fang et al. 2006). Upward extension lengths of 443 km and 670 km were also derived, which are not dissimilar to measurements obtained in Chapter 5. Finally, up-ward mass fluxes (which could potentially supply the required density to surges or filaments) were also estimated by this model. According to this model, both events were capable of displacing 6.5 g hr^{-1} into the upper atmosphere, or enough mass to supply a solar surge (mass estimated by Bong et al. 2014) within one minute. However, no evidence of spicule, surge, or filament structures is observed co-spatial to

these MMFs.

One of the most interesting (in this author's opinion) open questions with regards to Ellerman bombs is their apparently sporadic relationship with solar surges (see, for example, Roy 1973, Madjarska et al. 2009, Reid et al. 2015). Roy (1973) derived a flux cancellation rate (at the site of a bi-pole co-spatial to a surge) of around 3×10^{15} Mx s^{-1}, which is one order of magnitude larger than the cancellation displayed within the MMFs discussed in this Chapter. It is, however, conceivable that higher cancellation rates could be observed at the sites of other Ellerman bombs which are neglected in this study. The research presented within this Chapter could, therefore, lead towards the first insights into the reason for the occasional co-spatial formation of Ellerman bombs and surges. An excellent avenue for future study could focus on the cancellation rates of bi-poles co-spatial to a more statistically relevant sample of confidently identified Ellerman bombs in order to understand whether larger observed cancellation rates are pre-cursors for surge formation.

8.2.5 Co-Spatial Relationship Between a Surge and a Blinker

Finally, an isolated surge event is analysed in Chapter 7. Observations of the Hα line wings, collected using the DST/IBIS instrument on the 30th September 2012, were analysed with a FOV sampling a uni-polar plage region. Approximately 15 minutes of data were available for analysis. Photospheric line-of-sight magnetograms and coronal EUV emissions were also considered using data from the SDO/HMI and SDO/AIA instruments, respectively. Data from both of these instruments was cropped, aligned, and de-rotated through time to track the FOV of these DST/IBIS data. Overall, the large-scale structuring within this FOV remained constant during the course of these observations with no evidence of flux emergence or cancellation evident.

The initial stages of the observed surge were evident in the blue wing of the Hα line profile as fine threads all extending from the same footpoint. Within

a few minutes, these fine threads had evolved to form a 'blob' with an area of approximately $4'' \times 4''$ before the absorption faded along the structure starting from the footpoint. After around one minute, this feature then appeared and developed in the red wing of the Hα line profile with a similar area. If one were to consider the wings of the line profile as indicative of motions in the line-of-sight, a parabolic evolution profile can be inferred. Interestingly, even after the development of the blob, fine-scale spicule like events were evident within the larger structure. Due to the small-scale structuring within these features and their parabolic evolution, it was deemed possible that a process similar to that hypothesised to drive spicules (as discussed by De Pontieu et al. 2004) could be the driver of this surge. Briefly, this process outlines that p-mode wave leakage from the photosphere could lead to spicule formation.

The co-spatial EUV transition region and coronal response to this surge manifests as a $4'' \times 4''$ brightening event with a lifetime on the order of minutes. This feature is interpreted as a blinker (see, for example, Harrison 1997). These features have been hypothesised to form either due to compression in the upper atmosphere induced by mass supply from the photosphere (as was discussed by, *e.g.*, Priest et al. 2002, Subramanian et al. 2012) or through magnetic reconnection in the transition region (Doyle et al. 2004). It is interesting to note that the blinker forms co-temporally with the initial phases of the evolution of the surge potentially agreeing with the simulations presented by Yokoyama and Shibata (1996). These authors suggested that photospheric magnetic reconnection could lead to the formation of a shock which compresses the transition region. Overall, the evidence found in this Chapter suggests that this blinker forms as a response to compression in the upper atmosphere caused by a process in the photosphere.

It still remains to be found, however, whether this event is typical of the overall driving mechanism of blinkers. Indeed, Subramanian et al. (2012) concluded that two types of blinkers existed which could indicate that more than one formation process is possible. The potential links between mass supply from the

photosphere to small-scale blinker events in the upper solar atmosphere are also intruiging. Future research, potentially making use of the IRIS satellite, should be conducted to test whether smaller ejections (such as spicules) have a similar influence on the transition region and corona. This work could link well with the recent results from the Hi-C mission which observed small-scale 'sparkles' (Régnier et al. 2014) but would require extremely accurate co-alignment between instruments.

8.3 Concluding Remarks

The brief foray into the small-scale dynamical processes in the solar atmosphere which has been presented in this thesis has outlined the complex nature of the Sun in general. The Ellerman bomb phenomenon, in particular, has proved difficult to conclusively understand to date; however, I hope that the research presented here at least offers some clues and insight that could instigate future studies of increased sophistication.

Bibliography

Anderson-Huang, L. S. (1998). The Solar Quiet Chromosphere-Corona Transition Region. *Space Sci. Rev.*, 85:203–213.

Archontis, V. and Hood, A. W. (2009). Formation of Ellerman bombs due to 3D flux emergence. *Astron. Astrophys.*, 508:1469–1483.

Asensio Ramos, A., Janssen, K., Cauzzi, G., and Reardon, K. (2006). High-resolution IBIS Observations and Comparison with 3D Simulations . *Memorie della Societa Astronomica Italiana Supplementi*, 9:59.

Bello González, N., Danilovic, S., and Kneer, F. (2013). On the structure and dynamics of Ellerman bombs. Detailed study of three events and modelling of Hα. *Astron. Astrophys.*, 557:A102.

Berger, T., Testa, P., Hillier, A., Boerner, P., Low, B. C., Shibata, K., Schrijver, C., Tarbell, T., and Title, A. (2011). Magneto-thermal convection in solar prominences. *Nature*, 472:197–200.

Berger, T. E. and Title, A. M. (2001). On the Relation of G-Band Bright Points to the Photospheric Magnetic Field. *Astrophys. J.*, 553:449–469.

Berlicki, A. and Heinzel, P. (2014). Observations and NLTE modeling of Ellerman bombs. *Astron. Astrophys.*, 567:A110.

Bewsher, D., Parnell, C. E., and Harrison, R. A. (2002). Transition Region Blinkers I. Quiet-Sun Properties. *Solar Phys.*, 206:21–43.

Bewsher, D., Parnell, C. E., Pike, C. D., and Harrison, R. A. (2003). Dynamics of Blinkers. *Solar Phys.*, 215:217–237.

Bodnárová, M., Utz, D., and Rybák, J. (2014). On Dynamics of G-Band Bright Points. *Solar Phys.*, 289:1543–1556.

Bong, S.-C., Cho, K.-S., and Yurchyshyn, V. (2014). Kinematics of Solar Chromospheric Surges of AR 10930. *Journal of Korean Astronomical Society*, 47:311–317.

BOREXINO Collaboration (2014). Neutrinos from the primary proton-proton fusion process in the Sun. *Nature*, 512:383–386.

Boyle, W. S. and Smith, G. E. (1970). Charge coupled semiconductor devices. *Bell System Technical Journal*, 49(4):587–593.

Brooks, D. H., Kurokawa, H., and Berger, T. E. (2007). An Hα Surge Provoked by Moving Magnetic Features near an Emerging Flux Region. *Astrophys. J.*, 656:1197–1207.

Bruzek, A. (1972). Some Observational Results on Moustaches. *Solar Phys.*, 26:94–107.

Cameron, R., Vögler, A., and Schüssler, M. (2011). Decay of a simulated mixed-polarity magnetic field in the solar surface layers. *Astron. Astrophys.*, 533:A86.

Carlsson, M. and Stein, R. F. (1992). Non-LTE radiating acoustic shocks and CA II K2V bright points. *Astrophys. J. Lett.*, 397:L59–L62.

Carlsson, M. and Stein, R. F. (1995). Does a nonmagnetic solar chromosphere exist? *Astrophys. J. Lett.*, 440:L29–L32.

Carlsson, M. and Stein, R. F. (2002). Dynamic Hydrogen Ionization. *Astrophys. J.*, 572:626–635.

Cavallini, F. and IBIS Team (2004). IBIS: Instrument Description and First Results. In *American Astronomical Society Meeting Abstracts #204*, volume 36 of *Bulletin of the American Astronomical Society*, page 710.

Cegla, H. M., Shelyag, S., Watson, C. A., and Mathioudakis, M. (2013). Stellar Surface Magneto-convection as a Source of Astrophysical Noise. I. Multi-component Parameterization of Absorption Line Profiles. *Astrophys. J.*, 763:95.

Chae, J., Moon, Y.-J., and Park, S.-Y. (2003). Observational Tests of Chromospheric Magnetic Reconnection. *Journal of Korean Astronomical Society*, 36:13.

Chae, J., Moon, Y.-J., Wang, H., and Yun, H. S. (2002). Flux Cancellation Rates and Converging Speeds of Canceling Magnetic Features. *Solar Phys.*, 207:73–85.

Chae, J., Qiu, J., Wang, H., and Goode, P. R. (1999). Extreme-Ultraviolet Jets and Hα Surges in Solar Microflares. *Astrophys. J. Lett.*, 513:L75–L78.

Chae, J., Wang, H., Goode, P. R., Fludra, A., and Schühle, U. (2000). Comparison of Transient Network Brightenings and Explosive Events in the Solar Transition Region. *Astrophys. J. Lett.*, 528:L119–L122.

Charbonneau, P. (2010). Dynamo Models of the Solar Cycle. *Living Reviews in Solar Physics*, 7:3.

Chen, H., Jiang, Y., and Ma, S. (2009). An EUV Jet and Hα Filament Eruption Associated with Flux Cancelation in a Decaying Active Region. *Solar Phys.*, 255:79–90.

Chen, P.-F., Fang, C., and Ding, M.-D. D. (2001). Ellerman Bombs, Type II White-light Flares and Magnetic Reconnection in the Solar Lower Atmosphere. *Chin. J. Astron. Astrophys.*, 1:176–184.

Christensen-Dalsgaard, J., Dappen, W., Ajukov, S. V., Anderson, E. R., Antia, H. M., Basu, S., Baturin, V. A., Berthomieu, G., Chaboyer, B., Chitre, S. M., Cox, A. N., Demarque, P., Donatowicz, J., Dziembowski, W. A., Gabriel, M., Gough, D. O., Guenther, D. B., Guzik, J. A., Harvey, J. W., Hill, F., Houdek, G., Iglesias, C. A., Kosovichev, A. G., Leibacher, J. W., Morel, P., Proffitt, C. R., Provost, J., Reiter, J., Rhodes, Jr., E. J., Rogers, F. J., Roxburgh, I. W., Thompson, M. J., and Ulrich, R. K. (1996). The Current State of Solar Modeling. *Science*, 272:1286–1292.

Criscuoli, S., Del Moro, D., Giannattasio, F., Viticchié, B., Giorgi, F., Ermolli, I., Zuccarello, F., and Berrilli, F. (2012). High cadence spectropolarimetry of moving magnetic features observed around a pore. *Astron. Astrophys.*, 546:A26.

Crockett, P. J., Mathioudakis, M., Jess, D. B., Shelyag, S., Keenan, F. P., and Christian, D. J. (2010). The Area Distribution of Solar Magnetic Bright Points. *Astrophys. J. Lett.*, 722:L188–L193.

Culhane, J. L., Harra, L. K., James, A. M., Al-Janabi, K., Bradley, L. J., Chaudry, R. A., Rees, K., Tandy, J. A., Thomas, P., Whillock, M. C. R., Winter, B., Doschek, G. A., Korendyke, C. M., Brown, C. M., Myers, S., Mariska, J., Seely, J., Lang, J., Kent, B. J., Shaughnessy, B. M., Young, P. R., Simnett, G. M., Castelli, C. M., Mahmoud, S., Mapson-Menard, H., Probyn, B. J., Thomas, R. J., Davila, J., Dere, K., Windt, D., Shea, J., Hagood, R., Moye, R., Hara, H., Watanabe, T., Matsuzaki, K., Kosugi, T., Hansteen, V., and Wikstol, Ø. (2007). The EUV Imaging Spectrometer for Hinode. *Solar Phys.*, 243:19–61.

Danilovič, S. (2009). Magnetic fine structure in the solar photosphere: observations and MHD simulations.

Dara, H. C., Alissandrakis, C. E., Zachariadis, T. G., and Georgakilas, A. A.

(1997). Magnetic and velocity field in association with Ellerman bombs. *Astron. Astrophys.*, 322:653–658.

de la Cruz Rodríguez, J., Löfdahl, M. G., Sütterlin, P., Hillberg, T., and Rouppe van der Voort, L. (2015). CRISPRED: A data pipeline for the CRISP imaging spectropolarimeter. *Astron. Astrophys.*, 573:A40.

De Pontieu, B., Erdélyi, R., and James, S. P. (2004). Solar chromospheric spicules from the leakage of photospheric oscillations and flows. *Nature*, 430:536–539.

De Pontieu, B., McIntosh, S. W., Carlsson, M., Hansteen, V. H., Tarbell, T. D., Boerner, P., Martinez-Sykora, J., Schrijver, C. J., and Title, A. M. (2011). The Origins of Hot Plasma in the Solar Corona. *Science*, 331:55–.

De Pontieu, B., McIntosh, S. W., Carlsson, M., Hansteen, V. H., Tarbell, T. D., Schrijver, C. J., Title, A. M., Shine, R. A., Tsuneta, S., Katsukawa, Y., Ichimoto, K., Suematsu, Y., Shimizu, T., and Nagata, S. (2007). Chromospheric Alfvénic Waves Strong Enough to Power the Solar Wind. *Science*, 318:1574–.

De Pontieu, B., Title, A. M., Lemen, J. R., Kushner, G. D., Akin, D. J., Allard, B., Berger, T., Boerner, P., Cheung, M., Chou, C., Drake, J. F., Duncan, D. W., Freeland, S., Heyman, G. F., Hoffman, C., Hurlburt, N. E., Lindgren, R. W., Mathur, D., Rehse, R., Sabolish, D., Seguin, R., Schrijver, C. J., Tarbell, T. D., Wülser, J.-P., Wolfson, C. J., Yanari, C., Mudge, J., Nguyen-Phuc, N., Timmons, R., van Bezooijen, R., Weingrod, I., Brookner, R., Butcher, G., Dougherty, B., Eder, J., Knagenhjelm, V., Larsen, S., Mansir, D., Phan, L., Boyle, P., Cheimets, P. N., DeLuca, E. E., Golub, L., Gates, R., Hertz, E., McKillop, S., Park, S., Perry, T., Podgorski, W. A., Reeves, K., Saar, S., Testa, P., Tian, H., Weber, M., Dunn, C., Eccles, S., Jaeggli, S. A., Kankelborg, C. C., Mashburn, K., Pust, N., Springer, L., Carvalho, R., Kleint, L., Marmie, J., Mazmanian, E., Pereira, T. M. D., Sawyer, S., Strong, J., Worden, S. P., Carlsson, M., Hansteen, V. H., Leenaarts, J., Wiesmann,

M., Aloise, J., Chu, K.-C., Bush, R. I., Scherrer, P. H., Brekke, P., Martinez-Sykora, J., Lites, B. W., McIntosh, S. W., Uitenbroek, H., Okamoto, T. J., Gummin, M. A., Auker, G., Jerram, P., Pool, P., and Waltham, N. (2014). The Interface Region Imaging Spectrograph (IRIS). *Solar Phys.*, 289:2733–2779.

De Wijn, A. G., Stenflo, J. O., Solanki, S. K., and Tsuneta, S. (2009). Small-Scale Solar Magnetic Fields. *Space Sci. Rev.*, 144:275–315.

Denker, C., de Boer, C. R., Volkmer, R., and Kneer, F. (1995). Speckle masking imaging of the moustache phenomenon. *Astron. Astrophys.*, 296:567.

Dere, K. P., Landi, E., Mason, H. E., Monsignori Fossi, B. C., and Young, P. R. (1997). CHIANTI - an atomic database for emission lines. *Astron. Astrophys. Suppl.*, 125:149–173.

Ding, M. D., Henoux, J.-C., and Fang, C. (1998). Line profiles in moustaches produced by an impacting energetic particle beam. *Astron. Astrophys.*, 332:761–766.

Diver, D. A., Brown, J. C., and Rust, D. M. (1996). A Possible Mechanism Governing the Production and Evolution of Ellerman Bombs. *Solar Phys.*, 168:105–114.

Domingo, V., Fleck, B., and Poland, A. I. (1995). The SOHO Mission: an Overview. *Solar Phys.*, 162:1–37.

Doyle, J. G. and Butler, C. J. (1985). Ultraviolet radiation from stellar flares and the coronal X-ray emission for dwarf-Me stars. *Nature*, 313:378–380.

Doyle, J. G., Roussev, I. I., and Madjarska, M. S. (2004). New insight into the blinker phenomenon and the dynamics of the solar transition region. *Astron. Astrophys.*, 418:L9–L12.

Edwin, P. M. and Roberts, B. (1983). Wave propagation in a magnetic cylinder. *Solar Phys.*, 88:179–191.

Ellerman, F. (1917). Solar Hydrogen "bombs". *Astrophys. J.*, 46:298.

Ellison, M. A. (1949). Characteristic Properties of Chromospheric Flares. *Mon. Not. Roy. Astron. Soc.*, 109:3.

Fang, C., Tang, Y. H., Xu, Z., Ding, M. D., and Chen, P. F. (2006). Spectral Analysis of Ellerman Bombs. *Astrophys. J.*, 643:1325–1336.

Filippov, B., Koutchmy, S., and Vilinga, J. (2007). On the dynamic nature of the prolate solar chromosphere: jet formation. *Astron. Astrophys.*, 464:1119–1125.

Firstova, N. M. (1986). An investigation of the linear polarization in emission features of active regions. *Solar Phys.*, 103:11–20.

Freij, N., Scullion, E. M., Nelson, C. J., Mumford, S., Wedemeyer, S., and Erdélyi, R. (2014). The Detection of Upwardly Propagating Waves Channeling Energy from the Chromosphere to the Low Corona. *Astrophys. J.*, 791:61.

Gabriel, A. H. (1976). A magnetic model of the solar transition region. *Royal Society of London Philosophical Transactions Series A*, 281:339–352.

Georgoulis, M. K., Rust, D. M., Bernasconi, P. N., and Schmieder, B. (2002). Statistics, Morphology, and Energetics of Ellerman Bombs. *Astrophys. J.*, 575:506–528.

Goedbloed, J. P. H. and Poedts, S. (2004). *Principles of Magnetohydrodynamics*.

Golub, L., Deluca, E., Austin, G., Bookbinder, J., Caldwell, D., Cheimets, P., Cirtain, J., Cosmo, M., Reid, P., Sette, A., Weber, M., Sakao, T., Kano, R., Shibasaki, K., Hara, H., Tsuneta, S., Kumagai, K., Tamura, T., Shimojo,

M., McCracken, J., Carpenter, J., Haight, H., Siler, R., Wright, E., Tucker, J., Rutledge, H., Barbera, M., Peres, G., and Varisco, S. (2007). The X-Ray Telescope (XRT) for the Hinode Mission. *Solar Phys.*, 243:63–86.

Guglielmino, S. L., Bellot Rubio, L. R., Zuccarello, F., Aulanier, G., Vargas Domínguez, S., and Kamio, S. (2010). Multiwavelength Observations of Small-scale Reconnection Events Triggered by Magnetic Flux Emergence in the Solar Atmosphere. *Astrophys. J.*, 724:1083–1098.

Guglielmino, S. L., Zuccarello, F., Romano, P., and Bellot Rubio, L. R. (2008). Hinode Observations of Chromospheric Brightenings in the Ca II H Line during Small-Scale Flux Emergence Events. *Astrophys. J. Lett.*, 688:L111–L114.

Handy, B. N., Acton, L. W., Kankelborg, C. C., Wolfson, C. J., Akin, D. J., Bruner, M. E., Caravalho, R., Catura, R. C., Chevalier, R., Duncan, D. W., Edwards, C. G., Feinstein, C. N., Freeland, S. L., Friedlaender, F. M., Hoffmann, C. H., Hurlburt, N. E., Jurcevich, B. K., Katz, N. L., Kelly, G. A., Lemen, J. R., Levay, M., Lindgren, R. W., Mathur, D. P., Meyer, S. B., Morrison, S. J., Morrison, M. D., Nightingale, R. W., Pope, T. P., Rehse, R. A., Schrijver, C. J., Shine, R. A., Shing, L., Strong, K. T., Tarbell, T. D., Title, A. M., Torgerson, D. D., Golub, L., Bookbinder, J. A., Caldwell, D., Cheimets, P. N., Davis, W. N., Deluca, E. E., McMullen, R. A., Warren, H. P., Amato, D., Fisher, R., Maldonado, H., and Parkinson, C. (1999). The transition region and coronal explorer. *Solar Phys.*, 187:229–260.

Hansteen, V., De Pontieu, B., Carlsson, M., Lemen, J., Title, A., Boerner, P., Hurlburt, N., Tarbell, T. D., Wuelser, J. P., Pereira, T. M. D., De Luca, E. E., Golub, L., McKillop, S., Reeves, K., Saar, S., Testa, P., Tian, H., Kankelborg, C., Jaeggli, S., Kleint, L., and Martínez-Sykora, J. (2014). The unresolved fine structure resolved: IRIS observations of the solar transition region. *Science*, 346:315.

Harrison, R. A. (1997). EUV Blinkers: The Significance of Variations in the Extreme Ultraviolet Quiet Sun. *Solar Phys.*, 175:467–485.

Harrison, R. A., Lang, J., Brooks, D. H., and Innes, D. E. (1999). A study of extreme ultraviolet blinker activity. *Astron. Astrophys.*, 351:1115–1132.

Harrison, R. A., Sawyer, E. C., Carter, M. K., Cruise, A. M., Cutler, R. M., Fludra, A., Hayes, R. W., Kent, B. J., Lang, J., Parker, D. J., Payne, J., Pike, C. D., Peskett, S. C., Richards, A. G., Gulhane, J. L., Norman, K., Breeveld, A. A., Breeveld, E. R., Al Janabi, K. F., McCalden, A. J., Parkinson, J. H., Self, D. G., Thomas, P. D., Poland, A. I., Thomas, R. J., Thompson, W. T., Kjeldseth-Moe, O., Brekke, P., Karud, J., Maltby, P., Aschenbach, B., Bräuninger, H., Kühne, M., Hollandt, J., Siegmund, O. H. W., Huber, M. C. E., Gabriel, A. H., Mason, H. E., and Bromage, B. J. I. (1995). The Coronal Diagnostic Spectrometer for the Solar and Heliospheric Observatory. *Solar Phys.*, 162:233–290.

Harvey, K. and Harvey, J. (1973). Observations of Moving Magnetic Features near Sunspots. *Solar Phys.*, 28:61–71.

Hashimoto, Y., Kitai, R., Ichimoto, K., Ueno, S., Nagata, S., Ishii, T. T., Hagino, M., Komori, H., Nishida, K., Matsumoto, T., Otsuji, K., Nakamura, T., Kawate, T., Watanabe, H., and Shibata, K. (2010). Internal Fine Structure of Ellerman Bombs. *Pub. Astron. Soc. Japan*, 62:879–.

Henoux, J.-C., Fang, C., and Ding, M. D. (1998). A possible mechanism for the Hα broad wings emission of Ellerman bombs. *Astron. Astrophys.*, 337:294–298.

Henriques, V. M. J. (2012). Three-dimensional temperature mapping of solar photospheric fine structure using Ca ii H filtergrams. *Astron. Astrophys.*, 548:A114.

Heyvaerts, J., Priest, E., and Rust, D. M. (1977). An emerging flux model for solar flares. *Solar Phys.*, 53:255–258.

Hong, J., Ding, M. D., Li, Y., Fang, C., and Cao, W. (2014). Spectral Observations of Ellerman Bombs and Fitting with a Two-cloud Model. *Astrophys. J.*, 792:13.

Houston, W. V. (1927). A compound interferometer for fine structure work. *Phys. Rev.*, 29:478–484.

Howard, R. and Harvey, J. W. (1964). Photospheric Magnetic Fields and Chromospheric Features. *Astrophys. J.*, 139:1328.

Hu, F. M., Song, M. T., and Li, X. Q. (1995). H $_{alpha}$filtergram observations of ellerman bombs and its magnetic reconnection model. *Astrophys. Space Sci.*, 229:325–339.

Huang, Z., Madjarska, M. S., Xia, L., Doyle, J. G., Galsgaard, K., and Fu, H. (2014). Explosive Events on a Subarcsecond Scale in IRIS Observations: A Case Study. *Astrophys. J.*, 797:88.

Isobe, H., Proctor, M. R. E., and Weiss, N. O. (2008). Convection-driven Emergence of Small-Scale Magnetic Fields and their Role in Coronal Heating and Solar Wind Acceleration. *Astrophys. J. Lett.*, 679:L57–L60.

Isobe, H., Tripathi, D., and Archontis, V. (2007). Ellerman Bombs and Jets Associated with Resistive Flux Emergence. *Astrophys. J. Lett.*, 657:L53–L56.

Jess, D. B., Mathioudakis, M., Browning, P. K., Crockett, P. J., and Keenan, F. P. (2010a). Microflare Activity Driven by Forced Magnetic Reconnection. *Astrophys. J. Lett.*, 712:L111–L115.

Jess, D. B., Mathioudakis, M., Christian, D. J., Keenan, F. P., Ryans, R. S. I., and Crockett, P. J. (2010b). ROSA: A High-cadence, Synchronized Multicamera Solar Imaging System. *Solar Phys.*, 261:363–373.

Jess, D. B., Mathioudakis, M., and Keys, P. H. (2014). Nanoflare Activity in the Solar Chromosphere. *Astrophys. J.*, 795:172.

Judge, P. G. and Peter, H. (1998). The Structure of the Chromosphere Properties Pertaining to Element Fractionation. *Space Sci. Rev.*, 85:187–202.

Katsukawa, Y., Berger, T. E., Ichimoto, K., Lites, B. W., Nagata, S., Shimizu, T., Shine, R. A., Suematsu, Y., Tarbell, T. D., Title, A. M., and Tsuneta, S. (2007). Small-Scale Jetlike Features in Penumbral Chromospheres. *Science*, 318:1594–.

Kayshap, P., Srivastava, A. K., and Murawski, K. (2013). The Kinematics and Plasma Properties of a Solar Surge Triggered by Chromospheric Activity in AR11271. *Astrophys. J.*, 763:24.

Keys, P. H., Mathioudakis, M., Jess, D. B., Shelyag, S., Crockett, P. J., Christian, D. J., and Keenan, F. P. (2011). The Velocity Distribution of Solar Photospheric Magnetic Bright Points. *Astrophys. J. Lett.*, 740:L40.

Kitai, R. (1983). On the mass motions and the atmospheric states of moustaches. *Solar Phys.*, 87:135–154.

Kobayashi, K., Cirtain, J., Winebarger, A. R., Korreck, K., Golub, L., Walsh, R. W., De Pontieu, B., DeForest, C., Title, A., Kuzin, S., Savage, S., Beabout, D., Beabout, B., Podgorski, W., Caldwell, D., McCracken, K., Ordway, M., Bergner, H., Gates, R., McKillop, S., Cheimets, P., Platt, S., Mitchell, N., and Windt, D. (2014). The High-Resolution Coronal Imager (Hi-C). *Solar Phys.*, 289:4393–4412.

Kosugi, T., Matsuzaki, K., Sakao, T., Shimizu, T., Sone, Y., Tachikawa, S., Hashimoto, T., Minesugi, K., Ohnishi, A., Yamada, T., Tsuneta, S., Hara, H., Ichimoto, K., Suematsu, Y., Shimojo, M., Watanabe, T., Shimada, S., Davis, J. M., Hill, L. D., Owens, J. K., Title, A. M., Culhane, J. L., Harra,

L. K., Doschek, G. A., and Golub, L. (2007). The Hinode (Solar-B) Mission: An Overview. *Solar Phys.*, 243:3–17.

Kurokawa, H., Kawaguchi, I., Funakoshi, Y., and Nakai, Y. (1982). Morphological and evolutional features of Ellerman bombs. *Solar Phys.*, 79:77–84.

Kurokawa, H. and Kawai, G. (1993). H alpha Surge Activity at the First Stage of Magnetic Flux Emergence. In Zirin, H., Ai, G., and Wang, H., editors, *IAU Colloq. 141: The Magnetic and Velocity Fields of Solar Active Regions*, volume 46 of *Astronomical Society of the Pacific Conference Series*, page 507.

Landi, E., Young, P. R., Dere, K. P., Del Zanna, G., and Mason, H. E. (2013). CHIANTI - An Atomic Database for Emission Lines. XIII. Soft X-Ray Improvements and Other Changes. *Astrophys. J.*, 763:86.

Leenaarts, J., Carlsson, M., Hansteen, V., and Rutten, R. J. (2007). Non-equilibrium hydrogen ionization in 2D simulations of the solar atmosphere. *Astron. Astrophys.*, 473:625–632.

Leenaarts, J., Carlsson, M., and Rouppe van der Voort, L. (2012). The Formation of the Hα Line in the Solar Chromosphere. *Astrophys. J.*, 749:136.

Leenaarts, J., Rutten, R. J., Sütterlin, P., Carlsson, M., and Uitenbroek, H. (2006). DOT tomography of the solar atmosphere. VI. Magnetic elements as bright points in the blue wing of Hα. *Astron. Astrophys.*, 449:1209–1218.

Lemen, J. R., Title, A. M., Akin, D. J., Boerner, P. F., Chou, C., Drake, J. F., Duncan, D. W., Edwards, C. G., Friedlaender, F. M., Heyman, G. F., Hurlburt, N. E., Katz, N. L., Kushner, G. D., Levay, M., Lindgren, R. W., Mathur, D. P., McFeaters, E. L., Mitchell, S., Rehse, R. A., Schrijver, C. J., Springer, L. A., Stern, R. A., Tarbell, T. D., Wuelser, J.-P., Wolfson, C. J., Yanari, C., Bookbinder, J. A., Cheimets, P. N., Caldwell, D., Deluca, E. E., Gates, R., Golub, L., Park, S., Podgorski, W. A., Bush, R. I., Scherrer, P. H., Gummin, M. A., Smith, P., Auker, G., Jerram, P., Pool, P., Soufli, R., Windt,

D. L., Beardsley, S., Clapp, M., Lang, J., and Waltham, N. (2012). The Atmospheric Imaging Assembly (AIA) on the Solar Dynamics Observatory (SDO). *Solar Phys.*, 275:17–40.

Li, X. and Zhang, H. (2013). Moving Magnetic Features Around AR 10930 from High-resolution Data Observed by Hinode/SOT. *Astrophys. J.*, 771:22.

Lim, E.-K., Yurchyshyn, V., and Goode, P. (2012). First Simultaneous Detection of Moving Magnetic Features in Photospheric Intensity and Magnetic Field Data. *Astrophys. J.*, 753:89.

Lin, C.-H., Banerjee, D., O'Shea, E., and Doyle, J. G. (2006). Transition region counterpart of a moving magnetic feature. *Astron. Astrophys.*, 460:597–604.

Lites, B. W. and Ichimoto, K. (2013). The SP_PREP Data Preparation Package for the Hinode Spectro-Polarimeter. *Solar Phys.*, 283:601–629.

Litvinenko, Y. E. (1999). Photospheric Magnetic Reconnection and Canceling Magnetic Features on the Sun. *Astrophys. J.*, 515:435–440.

Litvinenko, Y. E., Chae, J., and Park, S.-Y. (2007). Flux Pile-up Magnetic Reconnection in the Solar Photosphere. *Astrophys. J.*, 662:1302–1308.

Litvinenko, Y. E. and Martin, S. F. (1999). Magnetic reconnection as the cause of a photospheric canceling feature and mass flows in a filament. *Solar Phys.*, 190:45–58.

Lockyer, J. N. (1868). Spectroscopic Observation of the Sun, No. II. *Royal Society of London Proceedings Series I*, 17:131–132.

Longcope, D. W. and Magara, T. (2004). A Comparison of the Minimum Current Corona to a Magnetohydrodynamic Simulation of Quasi-Static Coronal Evolution. *Astrophys. J.*, 608:1106–1123.

Lyot, B. (1944). Le filtre monochromatique polarisant et ses applications en physique solaire. *Annales d'Astrophysique*, 7:31.

Madjarska, M. S. and Doyle, J. G. (2003). Simultaneous observations of solar transition region blinkers and explosive events by SUMER, CDS and BBSO. Are blinkers, explosive events and spicules the same phenomenon? *Astron. Astrophys.*, 403:731–741.

Madjarska, M. S., Doyle, J. G., and de Pontieu, B. (2009). Explosive Events Associated with a Surge. *Astrophys. J.*, 701:253–259.

Madjarska, M. S., Doyle, J. G., Hochedez, J.-F., and Theissen, A. (2006). Macrospicules and blinkers as seen in Shutterless EIT 304 Å. *Astron. Astrophys.*, 452:L11–L14.

Marik, D. and Erdélyi, R. (2002). What is the real nature of blinkers? *Astron. Astrophys.*, 393:L73–L76.

Matsumoto, T., Kitai, R., Shibata, K., Nagata, S., Otsuji, K., Nakamura, T., Watanabe, H., Tsuneta, S., Suematsu, Y., Ichimoto, K., Shimizu, T., Katsukawa, Y., Tarbell, T. D., Lites, B. W., Shine, R. A., and Title, A. M. (2008a). Cooperative Observation of Ellerman Bombs between the Solar Optical Telescope aboard Hinode and Hida/Domeless Solar Telescope. *Pub. Astron. Soc. Japan*, 60:577–.

Matsumoto, T., Kitai, R., Shibata, K., Otsuji, K., Naruse, T., Shiota, D., and Takasaki, H. (2008b). Height Dependence of Gas Flows in an Ellerman Bomb. *Pub. Astron. Soc. Japan*, 60:95–.

McMath, R. R., Mohler, O. C., and Dodson, H. W. (1960). Solar Features Associated with Ellerman's "Solar Hydrogen Bombs". *Proceedings of the National Academy of Science*, 46:165–169.

Mikheyev, S. P. and Smirnov, A. Y. (1985). Resonance enhancement of oscillations in matter and solar neutrino spectroscopy. *Yadernaya Fizika*, 42:1441–1448.

Mitalas, R. and Sills, K. R. (1992). On the photon diffusion time scale for the sun. *Astrophys. J.*, 401:759.

Mitchell, W. M. (1909). Recent Solar Observations at Haverford. *Astrophys. J.*, 30:75.

Morton, R. J., Verth, G., Jess, D. B., Kuridze, D., Ruderman, M. S., Mathioudakis, M., and Erdélyi, R. (2012). Observations of ubiquitous compressive waves in the Sun's chromosphere. *Nature Communications*, 3:1315.

Nagai, F. (1980). A model of hot loops associated with solar flares. I - Gasdynamics in the loops. *Solar Phys.*, 68:351–379.

Nelson, C. J., Doyle, J. G., Erdélyi, R., Huang, Z., Madjarska, M. S., Mathioudakis, M., Mumford, S. J., and Reardon, K. (2013a). Statistical Analysis of Small Ellerman Bomb Events. *Solar Phys.*, 283:307–323.

Nelson, C. J., Scullion, E. M., Doyle, J. G., Freij, N., and Erdélyi, R. (2015). Small-scale Structuring of Ellerman Bombs at the Solar Limb. *Astrophys. J.*, 798:19.

Nelson, C. J., Shelyag, S., Mathioudakis, M., Doyle, J. G., Madjarska, M. S., Uitenbroek, H., and Erdélyi, R. (2013b). Ellerman Bombs - Evidence for Magnetic Reconnection in the Lower Solar Atmosphere. *Astrophys. J.*, 779:125.

Newton, H. W. (1942). Characteristic radial motions of Hα absorption markings seen with bright eruptions on the Sun's disc. *Mon. Not. Roy. Astron. Soc.*, 102:2.

Nindos, A. and Zirin, H. (1998). Properties and Motions of Ellerman Bombs. *Solar Phys.*, 182:381–392.

O'Dwyer, B., Del Zanna, G., Mason, H. E., Weber, M. A., and Tripathi, D. (2010). SDO/AIA response to coronal hole, quiet Sun, active region, and flare plasma. *Astron. Astrophys.*, 521:A21.

Ortiz, A., Bellot Rubio, L. R., Hansteen, V. H., de la Cruz Rodríguez, J., and Rouppe van der Voort, L. (2014). Emergence of Granular-sized Magnetic Bubbles through the Solar Atmosphere. I. Spectropolarimetric Observations and Simulations. *Astrophys. J.*, 781:126.

Otsuji, K., Shibata, K., Kitai, R., Ueno, S., Nagata, S., Matsumoto, T., Nakamura, T., Watanabe, H., Tsuneta, S., Suematsu, Y., Ichimoto, K., Shimizu, T., Katsukawa, Y., Tarbell, T. D., Lites, B., Shine, R. A., and Title Alan M. (2007). Small-Scale Magnetic-Flux Emergence Observed with Hinode Solar Optical Telescope. *Pub. Astron. Soc. Japan*, 59:649.

Pariat, E., Aulanier, G., Schmieder, B., Georgoulis, M. K., Rust, D. M., and Bernasconi, P. N. (2004). Resistive Emergence of Undulatory Flux Tubes. *Astrophys. J.*, 614:1099–1112.

Pariat, E., Schmieder, B., Berlicki, A., Deng, Y., Mein, N., López Ariste, A., and Wang, S. (2007). Spectrophotometric analysis of Ellerman bombs in the Ca II, Hα, and UV range. *Astron. Astrophys.*, 473:279–289.

Parker, E. N. (1957). Sweet's Mechanism for Merging Magnetic Fields in Conducting Fluids. *J. Geophys. Res.*, 62:509–520.

Parker, E. N. (1988). Nanoflares and the solar X-ray corona. *Astrophys. J.*, 330:474–479.

Parnell, C. E., Bewsher, D., and Harrison, R. A. (2002). Transition-Region Blinkers - II. Active-Region Properties. *Solar Phys.*, 206:249–271.

Parnell, C. E. and Jupp, P. E. (2000). Statistical Analysis of the Energy Distribution of Nanoflares in the Quiet Sun. *Astrophys. J.*, 529:554–569.

Pesnell, W. D., Thompson, B. J., and Chamberlin, P. C. (2012). The Solar Dynamics Observatory (SDO). *Solar Phys.*, 275:3–15.

Peter, H., Tian, H., Curdt, W., Schmit, D., Innes, D., De Pontieu, B., Lemen, J., Title, A., Boerner, P., Hurlburt, N., Tarbell, T. D., Wuelser, J. P., Martínez-Sykora, J., Kleint, L., Golub, L., McKillop, S., Reeves, K. K., Saar, S., Testa, P., Kankelborg, C., Jaeggli, S., Carlsson, M., and Hansteen, V. (2014). Hot explosions in the cool atmosphere of the Sun. *Science*, 346:1255726.

Pikel'Ner, S. B. (1974). Nature of point sources of spectral line, continuous, and x-ray emission on the sun. *Soviet Astron.*, 18:136.

Priest, E. R., Hood, A. W., and Bewsher, D. (2002). The Nature of Blinkers and the Solar Transition Region. *Solar Phys.*, 205:249–264.

Qiu, J., Ding, M. D., Wang, H., Denker, C., and Goode, P. R. (2000). Ultraviolet and Hα Emission in Ellerman Bombs. *Astrophys. J. Lett.*, 544:L157–L161.

Régnier, S., Alexander, C. E., Walsh, R. W., Winebarger, A. R., Cirtain, J., Golub, L., Korreck, K. E., Mitchell, N., Platt, S., Weber, M., De Pontieu, B., Title, A., Kobayashi, K., Kuzin, S., and DeForest, C. E. (2014). Sparkling Extreme-ultraviolet Bright Dots Observed with Hi-C. *Astrophys. J.*, 784:134.

Reid, A., Mathioudakis, M., Scullion, E., Doyle, J. G., Shelyag, S., and Gallagher, P. (2015). Ellerman Bombs with Jets: Cause and Effect. *ArXiv e-prints*.

Roberts, B. (1981a). Wave Propagation in a Magnetically Structured Atmosphere - Part Two - Waves in a Magnetic Slab. *Solar Phys.*, 69:39–56.

Roberts, B. (1981b). Wave propagation in a magnetically structured atmosphere. I - Surface waves at a magnetic interface. *Solar Phys.*, 69:27–38.

Roussev, I., Galsgaard, K., Erdélyi, R., and Doyle, J. G. (2001). Modelling of explosive events in the solar transition region in a 2D environment. I. General reconnection jet dynamics. *Astron. Astrophys.*, 370:298–310.

Roy, J. R. (1973). The Magnetic Properties of Solar Surges. *Solar Phys.*, 28:95–114.

Roy, J.-R. and Leparskas, H. (1973). Some Statistical Properties of Ellerman Bombs. *Solar Phys.*, 30:449–457.

Rust, D. M. (1968). Chromospheric Explosions and Satellite Sunspots. In Kiepenheuer, K. O., editor, *Structure and Development of Solar Active Regions*, volume 35 of *IAU Symposium*, page 77.

Rust, D. M. (1972). Flares and Changing Magnetic Fields. *Solar Phys.*, 25:141–157.

Rutten, R. J. (2008). Hα as a Chromospheric Diagnostic. In Matthews, S. A., Davis, J. M., and Harra, L. K., editors, *First Results From Hinode*, volume 397 of *Astronomical Society of the Pacific Conference Series*, page 54.

Rutten, R. J. (2010). The quiet chromosphere. Old wisdom, new insights, future needs. *Memorie della Societa Astronomica Italiana*, 81:565–576.

Rutten, R. J. (2012). The quiet-Sun photosphere and chromosphere. *Royal Society of London Philosophical Transactions Series A*, 370:3129–3150.

Rutten, R. J., Vissers, G. J. M., Rouppe van der Voort, L. H. M., Sütterlin, P., and Vitas, N. (2013). Ellerman bombs: fallacies, fads, usage. *Journal of Physics Conference Series*, 440(1):012007.

Scharmer, G. B. (2006). Comments on the optimization of high resolution Fabry-Pérot filtergraphs. *Astron. Astrophys.*, 447:1111–1120.

Scharmer, G. B., Bjelksjo, K., Korhonen, T. K., Lindberg, B., and Petterson, B. (2003). The 1-meter Swedish solar telescope. In Keil, S. L. and Avakyan, S. V., editors, *Innovative Telescopes and Instrumentation for Solar Astrophysics*, volume 4853 of *Society of Photo-Optical Instrumentation Engineers (SPIE) Conference Series*, pages 341–350.

Scharmer, G. B. and Henriques, V. M. J. (2012). SST/CRISP observations of convective flows in a sunspot penumbra. *Astron. Astrophys.*, 540:A19.

Scharmer, G. B., Narayan, G., Hillberg, T., de la Cruz Rodríguez, J., Löfdahl, M. G., Kiselman, D., Sütterlin, P., van Noort, M., and Lagg, A. (2008). CRISP Spectropolarimetric Imaging of Penumbral Fine Structure. *Astrophys. J. Lett.*, 689:L69–L72.

Scherrer, P. H., Bogart, R. S., Bush, R. I., Hoeksema, J. T., Kosovichev, A. G., Schou, J., Rosenberg, W., Springer, L., Tarbell, T. D., Title, A., Wolfson, C. J., Zayer, I., and MDI Engineering Team (1995). The Solar Oscillations Investigation - Michelson Doppler Imager. *Solar Phys.*, 162:129–188.

Scherrer, P. H., Schou, J., Bush, R. I., Kosovichev, A. G., Bogart, R. S., Hoeksema, J. T., Liu, Y., Duvall, T. L., Zhao, J., Title, A. M., Schrijver, C. J., Tarbell, T. D., and Tomczyk, S. (2012). The Helioseismic and Magnetic Imager (HMI) Investigation for the Solar Dynamics Observatory (SDO). *Solar Phys.*, 275:207–227.

Schmieder, B., Rust, D. M., Georgoulis, M. K., Démoulin, P., and Bernasconi, P. N. (2004). Emerging Flux and the Heating of Coronal Loops. *Astrophys. J.*, 601:530–545.

Schulz, T. J. (1993). Multiframe blind deconvolution of astronomical images. *Journal of the Optical Society of America A*, 10:1064–1073.

Schwarzschild, K. (1906). On the equilibrium of the Sun's atmosphere. *Nachrichten von der Königlichen Gesellschaft der Wissenschaften zu Göttingen. Math.-phys. Klasse, 195, p. 41-53*, 195:41–53.

Sekse, D. H., Rouppe van der Voort, L., and De Pontieu, B. (2012). Statistical Properties of the Disk Counterparts of Type II Spicules from Simultaneous Observations of Rapid Blueshifted Excursions in Ca II 8542 and Hα. *Astrophys. J.*, 752:108.

Severny, A. B. (1956). Fine structure in solar spectra. *The Observatory*, 76:241–242.

Severny, A. B. (1964). Solar Flares. *Ann. Rev. of Astron. Astrophys.*, 2:363.

Sheeley, Jr., N. R. (1969). The Evolution of the Photospheric Network. *Solar Phys.*, 9:347–357.

Shelyag, S., Keys, P., Mathioudakis, M., and Keenan, F. P. (2011). Vorticity in the solar photosphere. *Astron. Astrophys.*, 526:A5.

Shelyag, S., Schüssler, M., Solanki, S. K., and Vögler, A. (2007). Stokes diagnostics of simulated solar magneto-convection. *Astron. Astrophys.*, 469:731–747.

Shibata, K., Nishikawa, T., Kitai, R., and Suematsu, Y. (1982). Numerical hydrodynamics of the jet phenomena in the solar atmosphere. II - Surges. *Solar Phys.*, 77:121–151.

Shibata, K., Nozawa, S., and Matsumoto, R. (1992). Magnetic reconnection associated with emerging magnetic flux. *Pub. Astron. Soc. Japan*, 44:265–272.

Socas-Navarro, H., Martínez Pillet, V., Elmore, D., Pietarila, A., Lites, B. W., and Manso Sainz, R. (2006). Spectro-Polarimetric Observations and Non-Lte Modeling of Ellerman Bombs. *Solar Phys.*, 235:75–86.

Solanki, S. K. and Steiner, O. (1990). How magnetic is the solar chromosphere? *Astron. Astrophys.*, 234:519–529.

Stellmacher, G. and Wiehr, E. (1991). Modelling the moustache phenomenon in network regions. *Astron. Astrophys.*, 251:675–679.

Stenflo, J. O. (1973). Magnetic-Field Structure of the Photospheric Network. *Solar Phys.*, 32:41–63.

Sterling, A. C. (2000). Solar Spicules: A Review of Recent Models and Targets for Future Observations - (Invited Review). *Solar Phys.*, 196:79–111.

Subramanian, S., Madjarska, M. S., Doyle, J. G., and Bewsher, D. (2012). What is the true nature of blinkers? *Astron. Astrophys.*, 538:A50.

Suematsu, Y., Shibata, K., Neshikawa, T., and Kitai, R. (1982). Numerical hydrodynamics of the jet phenomena in the solar atmosphere. I - Spicules. *Solar Phys.*, 75:99–118.

Suematsu, Y., Tsuneta, S., Ichimoto, K., Shimizu, T., Otsubo, M., Katsukawa, Y., Nakagiri, M., Noguchi, M., Tamura, T., Kato, Y., Hara, H., Kubo, M., Mikami, I., Saito, H., Matsushita, T., Kawaguchi, N., Nakaoji, T., Nagae, K., Shimada, S., Takeyama, N., and Yamamuro, T. (2008). The Solar Optical Telescope of Solar-B (Hinode): The Optical Telescope Assembly. *Solar Phys.*, 249:197–220.

Sweet, P. A. (1958). The Neutral Point Theory of Solar Flares. In Lehnert, B., editor, *Electromagnetic Phenomena in Cosmical Physics*, volume 6 of *IAU Symposium*, page 123.

Syrovatskii, S. I. (1976). Current-sheet parameters and a thermal trigger for solar flares. *Soviet Astronomy Letters*, 2:13.

Takasao, S., Isobe, H., and Shibata, K. (2013). Numerical Simulations of Solar Chromospheric Jets Associated with Emerging Flux. *Pub. Astron. Soc. Japan*, 65:62.

Tarbell, T. D., Tsuneta, S., and SOT Team (2007). The Solar Optical Telescope on Hinode: Performance and Capabilities. In *American Astronomical Society Meeting Abstracts #210*, volume 39 of *Bulletin of the American Astronomical Society*, page 217.

Teriaca, L., Madjarska, M. S., and Doyle, J. G. (2001). Electron density variations during ultraviolet transient events. *Solar Phys.*, 200:91–114.

Testa, P., De Pontieu, B., Allred, J., Carlsson, M., Reale, F., Daw, A., Hansteen, V., Martinez-Sykora, J., Liu, W., DeLuca, E. E., Golub, L., McKillop, S., Reeves, K., Saar, S., Tian, H., Lemen, J., Title, A., Boerner, P., Hurlburt, N., Tarbell, T. D., Wuelser, J. P., Kleint, L., Kankelborg, C., and Jaeggli, S. (2014). Evidence of nonthermal particles in coronal loops heated impulsively by nanoflares. *Science*, 346:B315.

Thompson, M. J., Toomre, J., Anderson, E. R., Antia, H. M., Berthomieu, G., Burtonclay, D., Chitre, S. M., Christensen-Dalsgaard, J., Corbard, T., De Rosa, M., Genovese, C. R., Gough, D. O., Haber, D. A., Harvey, J. W., Hill, F., Howe, R., Korzennik, S. G., Kosovichev, A. G., Leibacher, J. W., Pijpers, F. P., Provost, J., Rhodes, Jr., E. J., Schou, J., Sekii, T., Stark, P. B., and Wilson, P. R. (1996). Differential Rotation and Dynamics of the Solar Interior. *Science*, 272:1300–1305.

Tsuneta, S., Ichimoto, K., Katsukawa, Y., Nagata, S., Otsubo, M., Shimizu, T., Suematsu, Y., Nakagiri, M., Noguchi, M., Tarbell, T., Title, A., Shine, R., Rosenberg, W., Hoffmann, C., Jurcevich, B., Kushner, G., Levay, M., Lites, B., Elmore, D., Matsushita, T., Kawaguchi, N., Saito, H., Mikami, I., Hill, L. D., and Owens, J. K. (2008). The Solar Optical Telescope for the Hinode Mission: An Overview. *Solar Phys.*, 249:167–196.

Uitenbroek, H. (2001). Multilevel Radiative Transfer with Partial Frequency Redistribution. *Astrophys. J.*, 557:389–398.

Utz, D., Hanslmeier, A., Muller, R., Veronig, A., Rybák, J., and Muthsam, H. (2010). Dynamics of isolated magnetic bright points derived from Hinode/SOT G-band observations. *Astron. Astrophys.*, 511:A39.

van Noort, M., Rouppe van der Voort, L., and Löfdahl, M. (2006). Solar Image Restoration by use of Multi-Object Multi-Frame Blind Deconvolution. In Leibacher, J., Stein, R. F., and Uitenbroek, H., editors, *Solar MHD The-*

ory and Observations: A High Spatial Resolution Perspective, volume 354 of *Astronomical Society of the Pacific Conference Series*, page 55.

van Noort, M., Rouppe van der Voort, L., and Löfdahl, M. G. (2005). Solar Image Restoration By Use Of Multi-frame Blind De-convolution With Multiple Objects And Phase Diversity. *Solar Phys.*, 228:191–215.

Vanninathan, K., Madjarska, M. S., Scullion, E., and Doyle, J. G. (2012). Off-limb (Spicule) DEM Distribution from SoHO/SUMER Observations. *Solar Phys.*, 280:425–434.

Vernazza, J. E., Avrett, E. H., and Loeser, R. (1981). Structure of the solar chromosphere. III - Models of the EUV brightness components of the quiet-sun. *Astrophysical Journal Supplement Series*, 45:635–725.

Vissers, G. and Rouppe van der Voort, L. (2012). Flocculent Flows in the Chromospheric Canopy of a Sunspot. *Astrophys. J.*, 750:22.

Vissers, G. J. M., Rouppe van der Voort, L. H. M., and Rutten, R. J. (2013). Ellerman Bombs at High Resolution. II. Triggering, Visibility, and Effect on Upper Atmosphere. *Astrophys. J.*, 774:32.

Vissers, G. J. M., Rouppe van der Voort, L. H. M., Rutten, R. J., Carlsson, M., and De Pontieu, B. (2015). Ellerman Bombs at High Resolution. III. Simultaneous Observations with IRIS and SST. *Astrophys. J.*, 812:11.

Vögler, A., Shelyag, S., Schüssler, M., Cattaneo, F., Emonet, T., and Linde, T. (2005). Simulations of magneto-convection in the solar photosphere. Equations, methods, and results of the MURaM code. *Astron. Astrophys.*, 429:335–351.

von der Luehe, O. (1993). Speckle imaging of solar small scale structure. I - Methods. *Astron. Astrophys.*, 268:374–390.

Vorpahl, J. and Pope, T. (1972). Solar Bright Points in 3840 Å and Hα. *Solar Phys.*, 25:347–356.

Vrabec, D. (1971). Magnetic Fields Spectroheliograms from the San Fernando Observatory. In Howard, R., editor, *Solar Magnetic Fields*, volume 43 of *IAU Symposium*, page 329.

Vrabec, D. (1974). Streaming Magnetic Features Near Sunspots. In Athay, R. G., editor, *Chromospheric Fine Structure*, volume 56 of *IAU Symposium*, page 201.

Watanabe, H., Kitai, R., Okamoto, K., Nishida, K., Kiyohara, J., Ueno, S., Hagino, M., Ishii, T. T., and Shibata, K. (2008). Spectropolarimetric Observation of an Emerging Flux Region: Triggering Mechanisms of Ellerman Bombs. *Astrophys. J.*, 684:736–746.

Watanabe, H., Vissers, G., Kitai, R., Rouppe van der Voort, L., and Rutten, R. J. (2011). Ellerman Bombs at High Resolution. I. Morphological Evidence for Photospheric Reconnection. *Astrophys. J.*, 736:71.

Welsch, B. T. and Longcope, D. W. (2003). Magnetic Helicity Injection by Horizontal Flows in the Quiet Sun. I. Mutual-Helicity Flux. *Astrophys. J.*, 588:620–629.

Wöger, F., von der Lühe, O., and Reardon, K. (2008). Speckle interferometry with adaptive optics corrected solar data. *Astron. Astrophys.*, 488:375–381.

Wöger, F., Wedemeyer-Böhm, S., Uitenbroek, H., and Rimmele, T. R. (2009). Morphology and Dynamics of the Low Solar Chromosphere. *Astrophys. J.*, 706:148–157.

Wolfenstein, L. (1978). Neutrino oscillations in matter. *Physical Review D (Particles and Fields*, 17:2369–2374.

Woods, T. N., Eparvier, F. G., Hock, R., Jones, A. R., Woodraska, D., Judge, D., Didkovsky, L., Lean, J., Mariska, J., Warren, H., McMullin, D., Chamberlin, P., Berthiaume, G., Bailey, S., Fuller-Rowell, T., Sojka, J., Tobiska, W. K., and Viereck, R. (2012). Extreme Ultraviolet Variability Experiment (EVE) on the Solar Dynamics Observatory (SDO): Overview of Science Objectives, Instrument Design, Data Products, and Model Developments. *Solar Phys.*, 275:115–143.

Yokoyama, T. and Shibata, K. (1996). Numerical Simulation of Solar Coronal X-Ray Jets Based on the Magnetic Reconnection Model. *Pub. Astron. Soc. Japan*, 48:353–376.

Zachariadis, T. G., Alissandrakis, C. E., and Banos, G. (1987). Observations of Ellerman bombs in H-alpha. *Solar Phys.*, 108:227–236.

Zirker, J. B. (1993). Coronal heating. *Solar Phys.*, 148:43–60.

Zuccarello, F., Romano, P., Guglielmino, S. L., Centrone, M., Criscuoli, S., Ermolli, I., Berrilli, F., and Del Moro, D. (2009). Observation of bipolar moving magnetic features streaming out from a naked spot. *Astron. Astrophys.*, 500:L5–L8.